AN INVESTIGATION OF TEMPERATURE IN FORM GRINDING

ZHIXIN LIN

A thesis submitted in partial fulfilment of the
requirements of Liverpool John Moores University
for the degree of Doctor of Philosophy

June 1999

ABSTRACT

The aims of the investigation were to predict temperature distributions in form grinding for a range of workpiece profiles and to evaluate the proportion of the energy entering the workpiece as a basis for the control of grinding temperatures and the avoidance of thermal damage. Based on previous work, the characteristics of form grinding were identified and theories and techniques established for analysis of form grinding temperatures.

The theory of the instantaneous infinite plane heat source was applied to form grinding. A temperature equation for grinding was established based on the assumption of a triangular heat flux distribution. A thermal model for form grinding was developed taking account of heat transfer to the grinding wheel, the chips, the fluid and to the workpiece. The thermal model was applied to a range of workpiece profiles to predict temperature distributions on different profiles.

A computer program for the thermal analysis was designed and developed. The distribution of temperature in the formed workpiece was calculated numerically using MATLAB. The program was designed for a range of typical workpiece profiles. It was used to calculate geometric contact length, real contact length, partition ratio and temperature distribution for each of the profiles. Temperature distributions were presented in the form of graphs.

Experiments were carried out to evaluate the thermal model and to reveal problems in form grinding. The temperature distributions for a vee form and for an inverted vee form were analyzed under dry and wet grinding conditions. The factors which effects grinding temperature were discussed. The factors include contact length, depth of cut, workspeed, temperature ratio, specific energy, partition ratio and workpiece shape. The experimental results show that predicted temperatures and measured temperatures agree reasonably well, when allowance is made for the experimental difficulties.

The investigation of the theoretical model was extended to the temperature distribution in creep feed grinding.

A method for optimizing a grinding operation was proposed and the application of the method was demonstrated. The method was based on the use of a design chart. The design chart can be used to determine grinding conditions so as to achieve maximum possible grinding productivity and to ensure workpiece quality at the same time.

ACKNOWLEDGEMENTS

I would like to express my sincere gratitude to Professor W. Brian Rowe, the Director of Studies, for his invaluable guidance and encouragement throughout the research and his creative suggestions in preparing this thesis.

Thanks are expressed to my second supervisor, Dr Michael Morgan, for his assistance in developing and calibrating the experimental system. Thanks are also due to my third supervisor, Professor B. Mills for his support during the period of research.

I would also like to thank Mr Paul Wright and the technical staff, for their support and advice in organizing the experimental facilities, Mr Michael A. Noord for his hard work and patience throughout the whole series of experiments, Mr Stephen Ebbrell for his hard work during the preliminary testing and Mr Peter Moran for his practical help in many aspects.

Thanks are due to the Advanced Manufacturing Technology Research Laboratory of Liverpool John Moores University for funding the research.

Finally, I wish to thank my parents and my family for their encouragement and patience over last few years.

NOMENCLATURE

Symbol	Meaning	S. I. Units
a	the wheel depth of cut	m
a_n	the normal depth of cut	m
a_{ns}	the normal depth of cut at the shoulder surface	m
a_{nc}	the normal depth of cut at the cylindrical surface	m
A	the area of the grinding contact zone	m^2
b	the width of cut	m
c	specific heat capacity	J/kgK
d_{se}	equivalent diameter of the grinding wheel	m
d_s	the diameter of the grinding wheel	m
d_w	the diameter of the workpiece	m
e_c	specific grinding energy	J/m^3
e_{cc}	specific grinding energy to the chips	J/m^3
e_f	specific grinding energy to the fluid	J/m^3
E_s	the modulus of elasticity of the grinding wheel	N/m^2
E_w	the modulus of elasticity of the workpiece	N/m^2
F_n	the normal grinding force	N
F_t	the tangential grinding force	N

h_w	height of the workpiece	m
h_c	convection coefficient of coolant	J/m^2sK
K_s	stiffness of the grinding wheel	m^2/N
K_w	stiffness of the workpiece	m^2/N
l	the contact length at any position in the contact zone	m
l_t	total contact length of the contact zone	m
l_g	the geometric contact length	m
l_f	the contact length between surfaces acted on by a normal force	m
l_c	the real contact length	m
n	concentration factor	
P	grinding power	W
P_{meas}	measured grinding power	W
P_c	the power distributed to the cuvre	W
P_n	the power distributed to a strip	W
q	heat flux distribution over the grinding area	W/m^2
q	average heat flux over the grinding area	W/m^2
r_s	radius of the grinding wheel	m
r_{sp}	radius of the rounded corner of the wheel	m
r_o	wear flat radius on the surface of the grain	m

R_w	fraction of the total energy partitioned to the workpiece	
R_s	fraction of the total energy partitioned to the grinding wheel	
R_{ch}	fraction of the total energy partitioned to the chips	
R_f	fraction of the total energy partitioned to the fluid	
R_{ws}	energy partitioning between the workpiece and wheel	
R_r	the roughness factor	
t	is the time since a position entered the contact zone	s
τ_o	is the total time of contact	s
v	heat source velocity	m/s
v_f	infeed rate	m/s
v_s	wheel velocity	m/s
v_w	workpiece velocity	m/s
xi	an arbitrary position in the grinding contact zone	m
Z	material removal rate	m^3/s
z	the distance between the heat source and the finished surface	m
XYZ	Cartesian coordinates referenced to workpiece	
α	thermal diffusivity, defined as k/rc	m^2/s
α,β	angles of profile on workpiece	degree
ϕ_f	infeed direction of the wheel in angle approach grinding	degree

ϕ_{ws}	angle between the workpiece axis and the grinding wheel axis	degree
κ	thermal conductivity	W/mK
κ_{ge}	thermal conductivity of the grain	W/mK
μ	the ratio between the tangential force and the normal force	
θ	temperature	K
θ_f	fluid temperature	K
θ_f	the temperature experienced by a flat plane	K
θ_m	maximum temperature	K
θ_{meas}	measured temperature	K
θ_{melt}	the melting temperature of the workpiece	K
θ_p	the temperature at a discontinuity	K
θ_w	temperature on the grinding surface	K
ρ	density	kg/m^3
υ_S	Poisson's ratio of the grinding wheel	
υ_w	Poisson's ratio of the workpiec	

CONTENTS

LIST OF FIGURES

LIST OF TABLES

Chapter 1 Introduction

1.1 Background to the investigation

Form grinding is used for many engineering components and cutting tools with complex forms which cannot be effectively manufactured using a plain cylindrical wheel. In form grinding as in other grinding processes, high temperatures can sometimes lead to loss of quality. The risk of damage is often increased in form grinding. One of the differences is that the interface zone between the grinding wheel and the workpiece in form grinding may be much bigger than in, for example, cylindrical grinding. Also it is more difficult to ensure the delivery of the coolant into the contact zone. The process may therefore be less efficient leading to greater heat generation. The heat accumulation in the workpiece causes temperature rises and if sufficient, leads to thermal damage. On the other hand, a large contact area spreads the heat over a larger area which reduces the maximum temperature.

The temperature distribution is an indicator of the heat accumulated in the workpiece. If the temperature distribution is known it can be used with a model of the grinding process to predict the onset of the workpiece thermal damage. Consequently there is also potential for process control and prevention of thermal damage using temperature prediction with an adaptive control system. It is therefore important to investigate the temperature distribution in form grinding in order to establish a basis for the development of strategies that enable thermal damage to be avoided.

1.2 Aims and objectives

The aims of the research were to develop an approach to investigate the temperature distribution in form grinding, and to evaluate the total grinding energy entering the workpiece. In order to achieve the aims it was decided to set the following objectives:

- to review previous research into temperatures generated in form grinding.

- to develop a thermal modelling approach for form grinding based on previous work on plane grinding and cylindrical grinding.

- to apply the thermal model to analyse temperature distributions for particular forms.

- to analyse the energy partition ratios for the workpiece, grinding wheel, chips and coolant.

- to undertake a series of experiments for form grinding and measure temperatures on the workpiece surface, the measured temperatures to be compared with the results of theoretical analysis for validation.

- to analyse the effects of workpiece shape on temperature distribution.

- to develop a design chart for optimum grinding conditions in order to advance quality and productivity based on the investigation.

1.3 Scope of the investigation

Previous investigations on grinding temperature and workpiece thermal damage are reviewed in chapter 2. Previous work includes thermal modelling, grinding temperature measurement and analysis, the analysis of the contact mechanism between the grinding wheel and the workpiece, energy partitioning, the coolant effect, form grinding and creep feed grinding. Finally, as the basis for the current investigation, some achievements in the Advanced Manufacturing Technology and Tribology Research Laboratory are summarised.

In chapter 3, a solution for the surface and sub-surface temperature is derived for a triangular heat flux distribution based on one dimensional heat transfer.

In chapter 4, a thermal model for form grinding is proposed. The contact area between the grinding wheel and workpiece plays a very important role in the thermal model, hence the geometric contact lengths in several typical grinding operations are analysed. The typical grinding operations include face grinding, vee form grinding, flute form grinding and angle approach grinding. The real contact length is also discussed. The grinding power distribution on the contact area and determination of the energy partitioning are key problems in grinding temperature prediction. The methodology

used to determine power distribution and to determine the partition ratios are described.

Finally, the influence of convection cooling on grinding temperature and the temperature distribution at a point of discontinuity on a formed workpiece is discussed.

The computer program for thermal analysis is introduced in chapter 5. The program was developed using MATLAB. The program was designed for several typical workpiece profiles including the face grinding, vee and inverted vee form grinding, flute form grinding and angle approach grinding. The program was used to calculate geometric contact length, real contact length, partition ratio and temperature distribution for each of the profiles. The output of the program can be numerical or graphical.

The experimental system developed for the investigation is described in chapter 6. The experimental system was required to measure grinding temperature, grinding power and the real depth of cut of the grinding wheel. The experimental system consisted of three sub-systems, the temperature measuring sub-system, the grinding power measuring sub-system and the depth of cut measuring sub-system. Issues concerning the grinding machine set up, jig assembly, thermocouple installation and calibration, power sensor calibration, signal conditioning, data logging and post processing and the method for depth of cut measurement are discussed. The experimental procedure is also described.

Experimental results are analysed in chapter 7. The temperatures measured from experiments are compared with those calculated using the thermal model. The temperatures of the vee form and inverted vee form workpieces under dry and wet grinding conditions are analysed. The factors affecting grinding temperature are discussed. The factors include contact length, depth of cut, workspeed, specific energy, partition ratio and workpiece shape. For each workpiece profile, such as the vee and inverted vee form the temperature on the short flank, long flank and apex of the inverted vee form or valley of the vee form are discussed separately.

An introduction to creep feed grinding is presented in Chapter 8. Previous creep feed grinding studies are reviewed and major characteristics of creep feed grinding are summarised. A theoretical investigation of temperature distributions in creep feed grinding based on the thermal model for form grinding is presented in chapter 3.

Temperature distributions at the contact interface and on the finished surface were calculated and illustrated graphically using the computer program. The results are analysed and explained.

A method for optimising a grinding operation is proposed in chapter 9. The method employs a design chart. The design chart is used to determine grinding conditions for maximum productivity and to ensure workpiece quality at the same time. The methodology for deriving the design charts is described. A worked example, using a design chart is presented.

In Chapter 10, a summary of the advances achieved, and the conclusions reached are presented.

Recommendations for further work are given in Chapter 11.

Chapter 2 Literature review

2.1 Thermal models of grinding

The foundation for almost all later work is the paper on moving heat sources by Jaeger [Jaeger, 1942]. The moving band source model is widely used as a basis for modelling shallow cut grinding processes. The multitude of short intense energy inputs which arise from all the grain-workpiece interactions taken together are usually assumed to be equivalent to a uniform band heat source moving along the workplace surface at the workspeed. The analysis of a moving heat source on a semi-infinite body by Jaeger was used in most theoretical investigations for temperature prediction.

Outwater and Shaw applied the moving heat source model to the grinding process to obtain an equation for the mean surface temperature [Outwater, 1952]. The equation predicted a surface temperature as high as 3000° F for a fine grinding operation. Values of the mean temperature between a chip and the grinding wheel were estimated using a wheel-work thermocouple. The analysis showed that virtually all grinding energy was dissipated as heat in the grinding zone but only a proportion of the grinding energy was applied to the workpiece as a band source. Outwater and Shaw attempted to use a shear plane model to determine the proportion.

Hahn challenged the assumption of the heat generation taking place at the shear plane [Hahn, 1956]. It was argued that in grinding unlike conventional single point cutting, the rubbing forces on the grain at the clearance face are appreciable. This was justified on two accounts. Firstly, the geometry of a grain indicated that there is no clearance angle in grinding. The second argument was based on the experimental evidence of the grinding forces. The ratio of tangential to normal force in grinding is found to be typically of the order of 0.3 to 0.5 which is characteristic of a sliding process. This suggests that the principal location of heat generation is at the grain wear flats. In turning, the ratio of tangential to normal forces is typically 2 to 3. Thus the grinding process is more realistically described by considering the frictional rubbing forces on the wear flat and neglecting the shear plane cutting forces. This was called the 'rubbing hypothesis'.

Hahn clarified some of these features by describing test results and then formulating suitable hypotheses to explain them [Hahn, 1962]. In the tests, the grinding wheel was pressed against the workpiece with a constant normal force under plunge grinding conditions so that a uniform force intensity across the grinding wheel face was obtained. The normal force between the grinding wheel and the workpiece was prescribed. The principal variable measured was the rate of material removal. The tangential grinding force was measured by a specially built strain gauge torque dynamometer upon which the work-holding chuck was mounted. It was found that higher force intensities are required in order to exceed the ploughing-cutting transition. A basic factor in the grinding of metals of the same hardness is the fracturing characteristics at the 'free' plastic surface. It was found that the rate of wheel wear for hard and soft wheels is a function of the actual length of the contact zone, and is not dependent on their mechanical strength until gross wheel breakdown occurs.

Des Ruisseaux and Zerkle investigated the temperature in the vicinity of chip formation and related this temperature to the temperature experienced by the workpiece surface which remained after grinding [Des Ruisseaux, 1970 (1)]. The results indicated that the temperature predicted in the region of chip formation can be substantially greater than those which resulted on the remaining surface of the workplace. Des Ruisseaux and Zerkle applied Jaeger's theory of moving heat sources to two models to determine the effect of convective surface cooling on temperature distributions [Des Ruisseaux, 1970 (2)]. The paper acknowledged the difficulty of determining and applying a convection coefficient which is different in the grinding zone from the surrounding area but suggested the importance of cooling in the contact region.

Lee, Zerkle and Ruisseaux made an experimental study of thermal aspects of cylindrical plunge grinding [Lee, 1970]. In cylindrical plunge grinding, the workpiece temperature was considered as a superposition of a base temperature and an interference zone temperature. A solution for the transient base temperature distribution was derived. The experiment was divided into two parts. Firstly, the heat transfer coefficient at the workpiece surface was measured. Secondly, specific grinding energy and workpiece temperatures were measured. The energy entering the workpiece during grinding was determined from the base temperature solution and experimental data. It was concluded that the energy entering the workpiece is 75 to 85 percent of the total grinding energy

during dry grinding and 25 to 35 percent during wet grinding. The proportion for wet grinding is much lower than the proportion found by later investigators, which suggests that the method for wet grinding was flawed.

Maris and Snoeys compared models for evaluation of temperature in the heat affected zone [Maris, 1973] and considered energy partitioning. The predicted temperature fields and theoretically determined heat affected zones were compared with experimental data. They suggested 70%-80% of the energy is applied to the workpiece and about 15%-20% is applied to the chips and the remaining part conducted to the grinding wheel, although the heat to the chips and to the wheel could not be accurately established. It was suggested that coolant is effective only when the coolant can penetrate into the contact zone in order to reduce the high local temperature in the contact area.

Malkin showed the importance of the grain wear flats for the specific energy in grinding. Malkin calculated the maximum heat which could be convected from the workpiece zone by the chips by considering the removal rate and the energy required to raise the material removed to melting temperature [Malkin, 1974].

Howes found that fluid film boiling severely limits cooling when the temperature in the grinding zone exceeds the boiling temperature for the fluid [Howes, 1987]. Above the boiling temperature the principal effect of the fluid is bulk cooling outside the contact zone. It was therefore concluded that the importance of the fluid for shallow cut grinding is the reduction in the grinding forces and grinding temperature due to more effective lubrication.

Rowe and Pettit developed a thermal model to predict the position of the burn boundary taking into account energy conducted to the grinding wheel [Rowe, 1988]. By the use of upper and lower bounds, it was also possible to take account of chip energy and energy convected by the fluid. Compared with previous thermal models, the advance of Rowe's model was the partitioning of the heat flux between the grinding wheel and the workpiece based on two bodies in relative sliding contact. This allowed more realistic values of heat flux to be employed in the model. The basis of thermal modelling proposed had the advantages of simplicity and reasonable accuracy of prediction. Rowe

adopted aspects of the previous work by Des Ruisseaux and Zerkle in that the coolant effects and the maximum chip convection effects by Malkin were used to modify the energy applied at the grain-workpiece interaction and the result compared with the results obtained without these effects. The effect of a deformable wheel was also included. These two methods led to upper and lower bound solutions which were found to enclose the burn boundary results obtained from several publications and also enclosed experimental results. A key feature of this work was the determination of the workpiece-wheel partitioning factor R_{WS} based on a simultaneous solution of the conduction into the grinding wheel and into the workpiece. The average temperature in the grinding zone was assumed to be equal for the wheel and for the workpiece.

Shaw proposed a simplified approach to grinding temperature modelling [Shaw, 1990]. Shaw linearized the Jaeger model and employed a simplified theory in estimating the partition of energy between wheel and workpiece. The linearized model provided a convenient means for estimating the fraction of the total grinding energy going into the workpiece.

Tönshoff, Peters, Inasaki and Paul reviewed modelling and simulation of grinding processes [Tönshoff, 1992]. Grinding energy models and force models were presented. The kinematic and energetic processes were taken into consideration for temperature models. Different approaches to modelling were compared in the paper. The benefits and the limitations of model application and simulation were also discussed. In the investigation, the distinction was made between physical models which were deductively derived from basic physical principles and empirical models which were developed on the basis of grinding tests. The approaches to the modelling and simulation of grinding processes were compared and critically evaluated. It was concluded that it is possible to describe grinding in the form of models in order to make grinding reproducible.

Chang and Szeri modelled the grinding process under the condition that a single phase coolant was applied [Chang, 1994]. It was found that due to the shortness of the residence time of both grit and coolant and the high rate of heat generation, local thermal equilibrium is unlikely to be reached within the grinding zone. Their model was therefore developed to calculate distinct temperatures for coolant and grit. The

wheel was viewed as a porous matrix, saturated by coolant and air. Volume averaging techniques were applied to solve the problem of heat conduction in the porous media. The heat conduction in the direction of motion was included in the model. The model was used to calculate the maximum temperature in the grinding zone, the workpiece temperature distribution, the partition ratio for grinding energy entering the workpiece and the critical grinding energy flux for workpiece burn. Calculations were compared with experimental data for two types of coolant, water and oil.

Lavine, Malkin and Jen analysed the heat transfer into the grains of the grinding wheel assuming the grains to be conical in shape [Lavine, 1989]. Later Rowe and Black [Rowe, 1996] showed that the cone assumption was less accurate than the plane grain assumption of Hahn [Hahn, 1962], despite the increased complexity of the cone assumption. Lavine experienced a difficulty in specifying the temperature matching condition [Lavine, 1991]. The difficulty arises when the energy conservation equation is based on a mixture of localised grain contact temperatures and a non localised background temperature. For convective cooling, Lavine's model considered the wheel and grinding fluid to be a composite solid. The heat flux entering the workpiece surface was taken as uniform. A problem encountered was that the properties of the composite solid were difficult to specify and that the specification of the properties depended on specifying the porosity of the wheel very near the workpiece surface.

An improved analysis for the partitioning of the grinding energy at the grain-workpiece interface was presented using Lavine's conical grain assumption [Rowe, 1991]. A method was proposed to establish a wheel-workpiece partition ratio based on temperature compatibility at the grain-workpiece interface. This method ensures temperature matching is applied at the interface and is explicit. It was argued that the analysis by Lavine failed to correctly identify temperature compatibility. The method of Rowe, 1988 avoided this difficulty by establishing a workpiece-wheel partition ratio based purely on a common background temperature of the wheel and workpiece interface.

Rowe and Morgan, 1991 suggested that the proportion of the grinding energy entering the workpiece might be analysed either for the whole grinding wheel-workpiece contact zone or for the average grain contact zone which was two orders smaller. It was considered that a grinding contact zone analysis which was simpler and relied on

composite wheel properties might be useful in practice. However, it was recognised that there was a need to determine the effective thermal properties of the composite wheel. Properties of composite wheels are not readily available. It was pointed out that there was a need to define an approximate average size of the grain contact area in order to achieve accurate solutions for the wheel-workpiece partition ratio with grain level analysis.

Rowe recognised that the deflections within the grinding contact zone influenced the intensity of the heat flux and hence the temperature in grinding [Rowe, 1993]. The relationship between the grinding wheel and the workpiece contact length was therefore established. The real contact length between the grinding wheel and the workpiece was modelled based on the theory of contact mechanics. The proposed model more accurately described the mechanics of grinding contact than previous contact models. Application of the proposed model to published experimental data for plunge surface grinding explained why measured contact length can be 50% to 200% greater than the geometric contact length. An increased contact length reduces the maximum background temperature for the same energy input. It was found that the main parameters influencing contact length are the real depth of cut, the elastic deflection of the grinding wheel and the surface topography of the grinding wheel.

New findings were presented for temperature, heat flux distribution and the implications for workpiece damage and partition ratio [Rowe, 1995]. Workpiece temperatures were measured using a 25μm single pole thermocouple assembly. It was found that the critical temperature under grinding conditions for the onset of temper colours for ferrous materials lies within the range 450 to 500 deg.C. Measured temperatures in the contact zone compared better with theory assuming a square law heat flux than assuming a uniform heat flux. The effective contact length for vitrified CBN and alumina wheels was confirmed to be greater than the geometric value. Substantially lower partition ratios were found with CBN compared to alumina. Rowe and Black compared triangular and square law heat flux distributions and indicated that both give improved prediction of measured temperature distributions.

Guo and Malkin developed a thermal model for the transient temperature distribution under regular and creep-feed grinding conditions [Guo, 1995]. Numerical results were

obtained using a finite difference method. The results indicated that the workpiece temperature rises rapidly during initial wheel-workpiece engagement. The temperature distribution subsequently reaches a quasi-steady state magnitude if the workpiece is sufficiently long.

Jen and Lavine further improved their model and used it to predict the occurrence of film boiling of the grinding fluid [Jen, 1996]. It was found that the predicted maximum temperatures were in better agreement with experimental results when the effect of film boiling was included.

The heat flux distributions and the convective heat transfer coefficient are important for the heat transfer analysis of grinding. Inverse heat transfer methods were used to estimate the heat flux and convection heat transfer coefficient distributions on the workpiece surface by Guo and Malkin [Guo, 1996 (1)]. Three inverse heat transfer methods were developed: temperature matching, integral and sequential methods. The accuracy and stability of each method was evaluated using simulated temperature data. The methods were applied to estimate the distributions of the heat flux and the convection heat transfer coefficient [Guo, 1996 (2)]. The results indicated that the heat flux to the workpiece was linearly distributed along the grinding zone and could be represented by a triangular heat source. It was predicted that about 70 to 75 percent of the total energy was transferred as heat to the workpiece when grinding steel with a conventional aluminium oxide wheel and 20 percent with CBN superabrasive wheels, based on a geometric contact length.

Rowe compared the theoretical values of partition ratio with the values of partition ratio evaluated from experimental measurements [Rowe, Morgan and Black, 1996]. Improved agreement was found for partition ratio and temperature when allowance was made for convection by the chips. It was concluded that energy convection by the chips is particularly important when the specify energy is low.

Rowe and Black further developed the models of Rowe and Morgan to predict the background temperature in grinding based on experimental findings [Rowe and Black, 1996]. The thermal model took into account a triangular heat flux distribution in the grinding zone, the real length of contact and experimentally validated grain thermal properties. It was shown that the plane grain assumption by Hahn in 1956 based on 2-D

heat transfer, was more accurate than Lavine's conical grain assumption based on 1-D heat transfer. This allowed a simple grain contact analysis to be developed to predict the energy partitioning between the workpiece and wheel. The analysis takes into account two dimensional transient heat transfer in the grain and maintains the temperature compatibility at the grain wear flat-workpiece interface. The proportion of the total energy entering the workpiece was estimated by correlating measured temperature distributions with theoretical distributions.

Rowe investigated temperatures in CBN grinding. The main advantage of a CBN grinding wheel is the long wheel life owing to the hardness of the CBN abrasive. Research has confirmed another advantage of CBN, which is cooler grinding. The new research allows the temperature in grinding to be predicted based on experimentally validated CBN thermal properties. A feature of CBN grinding wheels is the reduced risk of thermal damage to the workpiece. This advantage can allow a marked increase in removal rate whilst maintaining surface quality of the component compared to grinding with conventional abrasives such as aluminium oxide due to the lower grinding specific energy. The experimental investigation has shown that a major advantage of CBN grinding is that a lower proportion of the total grinding energy enters the workpiece compared to grinding with alumina wheels. The results further indicate that the effective thermal conductivity of CBN abrasive is considerably lower than its reported theoretical value of 1300W/mK.

2.2 Form grinding

Gordeev published a paper on angle approach form grinding [Gordeev, 1976]. The angle approach grinding operation consisted of the simultaneous machining of several adjacent surfaces on a cylindrical component. Gordeev proposed equations for contact lengths on both the cylindrical surface and the shoulder surface. It was found that the ratio of the two contact lengths varied with the ratio of grinding wheel diameter at a particular cross section and the diameter of the cylinder. The contact length ratio increased with increasing diameter ratio. The contact length ratio also increased with the approach angle.

Graham and Falconer investigated the problem of wheel-workpiece conformity in form grinding [Graham, 1978]. The conformity of fit between a grinding wheel and a

workpiece was defined in terms of the curvature difference between the appropriate adjacent wheel and workpiece surfaces. Both static and dynamic conformities were investigated and it was found they were simply related. In practical grinding situations, the static conformity was greater than the dynamic conformity by a factor equal to half the wheel/workpiece speed ratio. The investigation revealed that the conformity of fit was greater when the curvature difference between a wheel and a workpiece surface was smaller. Greater conformity tended to result in the production of relatively thin grinding chips. Thus, the grinding wheel tends to exhibit relatively hard grade characteristics and the specific energy of metal removal is high. It was also found that the conformity of fit between an annular face and the appropriate wheel surface is relatively sensitive to changes in wheelhead approach angle in an external cylindrical form grinding operation. When the wheelhead approach angle was increased from 10° to 45°, the conformity of fit between the wheel and the workpiece annular face was altered by a factor of four. The consequence of conformity of fit reduction was that chip thickness was increased and the effective hardness of the grinding wheel was reduced.

Saljé, Damlos and Teiwes investigated surface profile grinding and angular plunge profile grinding [Saljé, 1981]. Several problems were found and discussed. The first problem was that an axial force occurred when grinding asymmetrical profiles. The axial force caused a major problem, which was the deformation of the grinding wheel in the axial direction. The deformation of the grinding wheel resulted in an inaccurate workpiece profile. The second problem was that surface roughness of the workpiece profile varied with different dressing conditions and different plunge angles. It was suggested that the minimum deformation in the axial direction could be achieved by selecting correct grinding wheel geometry and stiffness. It was also suggested that the dressing conditions and plunge angle must be selected so as to avoid burn or chatter marks on the workpiece profile.

In form grinding operations, problems of burn marks, thermal cracks and inaccuracies in ground workpiece profiles are often encountered. Trmal carried out a general approach to those problems by geometrical analysis and comparing process parameters [Trmal, 1982]. A high wheel-workpiece conformity is indicative of the difference between plane and form grinding. The effect of wheel-work conformity was assessed experimentally. It was found that high conformity of the wheel face and work shoulder

resulted in a low level of self-dressing and increased risk of thermal problems on the workpiece surface. It was also found that the thermal problem could be reduced by coarser dressing, an increase in approach angle and better coolant application. The investigation showed that in angle approach grinding the use of two independent infeeds could provide means for optimisation of the cycle. Experiments showed that a grinding wheel with a slotted face could increase the level of self-dressing and improve the coolant application.

2.3 Contact length investigation

The contact length between the wheel and workpiece in the grinding has been identified as the chief factor influencing the grinding process and the accuracy of the ground surface.

Makino measured temperature using a thermocouple and identified that the actual length of the heat source was two to three times the geometric contact length [Makino, 1966]. The assumption of a geometric contact length overestimates the heat flux density in the contact zone and as a result predicts artificially high temperatures.

Verkerk investigated the real contact length in grinding by measuring the heat pulses due to the transition of grains past a thermocouple embedded in the workpiece [Verkerk, 1975]. It was found that the real contact length was substantially greater than the geometrical value. This means that the band heat source for deformable wheels will be much wider than for a rigid grinding wheel and the maximum grinding zone temperature is correspondingly reduced.

Gu and Wager investigated the contact zone in surface grinding and presented a technique for measuring the contact length between wheel and workpiece [Gu, 1990]. The techniques which were employed for the investigation of contact length were categorised into two groups. One group related to the thermocouple technique, where the contact length was measured in-process. The other group was based on the technique of suddenly interrupting the grinding process so as to obtain traces of grains left on the surface of the contact zone. By means of the technique, the profile and the length of the contact zone were obtained. Two major distinctions between these two groups were identified. First, different results were obtained. The results from the

former indicated contact lengths between the wheel and workpiece almost approaching the lengths of the trace left by the highest grain of the contact part on the wheel circumference, while those of the latter technique were traces of individual grains on the contact zone. Secondly, an interrupted patch technique presented the same, albeit many. grains repeatedly to the workpiece, whereas the thermocouple techniques could randomly sample a wider range of the total grains on the wheel. Thus, without a strict definition, it is difficult to determine which of the traces of individual grains by the latter technique could be taken as representative of the contact situation between the wheel and workpiece. In the absence of a clear definition of the contact length between the wheel and workpiece, it was proposed to use the longest of the traces left on the workpiece by individual grains. This provided more ready comparison with thermocouple techniques.

Two significant ways of dividing contact zones were used. The first way was dividing the contact region into two sliding regions and one cutting region using the thermal contact characteristics between the workpiece and grains. The evidence of the two sliding regions was presented. The second way was dividing the contact zone into the entry regions and exit region. The entry region was defined as the region between the starting contact point and the wheel centre. The exit region was defined as the remainder of the contact zone. The results indicated that such divisions led to a better understanding of the contact zone. The experiments indicated that there was a sliding region, following the cutting region. The sliding region influenced the roughness of the workpiece in conventional surface grinding. The relative lengths of the sliding region and the cutting region changed with grinding conditions. From strictly geometrical considerations with respect to the wheel centre, it was reasonable to divide the contact zone into the entry region and the exit region. The experiments showed that the two regions related to the symmetric models of other investigations only in the case of shallow cutting depths. For cutting depth greater than 0.007 mm, the contact length was shown to be the geometric contact length plus a constant.

Zhou and Lutterwelt investigated grinding contact length and divided the contact length distinctly into the maximum contact length and the local contact length [Zhou, 1992]. The maximum contact length, is the maximum interface length between the grains on the wheel peripheral surface and workpiece in the whole grinding zone. The local

contact length is the interface length between the grains on the wheel peripheral surface and workpiece at any point in the whole grinding zone. A method for measuring both contact lengths was proposed. The method was called the applied power source method. The method was characterised by two advantages over other methods. The first advantage was both maximum contact length and local contact length could be conveniently measured. The results were stable and reliable. The second advantage was that the method was simple, easy to implement and the signal for contact length was strong. The results obtained showed that the maximum contact length was about 22% to 25% longer than the local contact length.

Qi and Rowe proposed a contact length model based on the mechanics of cylinders in contact and included the effect of the surface roughness of the grinding wheel [Qi, 1994]. The contact length model expressed the contact length as the orthogonal combination of the contact length due to elastic deflections and the contact length due to the depth of cut. The contacting surfaces in the abrasive machining process are far from smooth. It was therefore not possible to model the elastic deflection using Hertz analysis. The real contact length based on the analysis of Hertz was modified using a roughness factor approach.

Qi, Rowe and Mills further investigated the contact behaviour between a grinding wheel and a workpiece in grinding [Qi, 1997]. The measurement methods for assessment of contact length were investigated. The applied power source method was judged to give the most reliable measurement of contact length. The measured results confirmed that the measured contact length is considerably longer than geometric contact length. It was stated that there was considerable evidence that the measurements represented real contact phenomena.

2.4 Grinding power partitioning

When calculating grinding temperatures using moving heat source theory, it is usually assumed that thermal properties are temperature-independent. Isenberg and Malkin took the effects of variable thermal properties on the temperatures into consideration in their numeric analysis of temperature [Isenberg, 1975]. Two non-linear cases were studied. One case was for carbon steel where the thermal conductivity decreased and the specific heat increased with temperature. The other case was for a material where

thermal conductivity decreased with temperature and the specific heat kept constant. Compared with the constant-property model, the maximum surface temperatures were found to be significantly higher with small Peclet numbers and strong heat sources, but the average surface temperature within the band was much less affected by the variations of thermal properties with temperature. The variable-property model also indicated significantly larger transverse temperature gradients, a phenomenon that should cause greater thermal stresses.

In order to predict the thermal damage threshold, the energy partitioning to the workpiece needs to be determined. However, it is not practicable to measure directly the heat input into the workpiece or energy partitioning to the various heat sinks within the grinding zone. Rowe, Morgan, Pettit and Lavine therefore employed heat transfer models to evaluate the energy partitioning analytically [Rowe 1990]. Several thermal models were developed by employing different energy partitioning assumptions. The effects of each model on the predicted critical values of temperature and specific energy were investigated. Based on the investigation, it was proposed to model the energy partition based on a grain model using a non-steady heat solution. A simple way of approximating the large reduction of heat into the grinding wheel resulting from the above effect was to employ a factor based on the ratio of the wear flat area to the workpiece contact area. This ratio was employed to modify the equation for the partition ratio. The assumption of a composite wheel was another way to introduce a modification of partition ratio which produced a similar order of change. In employing the composite wheel-workpiece thermal models the analysis was simplified. However, the results were wheel dependent.

Ramanath and Shaw investigated the abrasive grain temperature at the beginning of a cut in fine grinding [Ramanath, 1988]. In any grinding operation heat flows periodically into the abrasive grains in the surface of the wheel during wheel-work contact and is extracted during the remaining portion of a single revolution of the wheel. If an assumption could be made that all of the heat flowing inward is extracted outward during the cooling portion of a single wheel revolution, then the partition ratio for heat entering the workpiece might be readily estimated. The research was focused on the conditions under which the assumption represented an acceptable approximation. The

theoretical values of the partition ratio were claimed to be in good agreement with the measured values using aluminium grinding wheels and CBN grinding wheels.

2.5 The effect of coolant on temperature

Lavine proposed a simple model for convective cooling during the grinding process [Lavine, 1988]. The functions of the coolant were summarised. The first function was lubrication, thereby reducing the amount of heat generated. The second function was to remove heat from the wheel and workpiece surfaces via convection. The third function was to help to keep the grinding debris from sticking to these surfaces. Oil-based fluids were better lubricants and water-based fluids were better coolants. The model considered the wheel and grinding fluid to be a composite solid, moving at the wheel speed. The properties of this composite were difficult to specify and were very sensitive to the porosity of the wheel very near the workpiece surface. The model predicted the convective heat transfer coefficient at the workpiece surface, the fraction of energy entering the workpiece and the workpiece surface temperature. The model showed remarkable agreement with published data for conventional and creep feed grinding conditions.

Okuyama, Nakamura and Kawamura proposed a method to measure the heat transfer coefficient in the vicinity of the wheel-workpiece contact zone [Okuyama, 1991]. The accuracy of measurement was estimated by using the finite element method and the factor for correcting the measured results was derived. The experiments were carried out under different conditions of supplying coolant. The best methods to increase the cooling efficiency were found. The first method was to set the velocity of coolant to more than the critical value to penetrate the air flow layer formed around the wheel periphery. The second method was to use a nozzle with a thin throat, about 1mm in height, and attach a scraper plate above the nozzle outlet. The third method was to choose a wheel of large grain size and dress roughly. The fourth method was to set a higher wheel speed. Values of heat transfer coefficient were obtained in the investigation. Appropriate conditions for increasing the cooling efficiency were clarified.

Kim, Howes and Gupta conducted an investigation to determine whether an economic domain of shallow-cut grinding existed below the film boiling temperature [Kim,

Howes and Gupta, 1997]. The investigation identified the potential benefits of grinding below film boiling and provided preliminary theoretical evidence based on thermal analysis of grinding and the results of previous research. The evidence showed that an economic domain in shallow-cut grinding could exist. Their thermal analysis indicated that specific removal rates of 16 mm^3/mms might be possible with alumina wheels operating at conventional wheel speeds with very small depths of cut. Film boiling of the fluid in creep feed grinding was known to cause catastrophic overheating of the workpiece and consequential thermal damage. In shallow-cut grinding, the consequences of the fluid were less obvious but often just as catastrophic. The effect of film boiling was explained. When film boiling occurs, the grinding fluid does not act as an efficient coolant or lubricant, and the workpiece temperature and grinding forces rise to match those of dry grinding. It was concluded that grinding below film boiling offers several distinct advantages. Thermal damage to the workpiece surface was avoided as cooling and lubricating properties of the fluid remain intact. The economic grinding domain was identified for shallow-cut grinding.

Lavine and Jen used a thermal model which was previously developed to predict the temperature in the grinding zone to predict the occurrence of film boiling of the grinding fluid and to determine whether or not workpiece burn would subsequently occur [Lavine, 1991]. Both film boiling and workpiece burn were assumed to occur at critical grinding zone temperatures. The effect of various parameters such as fluid and grain types were explored under conventional or creep feed grinding conditions. Grinding fluids are used to lubricate and to remove grinding heat from the grinding zone. Under some circumstances, the grinding fluid may undergo film boiling, causing a sudden increase in temperature. The elevated temperature may or may not cause thermal damage to a workpiece depending on a variety of factors. The occurrence of film boiling was modelled by assuming that it occurs when a critical temperature was reached. The critical temperature was approximately 100°C to 130°C for water and 300°C for oil. On occurrence of film boiling, the heat transfer to the fluid was negligible. The consequence was a sharp rise in the workpiece background temperature. For alumina wheels, this rise was insufficient to cause workpiece burn in conventional grinding, but it did cause workpiece burn in creep feed grinding. For CBN wheels, the heat removed by the abrasive grains was significant. As a consequence, higher grinding

power was required to cause film boiling. Therefore, it was predicted that workpiece burn would usually not occur even after film boiling occurs.

Jen and Lavine modified the earlier model to allow film boiling over a portion of the grinding zone and later they indicated that the model was only valid when the grinding power input is uniformly distributed along the grinding zone [Jen, 1992]. Jen and Lavine developed an improved general grinding model [Jen, 1995]. The improved model accounted for the variation of heat fluxes along the grinding zone. With appropriate modification, the improved model was used to account for film boiling with variable heat fluxes [Jen, 1996]. An analysis that accounted for the effect of gas entrapment in a cavity was presented to estimate the required wall superheat to initiate the nucleate boiling of a bubble embryo. It was found that once nucleate boiling begins, the bubble growth time required to blanket the workpiece surface was much smaller than the time that a cavity stayed in the grinding zone, thus, the workpiece temperature rose rapidly after the onset of nucleate boiling because the cooling effect of the grinding fluid diminished in a very short time. It was claimed that the predicted maximum temperatures were in good agreement with the experimental results and the predicted workpiece temperature distributions along the grinding zone agreed qualitatively with experimental results. The experimental results showed that when film boiling occurred, the workpiece background temperature increase was greater under creep feed grinding conditions than under conventional grinding conditions.

Chapter 3 The triangular heat source solution

3.1 Theoretical basis

In grinding, a common cause of damage to machined parts arises from the intensity of the energy input in the grinding zone. It has been suggested [Rowe, 1991] that thermal damage can be avoided if the temperature of the workpiece surface is kept below a critical level. It is therefore important to predict temperatures in grinding to control thermal damage.

In order to identify the temperature distribution in grinding, it was initially assumed that the workpiece is a semi-infinite body and in order to simplify the heat transfer problem it was decided to take account of heat transfer in one dimension using the solution for an instantaneous infinite plane heat source.

In the instantaneous infinite plane heat source theory as shown in Figure 3.1, the temperature rise, due to an average heat flux resulting from a plane heat source at the point M is [Grigull and Sandner, 1984]:

$$\theta = \frac{\bar{q}}{c\rho(4\pi\alpha t)^{1/2}} \exp\left(-\frac{z^2}{4\alpha t}\right) \tag{3.1}$$

where

$\bar{q}$ is the average heat flux of the infinite plane heat source

z is the distance between the point M and the infinite plane heat source

t is the time period of temperature rise

It can be seen from equation 3.1 that the temperature at any point near the heat source varies with the distance, z between the point and the plane. In other words, it is one dimensional heat transfer.

3.2 Heat flux distribution over the contact length

The grinding temperatures are dependent on the heat flux generated in the contact zone. In order to calculate the grinding temperature, it is necessary to specify the heat flux distribution in the grinding zone. The heat flux is often modelled as either a rectangular or a triangular continuous planar heat source of average intensity q which moves along the surface at the workspeed, as shown in Figure 3.2.

In grinding, the depth of grain penetration varies at different points along the contact length between the grinding wheel and the workpiece. The largest depth of grain penetration occurs at the start of contact, which is the point where the grinding wheel contacts the workpiece first. The depth of grain penetration reduces gradually to zero along the contact length. The heat flux from the heat source in the grinding contact area is not a uniform distribution. This viewpoint can be supported from the undeformed chip thickness, since the idealized undeformed chip thickness is not uniform. The heat generation progressively varies between the maximum chip thickness and zero. A triangular distribution is therefore reasonable.

3.3 Modelling the temperature field for a triangular heat source

The temperature in the grinding zone can be analysed assuming one dimensional heat transfer for high values of Peclet number. In grinding, the Peclet number is high, so that the flow of heat parallel to the workpiece surface can be neglected with respect to the speed of the moving heat source. The heat flux generated in the grinding zone transfers below the surface in the Z direction only. An arbitrary position on the workpiece is affected by the heat source only when it traverses past the grinding contact zone, as shown in Figure 3.3.

The triangular heat flux at an arbitrary position x_i in the grinding contact area can be expressed as

$$q(x_i) = 2\bar{q}(1 - \frac{x_i}{l}) \qquad (3.2)$$

where:

$\bar{q}$ is the average intensity of the heat source in the grinding contact area.

l is the length of heat source.

x_i is an arbitrary position in the grinding contact zone.

In Figure 3.3

τ' is the time period from an arbitrary point i on the workpiece entering the grinding zone to the point reaching the position x_i.

τ_o is the time period from the point o entering the grinding contact zone to the point leaving the grinding zone.

so $x_i = \tau' v$ and $l = \tau_o v$. Substituting these expressions into equation 3.2 yields

$$q(x_i) = 2\bar{q}\left(1 - \frac{\tau' v}{\tau_o v}\right) \tag{3.3}$$

where

v is the velocity of the heat source

It can be seen that q is a function of argument τ' only, so the heat flux can be expressed as:

$$q(\tau') = 2\bar{q}\left(1 - \frac{\tau'}{\tau_o}\right) \tag{3.3a}$$

In the moment $d\tau'$ at the time τ', $q(\tau')$ is the instantaneous heat flux of the heat source. The quantity of heat transferred in this moment is,

$$q(\tau')d\tau' = 2\bar{q}\left(1 - \frac{\tau'}{\tau_o}\right)d\tau' \tag{3.4}$$

Therefore, the temperature rise of the arbitrary point M (x, 0, z) due to the effect of the heat source in the grinding contact zone can be solved from the instantaneous plane heat source, equation 3.1, based on superposition. The values in the temperature field generated over time are superimposed on each other and the solution for a continuously operating triangular heat source can be written as,

$$\theta_{(x,z)} = \int_{\tau'=0}^{\tau'=t} \frac{4\bar{q}\left(1-\frac{\tau'}{\tau_o}\right)dt_i}{c\rho\sqrt{4\pi\alpha(t-\tau')}} \exp\left(-\frac{z^2}{4\alpha(t-\tau')}\right) \qquad (3.5)$$

Evaluating the integration in equation 3.5 leads to, [Appendix 1]

$$\theta_{(x,z)} = \frac{\bar{q}\sqrt{t}}{c\rho\sqrt{\pi\alpha}}\left[4-\frac{8t}{3\tau_o}-\frac{2z^2}{3\alpha\tau_o}\right]\exp\left(-\frac{z^2}{4\alpha t}\right)+\frac{\bar{q}z}{c\rho\alpha}\left[\frac{z^2}{3\alpha\tau_o}-\left(2-\frac{2t}{\tau_o}\right)\right]\left[1-erf\left(\frac{z}{\sqrt{4\alpha t}}\right)\right] \qquad (3.6)$$

Equation 3.6 is the equation for the temperature rise of an arbitrary point M (x, z) in the temperature field generated by a triangular heat source.

The maximum temperature at any position in the contact zone is on the surface of the workpiece and therefore thermal damage always occurs at the grinding surface when grinding either metals or other material. The maximum temperature at the surface corresponds to z = 0. The temperature at the contact surface is given by

$$\theta_{(x,0)} = \frac{4\bar{q}\sqrt{t}}{c\rho\sqrt{\pi\alpha}}\left(1-\frac{2t}{3\tau_o}\right) \qquad (3.7)$$

where

t is the time since a position entered the contact zone expressed as

$$t = \frac{x_i}{v} \text{ or } t = \frac{l_i}{v} \qquad (3.7a)$$

l_i is the length of the heat source in the time t

τ_o is the total time of contact

$$\tau_o = \frac{l}{v} \tag{3.7b}$$

x_i is an arbitrary position in the grinding contact zone

$\bar{q}$ is the average heat flux in the grinding contact zone expressed as

$$\bar{q} = \frac{R_w P}{A} \tag{3.7c}$$

P is the grinding power

A is the area of the contact zone

R_w is the proportion of the energy entering the workpiece

α is the thermal diffusivity

$$\alpha = \frac{\kappa}{\rho c} \tag{3.7d}$$

The temperature in the contact zone is therefore obtained from equation 3.7 to 3.7d as

$$\theta_{(x,0)} = \frac{4R_w P\sqrt{l_i}}{A\sqrt{\pi(\kappa\rho c)_w v_w}}\left(1-\frac{2l_i}{3l}\right) \tag{3.8}$$

In order to evaluate the temperature distribution in the grinding zone each value in equation 3.8 has to be estimated. The problem of value estimation is discussed in chapter 4.

It is necessary to determine the maximum temperature value in the grinding contact zone. The maximum temperature in the grinding zone occurs at the position where the temperature gradient is zero.

$$\frac{\partial\theta}{\partial l_i} = 0 \tag{3.9}$$

Differentiating equation 3.8 with respect to l_i,

$$\frac{4R_w P}{A\sqrt{\pi(\kappa\rho c)_w v_w}}\left(\frac{1}{2\sqrt{l_i}} - \frac{2}{3l}\frac{3\sqrt{l_i}}{2}\right) = 0 \tag{3.10}$$

Rearranging equation 3.10, yields

$$l_i = \frac{1}{2}l \tag{3.11}$$

It can be seen from equation 3.11 that the maximum temperature occurs at the middle of the contact length.

Substituting equation 3.11 into 3.8 the maximum temperature is

$$\theta_m = 1.064\frac{R_w P}{A\sqrt{(c\rho\kappa)_w}}\sqrt{\frac{l}{v_w}} \tag{3.12}$$

3.4 Summary

It was assumed that the workpiece is a semi-infinite body so as to simplify the heat transfer problem into one dimension. The solution for an instantaneous plane heat source was applied to obtain the temperature solution for a triangular heat flux distribution. The maximum temperature is found at the middle of the contact length.

Chapter 4 A thermal model for form grinding

4.1. Geometric contact length for different forms

The area of the contact zone influences grinding temperature. In form grinding the contact area between the workpiece and the grinding wheels is different for different workpiece profiles. A complex workpiece profile can be considered to consist of several elementary shapes. It is therefore necessary to discuss some basic contact conditions separately.

The contact in form grinding is more complex than in cylindrical and surface grinding due to the variation of the contact length. The geometric contact length is discussed in the following sections for different shapes of workpiece and then the real contact length is introduced.

There are a variety of shapes of workpiece in which form grinding is required. Of the various shapes, the vee shape is one of the most common shapes in industrial application. The vee shape is an important elemental shape because many forms can be derived from an analysis of the vee shape. The vee shapes can be further classified as vee shapes, inverted vee shapes and unsymmetrical vee shapes.

4.1.1 Face grinding

Workpieces involving a vee section are illustrated in Figure 4.1. The shape with an angle of 90 degrees is a frequent occurrence. Such operations are commonly used to simultaneously grind an external cylindrical surface and a plane shoulder surface.

To simplify the problem, the operation considered initially is straight grinding of a horizontal plane surface and a vertical plane on a horizontal surface grinding machine. The surfaces to be ground are the horizontal surface, BC and the vertical surface, AB. The geometric contact length on the surface BC is given by the usual expression

$$l_g = \sqrt{a_e d_e} \tag{4.1}$$

where

a_e is the effective depth of cut of the grinding wheel

d_e is the effective diameter of the grinding wheel

The geometric contact length on the surface AB need to be studied in more detail.

The geometrical relationship between the grinding wheel and the workpiece is shown in Figure 4.2 for the surface AB. When grinding the vertical plane surface, the cutting load is concentrated near the edge of the wheel and the wheel corner will become rounded [Malkin, 1989]. To make it clear, the corner has been enlarged. It can be seen that the contact area between the grinding wheel and the workpiece consists of arcs M and N. The contact length in face grinding the surface AB, is approximately part of a circle centred on the grinding wheel axis. The contact length varies at different positions across the contact zone.

In Figure 4.2:

a is the depth of cut.

N is the wear radius on the edge of the wheel.

M is a contact arc on the workpiece in the contact zone.

h_w is the height of the workpiece face.

x, y, z are the Cartesian co-ordinates referenced to the workpiece

The zone of material removal between the workpiece and the grinding wheel is not the whole area of contact between the grinding wheel and the workpiece but is restricted to the edge of the grinding wheel. After dressing the grinding wheel, there is a small rounded corner on the grinding wheel profile. When grinding, the material removal rate is concentrated on the rounded corner of the wheel so that this area is worn rapidly and the radius of the rounded corner is enlarged. In practice, the operator always puts a small radius on the edge. The material removal is then concentrated on the radius which tends to increase in size as the grains wear.

The geometrical contact between a grinding wheel and a workpiece is illustrated in Figure 4.3. Figure 4.3 illustrates the cross-section D-D through the point P in the contact area and across to the grinding wheel axis. The curve of intersection between the cross section D-D and the edge of the grinding wheel is the arc AB. In order to calculate the contact length at the point P at the edge of the wheel, a tangential line can be drawn to point P. The profile angle α at the point P can be determined.

The depth of cut can be expressed as

$$a_{np} = h_w - \frac{1}{2}\left(d_s - d_{sp}\right) \tag{4.2}$$

The effective diameter of the grinding wheel at P can be expressed as

$$d_{ep} = d_{sp} \tag{4.3}$$

The geometric contact length at the point P in face grinding is therefore

$$l_g = \sqrt{a_{np} d_{sp}} \tag{4.4}$$

where

h_w is the height of the workpiece

d_{sp} is the diameter of grinding wheel at point P

α is the angle of the profile of the rounded corner of the grinding wheel at P

a_{np} is the depth of cut at point P

It can be seen from equation 4.4 that the contact length is varied with the height of the workpiece and the diameter of grinding wheel. It can also be seen that equation 4.4 can be expressed approximately as equation 4.5 if the rounded corner of wheel is ignored.

$$l_g = \sqrt{h_w d_s} \tag{4.5}$$

This follows because the radius of the rounded corner of the grinding wheel is very small compared with the diameter of the grinding wheel.

4.1.2 Vee and inverted vee form grinding

In this section, the geometric contact lengths for vee and inverted vee form workpieces will be discussed. The vee and inverted vee form surfaces consist of two flat surfaces which are inclined at the angles α and β relative to the vertical direction. The vee and inverted vee form workpieces and the grinding wheels are shown in Figure 4.4.

Figure 4.5 shows the geometric relationship between the workpiece and the grinding wheel in inverted vee form grinding. The grinding wheel is formed to the required profile of the workpiece to be ground. The infeed direction of the grinding wheel is 90° relative to the grinding wheel axis.

In Figure 4.5, the profile consists of a long flank and a short flank. The profile angle for the short flank is α and the profile angle for the long flank is β.

The contact length varies across the profile of the flank. The contact length at an arbitrary point on the contact profile can be viewed by making a cross section perpendicular to the axis of the grinding wheel through the point. In Figure 4.5, a cross section marked D-D is made through a point B on the contact profile. The plane of the projected view is made parallel to the short flank of the workpiece surface. Within the plane of the projected view, the wheel is an ellipse of major axis d_s and minor axis $d_s \sin\alpha$. A cutting point on the wheel periphery can be considered to move through the arc length of contact AB at the peripheral wheel velocity v_s. At point B, the radius of curvature of the ellipse is $d_s/2\sin\alpha$. The 'effective' diameter of the grinding wheel at this point is,

$$d_e = \frac{d_s}{\sin\alpha} \tag{4.6}$$

In this projected view, the 'effective' depth of cut of the grinding wheel normal to the flank surface is

$$a_n = a\sin\alpha \tag{4.7}$$

Based on the calculation of contact length in surface grinding, the contact length in the section D-D is calculated using the effective grinding wheel diameter and the normal depth of cut.

$$l_g = \sqrt{a_n d_e} \tag{4.8}$$

Substituting equations 4.6 and 4.7 into equation 4.8, yields,

$$l_g = \sqrt{a d_s} \tag{4.9}$$

From equation 4.9 it can be seen that the geometric contact length does not depend on the profile angles α and β and the geometric contact length is the same as in horizontal surface grinding of a horizontal flat surface. The geometric contact length is determined by the depth of cut and the diameter of the grinding wheel only. Because the vertical depth of cut is constant while the grinding wheel diameter varies across the inclined surface, the contact length varies across each flank. The contact length is shortest at the apex of the inverted vee form. The value of contact length increases across each flank from the apex to the sides of the flanks of the inverted vee form. The contact zone on each flank consists of all the contact lengths on the flank. It is seen from the above analysis that the contact zone on the inverted vee form is as shown in Figure 4.6.

The geometric contact lengths for the vee form can be evaluated by the same method as for the inverted vee form. It may also be seen from the above analysis that the value of the longest contact length is in the valley of the vee form because the maximum diameter of the grinding wheel contacts at this point. The contact length decreases along each flank from the valley to the tops of the flanks of the vee form.

4.1.3 Flute form grinding

In flute form grinding, the workpiece profile consists of curves with different values of radius of curvature as illustrated in Figure 4.7. The grinding wheel is formed to the required profile of the workpiece to be ground. The feed direction of the grinding wheel is normal to the grinding wheel axis. In Figure 4.7 a tangential line can be drawn at an

arbitrary point P of the profile. The angle α is defined as the angle between the tangential line at point P and the end surface of the grinding wheel. A cross section M-M through the point P on the contact profile and perpendicular to the grinding wheel axis can be considered. In the cross section, the contact length can be calculated using the same method as used for the vee and inverted vee forms.

The effective depth of cut of the grinding wheel normal to the tangential line of the point P is,

$$a_n = a\sin\alpha \tag{4.10}$$

The effective diameter of the grinding wheel at the point P is,

$$d_{es} = \frac{ds}{\sin\alpha} \tag{4.11}$$

The geometric contact length at the flute form is,

$$l_g = \sqrt{ad_s} \tag{4.12}$$

The geometric contact length between the workpiece and the grinding wheel is only determined by the vertical depth of cut of the grinding wheel and the diameter of grinding wheel at the point P. Since the vertical depth of cut is constant and the grinding wheel diameter varies across the curve profile of workpiece, the contact length also varies across the curve profile of the workpiece. The maximum contact length is in the valley in the flute form.

4.1.4 Angle approach grinding of a cylinder and a shoulder

The distinctive feature of angle approach grinding is that the grinding wheel axis and the workpiece axis are not parallel. The angle between the workpiece axis and the grinding wheel axis is defined as ϕ_{ws}, shown in Figure 4.8

The infeed direction of the grinding wheel is presented by the angle ϕ_f, which is the angle between the infeed direction and the workpiece axis. Based on the relationships

shown in Figure 4.8, the effective depth of cut of the grinding wheel normal to the external cylindrical surface is,

$$a_{nc} = a \sin \phi_f \tag{4.13}$$

The effective depth of cut of the grinding wheel normal to the shoulder surface is,

$$a_{ns} = a \cos \phi_f \tag{4.14}$$

In conventional grinding, the cylindrical surface is generated by infeeding the cylindrical wheel perpendicular to the axis of the workpiece. In angle approach grinding, the cylindrical surface is generated by infeeding the formed wheel at the angle ϕ_f to the axis of the workpiece. When the grinding wheel axis is inclined at an angle ϕ_{ws} relative to the workpiece axis, the periphery of the grinding wheel appears to be an ellipse [Malkin, 1989]. A projected cross-section I-I is shown at Figure 4.8 where the wheel diameter is $d_{sI.}$ The grinding wheel is an ellipse in the projected view when seen in a direction parallel to the workpiece axis. The grinding wheel appears as an ellipse of major axis d_{sI} and minor axis $d_{sI}\cos\phi_{ws}$. The workpiece is a circle of diameter d_{wI}. The radius of curvature at the cross section I-I is $d_{sI}/2\ \cos\phi_{ws}$. The effective equivalent diameter of the grinding wheel at the cross esction I-I is given approximately by,

$$d_{ec} = \frac{d_{sI}}{\cos \phi_{ws} + \dfrac{d_{sI}}{d_{wI}}} \tag{4.15}$$

When $\phi_{ws} = 0$, equation 4.15 is equal to the usual equation for external cylindrical grinding.

The geometric contact length between the cylindrical surface of the workpiece and the grinding wheel is,

$$l_{gc} = \sqrt{a_{nc} d_{ec}} \tag{4.16}$$

Substituting equations 4.13 and 4.15 into equation 4.16 gives

$$l_{gc} = \sqrt{a \sin \phi_f \frac{d_{sI}}{\cos \phi_{ws} + \frac{d_{sI}}{d_{wI}}}} \qquad (4.16a)$$

The contact length between the cylindrical surface and the grinding wheel is calculated using equation 4.16a.

The same method may be used for the analysis of the contact length on the shoulder surface. A projected view of the cross-section II-II is also shown at Figure 4.8 where the diameter of the wheel is d_{sII}. The projected view of the cross-section II-II is an ellipse of major axis d_{sII} and minor axis $d_{sII}\sin\phi_{ws}$, the radius of curvature at the cross section II-II is $d_{sII}/2\sin\phi_{ws}$. The effective equivalent wheel diameter at the cross section II-II

$$d_{es} = \frac{d_{sII}}{\sin \phi_{ws}} \qquad (4.17)$$

The contact length between the shoulder surface of the workpiece and the grinding wheel is,

$$l_{gs} = \sqrt{a_{es} d_{es}} \qquad (4.18)$$

Substituting equations 4.14 and 4.17 into equation 4.18 gives,

$$l_{gs} = \sqrt{a \cos \phi_f \frac{d_{sII}}{\sin \phi_{ws}}} \qquad (4.18a)$$

The contact length between the shoulder face and the grinding wheel is calculated using equation 4.18a.

It is seen from equation 4.16a that the contact length between the cylindrical surface and the grinding wheel is determined by the fixed angle ϕ_{ws}, the approach angle ϕ_f, the depth of cut, the diameter of the grinding wheel and the diameter of the cylindrical workpiece surface. It is seen from equation 4.18a that the contact length between the shoulder

surface and the grinding wheel is determined by the angle ϕ_{ws}, the approach angle ϕ_f, the depth of cut and the diameter of the grinding wheel.

It is also found that the depth of cut of the grinding wheel into the workpiece in the direction of the infeed is constant. However, the normal depths of cut on the shoulder surface and the cylindrical surface vary with the approach angle ϕ_f. As the approach angle ϕ_f is increased, the depth of cut increases in the cylindrical surface and the depth of cut reduces in the shoulder surface. Therefore, increasing the approach angle, which increases the depth of cut on the cylindrical surface, increases the contact length between the cylindrical surface and the workpiece. The depth of cut on the shoulder surface reduces and the contact length between the shoulder surface and the workpiece is reduced.

Where the infeed direction of the grinding wheel is normal to the grinding wheel axis, the relationship between the angle ϕ_{ws} and the approach angle ϕ_f is,

$$\phi_f + \phi_{ws} = 90^\circ \tag{4.19}$$

Substituting $\phi_f = 90^\circ - \phi_{ws}$ into equation 4.16a and equation 4.18a, yields

$$l_{gc} = \sqrt{a\cos\phi_{ws}\frac{d_{sI}}{\cos\phi_{ws} + \frac{d_{sI}}{d_{wI}}}} \tag{4.16b}$$

$$l_{gs} = \sqrt{ad_{sII}} \tag{4.18b}$$

a is the depth of cut measured in the infeed direction and is given by $a = \pi d_w \frac{v_f}{v_w}$

where v_f is the feedrate and v_w is the rotational speed of the workpiece.

Equation 4.16b is for the contact length between a cylindrical surface and the grinding wheel where the infeed direction is normal to the axis of the wheel. Equation 4.18b is for the contact length between the shoulder surface and the grinding wheel where the infeed direction is normal to the axis of the wheel.

It is seen from equation 4.16b that the contact length between the cylindrical surface and the grinding wheel is determined by the fixed angle ϕ_{ws}, the diameter of the grinding wheel, the diameter of the cylindrical surface of the workpiece and the depth of cut of infeed direction. When the angle ϕ_{ws} and the depth of cut are constant, the contact length between the cylindrical surface and the wheel is determined by the diameters of the wheel and the cylindrical surface. Therefore, increasing the diameter of the wheel, increases the contact length.

It is seen from equation 4.18b that the contact length between the shoulder surface and the grinding wheel is independent of the angles ϕ_{ws} and ϕ_f. The contact length is only determined by the diameter of the grinding wheel and the depth of cut.

It can be seen from above analysis that the geometric contact length is different for the different workpiece shapes.

The geometric contact length for the vertical face in horizontal surface grinding is,

$$l_g = \sqrt{a_{np} d_{sp}} \tag{4.4}$$

The geometric contact length for the vee form and the inverted vee form in horizontal surface grinding is,

$$l_g = \sqrt{a d_s} \tag{4.9}$$

The geometric contact length for the flute form in horizontal surface grinding is,

$$l_g = \sqrt{a d_s} \tag{4.12}$$

The geometric contact length between a cylindrical surface of a workpiece and the wheel in angle approach grinding is,

$$l_{gc} = \sqrt{a \sin \phi_f \frac{d_{sl}}{\cos \phi_{ws} + \frac{d_{sl}}{d_{wl}}}} \tag{4.16a}$$

The geometric contact length between the shoulder surface of a workpiece and the grinding wheel in angle approach grinding is,

$$l_{gs} = \sqrt{a\cos\phi_f \frac{d_{sII}}{\sin\phi_{ws}}} \tag{4.18a}$$

The diameter varies with position around the profile of the grinding wheel. The contact length at a particular position on the profile of the grinding wheel is determined by the diameter of the grinding wheel at that position. The maximum contact length is where the diameter of the grinding wheel is a maximum. Where the difference between the maximum and the minimum diameters of the grinding wheel in the contact area is small, the average diameter is used for calculation of the contact length.

4.2 The real contact length

Although the geometric contact length can be used in prediction of grinding temperature, it is found that real contact length may be 1.5 to 3 times the geometric contact length [Qi and Rowe, 1997]. If the difference between the real contact length and the geometric contact length is large, a significant error will result in the temperature predicted. To predict grinding temperature more accurately and reliably, it is necessary to use the real contact length. A real contact length model for grinding was developed by Rowe and Qi [Rowe and Qi, 1993]. This model was applied to temperature prediction for form grinding. The model indicates that the main parameters influencing contact length are the real depth of cut, the elastic deflection of the grinding wheel and the surface topography of the grinding wheel. The real length of contact, l_c, is given by the orthogonal relationship between the contact length due to deflection, l_f, and the geometric contact length l_g:

$$l_c = \left(l_f^2 + l_g^2\right)^{1/2} \tag{4.20}$$

The geometric contact length, l_g is given by the geometrec contact length for different workpiece shapes as shown in equation 4.4, 4.9, 4.12, 4.16a, 4.18a.

The contact length due to elastic deformation, l_f, is given by

$$l_f = \left(8R_r^{\,2} \frac{F_n}{b} (K_s + K_w) d_e \right)^{1/2} \tag{4.22}$$

where K_s, the compliance of the grinding wheel is

$$K_s = \frac{1 - \upsilon_s^2}{\pi E_s} \tag{4.23}$$

and K_w , the compliance of the workpiece is

$$K_w = \frac{1 - \upsilon_w^2}{\pi E_w} \tag{4.24}$$

R_r is a roughness factor which characterizes the grinding wheel topography

E_s is the modulus of elasticity of the grinding wheel

E_w is the modulus of elasticity of the workpiece

υ is the Poisson ratio

F_n is the normal grinding force

b is the grinding width

The application of equation 4.22 is limited as the value of the normal force must be known. The normal force cannot be readily obtained in most industrial grinding processes. However, the normal force can be estimated from the tangential force by assuming a value of the coefficient of friction. The tangential grinding force may be determined by measuring the grinding power and the wheel speed.

$$F_n = \frac{P}{\mu v_s} \tag{4.25}$$

where μ is the ratio between the tangential force and the normal force. The value of μ usually lies in the range 0.3-0.5 in grinding [Hahn, 1956].

Equation 4.25 shows the relationship between the grinding power and the normal force. If the grinding power and the grinding wheel speed are known, the normal force can be estimeted.

An average value of R_r suggested for dry grinding is $R_r = 13$ by [Rowe and Qi, 1997]. The power signal, P, was used to estimate the normal force using a value of friction coefficient of 0.4. The Poisson ratio was taken as 0.3. The modulus of elasticity of the grinding wheel was assumed to be 50 GN/m^2 and the modulus of elasticity of the workpiece was assumed to be 210 GN/m^2[Qi, 1995].

Substituting the above parameters into equation 4.20, yields the real contact length

$$l_c = \left(1.435 \times 10^{-10} R_r^2 \frac{P d_e}{v_s b} + l_g^{\ 2} \right)^{1/2} \tag{4.26}$$

Equation 4.26 was used in form grinding for calculation of the real contact length.

4.3 The layers under the contact zone

It is known from the above contact length analysis that the contact zone is not rectangular in form grinding. In order to analyze the temperature distribution in form grinding, the total grinding contact zone was divided into several strips across the width of the workpiece profile. In this way, each strip can be seen as an approximate rectangle if the width of each strip is small enough. Figure 4.9 shows the strips across the grinding zone. The volume of material under a strip forms a layer.

4.4 Determination of the power distribution

The grinding power is distributed to each curve or flank of the workpiece profile based on the removal rate along each curve. The grinding power distribution on each curve can be expressed as

$$P_c = \frac{P}{Z} Z_c \tag{4.27}$$

where

P is the grinding power

Z is the removal rate in grinding

P_c is the power distributed the curve

Z_c is the removal rate on the curve

The grinding power along each curve is then further distributed to each strip of the curve. The strips can be considered to divide the workpiece under the contact zone into a series of layers. A layer under the contact area is shown in Figure 4.10. The grinding power at each layer is obtained by assuming a proportional relationship with the removal rate at the strips. The assumption neglects the reducing depth of cut, a, across the corner radius r_{sp}, of the wheel. The removal rate for each strip is,

$$Z_n = ab_n v_w \tag{4.28}$$

where

b_n is the width of a strip

n is the number of strips, n=1,2,…,n

The power distributed to a strip is,

$$P_n = \frac{P_c}{Z_c} Z_n \tag{4.29}$$

The heat flux on each strip is,

$$\bar{q}_n = \frac{R_w P_n}{A_n} \tag{4.30}$$

where

$$A_n = b_n l_{cn} \tag{4.31}$$

and

A_n, p_n, $\overline{q_n}$ are the area, grinding power and heat flux on each strip.

l_{cn} is the contact length at each strip

Substituting equations 4.29 and 4.30 into equation 3.8 the heat flux entering the workpiece surface can be related to the temperature distribution.

$$\theta_{w(n,i)} = \frac{4R_w P_n}{A_n} \frac{1}{(\pi(\kappa\rho c)_w)^{1/2}} \sqrt{\frac{l_{cni}}{v_w}} \left(1 - \frac{2l_{cni}}{3l_{cn}}\right) \tag{4.32}$$

where

l_{cni} is the position of ith element on the contact surface at the nth contact length

$\theta_{w(n,i)}$ is the temperature of the workpiece at the surface of the nth strip at the ith element along the contact length

Equation 4.32 is used to express the temperature distribution in form grinding. If the workpiece and grinding wheel have been specified, every parameter in equation 4.32 is known except the partition ratio R_w.

4.5 Partition ratio

The rise of the workpiece temperature in grinding depends on how much of the grinding energy enters the workpiece. The more energy enters the workpiece, the higher the temperature rise. It is clear that the partition ratio is a key problem in calculation of the heat flux entering the workpiece surface. In this section the principles of energy partitioning are introduced.

In order to evaluate the workpiece surface temperature, it is necessary to specify the heat flux, q_w, entering the workpiece.

The total heat flux, q_t, generated in the grinding zone is comprised of the heat fluxes into the workpiece, q_w, into the grinding wheel, q_s, into the grinding chips, q_{ch}, and into the grinding fluid, q_f.

$$q_t = q_w + q_s + q_{ch} + q_f \tag{4.33}$$

The heat flux partitions are shown in Figure 4.11.

The partition ratio, R_w, is the proportion of the total heat energy conducted into the workpiece. It is expressed as

$$R_w = q_w / q_t \tag{4.34}$$

The proportions of the total heat entering the grinding wheel, chips, and fluid are defined as

$$R_s = q_s / q_t \tag{4.35}$$

$$R_{ch} = q_{ch} / q_t \tag{4.36}$$

$$R_f = q_f / q_t \tag{4.37}$$

Substituting equations 4.34 to 4.37 into equation 4.33, yields

$$1 = R_w + R_s + R_{ch} + R_f \tag{4.38}$$

Rearranging equation 4.38 yields

$$R_w + R_s = 1\text{-}R_{ch}\text{-}R_f \tag{4.39}$$

Equation 4.39 divided by R_w yields

$$\frac{1 - R_{ch} - R_f}{R_w} = \frac{R_w + R_s}{R_w} \tag{4.40}$$

Rearranging equation 4.40 gives

$$R_w = \frac{R_w}{R_w + R_s}\left(1 - R_{ch} - R_f\right) \tag{4.41}$$

For prediction of the partition ratio, it is convenient to introduce the concept of an energy partition between the workpiece and the grinding wheel, R_{ws}. The proportion of the energy shared by the workpiece and the wheel is $R_w + R_s$. The workpiece-wheel partition ratio is defined as $R_w/(R_w+R_s)$.

The partition ratio, R_{ws}, between the workpiece and grinding wheel is determined from the Hahn model, [Hahn, 1962].

$$R_{ws} = \frac{R_w}{R_w + R_s} = \left(1 + \frac{\kappa_{ge}}{\sqrt{r_o v_s (\kappa\rho c)_w}}\right)^{-1} \tag{4.42}$$

Substituting equation 4.42 into equation 4.41 yields

$$R_w = \left(1 + \frac{\kappa_{ge}}{\sqrt{r_o v_s (\kappa\rho c)_w}}\right)^{-1}\left(1 - R_{ch} - R_f\right) \tag{4.43}$$

It is seen from equation 4.43 that the partition ratio must be reduced by the factor (1 - R_{ch}) for dry grinding and the factor (1 - R_{ch} - R_f) for wet grinding.

In equation 4.43

κ_{ge} is the thermal conductivity of the abrasive grain

v_s is the wheel speed

r_o is the average effective radius of the individual grain contact

$(\kappa\rho c)_w$ is a thermal property of the workpiece

The value of the partition ratio, R_w is determined by the above the elements. The wheel surface speed and the thermal property are assumed to be constant when grinding. The grain contact radius of the wheel, increases with wear of the grinding wheel. The

reported values of wear flat radius in the contact area vary from 12μm to 65μm [Black, 1996]. An example of variation of the partition ratio between the workpiece and the grinding wheel with grain radius is shown in Figure 4.12. It is seen from Figure 4.12 that the partition ratio increases with grain radius, although the variation of the partition ratio for the condition shown is not sensitive for alumina and steel if the radius of the grain is greater than 15μm.

The value of thermal conductivity of the grains ranges from 16W/mK to 45 W/mK for an alumina wheel [Black, 1996]. The partition ratio between the workpiece and the grinding wheel against thermal conductivity is shown in Figure 4.13. The energy partitioning is relatively constant across the range of reported values.

4.5.1 The role of chips and coolant

It can be seen from equation 4.43 that the workpiece partition ratio can be obtained if the partition ratios for the chips and fluid are known. The partition ratios for the chips and fluid may be expressed in terms of specific energies,

$$R_{ch} = \frac{e_{ch}}{e_c} \tag{4.44}$$

$$R_f = \frac{e_f}{e_c} \tag{4.45}$$

From equation 4.43, 4.44 and 4.45, the workpiece partition ratio can be expressed as,

$$R_w = R_{ws}\left(1 - \frac{e_{ch} + e_f}{e_c}\right) \tag{4.46}$$

In equation 4.46, the total grinding specific energy is $e_c = P/(a.b.v_w)$.

where

a is the depth of cut of the grinding wheel

b is the width of the grinding contact

The maximum specific energy which can possibly be convected by the chips, e_{ch} is the energy required to melt the workpiece material removed

$$e_{ch} = \rho c \theta_{melt} \tag{4.47}$$

where

θ_{melt} is the melting temperature of the workpiece

Malkin [Malkin, 1991] proposed that the maximum energy carried away by the chips e_{ch}, is limited to the energy required for melting. A typical maximum specific energy value of e_{ch} is approximately 6 J/mm^3 for ferrous materials [Rowe, 1988]. The partition ratio for the chips based on the assumption that the chips achieve a temperature close to melting is,

$$R_{ch} = 6 / e_c \tag{4.48}$$

It can be seen from equations 4.46 and 4.48 that the effect on the workpiece partition ratio of energy entering the chips increases significantly at low value of specific energy. This indicates that the grinding temperature is reduced more effectively in high efficiency grinding.

The effect of the coolant on the grinding temperature is discussed in detail in section 4.7.

4.6 Measurement of the workpiece partition ratio

The experimental value of partition ratio was obtained based on the well established equation for heat conduction from a sliding heat source. The energy entering the workpiece is estimated from the measurement of workpiece temperature. The workpiece temperature was measured using thermocouples. The grinding power was measured using a power sensor. The contact length between the workpiece and the grinding wheel was estimated from the real contact length model. The depth of cut in grinding was measured using displacement transducers.

The experimental value of workpiece partition ratio was based on the sliding heat source temperature equation assuming a triangular heat flux distribution.

$$R_{wmea} = \frac{\theta_{meas} A(\kappa\rho c)_w^{0.5}}{1.064 P_{meas}} \left(\frac{v_w}{l_c} \right)^{0.5} \tag{4.49}$$

where

θ_{meas} is the measured maximum temperature

P_{meas} is the measured grinding power

v_w is the workspeed

A is the contact area between the workpiece and the grinding wheel

l_c is the real contact length based on measured depth of cut and measured power

Using equation 4.49, experimental values of workpiece partition ratio can be compared with theoretical value.

4.7 Influence of convection cooling on the grinding zone temperature

Most grinding operations take place with a grinding fluid. The influence of convective cooling on the workpiece surface temperature distribution was investigated by Des Ruisseaux [Ruisseaux, 1970]. A constant convection coefficient was assumed to act across the entire surface of a semi-infinite body, Figure 4.14. However, in form grinding the contact length varies across the contact area. It was therefore considered possible that the convection coefficient for the coolant within the contact zone modifies the shape of the temperature distribution.

In order to modify the shape of the temperature distribution, it is necessary to know the proportion of the total heat flux entering the coolant. The heat flux entering the coolant was expressed as

$$q_f = \theta_w h_c \tag{4.50}$$

The effect of the convection coefficient for the coolant was calculated from particular values of the convection coefficient and from the values of workpiece temperature calculated from equation 4.32.

However when the grinding fluid boils, the gas phase forms a partial barrier between the fluid and the surface, thus greatly reducing the convection of heat [Howes 1987]. If the workpiece surface temperature in the contact zone exceeds a critical value, typically 100° - 130° for a soluble coolant, and 300° for oil, the workpiece partition ratio suddenly increases toward the dry grinding condition due to the diminished value of R_f. In shallow grinding, it is found that the onset of thermal damage occurs at a temperature above the boiling point of a soluble coolant or of oil.

When the workpiece temperature at any point in the contact zone exceeds the boiling temperature of the fluid, it is assumed that the convection coefficient is reduced to a small value, $h_c = 500\ W/m^2K$. At fluid boiling condition the convection coefficient drastically reduces and essentially dry grinding conditions prevail. For dry grinding conditions it was assumed that $h_c = 500\ W/m^2K$ [Lee, 1971]. This magnitude of convective cooling was found to make negligible difference to the temperature distribution. The workpiece temperatures and the fluid partition ratio were solved iteratively until the solution converged.

The iteration procedure is shown in Figure 4.15. At the beginning of the iteration, the initial value of partition ratio for the fluid is assumed to be zero. Based on this assumption, the initial workpiece partition ratio is calculated. The temperatures of the workpiece surface are then calculated. The heat flux into the fluid is calculated from equation 4.50. The updated workpiece partition ratio is then re-calculated from equation 4.43 or 4.46. The initial value of workpiece partition ratio is compared with the updated value. If the difference between the initial value and the updated value is less than a pre-set value, the updated value of partition ratio is considered as an acceptable value of workpiece partition ratio. On the other hand, if the difference between the initial value and the updated value is greater than the pre-set value, the above calculation is repeated until the accuracy requirement is satisfied.

4.8 The temperature distribution at the discontinuity

A discontinuity occurs at a junction of two flanks or of two smooth curves of the workpiece in form grinding. The temperature at this point was calculated and expressed as a shape concentration factor, n. The shape concentration factor was derived from theoretical studies undertaken at Trinity College, Dublin using finite element methods [Walsh, 1998]. The concentration factor, n, was defined as the temperature at the discontinuity divided by the temperature experienced by a flat plane for the same grinding conditions $n = \theta_p/\theta_f$. The values of shape concentration factor were provided for included angles appropriate in angle approach grinding. The concentration factor was found to be a function of six dimensionless groups corresponding to the ratios of applied heat flux, contact length and included angle. The value for the shape concentration factor is,

$$n = f\left(\frac{q_1}{q}, \frac{q_2}{q}, \frac{\alpha_1}{\alpha}, \frac{\alpha_2}{\alpha}, \frac{l_1}{l_C}, \frac{l_2}{l_C}\right) \tag{4.51}$$

The function f in equation 4.51 was evaluated by Walsh using finite element analysis and a linear regression technique. The results of the analysis were expressed as a polynomial,

$$n = b_o + b_1p_1 + b_2p_2 + b_3p_3 + b_4p_4 + b_5p_5 + b_6p_6 \tag{4.52}$$

where the values of b were determined from linear regression and the values of p correspond to the dimensionless ratios,

$$p_1 = \frac{q_1}{q} \tag{4.53}$$

$$p_2 = \frac{q_2}{q}; \tag{4.54}$$

$$p_3 = \frac{\alpha_1}{\alpha}; \tag{4.55}$$

$$p_4 = \frac{\alpha_2}{\alpha}; \tag{4.56}$$

$$p_5 = \frac{l_1}{l_C}; \tag{4.57}$$

$$p_6 = \frac{l_2}{l_C}; \tag{4.58}$$

The ratios are defined by

α is the reference angle

α_1 is the angle between the flank1 and the vertical direction

α_2 is the angle between the flank2 and the vertical direction

q is the heat flux applied, based on the normal width of the flank plane

q_1 is the heat flux applied on the flank1

q_2 is the heat flux applied on the flank2

l_1 is the length of flank1

l_2 is the length of flank2

l_c is the contact length of flat plane

The temperature at the discontinuity was calculated by multiplying the flat plane temperature by the concentration factor.

$$\theta_p = n\theta_f \tag{4.59}$$

The coefficients b for a workpiece shape with included angles greater than 180° are,

$$b = [\ 0.6092, 0.3144, 0.3481, -0.2032, -0.2037, 0.0009, 0.0009\ ] \tag{4.60}$$

The coefficients b for the workpiece shape with included angles less than 180° are.

$$b = [\ 1.2284,\ 0.4755,\ 0.5670,\ -0.5520,\ -0.5862,\ -0.0043,\ -0.0040\ ] \quad (4.61)$$

4.9 Application of the thermal model in form grinding

The main equations employed were as follows.

The expression for the real contact length used in form grinding was

$$l_c = \left(1.435 \times 10^{-10} R_r^2 \frac{P d_e}{v_s b} + l_g{}^2 \right)^{1/2} \quad (4.26)$$

The power distributed to a strip was assumed to be,

$$P_n = \frac{P_c}{Z_c} Z_n \quad (4.29)$$

The temperature distribution along the strip is given by,

$$\theta_{w(n,i)} = \frac{4 R_w P_n}{A_n} \frac{1}{(\pi(\kappa\rho c)_w)^{1/2}} \sqrt{\frac{l_{cni}}{v_w}} \left(1 - \frac{2 l_{cni}}{3 l_{cn}} \right) \quad (4.32)$$

The proportion of the grinding energy conducted into the workpiece in the grinding area is

$$R_w = \left(1 + \frac{\kappa_{ge}}{\sqrt{r_o v_s (\kappa\rho c)_w}} \right)^{-1} \left(1 - R_{ch} - R_f \right) \quad (4.43)$$

The temperature at the discontinuity was calculated by multiplying the flat plane temperature by the concentration factor for the point.

$$\theta_p = n \theta_f \quad (4.59)$$

The geometric contact length calculation was discussed in section 4.1. The contact lengths for several typical workpiece were analyzed and equations for calculation of the

geometric contact lengths were derived. It was found from the analysis of geometric contact length that in form grinding the contact area between the workpiece and the grinding wheel is variable. The contact length in form grinding varies across the contact profile because the diameter of the grinding wheel varies along its axis. In some conditions, if the variation in workpiece profile is small, it is unnecessary to calculate the temperature distribution across the contact area and the average value of grinding wheel diameter can be used. In order to calculate the temperature distribution in the whole contact area accurately, the contact area was first divided into two contact areas, E and F from the discontinuity at A, shown in Figure 4.16a. E is the contact area at the short flank. F is the contact area at the long flank. The temperatures on each flank and at the discontinuity were calculated separately. The temperature at the discontinuity A was calculated using the functions for temperature distribution at the discontinuity provided by Walsh. In order to calculate the temperature distribution on E and F, each contact area was further divided into strips across the width of the workpiece profile, as shown in Figure 4.16a. If each strip is small enough, it can be considered as a rectangular area. For each strip, the contact length and the area of the strip were calculated based on the values of grinding wheel diameter and the depth of cut at this particular position. Next, each contact length of the each strip was divided evenly into a series of elements, as shown in Figure 4.16b. Figure 4.16b is the view projected normal to the surface F in Figure 4.16a. The temperature of each arbitrary element n, m was calculated and the temperature distribution over the whole contact area was established.

Table 4.1 shows the equations and variables used for calculating the temperature of an arbitrary element.

Table 4.1 The equations and variables used for calculating the temperature on an arbitrary element

Symbol and meaning	Equation
P_x the grinding power on the flank	$P_x = \frac{P_t}{Z_t} Z_x$
Z_x the material removal rate on the flank	$Z_x = a\cos\alpha \times flankwidth \times v_w$
Z_t the total material removal rate	$Z_t = \sum Z_x$
l_{gn} the geometric contact length at the nth strip	$l_{gn} = \sqrt{a_{nn} d_{esn}}$
a_{nn} the depth of cut normal to the grinding surface at the nth strip	$a_{nn} = a_n \sin\alpha$
d_{esn} the effective diameter of the grinding wheel at the nth strip	$d_{esn} = \frac{d_{sn}}{\sin\alpha}$
l_{cn} the real contact length at the nth strip	$l_{cn} = \sqrt{l_{fn}^{\ 2} + l_{gn}^{\ 2}}$
P_{xn} the grinding power distribution at the nth strip	$P_{xn} = \frac{P_x}{Z_x} Z_{xn}$
Z_{xn} the material removal rate at the nth strip	$Z_{xn} = a_{nn} \frac{flankwidth}{n} v_w$
$\theta_{w(n,i)}$ the temperature at element of nth strip and ith position	$\theta_{w(n,i)} = \frac{4R_{w\,n} P_{xn}}{A_{xn}} \frac{1}{[\pi(\kappa\rho c)_w]^{1/2}} \sqrt{\frac{l_{cni}}{v_w}} \left(1 - \frac{2l_{cni}}{3l_{cn}}\right)$
A_{xn} the area of nth strip	$A_{xn} = l_{cn} \frac{flankwidth}{n}$

R_{wn} the workpiece partition ratio at nth strip	$R_{wn} = \left[1 + \frac{\kappa_{ge}}{\sqrt{r_o v_s (\kappa\rho c)_w}}\right]^{-1} (1 - R_{chn} - R_{fn})$
R_{chn} the chips partition ratio at the nth strip	$R_{chn} = \frac{P_{chn}}{P_{xn}}$ or $R_{chn} = \frac{e_{cc}}{e_c}$
P_{chn} the grinding energy into the chips at nth strip	$P_{chn} = e_{cc} Z_{xn}$
R_{fn} the fluid partition ratio at the nth strip	$R_{fn} = \frac{q_{fn}}{q_{xn}}$
q_{fn} the heat flux convected by the coolant at the nth strip	$q_{fn} = \sum q_{f(n.i)}$
$q_{f(n,i)}$ the heat flux convected by the coolant at the ith element of the nth strip	$q_{f(n,i)} = \theta_{w(n,i)} h_c$
h_c the convection coefficient between the workpiece and the coolant	$h_c = 500$ for $\theta_{wni} \geq 130°C$ $h_c = 10000$ for $\theta_{wni} < 130°C$

4.10 Summary

A temperature model has been proposed for form grinding. The geometric contact length varies with the grinding wheel diameter across the workpiece profile. The contact lengths for five typical workpiece shapes were discussed. The geometric contact length is less than the real contact length, so the real contact length should be used in calculation of temperatures for form grinding in order to predict temperature more precisely. Since the contact area is not a rectangle in form grinding, the contact area was divided into several strips. Each strip can be considered as an approximate

rectangle. Grinding power was apportioned to each curve comprising the workpiece profile based on the proportion of the total material removal rate at each curve. The grinding power at each curve was further apportioned to small strips. Partition ratios for the energy entering the workpiece surface, the chips and the fluid were discussed separately. The temperature distribution at the discontinuity was calculated using shape concentration factors.

Chapter 5 The Computer Program

5.1 Development of the computer program

A computer program was designed and developed to calculate surface temperature and partition ratio for form grinding. The program was developed in the MATLAB environment and can be used to calculate temperature and partition ratios for several typical workpiece profiles [Appendix 2.1]. For a specific workpiece, the geometric parameters of the workpiece and the grinding wheel, the operation method and the grinding conditions are required to be input into the program. The program outputs geometric contact length, real contact length, partition ratio and temperature distribution for the workpiece.

5.2 The flowchart of the program

The flowchart of the program is shown in Figure 5.1. The program consists of four functional modules. Each module performs different functions.

5.2.1 The input module

The first module is the input module. In the input module, values are entered for the workpiece geometric parameters, workpiece material properties, grinding wheel parameters, the process method and the grinding condition. For vee form and inverted vee form workpieces, the geometric parameters include the flank lengths and the angles between the flank and the vertical direction. For a stepped shaft workpiece, the geometric parameters include the diameter and length for each step. When using angle approach infeed, the geometric parameters include the angle between the axis of the wheel and the axis of the workpiece and angle of infeed. For the fluted workpiece, the geometric parameters include the radius of the flute cross-section, the flank length and the angle between the flank and the vertical direction.

The process methods include selection the face grinding, vee and inverted vee form grinding, flute form grinding and angle approach grinding.

The grinding conditions include the depth of cut, workspeed, wheel speed, coolant application and value of grinding power measured from the grinding process.

The thermal properties of the workpiece material include thermal conductivity, density and heat capacity. The workpiece material parameters were found from a materials handbook [Rothman, 1978] [Higgins, 1983] [Smithells, 1992] [Woolman, 1996]

Grinding wheel parameters include the grinding wheel diameter, the radius assumed for the contact area of the grains and the effective thermal conductivity. The parameters of the input module are shown in Table 5.1

Table 5.1 The parameters required by the input module

Input module	Workpiece geometric parameters	face grinding	h_w, r_{sp}
		inverted vee form and vee form grinding	flank, α, β
		flute grinding	flank, α, r_w
		angle approach grinding	ϕ_{ws}, ϕ_f, d_w, b
	Workpiece material properties	thermal conductivity	κ
		density	ρ
		specific heat capacity	c
	Grinding wheel parameters	the maximum wheel diameter	d_s
		the radius of wheel edge	r_{sp}
		thermal conductivity of the grain	κ_{ge}
	The process method	face grinding vee and inverted vee form grinding flute form grinding angle approach grinding	
	The grinding conditions	the depth of cut	a
		the workspeed	v_w
		the wheel speed	v_s
		the grinding power	P
		convection coefficient of coolant	h_c

5.2.2 The module for calculation of contact lengths

The inputs to the calculation module include the maximum diameter of the grinding wheel, the flank angles, depth of cut, grinding power, surface roughness, modulus of elasticity and Poisson ratio of the workpiece, modulus of elasticity and Poisson ratio of

the grinding wheel. In the module for contact length calculation, the contact area was divided into strips. The contact length for each strip was calculated using the geometric contact length equation and real contact length equation in Chapter 4. The real contact length was compared with the geometric contact length in this step. The output of the module is geometric contact lengths and real contact lengths for the strips. The parameters of the module for calculation of contact lengths are shown in table 5.2

Table 5.2 The parameters of the module for calculation of contact lengths

The module for calculation of contact lengths	Inputs	the maximum diameter of the wheel	d_s
		the angles of the workpiece profile	α, β
		the depth of cut	a
		the grinding power	P
		the roughness factor	R_T
		the modulus of elasticity of the wheel	E_w
		the modulus of elasticity of the workpiece	E_s
		Poisson ratio of the workpiece	υ_w
		Poisson ratio of the wheel	υ_s
		the number of strips on the each curve/flank ?	
	Basic equation	$l_c = [l_f^2 + l_g^2]^{1/2}$	
	Outputs	contact length for each strip	

5.2.3 The module for calculation of partition ratios

The inputs to the partition ratio module include the effective thermal conductivity of the grinding wheel, the effective contact radius of the grain, the wheel speed, the thermal properties of the workpiece and the maximum specific energy absorbed by the grinding chips. The specific energy was calculated based on measured grinding power and material removal rate. The partition ratio module was based on equation 4.43 in Chapter 4. For dry grinding, $R_f = 0$. For wet grinding, the value of R_w was achieved using an iterative method. The output of the module is partition ratios for the

workpiece, grinding wheel, chips and fluid. The parameters of the module for calculation of the partition ratios are shown in Table 5.3

Table 5.3 The parameters of the module for calculation of partition ratios

The module for calculation of partition ratio	Inputs	thermal conductivity of the grain	k_{ge}
		radius on the surface of the grain	r_o
		the wheel speed	v_s
		thermal conductivity	κ
		density	ρ
		specific heat capacity	c
		specific grinding energy to the chips	e_{cc}
		grinding power	P
	Basic equation	$R_w = R_{ws}(1-R_{ch}-R_f)$	
	Outputs	workpiece partition ratio	R_w
		grinding wheel partition ratio	R_s
		chips partition ratio	R_{ch}
		coolant partition ratio	R_f

5.2.4 The module for calculation temperatures

The inputs to the temperature calculation module include the workpiece thermal properties, workspeed, grinding wheel speed, flank lengths and curve radius of the flute form, effective thermal conductivity of the grain, effective contact radius of the grains, specific energy for the chips, the grinding power and the real contact length. The parameters of the module for calculation of the temperature distribution are shown in Table 5.4

Table 5.4 The parameters of the module for calculation of the temperature distribution

The module for calculation of temperatures	Inputs	the thermal conductivity	κ
		density	ρ
		specific heat capacity	c
		thermal conductivity of the grain	κ_{ge}
		the workspeed	v_w
		the wheel speed	v_s
		grinding power	P
		contact length	l_c
	Basic equation	$\theta_{w(n,i)} = \frac{4R_{wn}P_{xn}}{A_{xn}} \frac{1}{[\pi(\kappa\rho c)_w]^{1/2}} \sqrt{\frac{l_{cni}}{v_w}} \left(1 - \frac{2l_{cni}}{3l_{cn}}\right)$	
	Outputs	the values of temperature in the grinding zone graph of maximum temperatures across the grinding zone	

Based on the input, the temperature distribution under dry and wet grinding conditions were calculated. The maximum temperature on each strip was calculated and plotted. The maximum temperature in the contact area was therefore known. Figure 5.2 shows the maximum temperature against each strip in the grinding zone. It can be seen that the maximum temperature across the strips remains almost constant for each flank. This is because the contact length is the main factor which has an effect on the temperature. The contact length is directed related with the diameter of the grinding wheel, as shown by equation 4.9. The increasing contact length reduces the grinding temperature. However the variation of the diameter of the grinding wheel is not significant across the profile so that the maximum temperature across the strips is almost constant.

Chapter 6 Experimental system

6.1 General description

The experimental system was designed to measure grinding temperature, grinding power and the real depth of cut. The experimental system consisted of three subsystems, for measuring temperature, grinding power and the depth of cut. The experimental system is illustrated in Figure 6.1.

The temperature measuring subsystem consisted of the workpiece with embedded thermocouples, an amplifier and the data logging device, the PC30PGH ADC board nested in a PC. Three 'grindable' single pole thermocouples were mounted in each workpiece with the required surface form. The thermocouples were exposed at the surface so that the temperatures were measured when the grinding wheel passed through the thermocouples. The workpiece was located in a jig which contained an embedded amplifier to amplify and compensate the temperature signal circuit. The temperature signals from the amplifier circuit were led to the PC30PGH board for data logging.

The grinding power measuring subsystem consisted of a Deemstop power transducer, a third order Butterworth analogue filter and the data logging device, the PC30PGH ADC board. The signal from the power transducer was filtered by the third order analogue filter and then logged in the PC.

The depth of cut of the grinding wheel was measured using a digital Mitutoyo gauge and three micrometers. The vertical infeed (set depth of cut) of the grinding wheel was monitored using the Mitutoyo gauge with a digital readout device situated in the vertical plane. The depth of cut on the two flank surfaces was calculated using the triangular relationship with the vertical infeed. It was noticed that there was a difference between the vertical infeed and the actual depth of cut of the grinding wheel because of the deflection of the wheel and spindle system, the wear of the wheel and the thermal expansion of the workpiece. It was therefore necessary to measure the depth of cut directly. The depth of cut of the grinding wheel was measured using a device consisting of three micrometers. Two of the micrometers were mounted in the direction normal to the two flanks and the other micrometer was mounted in the vertical direction. A

reference block was mounted in parallel with the workpiece to remove the effect of jig deflection on the measurement of the depth of cut. The measured depth of cut was recorded manually.

The logged data for temperatures and for grinding power were viewed on-line using the software WaveView and then saved as files in the PC. The files were further analysed using Excel or LabVIEW.

6.2 The grinding machine

6.2.1 Grinding machine specification

The grinding machine used for the investigation was an Abwood Series 5025 Surface Grinder. The specification of the grinding machine is shown in Table 6.1.

Table 6.1 The specification of the grinding machine

Longitudinal travel	530 mm
Cross traverse of head	260 mm
Vertical traverse of head	350 mm
Table traverse speed range	1.5 to 20 m/min
Maximum wheel size	200 mm x 25 mm x 31 mm

The coolant system comprised a separate mobile tank with a capacity of 120 litres. A submersible motorised pump which provided 30 litres of coolant per minute was mounted in the tank. The coolant was provided through an adjustable flared nozzle at the workhead.

The grinding wheel spindle belt drive and dc motor were replaced with an ac servo-motor. The rotational speed of the ac servo-motor was controlled by an inverter

manufactured by Control Techniques. The maximum rotational speed of the ac servo-motor was 6000 rpm.

The infeed position of the grinding wheel was controlled using a position measurement device mounted on the grinding machine. The position measurement device consisted of linear scales and a Digital-Read-Out unit manufactured by Goodwin Electronics. The linear scale for the vertical infeed axis (x-axis) had a resolution of 1 μm. The resolutions for the z-axis and y-axis were 10 μm.

A partial enclosure was fabricated around the work-table to facilitate tests with neat oil.

6.2.2 Grinding machine set-up

The machine was set-up before experiments were carried out. Machine set-up consisted of the following tasks.

(i) The grinding wheel was dressed.

(ii) The diameter of the grinding wheel was measured.

(iii) The grinding wheel was balanced and installed onto the spindle of the machine.

(iv) The rotational speed of the grinding wheel was measured using a tachometer.

(v) The jig was mounted in the appropriate position on the worktable.

(vi) The workpiece surface was ground so that the workpiece and the grinding wheel profile were in conformity.

(vii) The Mitutoyo gauge and the three micrometers were reset.

(viii) The difference in level between the test surface and the reference surface was measured using the Mitutoyo gauge.

(ix) The trigger level for capturing the temperature signal was set to between 0.4-0.7 volts using the single pole thermocouple.

(x) The preliminary grinding test was performed. The temperature signals were captured on the digital storage oscilloscope. The power and the temperature data were logged to a personal computer.

The machine was then ready for experiments.

6.3 Temperature measurement

6.3.1 The workpiece assembly

The workpiece surface temperature was measured using a 'grindable' single pole foil thermocouple exposed at the workpiece surface. The single pole foil thermocouple configuration gave reasonable quality signals in both dry and wet grinding [Rowe, 1995]. The thermocouple assembly consisted of a thin chrome foil, insulated on either side by mica, installed within two abutting sections of the workpiece. A batch of workpieces was designed and manufactured for temperature measurement. The workpiece is illustrated in Figure 6.2a. Figure 6.2a shows that the workpiece was split into two parts in the vertical plane in order to insert thermocouples. The thermocouple is housed in a pre-machined slot in the workpiece. Three thermocouples were mounted in the workpiece. One thermocouple was mounted at the apex of the formed surface and vertical to the base of the workpiece. The other two thermocouples for the two flanks were mounted in the middle of each flank and vertical to the flanks. The temperature measurement system can simultaneously measure temperatures at the three different positions during one pass of grinding. The junction thickness in the single-pole configuration was approximately 0.1 mm and the width 0.5mm as shown in Figure 6.2b. Thin mica sheets were used for insulation. The two split parts of the workpiece were completely insulated from the thermocouple wires to prevent a short circuit. The workpiece acts as the other pole. The single pole method attenuates the temperature spikes while preserving the background temperature distribution.

6.3.2 Calibration of the thermocouples

Calibration tests were conducted on the inverted vee form workpiece. Two single pole thermocouples were installed in each workpiece. Thermocouple calibrations were undertaken by immersing the workpiece upside down in a bath of heated oil. The oil

used was Vacta No 2A, which has a flash point temperature of approximately 250°C. The oil bath was heated on a Belling 2KW hot plate. The rate of temperature rise was controlled using a Zenith Variac type V30H-M with an output range of 0 to 270 volts at 15 A. The temperature of the oil was monitored using an RS digital thermometer, RS 610-067. The range of measurement of the digital thermometer was 0°C to 999°C. Calibration was carried out from ambient temperature (approximately 20°C) to 140°C. The calibration was stopped at 140°C since the oil began to emit vapours at that temperature.

The output from each of the thermocouples was recorded on a PC. The data logging was via the 12-bit Amplicon PC30PGH analogue/digital data acquisition card and card specific software. Output voltages from the thermocouples and measurements were recorded at approximately 5 degree intervals throughout the range, over a total period of six hours. The sampling frequency for data logging was 6 KHz.

The output voltages from two thermocouples represented the temperature of the oil in the bath. The voltages were averaged in order to reduce measuring errors. At the same time, the oil temperatures were measured using a digital thermometer and a mercury thermometer. The measured temperatures were represented by θ_d and θ_a. The readings of the temperature degree from the digital thermometer and mercury thermometer were also averaged. For each measuring interval, a pair of data, the averaged voltage and the averaged readings from the two thermometers, was acquired. A point can be located on the calibration plot based on such a pair of data. The calibration curve was obtained by drawing the best fit curve for all points on the plot. The calibration plot is shown in Figure 6.3.

It can be seen that outputs from the single pole thermocouples were linear over the range from 20°C to 140°C. The calibrated output from the single pole thermocouple was 6.45 mv / °C when the temperature was above ambient temperature.

6.3.3 Thermocouple signal amplification

The output from the thermocouple was amplified using a commercial standard thermocouple amplifier AD595 manufactured by Analogue Devices (RS 301-779). The AD 595 was a 14 pin monolithic chip. The amplification of the AD 595 was 10mv per

degree when used with a type K thermocouple. The measuring range of the chip was 0°C to 1100°C. The AD 595 was able to perform ice point compensation. The chip added a level to the thermocouple voltage. The voltage level was in direct proportion to the potential difference which exists between 0°C and the chip temperature.

It was found from previous tests that a single-ended input to the A/D card resulted in a floating voltage with a time constant of the order of minutes. The method of differential inputs was therefore employed to eliminate the problem of floating voltage. The outputs from the thermocouples were connected to the PC30PGH board through a 50 pin D-type connector. The signal connection with the connector is shown in Table 6.2.

Table 6.2 Signal connection

Pin	Connected to
42	analogue ground
4	channel 1 in
20	channel 1 return
6	channel 2 in
19	channel 2 return
24	channel 3 in
36	channel 3 return
7	channel 4 in
37	channel 4 return

All signal inputs to the PC30PFH board must be referred to ground when the differential input mode is employed. This was done by connecting a 10 KΩ resister from the low end of each input to analogue ground.

6.4 Grinding power measurement

6.4.1 Power sensor installation

The spindle power was measured using a low cost commercially available Hall Effect transducer manufactured by Deemstop Ltd. The Deemstop transducer produced an output signal that was scaled by adjustment of the number of turns wound through the Hall effect probes. The power transducer was installed to sample the current in two phases of the three phase voltage supply between the ac driver and the spindle motor. The power is calculated from the measurements of supply current and phase voltage. The power transducer connection is shown in Figure 6.4.

6.4.2 Power signal conditioning

The signal from the Deemstop power transducer was found to contain a high noise level. The noise mainly resulted from the high levels of radio frequency interference generated by other machinery and lighting circuits in the vicinity of the machine. A third order Butterworth low pass analogue filter with cut-off frequency of 6 Hz was employed to reduce the noise and improve the quality of the power signal. The design of the analogue filter is shown in Figure 6.5.

6.4.3 Power sensor calibration

The Deemstop power transducer had to be calibrated before it could be used to measure the spindle motor power because the transducer is not a general purpose power transducer. A Siemens B 1061 function meter was used as a standard power measuring instrument in the calibration. The function meter is a microprocessor based high quality multi-function instrument that could measure motor power with a high degree of accuracy. The accuracy of the function meter was indicated by the manufacturer as being better than +/- 7% over a signal frequency range of 0 to 20 kHz. The function meter was calibrated by the manufacturer and therefore considered to be of Laboratory

standard. The range of the power measured was monitored using the depth of cut. The range of the depth of cut was 5 to 50 microns and 5 microns intervals throughout the range. Each depth of cut was measured three times. The calibration plot was achieved based on power measurements of the function meter and voltages of the Deemstop. The calibration plot is shown in Figure 6.6.

6.5 Depth of cut measurement

It was found that the true depth of cut achieved on the long flank was considerably less than the programmed depth of cut. The depth of cut was less than the expected depth of cut based on the geometry of contact and the vertical displacement. Conversely, the depth of cut on the short flank was considerably greater than the expected depth of cut based on the geometry of contact and the vertical displacement. It was established that skewing of the wheel pushed the wheel off the longer flank and consequently pushed the wheel onto the short flank because the normal grinding force on the long flank is greater than that on the short flank.

A special device for measuring depth of cut was designed and fabricated in order to achieve more accurate measurement of depth of cut on each flank. Three Mitutoyo gauges which have a resolution of 1 μm were employed to measure the difference in level between the thermocouple junction on the ground workpiece surface and the level of a reference surface before and after grinding in three directions simultaneously. Figure 6.7 show the scheme for measurement of depth of cut. One of the gauges was situated in the vertical plane directly above the apex of the form to measure the vertical displacement. The other two gauges were mounted in the directions normal to each flank to measure the actual depth of cut. The vertical depth of cut was computed from the two normal flank readings. The difference was found between the measured depths of cut on the two flanks and the results calculated based on the value of the vertical displacement. The effect of the skewing of the wheel on the depths of cut is illustrated in Figure 6.8.

Figure 6.8 shows that the measured depth of cut is less than the calculated depth of cut on the longer flank and measured depth of cut is greater than the calculated depth of cut on the short flank. It can be seen that the slope of the results for the longer flank is

greater than the slope of the results for the shorter flank which is consistent with the fact that the normal force on the longer flank is greater than that on the shorter flank.

The difference between the measured and the calculated values of depth of cut was bigger when the set depth of cut was bigger. The difference was due to the deflection of the grinding wheel and wheel assembly under the unequal normal grinding forces from the two flanks.

6.6 Data logging and post-processing

6.6.1 PC30PGH specification

Data logging was carried out through the PC30PGH Analogue/Digital Conversion board installed on a IBM personal computer. The PC30PGH is a high accuracy ADC board manufactured by Amplicon Liveline Limited. The PC30PGH consists of three subsystems, an A/D subsystem, a D/A subsystem and a digital I/O subsystem. Only the A/D subsystem was used in this investigation. The specification of the A/D subsystem is shown in Table 6.3.

Table 6.3 The key specifications of the PC30PGH

Programmable gain	1, 2, 4, 6
A/D resolution	12 bits
A/D full scale input ranges	0 to +10V, -5 to +5V
Number of A/D inputs	16 single ended or 6 differential
A/D throughput rate	Maximum 200KHz, less than 30KHz for program transfer

6.6.2 PC30PGH configuration

(i) Sampling frequency

The sampling frequency depends on three factors. The first factor is to ensure the data acquired represents the real signal without distortion. The second factor is to ensure sufficient time available to log data in the whole process. The third factor is to ensure the volume of the logged data is smaller than the data processing capacity of the software in use. The relationship of the three factors is represented by equation 6.1.

$$n = ft \tag{6.1}$$

where

n is the data processing capacity

f is the sampling frequency

t is the time of logged data

The maximum data processing capacity of Excel is 8000 in each column. Four columns were required for the data from four channels. The total number of data that can be processed by Excel is therefore 32000. The time required for data logging was set as 4 seconds in the experiments. The sampling frequency was calculated from equation 6.1 as 8000 Hz.

(ii) Data transfer mode

The DMA mode was selected as the data input mode. DMA stands for Direct Memory Access. Data from PC30PGH was transferred to the memory of the PC directly when using the DMA mode and no action was required to be taken by the data acquisition software in use. The advantage of the DMA was that the rate of data transfer was not limited by the data processing capacity of the PC so that the data transfer rate was very high.

(iii) Input range

The input range of the PC30PGH could be either 0 to 10 volts or -5 to 5 volts. The input range for the present investigation was set as 0 to 10 volts, since the temperature and the power signals are positive in this investigation.

(iv) Gain setting

The gain for each analogue input channel of the PC30PGH was set to 1.

(v) Input channel arrangement

Channel 0 to channel 2 were used for logging signals from the three thermocouples. Channel 3 was used for logging the power signal from the Deemstop power transducer.

6.6.3 Post processing

The logged data was analysed on-line by the data acquisition software Waveview and saved as a text file to permit future viewing. The logged data was also saved as data files for post-processing using other commercially available software such as Excel and LabVIEW. LabVIEW was used as the data post-processing software in this investigation. A series of digital filters were designed in LabVIEW to smooth the data output from the data acquisition system. A median filter was applied to the temperature data and a third order Butterworth filter was applied to power data. The median filter was a non-linear filter that removes high frequency noise while preserving edge information. The Butterworth coefficients selected were as follows.

The sampling frequency was set as $f_s = 100$ Hz

In this instance a lowpass filter was used. The cut off frequency was set as 6Hz.

The sampling frequency was suitable based on the Nyquist criterion

Typical outputs signals from LabView for the inverted vee form are shown in Figure 6.9. The raw temperature data and power data sets are shown in the left hand column and the filtered data sets in the right hand column. The short flank data appears at the top, apex data in the second row, long flank data in the third row and power data in the bottom row.

Chapter 7 Experimental results

7.1 Introduction

In order to reveal the problems in form grinding and to evaluate the established temperature model for form grinding, a group of experiments was designed and carried out. Several typical forms were investigated under dry and wet grinding conditions.

7.2 Experimental procedure

(i) The workpiece and the reference block were ground.

(ii) The three gauges were moved to touch the reference block and set to zero.

(iii) The three gauges were moved to touch the workpiece and the initial readings were achieved.

(iv) The grinding wheel was fed vertically based on programmed depth of cut.

(v) The workpiece block was ground.

(vi) The temperature signals and the power signal were logged in the PC.

(vii) The waveforms of the temperatures and the power were displayed using the software WaveView and the temperatures, no-load power and total power were read from the waveforms.

(viii) The three gauges were moved to measure the reference block and the workpiece.

(ix) The actual depth of cut achieved was determined based on the initial and final readings of the reference block and the workpiece.

7.3 Experimental conditions and preliminary trial

7.3.1 Experimental conditions

All experiments were carried out under both dry and wet grinding conditions. It was found the signals were easier to obtain under dry grinding conditions than under wet grinding conditions.

Each grinding trial was repeated at least twice for the same condition.

(I) Workpiece form: inverted vee form

vee form

(ii) Grinding wheel: 77A601H8VLNAA (alumina)

B126T54 (CBN)

The wheel profile was generated using a variable speed hydraulic unit and diamond roll dresser, shown in Figure 7.1. A speed ratio between wheel speed and roll dresser speed of 1:2 was used throughout the tests.

Other parameters were:

Depth of cut: 15 to 50 microns

Wheel speed: 45 m/s

Workspeed: 0.1 to 0.3 m/s

Coolant: Hysol X, 25:1 dilution in water

7.3.2 Preliminary trial

A preliminary trial was performed to evaluate the ability to measure the power and temperature. The grinding conditions in the preliminary trial were

(i) Grinding wheel: 77A601H8VLNAA, d_s = 200mm. max

(ii) Workpiece: En31

The power signal and the temperature signal were recorded, displayed on the PC and oscilloscope. The data were transmitted to the PC using the 'Waveview' software and a serial communication link.

The preliminary trial showed that the measuring system was capable of providing power and three temperature signals reasonably reliably.

7.4 Dry grinding of the inverted vee form results

The workpiece of inverted vee form is illustrated in Figure 7.2. The wokpiece consisted of two inclined flanks which are the long flank and the short flank. The angle between the long flank and the side of the workpiece was 60°. The angle between the short flank and the other side of the workpiece was 30°. Three thermocouples were mounted at the three points in the workpiece for measurement three of the grinding temperatures.

The theoretical temperature distribution in the grinding zone is shown in Figure 7.3. It can be seen the temperature is highest at the apex. This is expected due to the reduced area for conduction of the heat flux and concentration of heat flux at the apex. The temperature is higher in the long flank than in the short flank, it can be explained by higher material removal rate from the long flank. The increasing the profile angle increases the depth of cut normal to the flank, leading to the high temperature distribution in the long flank.

7.4.1 Temperatures on the long flank, short flank and apex

Figure 7.4 shows temperatures measured under dry grinding conditions and varying depth of cut. It can be seen from Figure 7.4 that the temperatures on the long flank, short flank and apex rise and fall together. The temperatures vary with different grinding conditions. Theoretically, the highest temperature should be on the apex. The second highest temperature should be on the long flank since the direction of the feed is at 60° to this flank. The lowest temperature should be on the short flank since the direction of the feed is at 30° to this flank. It was found from experiments that the apex temperatures are the highest in most cases, which would be expected because of the reduced area for conduction of the heat flux and the concentration of flux in this region.

However, the temperature on the long flank is not always higher than that on the short flank. This was not expected. It was found that it was due to sideways push-off of the wheel away from the long flank leading to a decrease in depth of cut on the long flank and a lower removal rate compared with the short flank.

Theoretical temperature distribution in the grinding area was correlated with the measured temperature distribution by matching the magnitudes of the maximum temperature. It is expected from the theoretical analysis that the maximum temperature varies across the flank of the workpiece due to the different diameters of the grinding wheel at different points across the flank. Since the temperature was measured approximately at the mid point of each flank, the theoretical evaluation was made for the mid point of each flank.

7.4.2 The effect of contact length on temperature prediction

Temperatures were predicted based on contact lengths of lg, 1.5lg, 2lg and based on the contact length model of Rowe and Qi [Rowe, 1993]. Figures 7.5 to 7.7 show measured temperatures and temperature predictions for the various contact length assumptions. These results indicate that, in form grinding, the contact length affects the temperature significantly, as pointed out by Verkerk in relation to surface grinding [Verkerk, 1975]. It can be seen that the predicted temperature matches the measured temperatures reasonably well in all cases except when the contact length equals the geometric contact length lg. The predicted temperatures are much higher than the measured temperature when using l_g instead of the real contact length due to under-estimation of the grinding area. This is true for the long flank, the short flank and the apex. It also was found that the real contact length model gave the best fit on the long flank, the short flank and the apex. It is therefore considered important that the real contact length model is used in predicting temperature when the depth of cut varies from small to large. Reasonable agreement between theory and experiment was obtained using the real contact length model as shown in Figure 7.8 to Figure 7.9. It can be seen from Figure 7.10 the predicted temperatures are higher than the measured temperature though all test, the reason for this discussed later in relation to the effect of the corner radius.

It can be seen that the predicted temperatures are higher than the measured temperatures at some points. This would be expected under the present experimental conditions,

since the precision of temperature, depth of cut and power measurement were not as high as desired.

7.4.3 The effect of depth of cut on temperature

The effect of depth of cut on temperature was investigated for a range of workspeeds. The results are presented in Figure 7.11 to Figure 7.19. The depth of cut was set in the range from 15 to 50 μm and the workspeed range from 0.1 to 0.3 m/s. The range of depths of cut covers most grinding conditions in shallow grinding. It was found there was a difference between the measured depth of cut and the programmed depth of cut. The difference was due to system deflections under the normal forces on the long flank and the short flank. When the set depth of cut is increased, the normal forces increase and the system deflections increase. Good agreement was obtained between theoretical temperatures and measured temperatures in all cases when corrections were made for the depth of cut. The temperature was found to increase with depth of cut as expected due to the increased grinding power. Figures 7.11 shows the temperatures on the long flank when using a workspeed of 0.1 m/s. It can be seen in Figure 7.11 that predicted temperatures and measured temperatures match well at two points and reasonably well for the other two points. Figure 7.12 shows the temperatures on the long flank when using 0.2 m/s workspeed. It can be seen that predicted temperatures and measured temperatures match very well at all points. When a workspeed of 0.3 m/s was used, as shown in Figure 7.13, the predicted temperatures were higher than the measured temperatures in 3 out of 4 cases, the maximum error being approximately 25%. Similar results were found for the short flank as shown in Figure 7.14 to Figure 7.16. Figure 7.17 to Figure 7.19 show that temperatures on the apex when using workspeed ranging from 0.1 m/s to 0.3 m/s. The predicted temperatures are consistently higher than the measured temperatures at all points, the reason for this is discussed later in relation to the effect of the corner radius.

In almost all cases where there is a significant difference between theoretical and measured temperature, it was found that the measurement under estimated the value compared to the theory. It was considered that errors of this type which have a scattered characteristic are symptomatic of experimental errors rather than theoretical error. Theoretical errors are expected to be consistent and systematic, whereas the experience

in making the measurements was that it was difficult to achieve consistent results. Where there are consistent and systematic errors, it may be concluded that the experimental condition was incorrectly modelled.

The effect of depth of cut on temperature is a result of the tangential grinding force which increases with depth of cut so that the grinding power and hence the heat flux in the grinding area is increased.

7.4.4 The effect of workspeed on temperature

The effect of workspeed on temperature is shown in Figure 7.20 and 7.21. Figure 7.20 shows the predicted temperatures compared with measured temperatures on the long flank with workspeed ranging from 0.1 to 0.3 m/s. It can be seen that increasing workspeed tends to decrease grinding temperature when depth of cut is constant. The comparison between the predicted temperature and measured temperature on the short flank when workspeed is in the range of 0.1 to 0.3 m/s is shown in Figure 7.21. It can be seen in Figure 7.21 that increasing workspeed sometimes tended to increase grinding temperature.

The effect of workspeed on the temperatures for the apex is shown in Figure 7.22. The comparison between the predicted temperature and measured temperature on the apex when workspeed is in the range of 0.1 to 0.3 m/s, it can be seen that with increasing workspeed, the grinding temperature tended to remain constant.

The effect of increasing workspeed is to increase removal rate for the same depth of cut. This increases the heat flux and tends to increase the temperature. However, if the large removal rate causes more rapid fracture of the grains of the wheel, the effect can be to reduce specific energy, and hence reduce the temperature. At higher workspeeds, for the same heat flux, the temperature is also reduced due to the shorter contact period between the heat source and the workpiece. There is therefore, a weak relationship between workspeed and temperature in surface grinding. This would not be true if the removal rate were maintained constant.

7.4.5 Temperature ratio, specific energy and partition ratio

Temperature ratio defined as measured temperature divided by predicted temperature was used as a measure of the overall agreement between measured and predicted temperatures. For a large number of results it would be expected that a perfect model would give an average value of unity.

The temperature ratios are shown for the inverted vee form in Figure 7.23. The temperature ratios for the long flank had a mean value of 0.90, for the short flank a mean value of 0.93 and for the apex, the mean is 0.79. These results for the inverted vee form indicates that the theoretical model is reasonably accurate in predicting temperature for the two flanks when compared with experimental results but rather poor for the apex. Later, it is shown that the model needs to be modified to allow for the radius on the apex.

The relationship between the specific energy and the depth of cut for the inverted vee form in dry grinding is shown in Figure 7.24. The specific energy was found to reduce with increasing depth of cut. The specific energy at the workspeed of 0.1 m/s was higher than the specific energy at the workspeed of 0.3 m/s due to the higher material removal rate at the higher workspeed.

A comparison between predicted and measured partition ratios is shown in Figure 7.25. The average of the predicted partition ratio values is 0.74. The average value of measured partition ratios is 0.67 for the long flank and 0.70 for the short flank based on experimental data. The average value of the measured partition ratios for the long flank and the short flank are both lower than the predicted values of partition ratio. It appears to indicate that the predicted temperature is on the safe side for predicting the onset of thermal damage. However, it may also indicate a tendency for the measured temperature to be an under-estimate.

7.5 Wet grinding of the inverted vee form results

Grinding temperatures in wet grinding of the inverted vee form were investigated and it was found that grinding temperatures were slightly lower than the temperatures under dry grinding conditions. Figure 7.26 shows the measured temperatures varying with

depth of cut and workspeed under wet grinding conditions. The workspeed ranged from 0.1 to 0.3 m/s. It can be seen that the temperatures on the long flank, short flank and apex rise and fall together. The temperatures vary with different grinding conditions. Theoretically, the highest temperature should be on the apex, the second highest temperature should be on the long flank, and the lowest temperature should be on the short flank. However, the measured temperature on the long flank is lower than that on the short flank. The reason is the same as that found in dry inverted vee form grinding, which is due to the sideways push-off of the wheel away from the long flank leading to a decrease in depth of cut on the long flank and a lower removal rate.

Three values of convection coefficient were used in the present investigation to model the effect of convection cooling. The three values were 10,000, 500 and 6000 W/m^2K. In the present analysis it was assumed that convection cooling occurs at the workpiece surface. The effects of coolant on grinding temperature have been researched by several investigators under the condition of conventional shallow grinding. A realistic value of convection coefficient for the grinding fluid would appear to be h_c = 10,000 W/m^2K which is an average value quoted in the literature [Lee, 1971] [Sauer, 1972].

One of most important considerations for the fluid in the wet grinding process is to avoid boiling the film. When film boiling occurs, heat transfer to the coolant will be obstructed by air. This condition is similar to dry grinding. In this case, there is almost no cooling effect. The convection coefficient value h_c = 500 W/m^2K takes into consideration the condition of fluid boiling where the workpiece contact dries out. In practice it has been found that 'burn-out' takes place at approximately 120°C - 130° C [Howes, 1987] for soluble oil based grinding fluids.

For investigation of the effect of convection coefficient on the temperature of form grinding, the convection coefficient value h_c = 6000 W/m^2K was used in the present investigation.

7.5.1 The effects of convection coefficient on percentage reduction of temperature

In the present investigation, the percentage reduction of temperature is defined as the result of the difference between the predicted temperature in dry grinding and predicted temperature in wet grinding divided by the predicted temperature in dry grinding. The

percentage reduction of temperature was used to compare the effect of the different values of convection coefficient. The percentage reduction of temperature was expressed as

$$\theta_{red} = \left(1 - \frac{\theta_{wet}}{\theta_{dry}}\right)\% \qquad (7.1)$$

where

θ_{red} is the percentage reduction of temperature

θ_{wet} is the predicted temperature in wet grinding

θ_{dry} is the predicted temperature in dry grinding

In order to calculate the workpiece temperature when fluid boiling occurs, the convection coefficient $h_c = 500 W/m^2K$ was used where the workpiece temperature was equal or greater than 130°C, otherwise the convection coefficient $6000 W/m^2K$ was used. The convection coefficient $h_c = 6000\ W/m^2K$ and $h_c = 10000\ W/m^2K$ were used where fluid boiling was ignored.

The percentage reduction of maximum temperature due to cooling was averaged approximately and the results are shown in Table 7.1.

Table 7.1 Percentage Reduction of Maximum Predicted Temperature

	long flank	short flank	apex
$h_c = 10{,}000\ W/m^2K$	11%	13%	15%
$h_c = 6{,}000 W/m^2K$	7%	8%	9%
$h_c = 500\ W/m^2K(\theta \geq 130°C)$	0.3%	0.6%	0.56%

It can be seen from Table 7.1 that the maximum percentage reduction in temperature is at the apex. This is because the grinding temperature is higher, the influence of the coolant on the temperature is therefore greater. The heat flux taken away by the coolant is greater at the higher temperature. So that the difference between predicted temperature in the dry grinding and wet grinding is larger at the apex than on the flank. On the other hand, increasing the temperature increases the proportion of heat conducted into the coolant. It can also be seen, the percentage reduction of maximum temperature is very small when the convective coefficient 500 W/m^2K was used. This is because the coolant effect on the temperature vanished when the temperature was greater than 130°C.

7.5.2 The effects of depth of cut on percentage reduction of temperature

Increasing depth of cut, increases the contact length which means there is a greater area in which, convection can be effective.

Figures 7.27 to 7.29 show the effects of depth of cut on percentage reduction when using different values of convection coefficient. It can be seen from the three figures that the percentage reduction in temperature increases with increasing depth of cut except with h_c = 500 W/m^2K. The increasing percentage reduction in temperature is more obvious when the convection coefficient 10,000 W/m^2K and 6000 W/m^2K were used. Increasing the convection coefficient increases the percentage reduction in temperature. It can also be seen from Figure 7.27 to 7.29 that the percentage reduction in temperature reduces with increasing depth of cut when using a convection coefficient of 500 W/m^2K. The percentage reduction in temperature reduced sharply in the initial stage since the depth of cut was small and the grinding temperature was lower than the boiling temperature of the coolant, the convection coefficient 6000 W/m^2K was used. When depth of cut was increased, the grinding temperature rose. When the grinding temperature was higher than the boiling temperature of the coolant, the effect of the coolant vanished so that the percentage reduction in temperature was zero. The reason is that when grinding temperature exceeded the boiling temperature of the coolant, the convection coefficient was reduced from 6000 W/m^2K to 500 W/m^2K so that much less grinding heat was carried away by the coolant.

Figure 7.30 shows the percentage reduction in temperature on the long flank, short flank and apex against different values of convection coefficient. It can be seen from Figure 7.30 that , when a large value of convection coefficient is employed, the maximum percentage reduction is at the apex and that the largest value of convection coefficient results in a bigger percentage reduction. The fluid boiling temperature was more likely to be exceeded when the convection coefficient was $h_c = 500 W/m^2K$, and essentially dry grinding conditions prevail. This is the reason that the percentage reduction is nearly zero at some points.

7.5.3 Temperature ratios

Temperature ratios were determined for results obtained under different grinding conditions to show the significance of assuming a convection coefficient hc = 500 W/m^2K. Temperature ratios for wet grinding using different convection coefficients are shown in Figure 7.31 for the long flank and Figure 7.32 for the short flank.

It can be seen from Figure 7.31 and Figure 7.32 that the temperature ratio between a convection coefficient h_c = 500 W/m^2K and h_c = 0 W/m^2K is almost the same under different grinding conditions. It is therefore clear, that a convection coefficient h_c = 500 W/m^2K is too small to make any difference from assuming h_c = 0 W/m^2K which was the value assumed for dry grinding.

Predicted temperatures were compared with measured temperatures using a convection coefficient h_c = 500 W/m^2K. The comparison is shown in Figure 7.33. It can be seen from Figure 7.33 that the measured temperatures are much lower than the predicted temperatures when h_c = 500 W/m^2K. These results appear to indicate that coolant can carry away heat from the grinding area at any temperatures. The magnitude of convection coefficient h_c = 500 W/m^2K was found to make negligible difference to the temperature distribution. It was therefore decided to include the effect of convection for all temperature predictions, as follows.

A comparison between measured and predicted values of temperature ratio in wet grinding for the different convection coefficients is shown in Figure 7.34 and Figure 7.35. When h_c = 6000 W/m^2K was used in the temperature prediction, the temperature ratio was slightly lower than when h_c = 10000 W/m^2K was used. This is true for the

long flank and the short flank of the inverted vee form. The temperature ratio at h_c = 6000W/m^{2}K has a mean value of 0.78 for the long flank and 0.83 for the short flank. The temperature ratio at h_c = 10000W/m^{2}K has a mean value of 0.80 for the long flank and 0.86 for the short flank. It can be concluded that predicted temperatures agree better with measured temperatures using convection coefficients in the range of 6000 to 10000 W/m^{2}K. However, it can be seen that even, including the high value of convection coefficient does not eliminate the under-estimate of temperature from the measurements. It is clear therefore that there are other errors in the system which have not been accounted for.

It can be concluded that the temperature predictions are improved in the inverted vee form wet grinding using a convection coefficient ranging from 6000 to 10000 W/m^{2}K. The temperature prediction using a convection coefficient hc = 500 W/m^{2}K is the same as the temperatures predicted for dry grinding. The convection coefficient cooling h_c = 10,000 W/m^{2}K is not only reasonable for plane shallow grinding, but also gives a reasonable prediction of temperature in wet form grinding.

7.5.4 The theoretical and measured partition ratios

Figure 7.36 shows predicted and measured partition ratios under wet grinding conditions. It can be seen that predicted partition ratios are higher than measured partition ratios. This is probably because the measured temperatures are under estimated. A mean value of measured partition ratios is 0.54 for the long flank and 0.57 for the short flank of the inverted vee form. The mean value of predicted partition ratios is 0.68 under the wet grinding condition.

7.5.5 The effect of shape factor on temperature

A discontinuity occurs at a junction of two flanks or two smooth curves of a workpiece in form grinding. The temperature prediction at the discontinuity was based on a shape factor determined by the finite element method at Trinity College Dublin [Walsh, 1998]. The shape factor assumes that the apex is a sharp discontinuity. In practice, there is a radius of 0.15 mm imparted to the form due to the radius of the dressing roll. The width of the thermocouple at this point was approximately 0.5 mm across the curved edge, and therefore the measured temperature was an average spanning the flanks and the apex.

A comparison of temperature ratio between experimental and predicted temperatures with a computed shape factor value of 'n' and a shape factor value of '1', equivalent to a plane surface is shown in Figure 7.37 for dry grinding and 7.38 for wet grinding. It was found that the mean of the temperature ratios was 0.77 using the shape factor value 'n'. The mean temperature ratio was 1.03 using the shape factor value '1' for the dry grinding results. The mean of the temperature ratios was 0.69 using the shape factor value 'n' and 0.89 using the shape factor value '1' in wet grinding. It is clear that the radius on the form eliminates the sharp edge and reduces the concentration of heat energy at the discontinuity so as to reduce the temperature experienced at the apex. It can be seen that the agreement between theory and experiment is very much improved if the radius is treated as a plane horizontal surface. This demonstrates that even a small radius is capable of removing the shape effect at the discontinuity on the profile of the workpiece and avoids the concentration of high temperature at the apex.

7.6 Temperatures, specific energy and partition ratio for the inverted vee form

Figure 7.39 shows the grinding power against material removal rate in dry and wet grinding of the inverted vee form. It can be seen that the grinding power increases with the material removal rate as expected due to increasing grinding force. The grinding power in the dry grinding condition is slightly higher than in the wet grinding condition. However the difference is very small. These results indicate that the fact that a coolant lubricates the grinding zone and reduces the grinding force is not very obvious in these results. Usually, a larger difference would be expected in conventional grinding. However, forces and power also depend on the effectiveness of the dressing operation. Differences in dressing can mask effects due to other variables.

The predicted temperatures on the long flank, short flank and apex under dry and wet grinding conditions are shown in Figure 7.40 to Figure 7.43 for workspeeds of 0.1 and 0.2 m/s. It can be seen from Figures 7.40 to 7.41 that the long and short flank temperatures in dry grinding are both slightly higher than in wet grinding at 0.1 m/s. The reason is attributed to the fact that fluid carries away a portion of the heat from the grinding area. Also the fluid lubricates the workpiece surface so as to reduce the grinding power. The temperatures in dry grinding are also higher than the temperatures in wet grinding at 0.2 m/s, as shown in Figure 7.42 for the long flank and Figure 7.43 for the short flank.

The predicted temperatures at the apex under dry and wet grinding conditions are shown in Figure 7.44. The workspeed used was 0.2 m/s. It was found that the temperatures in dry grinding are slightly higher than in wet grinding. The reasons are the same as given above.

The values of specific energy in dry and wet grinding for the inverted vee form are compared in Figure 7.45 for a workspeed of 0.1 m/s and in Figure 7.46 for a workspeed of 0.2 m/s. The specific energy reduces with increasing depth of cut. The specific energy in dry grinding was slightly higher than the specific energy in wet grinding for a workspeed of 0.1m/s. The specific energy in dry grinding was always higher than the specific energy in wet grinding for a workspeed of 0.2 m/s. It is seen that grinding with coolant can substantially improve the efficiency of the grinding process.

The partition ratios for dry and wet grinding of the inverted vee form are compared in Figure 7.47. It can be seen that there is little difference between the partition ratios in dry and wet grinding of the inverted vee form. On average, 74% of the total energy entered the workpiece in dry grinding and 68% of the total energy entered the workpiece in wet grinding. In other words assuming the temperatures measurement to be accurate, 6% of the total energy entered the fluid and was carried away from the grinding area by the fluid. However, this result could be misleading, if the measurements in wet grinding under-estimated the temperature to a greater extent than in dry grinding, which appears to be quite likely. This result is not therefore conclusive, although it remains a possibility.

7.7 Dry grinding of vee form results

The workpiece of vee form is illustrated in Figure 7.48. The workpiece consists of two of inclined flanks, the long flank and the short flank. The angle between the long flank and the side of the workpiece is 60°. The angle between the short flank and the other side of the workpiece is 30°.

7.7.1 Temperatures on the long flank, short flank and valley

Grinding temperatures on the long flank, short flank and valley of the vee form workpiece were measured. The temperatures measured were obtained for a range of the

workpiece speeds between 0.1 and 0.2m/s. The values of depth of cut were set in the range, $15 < a_v < 50\mu m$. The temperatures measured are shown in Figure 7.49. It can be seen that the temperatures rise and fall together on the long flank, short flank and valley. The temperature varied with different grinding conditions. It can also be seen that the temperature is the highest on the long flank and is the lowest on the short flank. This would be expected because of the increased depth of cut on the long flank and reduced depth of cut on the short flank. The other reason is the removal rate on the long flank is greater than that on the short flank since the profile angle for the long flank is bigger than that for the short flank. Temperatures are expected to be lower in the valley than on the long flank due to the increased area for heat conduction and the thermal diffusion.

7.7.2 The effect of depth of cut on temperature

The predicted and measured temperatures at workspeeds of 0.1 to 0.2m/s are compared in Figure 7.50 to Figure 7.53. It can be seen that reasonable agreement was obtained between theory and experiment throughout the range of depth of cut normal to the flank from 1 to 34μm although measured values were generally lower than predicted. As previously, for the inverted vee form the temperatures increase with depth of cut. This is due to increasing depth of cut increasing grinding force so that grinding energy increases.

7.7.3 The effect of workspeed on temperature

The effect of workspeed on temperature is shown in Figure 7.54 and Figure 7.55. The predicted temperatures and measured temperatures when using a workspeed of 0.1m/s and 0.2m/s at the long flank are shown in Figure 7.54. It can be seen that increasing workspeed slightly reduced grinding temperature. The predicted and measured temperatures when using workspeeds of 0.1m/s and 0.2 m/s at the short flank are shown in Figure 7.55. It can be seen from Figure 7.54 to Figure 7.55 that increasing workspeed tended to reduce grinding temperature, whereas for the inverted vee form the temperatures were substantially higher at the higher workspeed than at the lower workspeed. It is probably safer not to generalise from these results. As explained previously, temperature tends to be reduced if the specific energy is reduced sufficiently

at the higher workspeed to offset the effect of the higher power required.

7.7.4 Temperature ratio, specific energy and partition ratio

Dimensionless temperature ratios for vee form grinding are shown in Figure 7.56. The temperature ratios for the long flank have a mean of 0.70, for the short flank the mean is 0.79 and for the valley the mean is 0.73. The significant differences between measured and predicted temperatures suggest that there is a systematic error in the experimental results. Given the magnitude of the scatter of the results, the overall agreement is reasonable, although the agreement is not good.

The relationship between specific energy and depth of cut in dry vee form grinding is shown in Figure 7.57. The specific energy was found to reduce with increasing depth of cut at a workspeed of 0.2 m/s. The specific energy at the 0.2 m/s workspeed was lower than the specific energy at the 0.1 m/s workspeed due to the higher material removal rate at the higher workspeed.

Predicted partition ratios for the workspeeds of 0.1 to 0.2 m/s are shown in Figure 7.58. The predicted partition ratios remain almost constant across the range of grinding conditions. The effect of workspeed on the partition ratio was not obvious.

Measured and predicted partition ratios are shown in Figure 7.59. It can be seen that the theoretical partition ratios are mostly higher than the measured partition ratios. The average of the predicted partition ratio values is 0.78. The average of the measured partition ratio values is 0.55 at the long flank and 0.68 at the short flank. As previously, it was considered, that there results reflect an under-estimate of measured temperatures.

7.8 Wet grinding of the vee form results

7.8.1 Temperatures on the long flank, short flank and valley

The temperatures on the long flank, short flank and valley of the vee form workpiece were measured during wet grinding experiments. Figure 7.60 shows the temperatures measured under the condition of wet grinding and varying depth of cut. It can be seen from Figure 7.60 that the temperatures on the long flank, short flank and valley rise and fall together. The temperature varied with different grinding conditions. It can also be

seen that the measured temperatures were subject to scatter. This is considered to be partly a consequence of the subjectivity in temperature and power data interpretation and partly the inherent error in normal depth of cut measurements, and temperature measurements. It is difficult to get three good temperature signals simultaneously at the three points in wet form grinding. In general, it was much more difficult to obtain consistent results in wet grinding than in dry grinding. It became clear that there was a tendency for the thermocouples to deteriorate with time. It was considered that the explanation for this was a tendency for the insulation to break down, an effect which was increased by the action of the coolant.

7.8.2 The effect of workspeed and depth of cut on temperature

The effect of workspeed and depth of cut on temperature are shown in Figure 7.61 and 7.62. The predicted and measured temperatures for workspeed of 0.2 m/s and 0.3 m/s on the long flank are shown in Figure 7.61. It can be seen that increasing workspeed reduced grinding temperature. Increasing depth of cut increased grinding temperature. The predicted and measured temperatures for workspeed of 0.2 m/s and 0.3 m/s on the short flank are shown in Figure 7.62.

7.8.3 Temperature ratio, specific energy and partition ratio

The dimensionless temperature ratios are shown for the vee form in Figure 7.63. The mean temperature ratio for the long flank is 0.68, for the short flank is 0.83 and for the valley is 0.83. In general the ratios are substantially less than 1. The scatter is very large for the long flank and these results must be considered unreliable although the general tendencies tend to agree with previous findings.

The relationship between the specific energy and the depth of cut in the wet vee form grinding is shown in Figure 7.64. The specific energy was found to reduce with increasing depth of cut. The specific energy at the workspeed of 0.2 m/s was higher than the specific energy at the workspeed of 0.3 m/s, due to the higher material removal rate at the higher workspeed.

Measured and predicted partition ratios are shown in Figure 7.65. It can be seen that the theoretical partition ratios are higher than the measured partition ratios. The average of

the predicted partition ratio values is 0.73. The average of the measured partition ratios is 0.55 for the long flank and 0.62 for the short flank based on experimental data. The average value of the measured partition ratios for the long flank and the short flank are both lower than the predicted values of partition ratio. It appears to indicate that the predicted temperature using the model is on the safe side for predicting onset of thermal damage. However, as previously, it is noted that the measured values are likely to be an under-estimate due to errors in the temperature measurement.

7.9 Grinding power and partition ratios in dry and wet vee form grinding

Figure 7.66 shows the grinding power against material removal rate for dry and wet vee form grinding. It can be seen that the grinding power increases with increasing material removal rate. The grinding power in dry grinding is almost the same as in wet grinding. In these results, the coolant seems to have been ineffective in lubricating the process or reducing the grinding force.

The predicted partition ratios in dry and in wet grinding are compared in Figure 7.67. It was found that there is little difference expected between the partition ratio in dry and wet grinding. Approximately 78% of the total energy is expected to enter the workpiece in dry grinding and 73% of total energy in wet grinding. This suggests that approximately 5% of the total energy would be expected to enter the fluid and be carried out by the fluid from the grinding area.

7.10 Comparison between the inverted vee form and the vee form

7.10.1 The effect of workpiece shape on temperature

The comparison of temperatures on the long flank for the profile angle of 60° and on the short flank for the profile angle of 30° are shown in Figure 7.68 to Figure 7.71. The workspeed of 0.1 and 0.2 m/s was used. It was found that grinding temperature varies with the profile angle. The large profile angle increases the grinding temperature in form grinding due to the high removal rate on the flank with the larger profile angle.

It can also be found from Figure 7.68 and Figure 7.71 that the measured temperatures on the long flank of the inverted vee form are very close to those on the short flank of the

inverted vee form for the same depth of cut. These results can be attributed to the depth of cut reducing on the long flank and increasing on the short flank.

A comparison of the predicted and measured temperatures for the inverted vee form and the vee form are shown in Figure 7.72 for the long flank and Figure 7.73 for the short flank. It can be seen from Figure 7.72 and Figure 7.73 that the temperatures on both flanks of the vee form were much higher than on the inverted vee form. This would be expected because of the higher grinding power experienced in the vee form grinding.

7.10.2 Comparison of the grinding power for the inverted vee form and the vee form

Figure 7.74 shows the grinding power against material removal rate for dry grinding of the inverted vee form and the vee form. It can be seen from the results that grinding power was much higher in the vee form grinding than in the inverted vee form grinding. An almost similar result was found using coolant as shown in Figure 7.75. The lower power when grinding the inverted vee form indicates that the grinding process was more efficient for this condition. These differences between the power measured for the two forms are explainable, if there was a difference in the sharpness of the two grinding wheel either due to the dressing process or due to the structure and properties of the wheel as supplied.

7.11 Comparison of temperature with alumina and CBN grinding wheels for the vee form

Comparisons were made between grinding the vee form with the alumina wheel and with the CBN wheel. The CBN grinding wheel was specially manufactured according to the workpiece shape for the experiments.

Theoretical temperatures were correlated with measured temperatures by matching the magnitude of the maximum temperature and using the contact length model of Rowe and Qi [Rowe.1994].

The measured and theoretical temperatures for the CBN grinding wheel are compared in Figure 7.76 for the long and the short flanks at a workspeed of 0.1m/s.

It can be seen that temperature increases with increasing depth of cut. The temperatures on the long flank were higher than on the short flank. This can be attributed to the larger removal rate on the long flank. Reasonable agreement was obtained between the theoretical and measured values throughout the entire range of depths of cut.

The temperature ratios for the long and the short flanks are shown in Figure 7.77. A mean of the temperature ratios is 0.84 for the long flank and 0.82 for the short flank. As in previous experiments, the measured temperatures were lower than predicted. However, it can be concluded from the temperature ratios that the theoretical model can give reasonable prediction of grinding temperatures with the CBN grinding wheel.

The specific energy is a fundamental parameter of the grinding process. The specific energy is related to the grinding power and the material removal rate. The specific energy values against depth of cut using the CBN grinding wheel are shown in Figure 7.78. The specific energy reduces with increasing depth of cut.

Measured and predicted partition ratios are compared in Figure 7.79. The measured partition ratios on the long and the short flanks are both lower than the theoretical partition ratios. The mean of the measured partition ratios for the long flank is 0.39, and for the short flank is 0.39. The mean theoretical partition ratio is 0.47.

The measured temperatures for the alumina and CBN grinding wheels for the long flank and the short flank are compared in Figure 7.80 and Figure 7.81. It can be seen that the temperatures in CBN grinding are higher than in alumina grinding for the long flank. The temperatures for the CBN wheel are slightly lower than for the alumina wheel on the short flank. Those results are reasonable since the specific energy in the CBN grinding was much higher than in alumina grinding. The difference between the results for the long flank and the short flank are explained by the sideways deflections of the grinding wheel which were greater for the CBN wheel.

The grinding power against the material removal rate for the CBN wheel and the alumina wheel are compared in Figure 7.82. The grinding power values with the CBN wheel are much higher than the values with the alumina wheel for the same material removal rate. The lower grinding power with the alumina wheel indicates that the alumina wheel was grinding more efficiently than the CBN wheel.

A comparison of the specific energy between the CBN and the alumina wheels are shown in Figure 7.83. It can be seen that the specific energy when grinding with the CBN wheel is almost double the specific energy when grinding with alumina wheel. Despite the higher specific energy for the CBN wheel, the temperatures are only slightly higher. The results indicate that an increased proportion of the total grinding energy is conducted into the wheel in CBN grinding compared to grinding with alumina [Black, 1996].

The theoretical partition ratios for the alumina grinding wheel and the CBN grinding wheel are compared in Figure 7.84. It was found that partition ratio is not sensitive to the grinding conditions in grinding. The partition ratios with the CBN wheel were substantially lower than the partition ratios with the alumina wheel.

7.12 Concluding discussion

The thermal model tended to predict higher temperatures in form grinding than were measured. Analysis of the errors suggested a tendency to under-estimate temperatures in the measurements. A number of results had to be discarded. The best temperature measurements as judged by the quality of the signal agreed most closely with the theoretical results. The general agreement between theory and experiment over a large number of results for a wide range of grinding conditions tends to give confidence in the method of making predictions.

The grinding temperature varies with the profile angle of the workpiece. Increasing profile angle increases the temperature in form grinding.

The grinding temperature on the apex of the inverted vee form is higher than the grinding temperature on the flanks, due to the higher removal rate. The temperature concentration due to the sharp corner may be reduced a small radius. The temperature on the apex is then similar to the temperature in flat surface grinding.

Increasing depth of cut increases grinding temperature.

Increasing workspeed tends to increase grinding temperature in surface grinding due to the higher removal rate. Temperatures may be reduced if there is sufficient reduction of specific energy with increasing removal rate.

Specific energy reduces with increasing depth of cut and increasing workspeed. Interpretation of the variation of temperatures with grinding variables needs to take account of variations in specific energy. The effect of specific energy variations is automatically taken into account in the approach used for temperature predictions.

Chapter 8 Creep Feed Grinding

8.1 Introduction

Furukawa and Ohishi investigated the avoidance of workpiece burn by selecting grinding conditions [Furukawa, 1979]. They reported that the chip geometry in creep feed grinding was different from that in conventional grinding, so that the force generation mechanism, surface integrity, machining accuracy and the critical conditions for thermal damage were all different from conventional grinding. They also investigated the difference between up grinding and down grinding in the creep feed process. It was found from their experiments that the specific energy for up grinding is 1.7 times higher than in down grinding and the mean specific energy in creep feed grinding was 5 to 10 times that in conventional grinding. It was also found that workpiece burn took place when the grinding energy flux exceeded a critical value of 7 J/mm^2s. Optimal grinding conditions from the viewpoint of workpiece thermal damage were presented in the form of nomographs.

Powell and Howes investigated the heat flux at which burn occurs in creep feed grinding [Powell, 1978]. A method was described of using an electrically heated mock workpiece to study the limiting heat transfer rate at which burn occurs in grinding. The method was analogous to established procedures for measuring burn-out heat flux in water boiler systems. The effects of variation of coolant temperature, the coolant availability and the heater arc length of contact on the onset of grinding burn were assessed through experiments. It was found that the limiting heat transfer rate at which burn occurred decreased with increasing coolant temperature and also with increasing heater arc length of contact. It was also found that re-entry of coolant into the grinding wheel in the nip between the wheel and the workpiece could make significant contribution to the coolant availability in the cutting zone. In other words, the entraining of coolant in the nip between the wheel and the workpiece could be an effective method of coolant application in grinding.

Creep grinding is an efficient grinding operation. The process of creep feed grinding differs from conventional grinding in that the depth of cut is large and the workspeed is low. The depth of cut can be as high as 30 mm and the workspeed can be as low as 0.5

mm/s [Peters, 1983]. Due to such large depths of cut used in creep feed grinding, the material removal rate is higher than in most conventional grinding. However, the principal limitation for creep feed grinding was found to be the possibility of workpiece thermal damage. So it is necessary to investigate the mechanism of temperature generation and selection of grinding conditions in creep grinding.

Ohishi and Furukawa further analysed the workpiece temperature in creep feed grinding [Ohishi, 1985]. The workpiece temperature and the mechanism of grinding burn in creep feed grinding were investigated. A thermal model was established using a three dimensional finite element method. The effect of coolant was included into Jaeger's moving heat source theory so as to estimate the partition of grinding energy entering the workpiece. The results of analysis were said to agree with the temperature distribution obtained from experiments. The experimental results showed that the occurrence of workpiece burn was closely related to boiling of the coolant. When the temperature in grinding zone reached a value at which bubbles formed, it was said that the bubbles grew up rapidly in the interface between the grinding wheel and the workpiece and blocked the heat transfer to the coolant.

Peters and Vansevenant developed a thermal model for both pendulum grinding and creep feed grinding [Peters, 1983]. It was found that if the depth of cut was increased and the work speed was decreased proportionally, the temperatures on the finished surface layer of the workpiece in creep grinding often falls below those achieved in conventional grinding. A survey was made and it was said that the temperature model proposed by Jaeger and Des Ruisseaux agreed with the experimental results of Werner. The investigation showed that coolant was more effective in creep feed grinding due to the longer contact time. It was found that the influence of the heat loss due to chip removal was rather small. When the depth of cut was in the range of creep feed grinding, which was above 2 mm, a steady state equation gave a good approximation to the real temperature.

Salter, Pearce and Howes carried out a fundamental investigation of workpiece burn in creep feed grinding [Salter, 1986]. The results of the investigation showed that workpiece burn was triggered when a critical workpiece temperature was reached and that the critical temperature was a function of coolant type. The results also showed that the amount of heat that can be removed from the grinding zone before reaching the

critical temperature depended on the workpiece material, geometry and wheel structure, as well as the coolant type. It was known that the proportion of the grinding heat entering the workpiece was responsible for thermal damage. The partition ratio for the heat entering the workpiece was therefore investigated. It was found that approximately 1% to 2% of the grinding energy was conducted into the workpiece when using a water-based fluid and this value rose to around 15% when using neat oil. It was also found that the onset of workpiece burn occurred at a surface temperature of around 130 C with the water-based fluid and around 300°C with neat oil.

Kim, Guo and Malkin investigated heat flux distribution and energy partition in creep feed grinding [Kim, 1997]. Transient grinding temperatures in the workpiece subsurface were measured using an embedded thermocouple. Temperature measurements in the subsurface were consistent with a triangular heat flux to the workpiece at the grinding zone. The overall energy partition was estimated from moving heat source theory as 3% for down grinding and 4.5% for up grinding. The measured temperatures were used in an inverse heat transfer analysis to calculate the heat flux and cooling distributions on the workpiece surface. It was claimed that the energy partition values from the inverse analysis were consistent with the results from moving heat source theory. In creep feed up grinding, a higher energy partition ratio was found, which might be attributed to thermal incompatibility at the grinding zone. It was concluded that creep feed down grinding should provide a more favourable thermal situation than up grinding.

Wang and Fuh proposed a heat transfer model based on numerical analysis of creep feed grinding [Wang, 1998]. The model was used to predict the workpiece surface temperature and to find the fraction of heat entering the workpiece. The model showed that the fraction of grinding energy entering the workpiece was small in creep feed grinding. The effects of Peclet number was discussed by applying analysis and numerical methods. It was said that conduction in the moving direction could not be neglected. The model was used to analyse the effectiveness of coolant, to predict the maximum surface temperature and to determine the critical energy for grinding burn.

8.2 The theoretical model for creep grinding

Creep feed grinding is usually an operation in one pass at full depth of cut, so that the effect of grinding heat on the surface integrity and the thermal deformation of the workpiece is important. If the temperature at burn is predicted, it may be possible to anticipate analytically the grinding energy flux just before burn for any workpiece shape and to select grinding conditions to avoid burning.

The primary theoretical investigation for temperature distribution in creep feed grinding on the final ground surface was based on the triangular heat source for form grinding derived in Chapter 3. The temperature model for form grinding was used to predict the surface temperature in form grinding developed in Chapter 4. In conventional grinding, the depth of cut is usually small. Therefore, it was assumed that temperature of the ground surface was the same as the temperature of the final workpiece surface. However, the depth of cut is significant when using creep feed grinding and the temperature difference in the z direction can no longer be neglected. Temperature at an arbitrary point under the workpiece surface can be calculated by substituting the value of z at the point into the thermal model. This means that the temperature of the finished workpiece surface is different from the temperature of the grinding contact surface. The maximum grinding temperature between the workpiece and grinding wheel is at the middle of the contact length. This maximum grinding temperature in creep feed grinding is not generated on the finished surface. The grinding heat generated between the workpiece and the grinding wheel is partly conducted into the finished workpiece surface and partly taken away by the chips and the coolant. Due to this reason, the grinding temperature on the finished surface in creep feed grinding is much less than in conventional grinding.

The thermal model was established based on the theory that the instantaneous plane heat source passes a semi-infinite body. In the theory, it is assumed that the heat source distribution is triangular. The basic temperature model may be expressed as,

$$\theta_{(x,z)} = \frac{\bar{q}\sqrt{t}}{c\rho\sqrt{\pi\alpha}}\left[4 - \frac{8t}{3t_t} - \frac{2z^2}{3\alpha t_t}\right]\exp\left(-\frac{z^2}{4\alpha t}\right) + \frac{\bar{q}z}{c\rho\alpha}\left[\frac{z^2}{3\alpha t_t} - \left(2 - \frac{2t}{t_t}\right)\right]\left[1 - erf\left(\frac{z}{\sqrt{4\alpha t}}\right)\right] \tag{8.1}$$

In conventional grinding, z was set to zero, in the temperature equation to calculate the surface temperature. In creep feed grinding, the temperature in the finished workpiece surface can be calculated directly using equation 8.1. The procedure for temperature calculation in creep feed grinding is as follows.

Step 1: Division of the grinding zone into a number of small strips across the width of workpiece profile. An illustration is shown in Figure 8.1. Each small strip is represented as a rectangle when calculating the temperature distribution in the grinding contact zone. The contact area of a strip can be expressed as

$$A_i = l_{ci} b_i \tag{8.2}$$

where

l_{ci} is the contact length of the strip

b_i is the width of the strip and can be expressed as

$$b_i = \frac{b}{n} \tag{8.3}$$

i = 1, 2,…, n

Step 2: Determination of the contact length of each strip. The real contact model was used to calculate the contact length.

$$l_{ci} = \left(1.435 \times 10^{-10} R_r^2 \frac{P d_{ei}}{v_s b_i} + a_i d_{ei}\right)^{1/2} \tag{8.4}$$

where

P is the grinding power

d_{ei} is the equivalent diameter of the grinding wheel at the strip

a_i is the depth of cut for the strip

Step 3: Grinding power distribution. The grinding power is distributed to each strip. The grinding power on each strip is obtained by assuming a proportional relationship with the removal rate at the strip

$$P_i = \frac{P}{Z} Z_i \tag{8.5}$$

where

Z_i is the removal rate at the strip, expressed as

$$Z_i = a_i b_i v_w \tag{8.6}$$

i = 1, 2,…, n

Step 4: Determination of partition ratio. To calculate the grinding temperature, it is required to estimate the energy partition to the workpiece. The partition ratio is calculated for the strip, from equation 4.41

$$R_{wi} = \left(1 + \frac{\kappa_{ge}}{\sqrt{r_o v_w (\kappa \rho c)_w}}\right)^{-1} \left(1 - R_{chi} - R_{fi}\right) \tag{8.7}$$

The workpiece partition ratio must be reduced by $(1\text{-}R_{ch}\text{-}R_f)$ for creep feed grinding. The maximum grinding energy carried away by the chips $R_{ch} = e_{ch}/e_c$ is limited to the energy required for melting the material [Malkin, 1991]. A typical maximum specific energy value of e_{ch} is approximately 6 J/mm^3 for ferrous materials [Rowe, 1988].

$$R_{wi} = \left(1 + \frac{\kappa_{ge}}{\sqrt{r_o v_w (\kappa \rho c)_w}}\right)^{-1} \left(1 - \frac{6}{e_c} - R_{fi}\right) \tag{8.8}$$

where

$(\kappa\rho c)_w$ is the thermal property of the workpiece

R_{fi} is the proportion of the total energy partitioned to the fluid expressed as

$$R_{fi} = \frac{q_{fi}}{q_t} \tag{8.9}$$

q_{fi} is the energy entering the fluid expressed as

$$q_{fi} = \theta_{wi} h_c \tag{8.10}$$

In order to calculate the partition ratio for the coolant, an iteration technique was used. This was the same as the procedure for conventional grinding, although this aspect now assumes greater importance.

Step 5: Temperature distribution on the finished surface

In order to calculate the temperature on the finished surface, it is necessary to know the depth of cut for each point on the contact curve between the grinding wheel and the workpiece. This depth of cut is the distance between the heat source and the finished surface is used in the temperature model. A simplified method to estimate the depth of cut for an arbitrary point on the contact curve was used. In the simplified method, the contact curve was divided evenly into elements. The distance z between each point and the finished surface was calculated. The distance is the value of the z co-ordinate required in the thermal model. The temperature at the corresponding point of the finished surface was calculated using the thermal model. The temperature distribution on the finished surface was therefore achieved. The geometrical relationship for the calculation described above is illustrated in Figure 8.2.

In Figure 8.2, the distance from the contact curve to the finished surface is z in creep feed grinding. The grinding wheel diameter is d_s, the depth of cut of the grinding wheel is a. The curve QC is the geometric contact length between the grinding wheel and the workpiece. CD is the finished surface in creep feed grinding. AC is the real contact length l_c. d_{sr} is the diameter of the real contact curve. AE is half of the chord length of

the real contact curve. For calculation of the distance z between each point on the contact curve and the finished surface, the contact curve was divided evenly into several small elements based on divisions of the depth of cut. Lines were drawn parallel to the finished surface at each division of the depth of cut. The distance z_j between each point and the finished surface was calculated from

$$z_j = \frac{a_j}{\cos\alpha_j} \tag{8.11}$$

where

$$j = 0, 1, 2, \ldots, m$$

a_j is the height of each point between the contact curve and finished surface

$\cos\alpha_j$ was expressed as

$$\cos\alpha_j = \frac{d_{sr} - 2a_j}{d_{sr}} \tag{8.12}$$

where d_{sr}, the diameter of the real contact curve is

$$d_{sr} = \frac{AE^2 + a^2}{a} \tag{8.13}$$

where

AE is the side of the triangular ACE

The ratio between the real contact curve and the depth of cut is large, so that the real contact curve may be seen approximately as a chord of the triangle ACE. AE can therefore be expressed as

$$AE = \sqrt{l_c^2 - a^2} \tag{8.14}$$

Substituting equation 8.14 into equation 8.13 and rearranging yields

$$d_{sr} = \frac{l_c^{\ 2}}{a} \tag{8.15}$$

substitution equation 8.15 into equation 8.12 and rearranging, yields

$$\cos\alpha_j = 1 - \frac{2aa_j}{l_c^2} \tag{8.16}$$

Substituting equation 8.16 into equation 8.11, the distance between the contact curve and the finished surface can be expressed as

$$z_j = \frac{a_j l_c^2}{l_c^2 - 2aa_j} \tag{8.16}$$

The value of the distance z_j substituted into equation 8.1, gives the temperature distribution on the finished surface.

8.3 Theoretical results

A computer program was developed in order to calculate the temperature on the finished surface [Appendix 2.2].

The temperature distribution calculated by the program is shown in Figure 8.3. There are three curves of temperature distribution in Figure 8.3. The upper curve shows the temperature profile along the grinding contact interface without coolant. The middle curve shows the temperature profile along the grinding contact interface with coolant. The lower curve shows the temperature profile on the finished surface with coolant. It can be seen from the temperature distribution curve for the finished surface that the lowest temperature is at the position where cutting starts. The temperature changes rapidly in the first third of the contact length and then is nearly constant in the remainder of the contact length. In other words, the temperature curve is almost flat over the remainder of the contact length. It was found that there was no difference between the contact surface temperature and the finished surface temperature from the middle of the contact area to the end of the contact length. The largest difference in temperature is from the start of the contact length to the middle of the contact length.

This is because the point at the end of the contact interface is directly under the heat source. In other words, the value of the z dimension is zero for the point on the contact interface. The temperature of the finished surface is determined by the depth under the contact curve surface.

In creep feed grinding, a high material removal rate can be achieved without thermal damage of the workpiece because much more of the heat enters the chips and the coolant. Figure 8.4 shows the predicted maximum temperature varying with depth of cut. It was found that the predicted maximum temperature increased with increasing depth of cut. This is expected because increasing the depth of cut increases grinding force so that grinding energy increases.

The predicted partition ratio varying with the depth of cut is shown in Figure 8.5. It was found the predicted workpiece partition ratio is much lower in creep feed grinding than in shallow grinding. It can be seen from Figure 8.5 that the partition ratio for the coolant is increased with increasing depth of cut. This is due to increasing depth of cut increasing grinding temperature. The coolant can carry away more heat at higher temperature, as can be seen from equation 8.10. The predicted workpiece partition ratio was found to reduce with increasing depth of cut. This is because increasing the partition ratio for the coolant decreases the workpiece partition ratio. This fact indicates that coolant plays a significant role in removing more of the heat from the grinding zone in creep feed grinding. To ensure that the cooling effect is maintained, the coolant should be sufficiently supplied to the grinding zone by a suitable method of application.

A characteristic of creep feed grinding is the large depth of cut and the slower workpiece speed. The effect of the workpiece speed and the grinding depth of cut is that the energy entering the workpiece decreases as the wokpiece speed is reduced and the grinding depth of cut is increased. This is because increasing the depth of cut results in a longer contact length in the grinding zone. A slower workpiece speed causes an increase in heating time over the contact zone and provides a larger area for convection. The grinding temperature is lower in creep feed grinding due to the lower partition ratio.

It can be concluded from the above analysis that creep feed grinding has advantages over conventional grinding for the same specific energy value, not only because the

removal rate is much higher but also because that the grinding temperature is much lower so that the danger of thermal damage is reduced.

A disadvantage of creep feed grinding is that the increased contact length increases the rate of wheel wear, so that there is a danger of loss of wheel sharpness and increased grinding energy.

8.4 Summary

Creep feed grinding is characterised by large depths of cut and low workspeed. The high removal rate in creep feed grinding results in a large quantity of grinding heat. It is therefore important to investigate temperature control in creep feed grinding.

A theoretical model for creep feed grinding has been established based on the theory that an instantaneous plane heat source passes a semi-infinite body. The procedure for temperature modelling is presented. The temperature distribution on the finished surface was predicted using the computer program developed for conventional and creep feed form grinding.

Chapter 9 Design chart for optimum quality and productivity

9.1 Introduction

In manufacture, product quality and machining productivity are increasingly important. It is required that productivity should be as high as possible and that the surface integrity of the machined parts is fully ensured. This is especially important in grinding operations since grinding is usually the last operation in machine part production. If the grinding parameters can be selected so as to achieve the highest possible productivity with satisfactory surface integrity, the grinding operation is considered to be optimized. It would be very useful to find such a method of optimization. A design chart is one of the methods for grinding operation optimization.

9.2 The principle of the design chart

The design chart is based on the principle of achieving the maximum removal rate within the critical conditions for thermal damage. For a given workpiece material, the critical temperature can be estimated from a materials handbook. The specific energy for chip formation can be determined from trials. For a particular value of the specific energy, a relational curve between workspeed and real depth of cut can be drawn. If specific energy and workspeed are known, the maximum depth of cut can be found from the curve.

The design chart was established based on the temperature model for form grinding. In order to avoid causing damage to the machined part, one method is to ensure that the maximum predicted temperature of the workpiece is lower than the critical temperature. The maximum temperature of the workpiece can be obtained from Chapter 3 equation 3.12

$$\theta_{(m)} = 1.064 \frac{R_w P}{A\sqrt{(\kappa\rho c)_w}} \sqrt{\frac{l_c}{v_w}} \tag{9.1}$$

For shallow cut grinding, the workpiece partition ratio is calculated ignoring fluid convection

$$R_w = R_{ws}(1 - R_{ch}) \tag{9.2}$$

The grinding power is calculated from the removal rate and the specific energy.

$$P = e_c a b v_w \tag{9.3}$$

The contact area in grinding is

$$A = b l_c \tag{9.4}$$

Substituting equations 9.3 and 9.4 into equation 9.1, yields

$$\theta_{(m)} = 1.064 \frac{R_w e_c a}{\sqrt{(\kappa \rho c)_w}} \sqrt{\frac{v_w}{l_c}} \tag{9.5}$$

Rearranging equation 9.5 yields

$$\sqrt{l_c} = 1.064 \frac{R_w e_c a}{\theta_m \sqrt{(\kappa \rho c)_w}} \sqrt{v_w} \tag{9.6}$$

Squaring equation 9.6 and then dividing by lg, yields

$$\frac{l_c}{l_g} = \frac{1.064^2 R_w^2 e_c^2 v_w}{\theta_m^2 (\kappa \rho c)} \frac{a^2}{\sqrt{a d_e}} \tag{9.7}$$

According to the real contact length model, the contact length is

$$l_c = \left(1.435 \times 10^{-10} R_r^2 \frac{P d_e}{v_s b} + a d_e \right)^{1/2} \tag{9.8}$$

Substituting equation 9.3 into the equation 9.8 yields

$$l_c = \left(1.435 \times 10^{-10} R_r^2 \frac{e_c a b v_w d_e}{v_s b} + a d_e \right)^{1/2} \tag{9.9}$$

Simplified equation 9.9 and dividing equation 9.9 by the geometric contact length, lg, yields

$$\frac{l_c}{l_g} = \left(1.435\times10^{-10} R_r^2 \frac{e_c b v_w}{v_s b} + 1\right)^{1/2} \tag{9.10}$$

Substituting equation 9.10 into equation 9.7 and rearranging, yields

$$\frac{a^{3/2}}{d_e^{1/2}} = \frac{\theta_m^2 (\kappa\rho c)_w}{1.134 R_w^2 e_c^2 v_w}\left(1.435\times10^{-10} R_r^2 e_c \frac{v_w}{v_s} + 1\right)^{1/2} \tag{9.12}$$

For a given workpiece material, workpiece and grinding wheel geometrical parameters, the critical temperature is known and the equivalent diameter can be evaluated. For a particular value of specific energy, a curve of workspeed against depth of cut can be drawn. Several typical values of specific energy were selected, a curve was drawn for each value to provide a design chart.

Figure 9.1 is a design chart for the workpiece material En31. The critical temperature for En31 was assumed to be 380°C based on the temperature which cause tempering. The horizontal axis of the design chart represents workspeed and the vertical axis of the design chart represents the ratio of normal depth of cut and equivalent diameter of the grinding wheel. It can be seen from the design chart that the change in the value of depth of cut is small when the workspeed is between 0.1 m/s and 0.3 m/s. Such a range of workspeed is usually used for shallow grinding operation. When the workspeed is much less than 0.1 m/s, the grinding operation is considered as creep grinding. In this workspeed range, the workspeed influences depth of cut significantly. When a value of workspeed is determined and a required value of specific energy is determined, the critical value of depth of cut can be determined indirectly according to the design chart. This value of depth of cut is the critical value for workpiece thermal damage. The value of the specific energy should be as small as possible and the grinding power should be less than the allowable power of the grinding machine. This is because a low specific energy allows a high material removal rate, in other words, high productivity.

The values of critical temperature for two typical workpiece materials are shown in Table 9.1. The values were obtained through cooperative work undertaken by the Swedish Institute of Metals Research.

Table 9.1 Experimental grinding temperature corresponding to different thermal damage criteria for the materials tested

No	Materials / Damage criterion used	Grinding Temp[a].θ_g		Conditions
		M2	EN31	
1	Hardness (a)	461	380	$(HV) - (HV)_g \leq 5\%$
	(b)	648	580	$(HV)_g$min
2	Residual stress (a)	570	380	$\sigma_{11} \leq -200$MPa
	(b)	605	438	$\sigma_{11} = 0$

The suffix 'g' corresponds to the 'as ground' value of a specific parameter of interest, such as the Vickets hardness number.

a – based on measured temperature

b – based on calculated temperature

Based on, the values of critical temperature in Table 9.1, a group of design charts were determined, as shown in Figure 9.2 to Figure 9.5.

9.3 An example of using the design chart

An example is given to demonstrate the application of the design chart. The angle approach method is used to grind a cylindrical surface and a shoulder surface. The specification of the grinding operation is as follows.

workpiece material En31

grinding wheel specification Alumina

wheel speed	40 m/s
wheel maximum diameter	200 mm
workpiece start diameter	40 mm
workpiece final diameter	39.5 mm
start length of cylindrical diameter	15 mm
final length of cylindrical diameter	15.5 mm

The workpiece is shown in Figure 9.6. Grinding is the last operation for the workpiece. In order to avoid thermal damage, it is required that the maximum temperature on the workpiece must not exceed the critical temperature of the workpiece material, which is 380°C. Based on the operation specification, it was decided to use shallow grinding. The workspeed was selected as 0.2 m/s. The specific energy was selected as 70 J/mm^3 taking grinding efficiency and the machine tool power limitation into consideration. Based on the selected values of workspeed and specific energy, it was found from the design chart Figure 9.1 that the value of the vertical co-ordinate axis, the ratio of $a_n^{3/2}/d_n^{1/2}$ is 6.53×10^{-8} m. From the design chart,

$$\frac{a^{3/2}}{d_e^{1/2}} = 6.53\times10^{-8} m \tag{9.13}$$

In equation 9.13, it is clear that the equivalent diameter of the grinding wheel can be evaluated when the geometrical parameters of the workpiece and the grinding wheel are given.

The equivalent diameter of the grinding wheel when using angle approach on the shoulder surface is

$$d_{se1} = \frac{d_{s1}'}{\sin 30^o} \tag{9.14}$$

On the cylindrical surface the equivalent diameter is

$$d_{se2} = \frac{d_{s2}'}{\cos 30^o + \frac{d_{s2}'}{d_{w2}}} \tag{9.15}$$

In equations 9.14 and 9.15, d_{s1}'is the average diameter of the grinding wheel at the shoulder surface and d_{s2}' is the average diameter of the grinding wheel at the cylindrical surface. The average diameters at the shoulder surface are

$$d_{s1}' = \frac{d_s + d_{ssh}}{2} \tag{9.16}$$

At the cylindrical surface

$$d_{s2}' = \frac{d_s + d_{scy}}{2} \tag{9.17}$$

In equations 9.16 and 9.17, d_{ssh} is the minimum diameter of the grinding wheel at the shoulder surface and d_{scy} is the minimum diameter of the grinding wheel at the cylindrical surface. These two values of the minimum diameter of the grinding wheel can be calculated according to the geometrical relationships shown in Figure 9.6. The minimum diameter at the shoulder surface is

$$d_{ssh} = 200 - 2\left(\frac{60-40}{2}\right)\cos 30^o = 183 \text{ mm}$$

The minimum diameter at the cylindrical surface is

$$d_{scy} = 200 - 2(15\sin 30^o) = 185 \text{ mm}$$

Substituting the above values into equations 9.14 to 9.17, the equivalent diameters are

$d_{se1} = 383$ mm

$d_{se2} = 34$ mm

Substituting the value of d_{se1} and d_{se2} into equation 9.13, the value of depth of cut can be calculated as follows.

$$a_{sh} = \sqrt[3]{383 \times \left(6.53 \times 10^{-5}\right)^2} = 1.18 \times 10^{-2} \text{ mm}$$

$$a_c = \sqrt[3]{34 \times \left(6.53 \times 10^{-5}\right)^2} = 5.26 \times 10^{-3} \text{ mm}$$

The results $a_{sh} = 1.18 \times 10^{-2}$ mm and $a_c = 5.26 \times 10^{-3}$ mm are the critical depths of cut for thermal damage at the shoulder surface and the cylindrical surface respectively.

In angle approach grinding, the infeed direction is not usually perpendicular to the grinding wheel axis. In the present example, the angle between the grinding wheel axis and workpiece axis is 30°, and the angle between the infeed direction and the axis of workpiece surface is 60°. From the geometrical relationship of angle approach grinding the relationships between depths of cut on the shoulder surface and the cylindrical surface and the infeed direction is shown in Figure 9.6. The relationships are,

$$a_{sh} = a \cos 60^\circ \tag{9.18}$$

$$a_c = a \sin 60^\circ \tag{9.19}$$

where a is the depth of cut in the infeed direction.

$$a = \pi d_w \frac{v_f}{v_w} \tag{9.20}$$

Substituting equation 9.20 into equation 9.18 and 9.19, the infeed rate normal to the shoulder surface can be calculated.

$$v_{fsh} = \frac{a_{sh} v_w}{\pi d_w \cos 60^o} = 2.5 \times 10^{-2} \, mm/s$$

The infeed rate normal to the cylindrical surface is

$$v_{fc} = \frac{a_c v_w}{\pi d_w \sin 60^o} = 9.67 \times 10^{-3}\, mm/s$$

$v_{fsh} = 2.5\times10^{-2}$ mm/s is the maximum infeed rate towards the shoulder surface and $v_{fc} = 9.67\times10^{-3}$ mm/s is the maximum infeed rate towards the cylindrical surface with an approach angle of 60°. When using these two values in grinding operation, the maximum productivity can be achieved free of thermal damage.

The disadvantage of this method is that the cylindrical grinding and the shoulder grinding may not be finished simultaneously. Under such circumstance, the highest possible productivity may not be achieved. In order to ensure the cylindrical grinding and the shoulder grinding to be finished simultaneously and to achieve the maximum productivity, the approach angle should be calculated based on the stock to be removed from each surface,

$$\phi_f = \arctan\frac{a_c}{a_{sh}} \tag{9.21}$$

Using the approach angle calculated from equation 9.21, the cylindrical surface and the shoulder surface can be ground simultaneously. Substituting the approach angle into equations 9.18, 9.19 and equation 9.20, the required infeed rates for both the cylindrical surface and the shoulder surface are achieved. The results are the maximum infeed rate at the shoulder surface and the cylindrical surface with an approach angle of ϕ_f. When using these two values, the maximum productivity can be achieved free of thermal damage and the shoulder surface and the cylindrical surface grinding can be finished simultaneously.

In order to estimate whether the power limit is reached under such circumstances, the grinding power can be calculated based on the selected specific energy and removal rate. The total grinding power is,

$$P_t = e_c Z_t \tag{9.22}$$

where

$$Z_t = Z_{sh} + Z_{cy} \tag{9.23}$$

is the total removal rate. The removal rate from the shoulder surface is.

$$Z_{sh} = \pi d_{w1} v_{fsh} b_{w1} \tag{9.24}$$

the removal rate from the cylindrical surface is,

$$Z_{cy} = \pi d_{w2} v_{fc} b_{w2} \tag{9.25}$$

If the grinding power required is greater than the power the grinding machine can supply and the total material removal rate is kept constant, a lower specific energy must be achieved to reduce the grinding power required. Thermal damage can be avoided and economic and high efficiency grinding operations can be performed, when there optimised conditions have been achieved. Further reducing the specific energy will allow even higher feed rates to be employed.

9.4 Summary

The design chart is a tool for grinding process optimization. The design chart was established based on the temperature model for form grinding. The design chart provides a method to select optimum values of grinding parameters so as to achieve high grinding efficiency and to avoid thermal damage caused by a temperature which is higher than the critical temperature of the workpiece material.

To use the design chart, the workspeed is determined first. The specific energy is then estimated. The depth of cut to be used can then be selected from the design chart and the infeed rate calculated. The grinding power is then checked to ensure that it falls within the power limitation of the machine. If not, the specific energy must be reduced or the feed rate must be reduced.

An example of using the design chart for grinding parameter selection is demonstrated in angle approach grinding.

Chapter 10 Conclusions

The theory of a sliding instantaneous infinite plane heat source with a triangular heat flux distribution was used together with other models of conduction and convection to develop a temperature model for predicting grinding temperatures in form grinding. The predicted temperatures agree reasonably well with the experimental results taking into consideration the scatter in the experiments.

In form grinding, the temperature distribution across the profile is closely related to the workpiece profile angle. Where the profile angle is large, the temperature is high. Where the profile angle is small, the temperature is low.

At a discontinuity, it was found that there is a significant difference between the predicted temperatures and measured temperatures from experiments. The difference was attributed to the shape factor. Theoretically, the intersection of two flanks is a sharp angle. In practice, the intersection of two flanks is a curve with a radius of at least 0.15 mm. Due to the radius, the discontinuity is effectively eliminated.

The real contact length should be used for temperature prediction, rather than the geometric contact length. Using the real contact length is important to obtain agreement between theory and experiment.

Experimental results show that the temperature signals obtained under dry grinding conditions are better than those obtained under wet grinding conditions. It was concluded that the measured temperatures were under-estimated, particularly under wet grinding conditions.

Under the same grinding conditions, the partition ratio is lower when using a CBN grinding wheel than when using an alumina wheel. This is because a CBN grinding wheel has a greater thermal conductivity than an alumina grinding wheel.

In angle approach grinding of a cylinder and a shoulder where the angle is 60°, the predicted temperatures on the cylindrical surface are higher than those on the shoulder surface under the condition that the infeed direction is perpendicular to the axis of

grinding wheel. This is mainly because the removal rate is larger on the cylindrical surface.

A method of optimising a grinding operation is proposed using a design chart. The design chart gives a group of grinding parameters which ensure the highest productivity under the constraint of no thermal damage.

It was shown that the thermal model can be applied both to conventional shallow grinding and to creep feed grinding. For creep feed grinding, more heat can be extracted by the coolant than in shallow grinding due to the greater contact length, and the greater time of contact.

Chapter 11 Suggestions for further work

The predicted temperatures were found to give the best agreement with the measured temperatures in dry grinding. However, an exact match was not obtained in wet grinding. Further research on the temperature technique is required to achieve greater consistency of results and more reliable signal quality. The experimental measurement system is required to be further improved for temperature measurement to ensure that the temperature signal is not influenced by the coolant. It is also suggested that neat oil is likely to produce better results than soluble oil in water emulsion

Further theoretical work is required to investigate alternative values of convection coefficient to obtain improved correlation with the measurements.

Further work is required to obtain temperature measurements under creep feed conditions to allow refinement of the model including fluid convection.

When calculating the temperature at the discontinuity on the workpiece profile, a shape factor was used. At present, the effect of the dressing roll radius is not taken into consideration. Further investigation that accounts for the effect of the radius should give more accurate predictions. It is suggested to use wire thermocouples instead of foil thermocouples in grinding experiments to ensure the minimum width at the discontinuity.

Further improvements are needed for the depth of cut measurement subsystem, to relate the depth of cut measurement more precisely to the position of the temperature measurement.

REFERENCES

Ashby M F and Jones D R H, 1986, ''Engineering Materials 2: An introduction to microstructures'', processing and design, Published by Pergumon Ltd.

Chang C C and Szeri A Z, 1994, ''A thermal analysis of grinding, Mechanics in Materials Processing and Manufacturing'', ASME AMD Vol. 194, pp103-119.

Black S C E, 1996, ''The effect of abrasive properties on the surface integrity of ground ferrous materials'', PhD thesis, Liverpool John Moores University.

Des Ruisseaux N R and Zerkle R D, 1970, ''Thermal analysis of the grinding process'', Journal of Engineering for Industry, Transaction of ASME, pp428-434.

Des Ruisseaux N R and Zerkle R D, 1970, ''Temperature in semi-infinite and cylindrical bodies subjected to moving heat source and surface cooling'', Journal of Heat Transfer, Transaction of ASME, Vol. 92, pp456-464.

DeVries R C, 1972, ''Cubic Boron Nitride: Handbook of properties'', General Electric Technical Information series, General Electric Company Corporate Research and Development, No 72CRD178.

Davies D J and Oelman L A, 1983, ''The structure properties and heat treatment of metals'', Published by Pitman Ltd.

Furukawa Y, Ohishi S and Shiozaki S, 1979, ''Selection of Creep Feed Grinding Condition in View of Workpiece Burning'', Annals of the CIRP, Vol28, 1, pp213-218.

Gordeev A V, 1976, ''Grinding with angular wheels, Machines and Tooling'', Annals of the CIRP, Vol. 47, No 6, pp34-35.

Graham W and Falconer D, 1978, ''Wheel - workpiece conformity in form grinding''. 19th MTDR conference, pp615-621.

Gu D Y and Wager J G, 1990, ''Further evidence on the contact zone in surface grinding'', Annals of the CIRP, Vol. 39, No 1, pp349-352.

Guo C and Malkin S, 1995, ''Analysis of transient temperatures in grinding'', Journal of Engineering for Industry, Transaction of ASME, Vol. 117, pp571-577.

Guo C and Malkin S, 1996 (1), ''Inverse heat transfer analysis of grinding. part 1: method'', Journal of Engineering for Industry, Transaction of ASME, Vol. 118, pp137-142.

Guo C and Malkin S, 1996 (2), ''Inverse heat transfer analysis of grinding, part 2: application'', Journal of Engineering for Industry, Transaction of ASME, Vol. 118, pp143-149.

Graham W and Falconer D, 1978, ''Wheel-workpiece conformity in form grinding'', Proceedings of MTDR, pp 615 – 622.

Grigull U and Sandner H, 1984, ''Heat Conduction'', published by Hemisphere Publishing Corporation, pp 122.

Hahn R S, 1956, ''The relation between grinding conditions and thermal damage in workpiece'', Transaction of ASME, Vol. 78, pp807-812.

Hahn R S, 1962, ''On the nature of the grinding process'', Proceedings of the 3rd MTDR Conference, pp129-154.

Higgins R A, 1983, ''Engineering metallurgy-Part 1'', 5th Edition, Published by Hodder and Stoughton Ltd.

Howes T D, Neailey K, Harrison A J, 1987, ''Fluid film boiling in shallow - cut grinding'', Annals of the CIRP, Volume 36/1, pp223-226.

Isenberg J and Malkin S, 1975, ''Effects of variable thermal properties on moving-band-source temperatures'', Journal of Engineering for Industry, Transactions of the ASME, August 1975, pp1074-1078.

Jaeger J C, 1942, ''Moving sources of heat and the temperature at sliding contacts'', Proceedings of Royal Society of New South Wales, Vol. 76, pp203-224.

Jen T C and Lavine A S, 1992, ''Thermal aspects of grinding: An improved model of heat transfer to workpiece, wheel and fluid, Heat Transfer in Material Processing'', ASME HTD, Vol. 224, pp1-7.

Jen T C and Lavine A S, 1995, ''A variable heat flux model of heat transfer in grinding: Model development'', Journal of Heat Transfer, Transaction of ASME, Vol. 117, pp473-478.

Jen T C and Lavine A S, 1996, ''A variable heat flux model of heat transfer in grinding with boiling, Journal of Heat Transfer'', Transaction of ASME, Vol. 118, pp463-470.

Kim J W, Howes T.D and Gupta H, 1997, ''The search for an economic domain of operation when grinding below the film boiling limit'', International Journal of Machine Tool Manufacturing, Vol. 37, No. 4, pp391-399.

Lavine A S, 1988, ''A simple model for convective cooling during the grinding process'', Transactions of the ASME, Journal of Engineering for Industry, Vol. 110, pp1-6.

Lavine A S and Malkin S, 1989, ''Thermal aspects of grinding with CBN wheels'', Annals of the CIRP, Vol. 38/1, pp557-560

Lavine A S and Jen T C, 1991, ''Coupled heat transfer to workpiece, wheel, and fluid in grinding, and the occurrence of workpiece burn'', International Journal of Heat Mass Transfer, Vol. 34, No 4/5, pp983-992.

Lavine A S and Jen T C, 1991, ''Thermal aspects of grinding: heat transfer to workpiece, wheel and fluid, Journal of Heat Transfer'', Transaction of ASME. Vol. 113, pp296-303.

Lee D G, Zerkle R D and Des Ruisseaux N R, 1971, ''An experimental study of thermal aspects of cylindrical plunge grinding'', ASME paper WA-71/prod-4

Malkin S and Cook N H, 1971, ''The wear of grinding wheels, Part 2 – fracture wear'', Journal of engineering for industry, November, pp1129-1133.

Malkin S, 1974, ''Thermal aspects of grinding, Journal of Engineering for Industry'', Transaction of ASME, Vol.96, pp456-464.

Malkin S, 1989, ''Grinding technology theory and applications of machining with abrasives'', Ellis Horwood Limited.

Makino, Suto, Fokushima, 1966, ''An experimental investigation of the grinding process'', Journal of Mechanical Laboratory of Japan, 12,1,17.

Maris M, Snoeys R, 1973, ''Head affected zone in grinding operations'',14th MTDR Conf. Pp504.

Ohishi S and Furukawa Y, 1985, ''Analysis of workpiece temperature and grinding burn in creep feed grinding'', Bulletin of the JSME V28, n242, Aug, pp1775-1781.

Okuyama S, Nakamura Y and Kawamura S, 1991, ''Cooling action of grinding fluid in shallow grinding'', International Journal of Machine Tool Manufacturing, Vol. 33, No.1, pp 13-23.

Outwater J O and Shaw M C, 1952, ''Surface temperature in grinding'', Transaction of ASME, Vol. 74, pp73-85.

Peters J and Vansevenant E, 1983, ''A thermal model covering pendulum grinding and creep feed grinding'', Annals of the CIRP, V32. 1, pp491-495.

Powell J W and Howes T D, 1978, ''A study of the heat flux at which burn occurs in creep feed grinding'', 19th MTDR Conf., pp 629-637.

Rothman M F, 1978, ''High temperature property data-ferrous alloys''. Published by SAM Int.

Ramanath S and Shaw M C, 1988, ''Abrasive grain temperature at the beginning of a cut in fine grinding'', Transaction of the ASME, Journal of Engineering for Industry, Vol. 110, pp15-18.

Rowe W B, Pettit J A, Boyle A and Moruzzi J L, 1988, ''Avoidance of the thermal damage in grinding and prediction of the damage threshold'', Annals of the CIRP, Vol. 37, No 1, pp327-330.

Rowe W B, Morgan M N, Pettit J A and Lavine A S, 1990, ''A discussion of thermal models in grinding'', Proceedings of 4th International Grinding Conference, MR90-516.

Rowe W B, Morgan M N and Allanson D A, 1991, ''An advance in the modelling of thermal effects in the grinding process'', Annals of the CIRP, Vol. 40, No 1, pp339-342.

Rowe W B, Morgan M N, Qi H S and Zheng H W, 1993, ''The effect of deformation on the contact area in grinding'', Annals of the CIRP, Vol. 42/1, pp409-412.

Rowe W B, Black S C E, 1995, ''Experimental investigation of heat transfer in grinding'', Annals of the CIRP, Vol. 44, pp329-332.

Rowe W B, Black S C E, 1996, ''Analysis of grinding temperatures by energy partitioning'', Proc Instn Mech Engrs, Vol. 201, Part B, pp579-588.

Saljé E, Damlos H.-H and Teiwes H, 1981, ''Problems in profile grinding – annular plunge grinding and surface grinding'', Annals of the CIRP, Vol. 30, No 1, pp219-222.

Saljé E, Damlos H.-H, 1984, ''Engagement conditions for surface profile grinding'', Proc. of S. M. E. International Grinding Conference, August, pp27-29.

Salter N D, Pearce T R A and Howes T D, 1985, ''A fundamental investigation of workpiece burn in creep feed grinding'', America Society of Mechanical Engineers, Production Engineering Division PED V16 pp199-208.

Shaw M C, 1989, ''A simplified approach to workpiece temperatures in fine grinding'', Annals of the CIRP, Vol. 39, No 1, pp345-347.

Snoeys R, Leuven K U, Maris M, Wo N F, Peters J and Leuven K U, 1978, ''Thermally induced damage in grinding'', Annals of the CIRP, Vol. 27, No 2. pp571 – 581.

Butterworth Heineman, 1992, ''Smithells Metal reference Book'', Published by Butterworth Heineman Ltd., 7th edition.

Tönshoff H K, Peters J, Inasaki I and Paul T, 1992, ''Modelling and simulation of grinding processes'', Annals of the CIRP, Vol. 41, No 2, pp 677-688.

Trmal G J, 1982, ''Form grinding - problems and solutions'', Proceedings of the Third Polytechnic Symposium on Manufacturing Engineering, May 25 – 26, pp237 – 245.

Qi H S, Mills B and Rowe W B, 1994, ''An analysis of real contact length in abrasive machining processes using contact mechanics'', Wear, Vol. 176, pp137-141.

Qi H S, Rowe W B, 1997, ''Contact length in grinding'', Proc Instn Mech Engrs, Vol 211 Part J, pp77-85.

Zhou Z X and Lutterwelt C A V, 1992, ''The real contact length between grinding wheel and workpiece – a new concept and a new measuring method'', Annals of the CIRP, Vol41, No1, pp387-391.

Verkerk J., 1975, ''The real contact length in cylindrical plunge grinding'', Annals of the CIRP, V24, 1, pp259-264.

Wang S.-B, Fuh K.-H, 1998, ''The workpiece temperature, fluid cooling effectiveness and burning threshold of grinding energy in creep feed grinding'', Journal of Engineering Manufacture V212, nB5, pp383-391.

D. Walsh and A.A. Torrance, 1998 to be published, ''Influence of form on surface temperature in form grinding'',Journal of Mechanical Engineering Science, Part C of the Proceedings of the Institution of Mechanical Engineers

Woolman J, Mottram R A, 1996, ''The mechanical and physical properties of the British standard En steel'', Published by the British Iron and Steel Research Association, Pergamon Press Oxford

APPENDIXES

Appendix 1 Derivation of the temperature equation for a triangular heat distribution

For an instantaneous infinitely wide plane heat source

$$\theta = \frac{q_m}{c\rho(4\pi\alpha t)^{1/2}} \exp\left(-\frac{z^2}{4\alpha t}\right) \tag{A.1}$$

A triangular heat source can be expressed as

$$2\bar{q}\left(1-\frac{\tau'}{\tau_o}\right) \tag{A.2}$$

The quantity of the heat flux in the moment dτ', is

$$q_m = 2\bar{q}\left(1-\frac{\tau'}{\tau_o}\right)d\tau' \tag{A.3}$$

The temperature rise is influenced by the heat flux in the moment dτ'

$$d\theta_{(x,z)} = \frac{2\bar{q}\left(1-\frac{\tau'}{\tau_o}\right)d\tau'}{c\rho\sqrt{4\pi\alpha(t-\tau')}} e^{-\frac{z^2}{4\alpha(t-\tau')}} \tag{A.4}$$

The temperature due to the sliding heat source is found by integrating equation A.4

across the length of the head source

$$\theta_{(x,z)} = \int_{\tau'=0}^{\tau'=t} \frac{2\bar{q}\left(1-\frac{\tau'}{\tau_o}\right)d\tau'}{c\rho\sqrt{4\pi\alpha(t-\tau')}} e^{-\frac{z^2}{4\alpha(t-\tau')}} \tag{A.5}$$

The workpiece may be assumed to be a semi-infinite body and therefore the temperature

is twice the temperature rise for an infinite heat sink,

$$\theta_{(x,z)} = \int_{\tau'=0}^{\tau'=t} \frac{4\bar{q}\left(1-\frac{\tau'}{\tau_o}\right)d\tau'}{c\rho\sqrt{4\pi\alpha(t-\tau')}} e^{-\frac{z^2}{4\alpha(t-\tau')}} \tag{A.6}$$

Introducing substitution variables,

$$u = \frac{z}{\sqrt{4\alpha(t-\tau')}} \tag{A.7}$$

Squaring equation A.7, yields

$$u^2 = \frac{z^2}{4\alpha(t-\tau')} \tag{A.8}$$

$$du = z\left(-\frac{1}{2}\right)[4\alpha(t-\tau')]^{-\frac{3}{2}}(-4\alpha d\tau') \tag{A.9}$$

$$du = z[4\alpha(t-\tau')]^{-\frac{3}{2}}2\alpha d\tau' \tag{A.10}$$

$$du = \frac{2z\alpha}{[4\alpha(t-\tau')]^{3/2}}d\tau' \tag{A.11}$$

$$d\tau' = \frac{[4\alpha(t-\tau')]^{3/2}}{2z\alpha}du \tag{A.12}$$

Substituting equation A.12 into equation A.6, yields

$$\theta_{(x,z)} = \int_{\frac{z}{\sqrt{4\alpha t}}}^{\infty} \frac{4\bar{q}\left(1-\frac{\tau'}{\tau_o}\right)}{c\rho\sqrt{4\pi\alpha(t-\tau')}} \frac{[4\alpha(t-\tau')]^{3/2}}{2z\alpha} e^{-u^2}du \tag{A.13}$$

Simplifying equation A.13,

$$\theta_{(x,z)} = \int_{\frac{z}{\sqrt{4\alpha t}}}^{\infty} \frac{2\bar{q}\left(1-\frac{\tau'}{\tau_o}\right)}{c\rho\sqrt{\pi}} \frac{4\alpha(t-\tau')}{z\alpha} e^{-u^2}du \tag{A.14}$$

Substituting equation A.7 into equation A.14 and rearranging A.14, yields

$$\theta_{(x,z)} = \int_{\frac{z}{\sqrt{4\alpha t}}}^{\infty} \frac{2\bar{q}\left(1-\frac{\tau'}{\tau_o}\right)}{c\rho\sqrt{\pi}} \frac{z}{\alpha}\frac{1}{u^2} e^{-u^2}du \tag{A.15}$$

Simplifying A.15, yields

$$\theta_{(x,z)} = \frac{2\bar{q}z}{c\rho\alpha\sqrt{\pi}} \int_{\frac{z}{\sqrt{4\alpha t}}}^{\infty} \left(1 - \frac{\tau'}{\tau_o}\right) \frac{1}{u^2} e^{-u^2} du \qquad \text{(A.16)}$$

Rearranging A.16, yields

$$\theta_{(x,z)} = \frac{2\bar{q}z}{c\rho\alpha\sqrt{\pi}} \left[\int_{\frac{z}{\sqrt{4\alpha t}}}^{\infty} \frac{1}{u^2} e^{-u^2} du - \int_{\frac{z}{\sqrt{4\alpha t}}}^{\infty} \frac{\tau'}{\tau_o} \frac{1}{u^2} e^{-u^2} du \right] \qquad \text{(A.17)}$$

From equation A.8

$$t - \tau' = \frac{z^2}{4\alpha u^2} \qquad \text{(A.18)}$$

So that

$$\tau' = t - \frac{z^2}{4\alpha u^2} \qquad \text{(A.19)}$$

Substituting equation A.18 into equation A.16, yields

$$\theta_{(x,z)} = \frac{2\bar{q}z}{c\rho\alpha\sqrt{\pi}} \left[\int_{\frac{z}{\sqrt{4\alpha t}}}^{\infty} \frac{1}{u^2} e^{-u^2} du - \frac{1}{\tau_o} \int_{\frac{z}{\sqrt{4\alpha t}}}^{\infty} \left(t - \frac{z^2}{4\alpha u^2}\right) \frac{1}{u^2} e^{-u^2} du \right] \qquad \text{(A.20)}$$

Rearranging A.20, yields

$$\theta_{(x,z)} = \frac{2\bar{q}z}{c\rho\alpha\sqrt{\pi}} \left[\int_{\frac{z}{\sqrt{4\alpha t}}}^{\infty} \frac{1}{u^2} e^{-u^2} du - \frac{t}{\tau_o} \int_{\frac{z}{\sqrt{4\alpha t}}}^{\infty} \frac{1}{u^2} e^{-u^2} du + \frac{z^2}{4\alpha\tau_o} \int_{\frac{z}{\sqrt{4\alpha t}}}^{\infty} \frac{1}{u^2} \frac{1}{u^2} e^{-u^2} du \right] \qquad \text{(A.21)}$$

From standard integrals

$$\int_{\frac{z}{\sqrt{4\alpha t}}}^{\infty} \frac{1}{u^2} e^{-u^2} du = e^{-\frac{z^2}{4\alpha}} \frac{\sqrt{4\alpha t}}{z} - \sqrt{\pi}\left(1 - erf\left(\frac{z}{\sqrt{4\alpha t}}\right)\right) \qquad \text{(A.22)}$$

and

$$\int_{\frac{z}{\sqrt{4\alpha t}}}^{\infty} \frac{1}{u^2}\frac{1}{u^2}e^{-u^2}du = e^{-\frac{z^2}{4\alpha}}\frac{\left(\sqrt{4\alpha t}\right)^3}{3z^3} - \frac{2}{3}\left(e^{-\frac{z^2}{4\alpha t}}\frac{\sqrt{4\alpha t}}{z} - \sqrt{\pi}\left(1 - erf\left(\frac{z}{\sqrt{4\alpha t}}\right)\right)\right) \quad \text{(A.23)}$$

Substitution equating A.22 and equation A.23 into equation A.21, yields

$$\theta_{(x,z)} = \frac{2\bar{q}z}{c\rho\alpha\sqrt{\pi}}\left(e^{-\frac{z^2}{4\alpha}}\frac{\sqrt{4\alpha t}}{z} - \sqrt{\pi}\left(1 - erf\left(\frac{z}{\sqrt{4\alpha t}}\right)\right)\right)$$

$$-\frac{t}{\tau_o}\left(e^{-\frac{z^2}{4\alpha}}\frac{\sqrt{4\alpha t}}{z} - \sqrt{\pi}\left[1 - erf\left(\frac{z}{\sqrt{4\alpha t}}\right)\right]\right) \quad \text{(A.24)}$$

$$+\frac{z^2}{4\alpha\tau_o}\left(e^{-\frac{z^2}{4\alpha}}\frac{\left(\sqrt{4\alpha t}\right)^3}{3z^3} - \frac{2}{3}\left(e^{-\frac{z^2}{4\alpha}}\frac{\sqrt{4\alpha t}}{z} - \sqrt{\pi}\left[1 - erf\left(\frac{z}{\sqrt{4\alpha t}}\right)\right]\right)\right)$$

Simplifying and rearranging equation A.24, yields

$$\theta_{(x,z)} = \frac{2\bar{q}z}{c\rho\alpha\sqrt{\pi}}\left(e^{-\frac{z^2}{4\alpha}}\frac{\sqrt{4\alpha t}}{z}\left(1 - \frac{t}{\tau_o}\right) - \sqrt{\pi}\left(1 - erf\left(\frac{z}{\sqrt{4\alpha t}}\right)\right)\left(1 - \frac{t}{\tau_o}\right)\right) \quad \text{(A.25)}$$

$$+e^{-\frac{z^2}{4\alpha}}\frac{\sqrt{4\alpha t}}{z}\frac{t}{3\tau_o} - e^{-\frac{z^2}{4\alpha}}\frac{\sqrt{4\alpha t}}{z}\frac{2}{3}\frac{z^2}{4\alpha\tau_o} + \frac{2}{3}\frac{z^2}{4\alpha\tau_o}\sqrt{\pi}\left(1 - erf\left(\frac{z}{\sqrt{4\alpha t}}\right)\right)\Bigg)$$

Simplifying equation A.25, yields

$$\theta_{(x,z)} = \frac{2\bar{q}z}{c\rho\alpha\sqrt{\pi}}$$

$$\left(e^{-\frac{z^2}{4\alpha}}\frac{\sqrt{4\alpha t}}{z}\left(1 - \frac{t}{\tau_o} + \frac{t}{3\tau_o} - \frac{2}{3}\frac{z^2}{4\alpha\tau_o}\right) - \sqrt{\pi}\left(1 - erf\left(\frac{z}{\sqrt{4\alpha t}}\right)\right)\left(1 - \frac{t}{\tau_o} - \frac{z^2}{6\alpha\tau_o}\right)\right) \quad \text{(A.26)}$$

Rearranging equation A.26, yields

$$\theta_{(x,z)} = \frac{2\bar{q}\sqrt{4\alpha t}}{c\rho\alpha\sqrt{\pi}}e^{-\frac{z^2}{4\alpha}}\left(1 - \frac{t}{\tau_o} + \frac{t}{3\tau_o} - \frac{z^2}{6\alpha\tau_o}\right) - \frac{2\bar{q}z}{c\rho\alpha}\left(1 - erf\left(\frac{z}{\sqrt{4\alpha t}}\right)\right)\left(1 - \frac{t}{\tau_o} - \frac{z^2}{6\alpha\tau_o}\right) \quad \text{(A.27)}$$

For the contact surface temperature, z = 0

$$\theta_w = \frac{4\bar{q}}{\sqrt{\pi(\kappa\rho c)_w}}\left(1 - \frac{t}{\tau_o} + \frac{t}{3\tau_o}\right) \tag{A.28}$$

Simplifying and rearranging equation A.28,

$$\theta_w = \frac{4\bar{q}}{\sqrt{\pi(\kappa\rho c)_w}}\left(1 - \frac{2t}{3\tau_o}\right) \tag{A.29}$$

Appendix 2 Computer programs

A2.1 Matlab program for form grinding temperature

```
clc, clear, format short
%%%% INPUT THE DATA FROM USER
%%%% 'There are five form option in this program'
disp('*************************************************')
disp('*                                               *')
disp('*        Welcome to Grinding Temperature System *')
disp('*                                               *')
disp('*************************************************')
disp('                                                 ')
disp('SPECIFY WORKPIECE SHAPE BY CHOOSING ONE OPTION: ')
disp('                                                 ')
disp('  1. vee form                                    ')
disp('  2. inverted vee form                           ')
disp('  3. angle approach for vee form                 ')
disp('  4. angle approach for inverted vee form        ')
disp('  5. groove                                      ')
disp('  6. directed feed for face grinding             ')
disp('                                                 ')
option=input(' ENTER YOUR CHOICE HERE :    ')

disp(' Enter the parameter of grinding condition :     ')
disp('                                                 ')
ds_ma=input('Maximum diameter of wheel in (mm)? ');
ds_mi=ds_ma-2*6.75;
vs=input('speed of wheel in (m/s)?         ');
vw=input('Enter speed of workpiece in (m/s)?   ');
power=input(' grinding power in (W)?              ');

%%Measured temperature for the calculation measured partition ratio
t1=input(' measured temperature at the long flank ?  ');
t2=input(' measured temperature at the short flank ? ');
t3=input(' measured temperature at the apex  ?  ');

%% CALCULATION OF CONTACT LENGTH FOR DIFFERENT SHAPE OF
%% WORKPIECE CONTACT LENGTH AT EACH LAYER
%%ON CONTACT AREA REPRESENTS A SMALL AREA
%% CALCULATE LENGTH OF CONTACT FOR EACH SMALL AREA

if option==1 |option==2
 v_doc=input('Depth of cut of vertical on vee form (um) ?  ');
 mea_doc1=input('Measured normal depth of cut on the long flank (um) ? ');
 mea_doc2=input('Measured normal depth of cut on the short flank (um) ? ');
 disp('  Enter the size of workpiece :  ')
 disp('                                                 ')
```

```
 flank1=input('length of long flank of workpiece in (mm) ? ');
 flank2=input('length of short flank of workpiece in (mm) ? ');
 angle1=input('angle between long flank with perpendicular  ');
 angle2=input('angle between short flank with perpendicular  ');

elseif option==3 |option==4
 ax=input(' The depth of cut normal to the shoulder face (um)   ')
 ay=input(' The depth of cut normal to the  cylindrical face (um)   ')
 disp('  Enter the size of workpiece :  ')
 disp('                                          ')
 dw1=input(' big diameter of operation axis in (mm)  ');
 dw2=input(' small diameter of operation axis in (mm)  ');
 flank2=input(' cylindrical long of operation in (mm)  ');
 abe=input(' Angle between wheel axis and workpiece axis ');
 flank1=(dw1-dw2)/2;
 vw2=dw2*vw/dw1;
%%DITERMIED INFEED DIRACTION AT ANGLE APPORACH GRINDING
  disp(' 1. infeed direction is normal to the axis of wheel  ')
  disp(' 2. infeed direction is determined by depth of cut   ')
  choi=input('  enter your choice here:     ')
  if choi= (For determined the angle between workpiece axis and infeed direction ')
    ain=90-abe;
  else
    ain=atan(ay/ax)*180/pi;
  end
disp(' The angle of infeed in the angle approach is ')
disp( ain )

elseif option==5
 doc=input('Vertical depth of cut in (um)?  ');
 mea_d=8.6;
 disp('  Enter the size of workpiece :  ')
 disp('                                          ')
 angle=input('angle between longer flank with perpendicular  ');
 height1=input('height of flank in (mm)  ');
 height2=input('height of circular in (mm)  ');
 %%growid=input('width of workpiece groove in (mm)  ');
 cir_rad=input('radius of groove circular part in (mm)  ');
 flank=height1/sin(angle*pi/180);

elseif option==6
 a=input(' The depth of cut normal to the face (um)   ')
 disp('  Enter the size of workpiece :          ')
 disp('                                          ')
 hw=input(' the height of workpiece              ')
end

nlayer=input('How many layer do you want  ');

if option ==1
```

```
  [dse1,flalay1]=vefdia(flank1,angle1,ds_ma,nlayer);
  [dse2,flalay2]=vefdia(flank2,angle2,ds_ma,nlayer);
  [real_doc1,lg1]=contlen(angle1,dse1,v_doc,mea_doc1);
  [real_doc2,lg2]=contlen(angle2,dse2,v_doc,mea_doc2);
  [lg3]=plan(v_doc,flank1,vw,ds_ma,power);
  b=[0.6092,0.3144,0.3481,-0.2032,-0.2037,0.0009,0.0009];

elseif option==2
  [dse1,flalay1]=invefdia(flank1,angle1,ds_mi,nlayer);
  [dse2,flalay2]=invefdia(flank2,angle2,ds_mi,nlayer);
  [real_doc1,lg1]=contlen(angle1,dse1,v_doc,mea_doc1);
  [real_doc2,lg2]=contlen(angle2,dse2,v_doc,mea_doc2);
  [lg3]=plan(v_doc,flank1,vw,ds_mi,power);
  b=[1.2284,0.4755,0.5670,-0.5520,-0.5862,-0.0043,-0.0040];

elseif option==3
  [dse1,flalay1,ha]=vefdia(flank1,abe,ds_ma,nlayer);
  [dse2,flalay2]=vefdir(flank2,abe,ds_ma,nlayer,dw2);
  [lg1,vfx]=d_o_c(ax,ain,dw1,vw,dse1);
  [lg2,vfy]=d_o_c(ay,(90-ain),dw2,vw2,dse2);

elseif option==4
  [dse1,flalay1]=invefdia(flank1,abe,ds_mi,nlayer);
  [dse2,flalay2]=invefdir(flank2,abe,ds_mi,nlayer,dw1);
  [lg1,vfx]=d_o_c(ax,ain,dw1,vw,dse1);
  [lg2,vfy]=d_o_c(ay,(90-ain),dw2,vw2,dse2);

elseif option ==5
  [ydiv,arc_ang,yd,sub_ang]=cir_ang(height2,cir_rad,nlayer);
  [dse1,flalay1]=vefdia(flank,angle,ds_ma,nlayer);
  [dse2,flalay2,ha]=gro_dia(yd,nlayer,sub_ang,ds_ma);
  [real_doc1,lg1]=contlen(angle,dse1,doc,mea_d);
  [real_doc2,sub_doc,lg2]=len_gv(sub_ang,arc_ang,dse2,doc);

elseif option==6
 [lg,z]=pla(hw,a,vw,ds_ma)
end

if option==1|option==2
 disp('Theoretical normal depth of cut on the long flank is')
 disp(real_doc1)
 disp('Theoretical normal depth of cut on the short flank is')
 disp(real_doc2)
 disp('Geometric contact length of long flank in grinding zone is')
 disp(lg1)
 disp('Geometric contact length of short flank in grinding zone is')
 disp(lg2)
 disp('Geometric contact length of n0n-continuous point in grinding zone is')
 disp(lg3)
elseif option==3|option==4
```

```
disp('Geometric contact length of shoulder face in grinding zone is')
disp(lg1)
disp('Geometric contact length of cylindrical face in grinding zone is')
disp(lg2)
disp('The infeed rate to the shoulder face is    ')
disp(vfx)
disp('The infeed rate to the cylindrical face is    ')
disp(vfy)
elseif option==5
 disp('Geometric contact length of flank in grinding zone is')
 disp(lg1)
 disp('Geometric contact length of circle in grinding zone is')
 disp(lg2)
elseif option==6
 disp('Geometric contact length in grinding zone is')
 disp(lg)

end
 disp('Press any key to continue'),pause
 %% Calculation removal rate of metal on grinding zone
%% and power distribution on grinding zone
 if option==1 | option==2
  [z1,zn1]=movera(mea_doc1,flank1,vw,nlayer);
  [z2,zn2]=movera(mea_doc2,flank2,vw,nlayer);

 elseif option==3
  [z1,zn1,van,dwn]=remo_fa(nlayer,dw2,flalay1,vw2,ax);
  [z2,zn2]=movera(ay,flank2,vw2,nlayer);

 elseif option==4
  [z1,zn1,van,dwn]=rem_infa(nlayer,dw1,flalay2,vw,ax);
  [z2,zn2]=movera(ay,flank2,vw,nlayer);

 elseif option==5
  [z1,zn1]=movera(mea_d,flank,vw,nlayer);
  [z2,zn2,sma_arc]=cir_mo(arc_ang,vw,nlayer,cir_rad,sub_doc);
end

if option==6
 ec=power/z;
else
 [pow1,ec]=s_pow(z1,z2,power);
 [pow2,ec]=s_pow(z2,z1,power);
end

if option==5
  [le1]=new_len(pow1,dse1,flank,vs,lg1)
  le2=2*lg2;
elseif option==6
  [le]=new_len(power,ds_ma,a,vs,lg);
```

```
else
 [le1]=new_len(pow1,dse1,flank1,vs,lg1);
 [le2]=new_len(pow2,dse2,flank2,vs,lg2);
 [le3,flat]=apex_lg(flank1,flank2,angle1,angle2,power,vs,v_doc,ds_mi);
 le1,le2,le3
end

disp(' contact length ratio lc/lg  ')

if option==1|option==2
 lerati1=le1/lg1,lerati2=le2/lg2,lerati3=le3/lg3
 lg1=le1;
 lg2=le2;
 lg3=le3;
 powin=pow1*cos(angle2*pi/180)+pow2*cos(angle1*pi/180);
 z3=v_doc*flat*vw;
 ec3=powin/z3;
else
 lerati1=le1/lg1,lerati2=le2/lg2
 lg1=le1;
 lg2=le2;
end

%%%% ANALYSIS OF TEMPERATURE DISTRIBUTION IN GRINDING
%%%% ZONE BETWEEN WORKPIECE AND GRINDING WHEEL
disp( '  Enter grinding parameter      ' )
disp('                                 ')
k=input('Enter thermal conductivity of workpiece in (W/m*K) ');
c=input('Enter heat capacity of workpiece in (J/Kg*K) ');
pc=input('Enter density of workpiece in (Kg/m^3) ');
kge= ('kge=? in (W/m*K) ');
ro=input('ro=? in (um) ');
ecc=input('ecc=? in (J/mm^3) ');
hc1=input('Maximum Heat convective coefficient?  (W/m^2*K) ');
hc2=input('Heat convection coefficient when coolant boil? (W/m^2*K) ');
boil_tem=input('Boiling point temperature of coolant? (K) ')
prop=(sqrt(k*c*pc))/1000000;%%(mm.^-2*K*J*s.^-0.5)
cond=(k/(c*pc))*1000000;%%(mm.^2/s)

%% Calculation partition ratio for dry grinding
if option==6
 [Rws,Rw0,me_pr,pch]=parti(kge,ro,vs,k,c,pc,ecc,ec,z);
else
 [Rws,Rw0,me_pr,Rwp]=parti_ra(kge,ro,vs,k,c,pc,ecc,ec,nlayer);
end

%% Calculation temperature distribution on grinding zone
if option==1 | option==2
 [n]=n_fact(b,angle1,angle2,flank1,flank2,lg1(3),lg2(3));
%%n=1;
```

```
  [pn1,pchn1]=pow_dis(pow1,nlayer,ecc,zn1,vw);
  [pn2,pchn2]=pow_dis(pow2,nlayer,ecc,zn2,vw);
  [temp1,all_ma1,hd,lx1]=temp_dis(me_pr,pn1,flalay1,lg1,Rw0,vw);
  [temp2,all_ma2,hd,lx2]=temp_dis(me_pr,pn2,flalay2,lg2,Rw0,vw);
  [tem3]=t_apex(me_pr,powin,lg3,Rwp,vw,n,flat);

elseif option==3 | option==4
  [pn1,pchn1]=p_face(nlayer,zn1,z1,pow1,ecc);
  [pn2,pchn2,vwr]=pow_dis(pow2,nlayer,ecc,zn2,vw2);
  [temp1,all_ma1,hd,lx1]=temp_dis(me_pr,pn1,flalay1,lg1,Rw0,vw);
  [temp2,all_ma2,hd,lx2]=temp_dis(me_pr,pn2,flalay2,lg2,Rw0,vw2);

elseif option==5
  [pn1,pchn1]=pow_dis(pow1,nlayer,ecc,zn1,vw);
  [pn2,pchn2]=cir_pow(pow2,nlayer,ecc,zn2,z2,vw);
  [temp1,all_ma1,hd,lx1]=temp_dis(me_pr,pn1,flalay1,lg1,Rw0,vw);
  [temp2,all_ma2,hd,lx2]=cir_temp(me_pr,pn2,sma_arc,lg2,Rw0,vw);

elseif option==6
 [lx,temp]=p_tem(power,Rw0,a,me_pr,le,vw);
 disp('Each point temperature on flat in grinding area  ')
 disp(temp)

end

if option==1| option==2
 disp('Each point temperature on each layer of long flank in grinding area  ')
 disp(temp1)
 disp('Each point temperature on each layer of short flank in grinding area  ')
 disp(temp2)
 disp('Non-continuous point temperature in grinding area  ')
 disp(tem3)
elseif option==6
 disp('Each point temperature on each layer of long flank in grinding area  ')
 disp(temp)
else
 disp('Each point temperature on each layer of long flank in grinding area  ')
 disp(temp1)
 disp('Each point temperature on each layer of short flank in grinding area  ')
 disp(temp2)
end

if option==6
  hold on, plot(lx, temp, 'g'),
  xlabel('contact length, mm'), ylabel('Temperature, deg.C')
else
  figure, hold on, plot(hd,all_ma1,'g')
         plot(hd, all_ma2,'r')
end
```

```
 title('Maximum temperature on the grinding zone')
 xlabel('position of layer'),ylabel('Temperature, deg.C')

if option==1| option==2
 [pf_line1]=flu_pow(le1,temp1,hc1,hc2,flalay1,boil_tem);
 [pf_line2]=flu_pow(le2,temp2,hc1,hc2,flalay2,boil_tem);
 [pfline,pch_poi]=flulin(lg3,tem3,hc1,hc2,flat,v_doc,vw,ecc,boil_tem);

elseif option==3| option==4
 [pf_line1]=flu_pow(le1,temp1,hc1,hc2,flalay1,boil_tem);
 [pf_line2]=flu_pow(le2,temp2,hc1,hc2,flalay2,boil_tem);

elseif option==5
 [pf_line1]=flu_pow(le1,temp1,hc1,hc2,flalay1,boil_tem);
 [pf_line2]=flu_arc(le2,temp2,hc1,hc2,sma_arc,boil_tem);

elseif option==6
 [pf_line]=flu_pow(le,temp,hc1,hc2,a,boil_tem);
end

%% Calculation temperature and partition ratio in wet grinding

condition=input(' dry or wet grinding, if dry press  1,  else press  2  ')
 if condition==1
   if option==6
    [Rw,Rs,Rch]=dry(Rw0,Rws,ecc,ec);
  elseif option==1|option==2
    [Rw1,Rs1,Rch1]=dry(Rw0,Rws,ecc,ec);
    [Rw2,Rs2,Rch2]=dry(Rw0,Rws,ecc,ec);
    [Rw3]=dry_poi(powin,Rws,ecc,vw,v_doc,flat);
  else
    [Rw1,Rs1,Rch1]=dry(Rw0,Rws,ecc,ec);
    [Rw2,Rs2,Rch2]=dry(Rw0,Rws,ecc,ec);
  end
else
 if option==1 | option==2
  [Rw1,Rs1,Rf1,Rch1,tem_wet1]=wet_v(pf_line1,pn1,pchn1,Rw0,Rws,lg1,me_pr,
   flalay1,vw,hc1,hc2,boil_tem)
  [Rw2,Rs2,Rf2,Rch2,tem_wet2]=wet_v(pf_line2,pn2,pchn2,Rw0,Rws,lg2,me_pr,
   flalay2,vw,hc1,hc2,boil_tem)
  [tem_wet3,Rw3,Rf3,Rs3,Rch3]=wpoin(pfline,powin,pch_poi,Rwp,Rws,lg3,me_pr,
   vw,hc1,hc2,n,flat,boil_tem)

elseif option==3 | option==4
  [Rw1,Rs1,Rf1,Rch1,tem_wet1,count]=wet_v(pf_line1,pn1,pchn1,Rw0,Rws,lg1,
   me_pr,flalay1,vw,hc1,hc2,boil_tem)
  [Rw2,Rs2,Rf2,Rch2,tem_wet2,count]=wet_v(pf_line2,pn2,pchn2,Rw0,Rws,lg2,
    me_pr,flalay2,vw2,hc1,hc2,boil_tem)
elseif option==5
 [Rw1,Rs1,Rf1,Rch1,tem_wet1]=wet_v(pf_line1,pn1,pchn1,Rw0,Rws,lg1,me_pr,
```

```
 flalay1,vw,hc1,hc2,boil_tem)
[Rw2,Rs2,Rf2,Rch2,tem_wet2]=wet_g(pf_line2,pn2,pchn2,Rw0,Rws,lg2,me_pr,
  sma_arc,vw,hc1,hc2,boil_tem)
elseif option==6

 [pf_linef]=flu_pla(le,temp,hc1,hc2,a,boil_tem);
 [Rwf,Rsf,Rff,Rchf,tem_w,count]=wet(pf_linef,power,pch,Rw0,Rws,le,me_pr,a,
  vw ,hc1,hc2,boil_tem);

 end
end

%%Calculation measured partition ratio for vee and inverted vee form
if option==1 | option==2
   [Rwm1]=mp(t1,pow1,le1(3),flank1,vw,k,c,pc)
   [Rwm2]=mp(t2,pow2,le2(3),flank2,vw,k,c,pc)
   [Rwm3]=mp(t3,powin,le3,flat,vw,k,c,pc)
end
```

A2.2 Matlab program for creep feed grinding temperature

```
clc, clear, format short
%%This programming is calculated grinding temperature for creep feed

%%%% 'There are two creep feed option in this program'
disp('*************************************************')
disp('*                                               *')
disp('*          The Creep feed Grinding Temperature System          *')
disp('*                                               *')
disp('*************************************************')
disp('                                                 ')
disp('   CHOOSING ONE OPTION FOR :                     ')
disp('                                                 ')
disp('   1. SURFACE CREEP-FEED GRINDING                ')
disp('   2. FLUTE FORM CREEP-FEED GRINDING             ')
disp('                                                 ')
option=input('  ENTER YOUR CHOICE HERE :               ')

if option==2
  %%This programming is calculated grinding temperature
  %%for creep feed in flute form grinding
  disp(' The parameter of grinding                     ')
  a=input(' Vertical depth of cut in (um)?             ')
  power=input(' Grinding power in (W)?                 ')
  vs=input(' Wheel speed in (m/s)?                     ')
  ds=input(' Wheel diameter in (mm)?                   ')
  vw=input(' Workpiece speed in (m/s)?                 ')
  ra=input(' Radius of workpiece in (mm)?              ')
  ang=input(' The angle between workpiece flank and vertical?  ')
  nlayer=input(' How many layer do you wait?           ')

  %%Calculation width of flute
  wr=sqrt(ra.^2-(ra-a/1000).^2);
  wf=a/1000*tan(ang*pi/180);

else
  %%This programming is calculated grinding temperature
  %%for creep feed in surface grinding
  a=input(' Vertical depth of cut in (um)?       ')
  vw=input(' Workspeed in (m/s)?       ')
  ds=)input(' Wheel diameter in (mm)?          ')
  %%power=input(' Grinding power in (W)? ')
  vs=input(' wheel speed in (m/s)?             ')
  wid=input(' The width of grinding in (mm)?          ')
  ec=input(' The specific energy in (J/mm3) ?  ')
end
```

```
%%CALCULATION THE CONTACT LENGTH FOR CREEP FEED GRINDING
%%CALCULATION REMOVAL RATE AND PARTION RATIO IN DRY
CONDITION
if option==1
 %%[lg,z,ec]=plan(a,wid,vw,ds,power);
 [lg,z,power]=varyp(a,wid,vw,ds,ec);
else
 [lgr,dsnr,anr]=lenr(nlayer,ds,a,wr,ra);
 [lgf,dsnf,anf]=lenf(nlayer,ds,a);

 [zc,zcn,widcn]=rem_r(a,anr,vw,nlayer,wr);
 [zf,zfn,widfn]=crem_f(a,vw,nlayer,wf);

 [powf,ec]=s_pow(zf,zc,power);
 [powc,ec]=s_pow(zc,zf,power);

 [lef]=new_len(powf,dsnf,wf,vs,lgf);
 [ler]=new_len(powc,dsnr,wr,vs,lgr);
end

%%%% ANALYSIS OF TEMPERATURE DISTRIBUTION IN GRINDING
%%%% ZONE BETWEEN WORKPIECE AND GRINDING WHEEL
disp(' Enter grinding material property                    ');
disp('                                  ')
k=input('Enter thermal conductivity of workpiece in (W/m*K) ? ');
c=input('Enter heat capacity of workpiece in (J/Kg*K) ? ');
pc=input('Enter density of workpiece in (Kg/m^3) ? ');
kge=input('kge=? in (W/m*K) ');
ro=input('ro=? in (um) ');
ecc=input('ecc=? in (J/mm^3) ');
prop=(sqrt(k*c*pc))/1000000;%%(mm.^-2*K*J*s.^-0.5);
cond=(k/(c*pc))*1000000;%%(mm.^2/s);

hc1=input('Maximum Heat convective coefficient in (W/m^2*K) ? ');
hc2=input('Heat convection coefficient when coolant boil in (W/m^2*K) ? ');
boil_t=input('Boiling point temperature of coolant in (K) ? ')

%% Calculation temperature distribution on grinding zone

if option==2

[powfn,pchf]=pdisf(powf,nlayer,ecc,zf,zfn,vw,ec);
[powcn,pchc]=pdisf(powc,nlayer,ecc,zc,zcn,vw,ec);

[Rwsc,Rw0c,me_pr]=parti_ra(kge,ro,vs,k,c,pc,pchc,powcn,nlayer);
[Rwsf,Rw0f,me_pr]=parti_ra(kge,ro,vs,k,c,pc,pchf,powfn,nlayer);

[tempf,all_ma1,hd]=temp_dis(me_pr,powfn,widfn,lef,Rw0f,vw);
[tempc,all_ma2,hd,lx,rwc]=cir_temp(me_pr,powcn,widcn,ler,Rw0c,vw);
```

```
disp('Each point temperature on each layer of  flank in grinding area  ')
disp(tempf)
disp('Each point temperature on each layer of circle in grinding area  ')
disp(tempc)

figure, plot(hd, all_ma1,'g')
hold on, plot(hd, all_ma2,'r')
xlabel(' position of layer'),ylabel('Maximum temperature, deg ')
hold off,pause

[pf_linef]=flu_pow(lef,tempf,hc1,hc2,widfn,boil_t);
[pf_linec]=flu_arc(ler,tempc,hc1,hc2,widcn,boil_t);


[Rwf,Rsf,Rff,Rchf,tem_wf,count]=wet_v(pf_linef,powfn,pchf,Rw0f,Rwsf,lef,me_pr,wi
dfn,vw,hc1,hc2,boil_t);

[Rwc,Rsc,Rfc,Rchc,tem_wc]=wet_g(pf_linec,powcn,pchc,Rw0c,Rwsc,ler,me_pr,widcn,
vw,hc1,hc2,boil_t);
 %%hold off,pause

 %%Calculation Peclet number
 %%ll=vw*1000*lg/4/cond;

 %%Calculate the distance between the heat source and
 %%the finished surface for the geometric contact length
 numb=input( ' How many point to you what to divide ?  ')
 [hhr,nhr]=ndista(lgr(1),dsnr(1));%% for first contact length
 [hhf,nhf]=ndista(lgf(1),dsnf(1));

 %%Calculation the temperature on the finish surface

[ftef,lgxf]=fin_tem(lgf(1),vw,nhf,prop,cond,powcn(1),Rwf(1),widcn(1),k);
[nftr,lgxr]=fin_tem(lgr(1),vw,nhr,prop,cond,powcn(1),Rwc(1),widcn(1),k);

 disp('temperature distribution in flank finish surface ')
 disp(ftef )
 disp('temperature distribution in circle finish surface ')
 disp(nftr )

 figure, plot(lgxf,ftef,'w')
 xlabel('contact length'),ylabel('Temperature, deg.C')

else
 [Rws,Rw0,me_pr,pch]=parti(kge,ro,vs,k,c,pc,ecc,ec,z);
 [lx,temp]=p_tem(power,Rw0,wid,me_pr,lg,vw);
 disp('Each point temperature on flat in grinding area  ')
 disp(temp)
  hold on, plot(lx, temp, 'g'),
  xlabel('contact length, mm'), ylabel('Temperature, deg.C')
```

```
%%Calculation the effect of fluid on temperature in creep feed grinding

[pf_linef]=flu_pla(lg,temp,hc1,hc2,wid,boil_t);

[Rwf,Rsf,Rff,Rchf,tem_w,count]=wet(pf_linef,power,pch,Rw0,Rws,lg,me_pr,wid,vw,h
c1,hc2,boil_t);
 hold off,pause

 %%Calculate the distance that is from heat source to
%% surface required calculate temperature
[hh,nh]=ndista(lg,ds);

%%Calculation the temperature on the finish surface
[ftem,lgx]=fin_tem(lg,vw,hh,prop,cond,power,Rwf,wid,k);
[nftem,lgx]=fin_tem(lg,vw,nh,prop,cond,power,Rwf,wid,k);

 hold on, plot(lgx,ftem,'w')
 hold on, plot(lgx,nftem,'r')
 xlabel(' Grinding contact length, mm '),ylabel('Temperature, deg.C')

 %%Calculate peclet number
 ll=vw*1000*lg/4/cond;
end
```

A2.3 The program function for form and creep feed grinding

```
%%This function is calculated the real contact length in the discontinuity of
%%workpiece.
function [le,flat]=apex_lg(f1, f2, a1, a2,p,v,a,de)
      flat=f1*sin(a1*pi/180)+f2*sin(a2*pi/180)
      lf=10.^2*(1.4345/10000)*(p*de/(v*flat));
      le=sqrt(lf+de*a/1000);
```

```
%%This function is calculated profile angle on the curve of workpiece
function [ydiv,arc_ang,yd,sub_ang]=cir_ang(depth,cir_rad,nlayer);
     ydiv=depth/nlayer;
     for i=1:nlayer
      arc_ag(i)=acos((cir_rad-i*ydiv)/cir_rad);
      arc_ang(i)=arc_ag(i)*180/pi; %the angle of each layer on circle
      yd(i)=i*ydiv-ydiv/2; %the middle of layer
      ang(i)=asin((cir_rad-yd(i))/cir_rad);
      sub_ang(i)=ang(i)*180/pi;
     end
```

```
%%This function is calculation remove rate of the metal on the curve of workpiece
function [z,zn,sma_arc]=cir_mo(arc_ang,vw,nlayer,cir_rad,sub_doc)
  sma_arc(1)=cir_rad*arc_ang(1)*pi/180;
    for i=2:nlayer
    sma_arc(i)=cir_rad*(arc_ang(i)-arc_ang(i-1))*pi/180 ;
    %%zn(i)=real_doc(i)*sma_arc(i)*vw;
    end
    zn=sub_doc.*sma_arc*vw*1000;
    z=sum(zn);
```

```
%% Power distribution on side of circle of grinding
function [pn,pchn]=cir_pow(pow,nlayer,ecc,zn,z,vw)
       for i=1:nlayer
        pn(i)=(zn(i)/z)*pow;
        pchn(i)=ecc*zn(i);
       end
```

```
%%This is calculation the grinding temperature distribution on the curve of workpiece

function [temp,all_ma,hd,lx]=cir_temp(me_pr,pn,sma_arc,lg,Rw0,vw)
  for i=1:length(lg)
    hd(i)=i;
    lgx(i)=lg(i)/10;
    heat(i)=Rw0(i)*pn(i)/(sma_arc(i)*lg(i)/1000000);
    for j=1:11
```

```
  lx(i,j)=(j-1)*lgx(i);
  tim_vary(i,j)=lx(i,j)/(vw*1000);
  posi_vary(i,j)=1-((2/3)*lx(i,j)./lg(i));
  temp(i,j)=(4/me_pr)*heat(i)*sqrt(tim_vary(i,j))*posi_vary(i,j);
 end
 [maxi,posi]=max(temp(i,:));
 all_ma(i)=maxi;
end
plot(lx(1,:),temp(1,:),'r')
xlabel('Contact lenth, le'),ylabel('Temperature, deg.C')
disp('press any key') ,pause
```

```
%% Calculation geometric contact length
function [real_doc,lg]=contlen(angle,dse,doc,mea_d)
        real_doc=(doc/1000)*sin(angle*pi/180);
        lg=sqrt(dse.*mea_d/1000);


function [lg,vf]=d_o_c(a,angle,dw,vw,dse)
        vf=a*vw/pi/dw/cos(pi*angle/180);
        lg=sqrt(a/1000*dse);


%%% This is calculation contact lenth for surface grinding
function [lg,z,ec]=plan(a,w,v,ds,p)
  z=a/1000*w*v*1000;
  lg=sqrt((a/1000)*ds);
  ec=p/z;


%% This function for calculation partition ratio
function[Rw,Rs,Rch]=dry(Rw0,Rws,ecc,ec,pchn,pn)
        Rw=Rw0;
        Rs=Rw/Rws-Rw;
        Rch=ecc/ec;


%%This function is calculated discontinuity partition ratio
function [Rw]=dry_poi(p,Rws,ecc,v,a,flat)
      ec=p/(a*flat*v);
      Rw=Rws(1-ecc/ec);


%%This function for calculation grinding energy enter the fluid
%% at arc surface
function [pf_line]=flu_arc(lg,temp,hc1,hc2,layarc,boi_tem)
     for i=1:length(lg)
       lgx(i)=lg(i)/10;
       for j=1:11
```

```
    lx(j)=(j-1)*lgx(i);
    if temp(i,j)>=boi_tem
      qf(i,j)=(boi_tem-20)*hc2;
    else
      qf(i,j)=temp(i,j)*hc1;
    end
    pf_point(i,j)=qf(i,j).*layarc(i).*lx(j)/1000000;
  end
  pf_line=sum(pf_point');
end
```

```
%%This function for calculation grinding energy enter the fluid
%% at grinding discontinuity
function [pf_poi,pch_poi]=flu_poi(lg,tem,hc1,hc2,flat,doc,v,ecc,boi_tem)

    if tem >=boi_tem
      qf_poi=(boi_tem-20)*hc2;
    else
      qf_poi=tem*hc1;
    end
      pf_poi=qf_poi*flat*lg/1000000;
      pch_poi=ecc*doc*flat*v;
```

```
%%This function for calculation grinding energy enter the fluid at grinding surface
function [pf_line]=flu_pow(lg,temp,hc1,hc2,flalay,boi_tem)
    for i=1:length(lg)
      lgx(i)=lg(i)/10;
      for j=1:11
        lx(j)=(j-1)*lgx(i);
        if temp(i,j)>=boi_tem
          qf(i,j)=(boi_tem-20)*hc2;
        else
          qf(i,j)=temp(i,j)*hc1;
        end
        pf_point(i,j)=qf(i,j)*flalay.*lx(j)/1000000;
      end
      pf_line=sum(pf_point');
    end
```

```
%%This function is calculated the diamerter of the workpiece
%%on the each strip of flute form
function [dse,flalay,ha]=gro_dia(yd,nlayer,ang,ds_ma);
      for i=1:nlayer
        ha(i)=i*yd(i);
        dslay(i)=ds_ma-2*ha(i);
        dse(i)=dslay(i)/sin(ang(i)*pi/180);
      end
```

```
%% The diameter of grinding wheel on the divided strips
function [dse,flalay]=invefdia(flank,angle,ds,nlay)
        flalay=flank/nlay;
        lay_hw=flalay*cos(angle*pi/180);
        for i=1:nlay
          ha(i)=i*lay_hw;
          dslay(i)=ds+2*ha(i);
          dse(i)=dslay(i)/sin(angle*pi/180);
        end

%%This function is calculated the diamerter of the workpiece
%%on the each strip of inverted vee form
function [dse,flalay]=invefdir(flank,angle,ds,nlayer,dw);
        flalay=flank/nlayer;
        lay_hw=flalay*sin(angle*pi/180);
        for i=1:nlayer
          ha(i)=i*lay_hw;
          dslay(i)=ds+2*ha(i);
          dse(i)=dslay(i)/(cos(angle*pi/180)+dslay(i)/dw);
        end


%% Calculation contact length
function [re_a,sub_a,lgs]=len_gv(sub_ang,arc_ang,dse,doc)
        sub_a=(doc/1000)*sin(sub_ang*pi/180);
        lgs=sqrt(dse.*sub_a);


%% Removal rate of the metal for flank
function [z,zn]=movera(real_doc,flank,vw,nlayer)
        z=real_doc/1000*flank*vw*1000;
        for i=1:nlayer
         zn(i)=z/nlayer;
        end


%%Calculation measured partition ratio
  function [Rwm]=mp(t,p,l,f,v,k,c,rol)
     propor=(sqrt(34.3*506*7815))/1000000;
     area=l*f;
     time=sqrt(l/(v*1000));
     Rwm=(t*area*propor)/(1.064*p*time);


%% Calculation concentration factor
function [n]=n_fact(b,a1,a2,f1,f2,l1,l2)
        s0=1; s1=sin(a1*pi/180); s2=sin(a2*pi/180);
        s3=a1/90; s4=a2/90;
        s5=f1/l1; s6=f2/l2;
        s=[s0,s1,s2,s3,s4,s5,s6];
```

```
        n=b*s';


%%The real contact length model
function [le]=new_len(p,d,f,v,lg)
  factor=p.*d/(f*v);
     le=sqrt(10.^2*1.4345/10000.*factor+lg.^2);


%% Power distribution on face grinding zone
function [pn,pchn,vwa]=p_face(nlayer,znf,ztf,pow,ecc,vw,dw)
        for i=1:nlayer
         pn(i)=(znf(i)./ztf)*pow;
         pchn(i)=ecc.*znf(i);
         %%vwa(i)=vw*dwn(i)./dw;
        end


function [Rws,Rw0,me_pr,Rwp]=parti_ra(kge,ro,vs,k,c,pc,ecc,ec,nlayer)
       kcp=k*c*pc;
        me_pr=sqrt(pi*kcp);
        Rws=(1/(1+(kge/sqrt(ro*vs*kcp/1000000))));
        for i=1:nlayer
          Rw0(i)=Rws*(1-ecc/ec);
        end
        Rwp=Rws*(1-ecc/ec);


%% Power distribution on grinding zone
function [pn,pchn,vwr]=pow_dis(pow,nlayer,ecc,zn,vw)
        for i=1:nlayer
         pn(i)=pow/nlayer;
         pchn(i)=ecc*zn(i);
         vwr(i)=vw;
        end


%%This function is calculated the grinding power distribution different flank
function [pow,ec]=s_pow(x,y,p)
  pow=(x/(x+y))*p
  ec=p/(x+y);


%%Temperature distribution on the discontinuity of the workpiece
function [tem]=tem_apex(me_pr,p,lg,Rw0,vw,n,flat)

    tem1=p*Rw0/(flat*lg/1000000);
    tem2=4*(1-1/3)/me_pr;
    tem3=sqrt(lg/(2*vw*1000));
    tem=n*tem1*tem2*tem3;
```

```
%%Temperature distribution on the flank for dry grinding
function [temp,all_ma,hd,lx]=temp_dis(me_pr,pn,flalay,lg,Rw0,vw)
   for i=1:length(lg)
    hd(i)=i;
    lgx(i)=lg(i)/10;
    heat(i)=Rw0(i).*pn(i)/(flalay.*lg(i)/1000000);
    for j=1:11
     lx(i,j)=(j-1)*lgx(i);
     tim_vary(i,j)=lx(i,j)/(vw*1000);
     posi_vary(i,j)=1-((2/3)*lx(i,j)./lg(i));
     temp(i,j)=(4/me_pr)*heat(i)*sqrt(tim_vary(i,j))*posi_vary(i,j);
    end
    [maxi,posi]=max(temp(i,:));
    all_ma(i)=maxi;
   end
    plot(lx(1,:),temp(1,:),'g')
    xlabel('Contact length, le'), ylabel('Temperature, deg.C')
disp('press any key') ,pause


%%This function is calculation the equivalent diameter
function [dser,flalay]=vefdir(flank,angle,ds,nlayer,dw);
       flalay=flank/nlayer;
       lay_hw=flalay*sin(angle*pi/180);
       for i=1:nlayer
        hr(i)=i*lay_hw;
        dslay(i)=ds-2*hr(i);

        dd1(i)=dslay(i)/dw;
        dd2(i)=cos(angle*pi/180)+dd1(i);
        dser(i)=(dslay(i))/dd2(i);
       end


%%%% Influence of coolant on temperature at total grinding zone
function[Rw,Rs,Rf,Rch,tem_weta]=wet_g(pf_line,pn,pchn,Rw0,Rws,lg,me_pr,sma_arc,
vw,hc1,hc2,bo_t)
count=1;
 pf(count,:)=pf_line*0;
 pf(count+1,:)=pf_line;
 p(count,:)=pn;
 pws(count,:)=p(count,:)-pf(count,:)-pchn(count,:);
 pws(count+1,:)=p(count,:)-pf(count+1,:)-pchn(count,:);
 Rw(count,:)=Rw0;
 pw(count,:)=p(count,:).*Rw;
while abs(pws(count+1,:)-pws(count,:))>0.02
 pw(count+1,:)=pws(count+1,:)*Rws;
 Rw(count+1,:)=pw(count+1,:)./p(count,:);
 for x=1:length(lg)
   harc(x)=x;
   lxn(x)=lg(x)/10;
```

```
 wet_heat(count+1,x)=pw(count+1,x)/(sma_arc(x)*lg(x)/1000000);
for y=1:11
 lyn(x,y)=(y-1)*lxn(x);
 wet_tim_vary(x,y)=lyn(x,y)/(vw*1000);
 wet_pos_vary(x,y)=1-((2/3)*(lyn(x,y)/lg(x)));

tem_dis(x,y)=(4/me_pr)*wet_heat(count+1,x)*sqrt(wet_tim_vary(x,y))*wet_pos_vary(
x,y);
        if tem_dis(x,y)>=bo_t
          qf(x,y)=(bo_t-20)*hc2;
        else
          qf(x,y)=tem_dis(x,y)*hc1;
        end
  pf_point(x,y)=qf(x,y)*sma_arc(x)*lyn(y)/1000000;
 end
pf_line=sum(pf_point');

 tem_weta=tem_dis;
 [maxi,posit]=max(tem_weta(x,:));
 wet_max(x)=maxi;
end

p(count+1,:)=p(count,:);
pchn(count+1,:)=pchn(count,:);
count=count+1;
 pf(count+1,:)=pf_line;
 pws(count+1,:)=p(count,:)-pf(count+1,:)-pchn(count,:);
end
hold on, plot(harc,wet_max,'y')

Rf=pf(count+1,:)./p(count,:);
Rw=Rw(count,:);
Rs=(pws(count+1,:)-pw(count,:))./p(count,:);
Rch=pchn(count,:)/p(count,:);


%%%% Influence of coolant on temperature at discontinuity
function[tem,Rw,Rf,Rs,Rch]=wpoin(pf_poi,p,pch,Rwp,Rws,lg,me_pr,vw,hc1,hc2,n,flat,
boil_tem)
count=1;
 pf(count)=pf_poi(count)*0;
 pf(count+1)=pf_poi(count);
 p(count)=p;
 pws(count)=p(count)-pf(count)-pch(count);
 pws(count+1)=p(count)-pf(count+1)-pch(count);
 Rw(count)=Rwp;
 pw(count)=p(count)*Rw(count);
%% diffe=pws(count+1)-pws(count)
while abs(pws(count+1)-pws(count))>0.02
 pw(count+1)=pws(count+1)*Rws;
```

```
Rw(count+1)=pw(count+1)/p(count);
   tem1(count+1)=p(count)*Rw(count+1)/(flat*lg/1000000);
   tem2=4/me_pr;
   lx=lg/10;
  for i=1:11
   lc(i)=(i-1)*lx;
   tem3(i)=sqrt(lc(i)/(vw*1000));
   tem4(i)=1-((2/3)*lc(i)/lg);
   tem(i)=n*tem1(count+1)*tem2*tem3(i)*tem4(i);

      if tem(i)>=boil_tem;
        qf_poi(i)=(boil_tem-20)*hc2;
      else
        qf_poi(i)=tem(i)*hc1;
      end
        pf_poi(i)=qf_poi(i)*flat*lx/1000000;
      pf_lin=sum(pf_poi');
    end
 p(count+1)=p(count);
 pch(count+1)=pch(count);
 count=count+1;
 pf(count+1)=pf_lin;
 pws(count+1)=p(count)-pf(count+1)-pch(count);
end
count
Rf=pf(count+1)/p(count);
Rw=Rw(count);
Rs=(pws(count+1)-pw(count))/p(count);
Rch=pch(count)/p(count);


%%%% Influence of coolant on temperature at total grinding zone
function[Rw,Rs,Rf,Rch,tem_wet,count]=wet_v(pf_line,pn,pchn,Rw0,Rws,lg,me_pr,flal
ay,vw,hc1,hc2,boil_tem)
count=1;
  pf(count,:)=pf_line*0;
  pf(count+1,:)=pf_line;
  p(count,:)=pn;
  pws(count,:)=p(count,:)-pf(count,:)-pchn(count,:);
  pws(count+1,:)=p(count,:)-pf(count+1,:)-pchn(count,:);
  Rw(count,:)=Rw0;
  pw(count,:)=p(count,:).*Rw;
while abs(pws(count+1,:)-pws(count,:))>0.02
 pw(count+1,:)=pws(count+1,:)*Rws;
 Rw(count+1,:)=pw(count+1,:)./p(count,:);
 for x=1:length(lg)
    h(x)=x;
    lxn(x)=lg(x)/10;
    wet_heat(count+1,x)=pw(count+1,x)/(flalay*lg(x)/1000000);
  for y=1:11
     lyn(x,y)=(y-1)*lxn(x);
```

```
    wet_tim_vary(x,y)=lyn(x,y)/(vw*1000);
    wet_pos_vary(x,y)=1-((2/3)*(lyn(x,y)/lg(x)));

tem_dis(x,y)=(4/me_pr)*wet_heat(count+1,x)*sqrt(wet_tim_vary(x,y))*wet_pos_vary(
x,y);
          if tem_dis(x,y)>=boil_tem; qf(x,y)=(boil_tem-20)*hc2;
          else
            qf(x,y)=tem_dis(x,y)*hc1;
          end
     pf_point(x,y)=qf(x,y)*flalay*lyn(y)/1000000;
    end
     pf_line=sum(pf_point');

    tem_wet=tem_dis;
    [maxi,posit]=max(tem_wet(x,:));
    wet_max(x)=maxi;
    end

p(count+1,:)=p(count,:);
 pchn(count+1,:)=pchn(count,:);
 count=count+1;
 pf(count+1,:)=pf_line;
 pws(count+1,:)=p(count,:)-pf(count+1,:)-pchn(count,:);
end
hold on, plot(h,wet_max,'y')
count
Rf=pf(count+1,:)./p(count,:);
Rw=Rw(count,:);
Rs=(pws(count+1,:)-pw(count,:))./p(count,:);
Rch=pchn(count,:)/p(count,:);


%%This function for calculation effective diameter of grinding wheel
%% at the each strips
function [dsea,flalay,ha]=vefdia(flank,angle,ds_ma,nlayer);
      flalay=flank/nlayer;
        lay_hw=flalay*cos(angle*pi/180);
        for i=1:nlayer
          ha(i)=i*lay_hw;
          dslay(i)=ds_ma-2*ha(i);
          dsea(i)=dslay(i)/sin(angle*pi/180);
        end


%%% This is calculation contact length for surface grinding
function [lg,z,ec]=pla(hw,a,v,ds)
  z=hw*a/1000*v*1000;
  lg=sqrt(hw*ds);
```

```
%%This function for calculation partition ratio
function [Rws,Rw0,me_pr,pch]=parti(kge,ro,vs,k,c,pc,ecc,ec,z)
      kcp=k*c*pc;
      me_pr=sqrt(pi*kcp);
      Rws=(1/(1+(kge/sqrt(ro*vs*kcp/1000000))));
      Rw0=Rws*(1-ecc/ec);
      pch=ecc*z;


%% Removal rate of the material on angle approach
function [z,zn,v,dwn]=remo_fa(nlayer,dw,flalay,vw,a)
      for i=1:nlayer
       cre_dw(i)=i*flalay;
       dwn(i)=dw+2*cre_dw(i);
       v(i)=vw*dwn(i)/dw;
       zn(i)=flalay*a*v(i);
      end
       z=sum(zn);


%% Removal rate of the metal on face
function [z,zn,v,dwn]=rem_ivfa(nlayer,dw,flalay,vw,a)
      for i=1:nlayer
       cre_dw(i)=i*flalay;
       dwn(i)=dw-2*cre_dw(i);
       v(i)=vw*dwn(i)/dw;
       zn(i)=flalay*a*v(i);
      end
       z=sum(zn);
       dwt=sum(dwn);


%%This function for calculation partition ratio
function [Rws,Rw0,me_pr,pch]=parti(kge,ro,vs,k,c,pc,ecc,ec,z)
      kcp=k*c*pc;
      me_pr=sqrt(pi*kcp);
      Rws=(1/(1+(kge/sqrt(ro*vs*kcp/1000000))));
      Rw0=Rws*(1-ecc/ec);
      pch=ecc*z;


%% power distribution on face grinding zone
function [pn,pchn]=p_face(nlayer,znf,ztf,pow,ecc)
      for i=1:nlayer
       pn(i)=(znf(i)./ztf)*pow;
       pchn(i)=ecc.*znf(i);
      end
```

A2.4 Matlab program for optimised grinding conditions

```
%%This program is for the Optimisation Chart
disp(' Which materials do you wait ' )
disp('                                    ')
disp('       1. En31                      ')
disp('       2. En9B                      ')
disp('       3. M2                        ')
disp('                                    ')
material =input('  ENTER YOUR CHOICE HERE :       ')

if material==1
  kpc=34.3*7815*506;%*10.^(-12);
elseif material==2
  kpc=42.6*7840*477;%*10.^(-12);
elseif material==3
  kpc=23.5*7860*515;%*10.^(-12);
end

tm=input(' The critical temperature for this materials ? (deg.C)  ')
ec=input(' The value of specific energy ? (J/mm3)  ')
ds= input(' The diameter of the grinding wheel ? (mm) ');
ro=input(' The radius of the grain wear ? (um) ? ')
kge= input(' The thermal property of wheel (W/m*K) ') ;
ecc=input( ' ecc=? in (J/mm^3) ');
vs= input(' Wheel speed in (m/s)? ');
vw=0:0.005:0.03;  %%(m/s)
 Rws=(1/(1+(kge/sqrt(ro/1000000*vs*kpc))))
 term1=tm.^2*kpc/1000.^4;%%(J2/smm4)
 for i=1:length(ec)

  for j=1:length(vw)
   Rw(i,j)=Rws*(1-ecc/ec(i));
   term2(i,j)=(1.064*Rw(i)*ec(i)).^2;%%(J2/mm6)
   term3(i,j)=ds/(vw(j)*1000);%%(s)
   leng(i,j)=(1.4345*10.^(-2)*ec(i)*1000*vw(j)/vs+1).^(1/2);%%(leng=lc/lg2)(mm)
   depth(i,j)=term1/term2(i)*term3(i,j)*leng(i,j)/1000;  %%(um)
  end
end
%%plot (vw, depth, 'w')
%%depth'
```

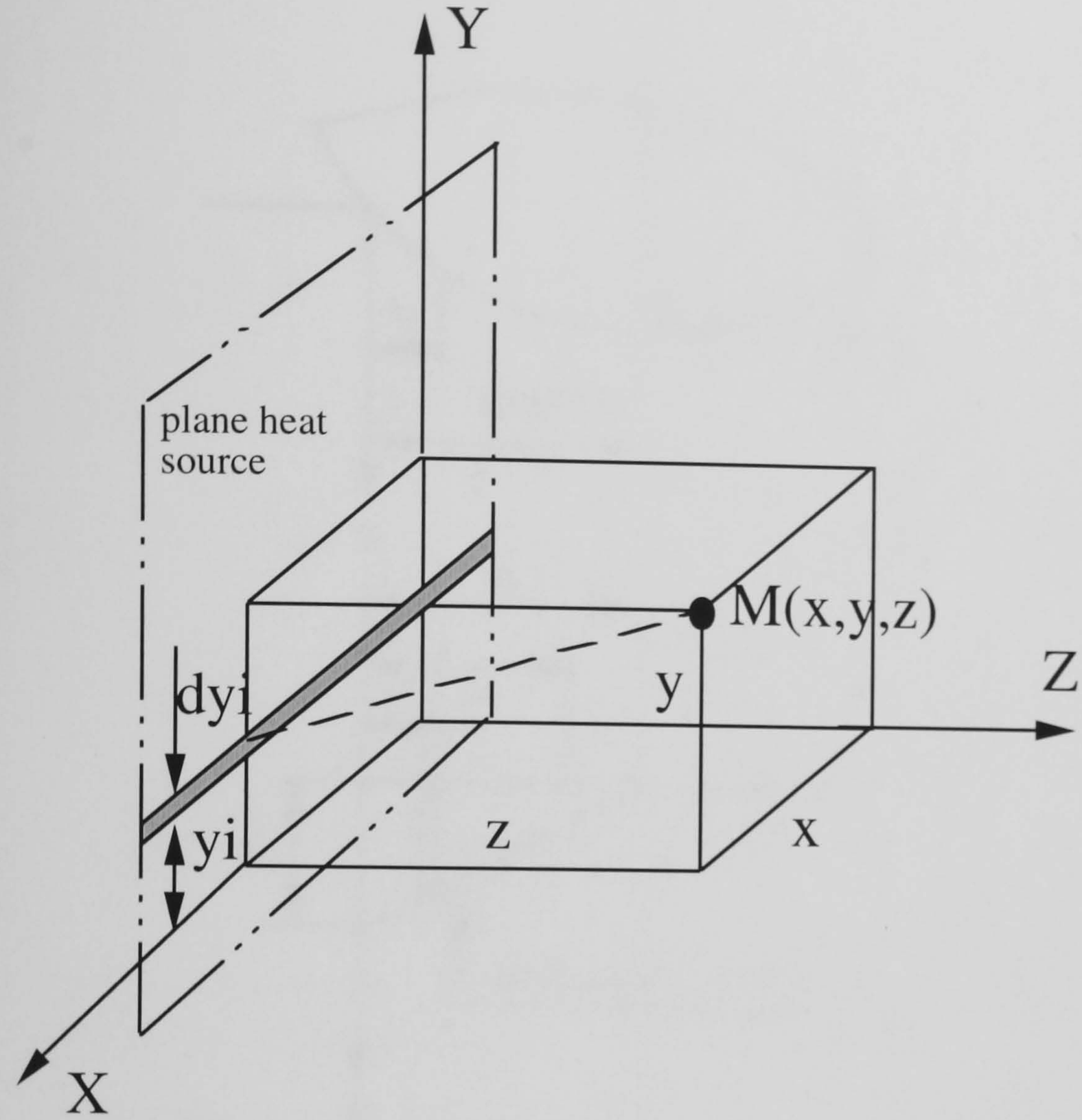

Figure 3.1. Coordinates of the instantaneous infinite plane heat source

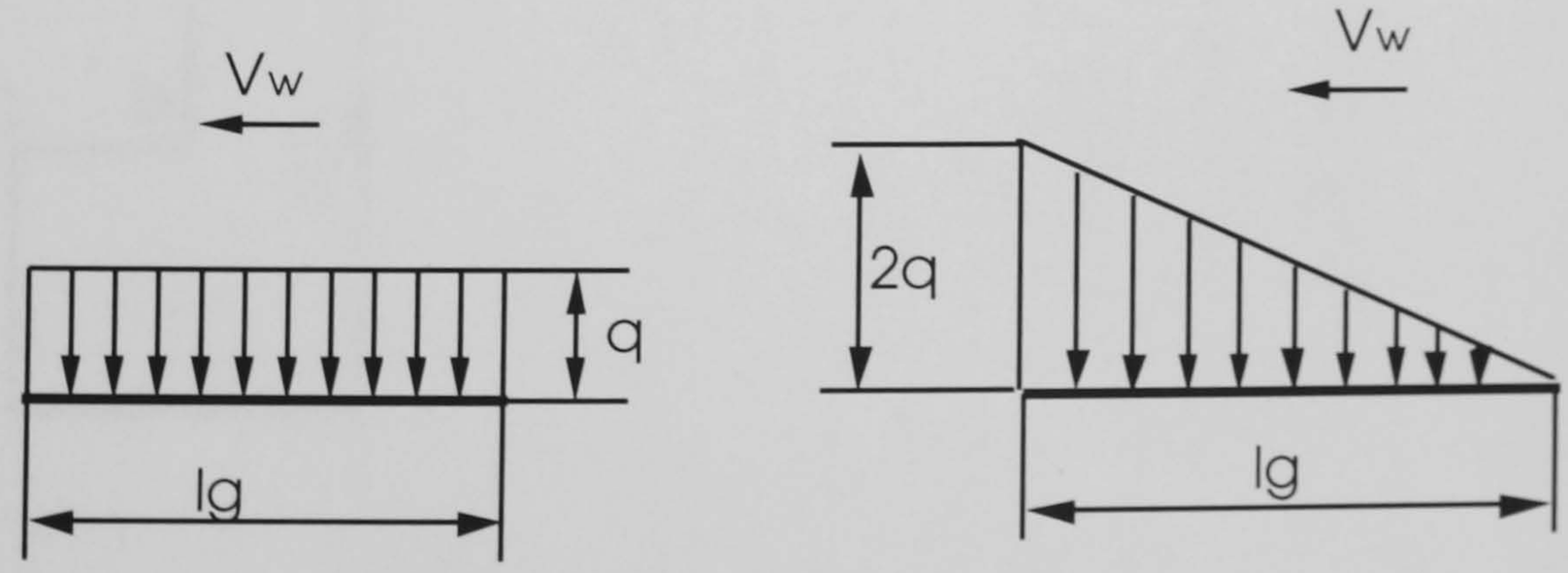

Figure3.2. (a) A uniform heat flux distribution (b) A triangular heat flux distribution

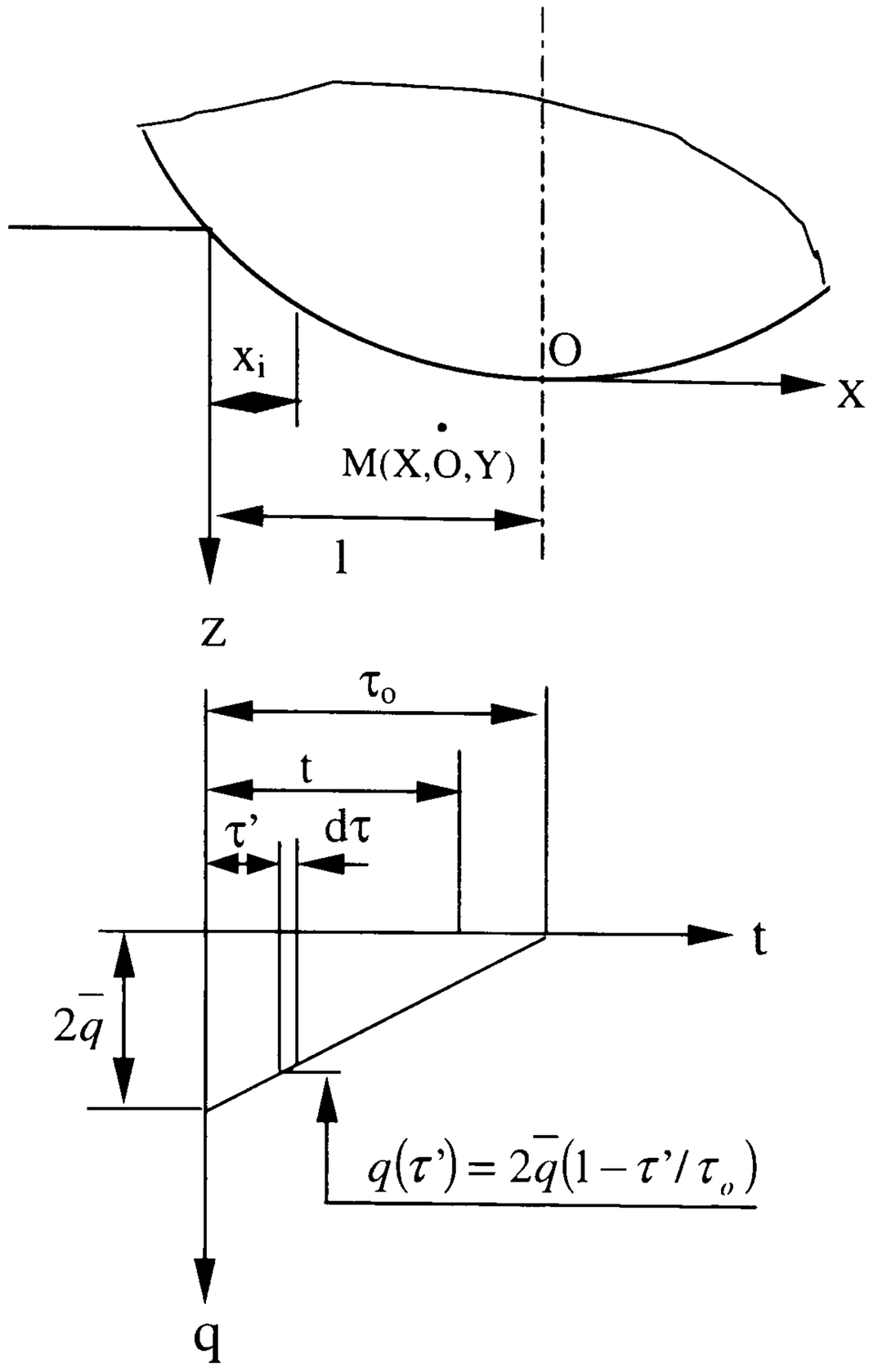

Figure 3.3 A sliding triangular heat source on a semi-infinite plane

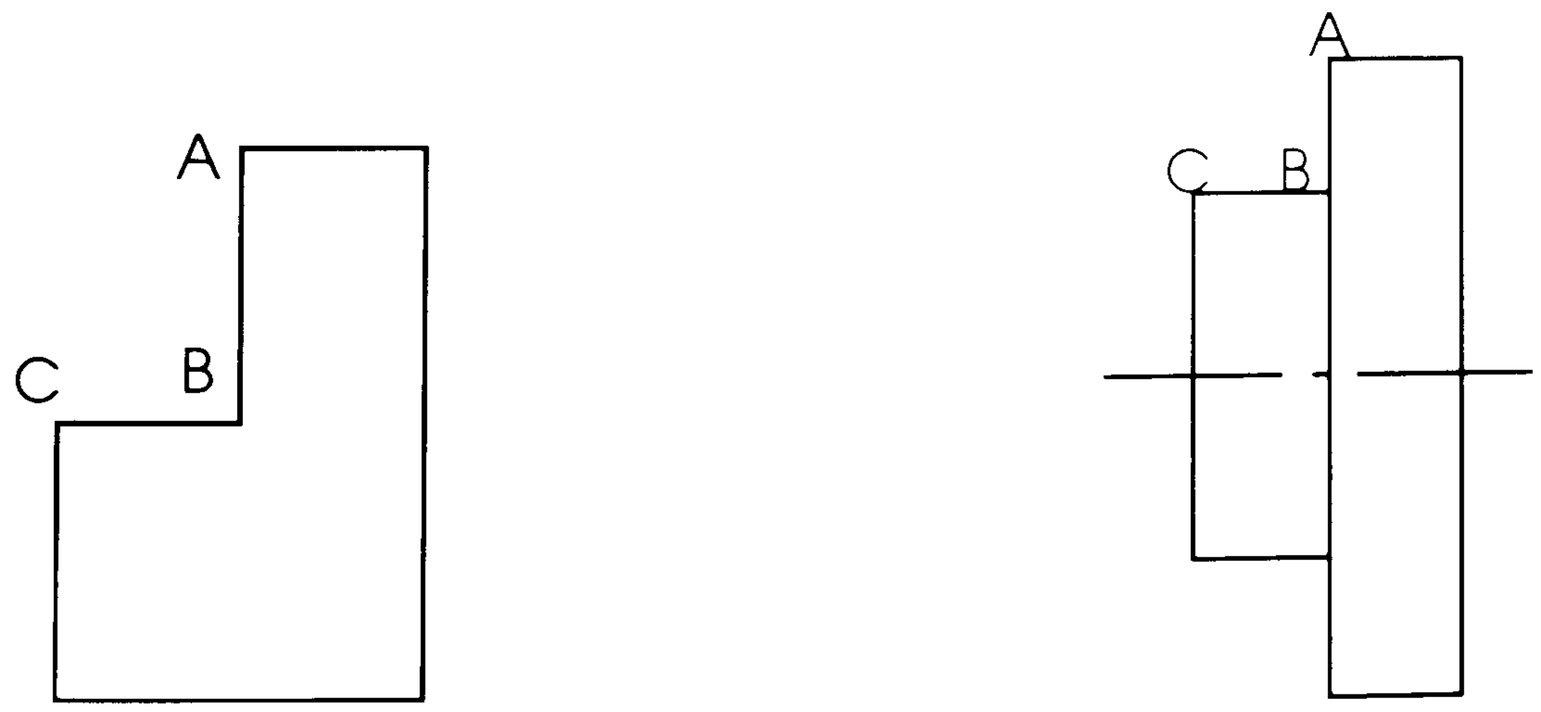

(a) Flat surfaces of a block

(b) An axi-symmetric workpiece

Fig 4.1 Form grinding shapes involving a vee section wheel

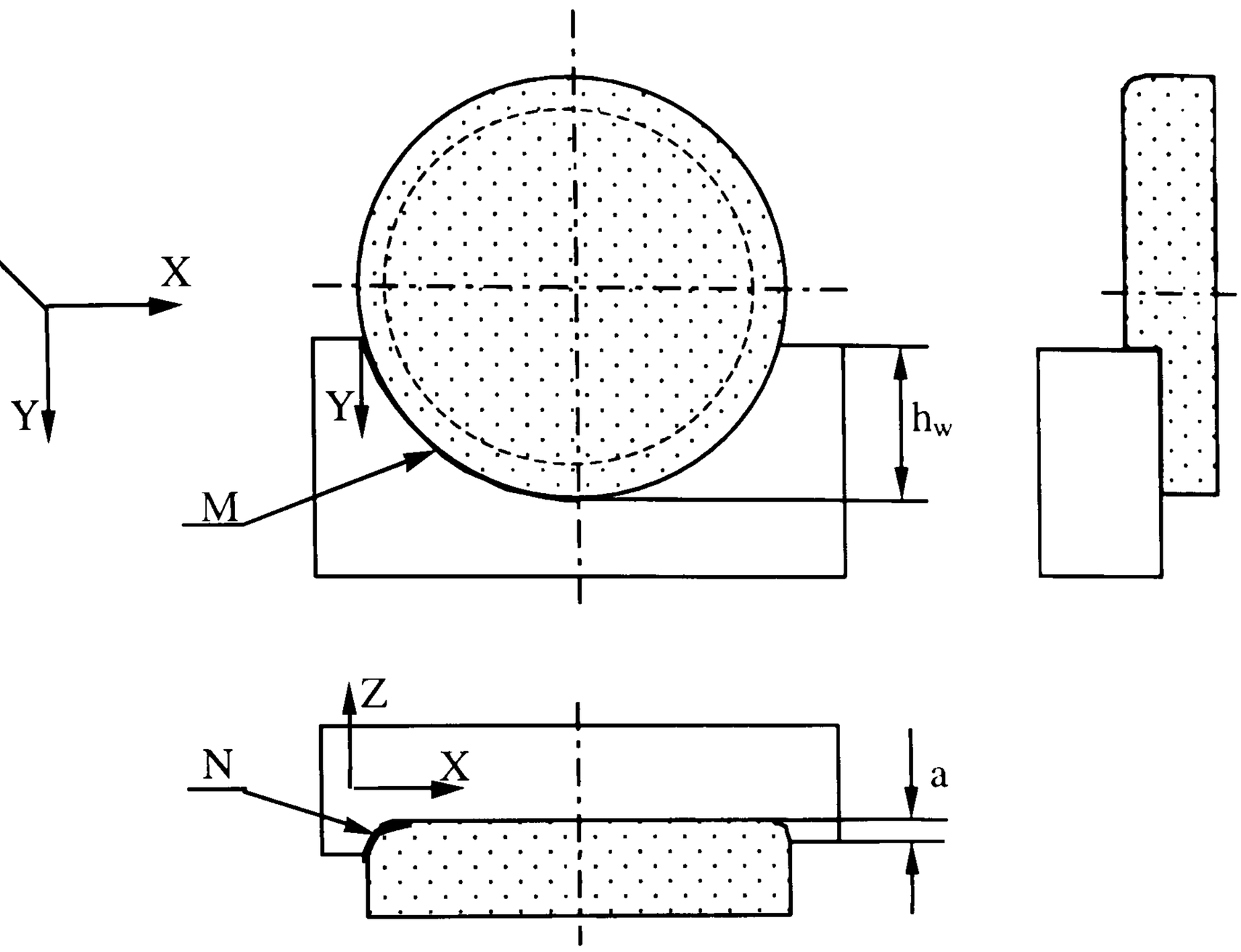

Figure 4.2 The geometric relationship between the grinding wheel and the workpiece in face grinding on a horizontal surface grinding machine

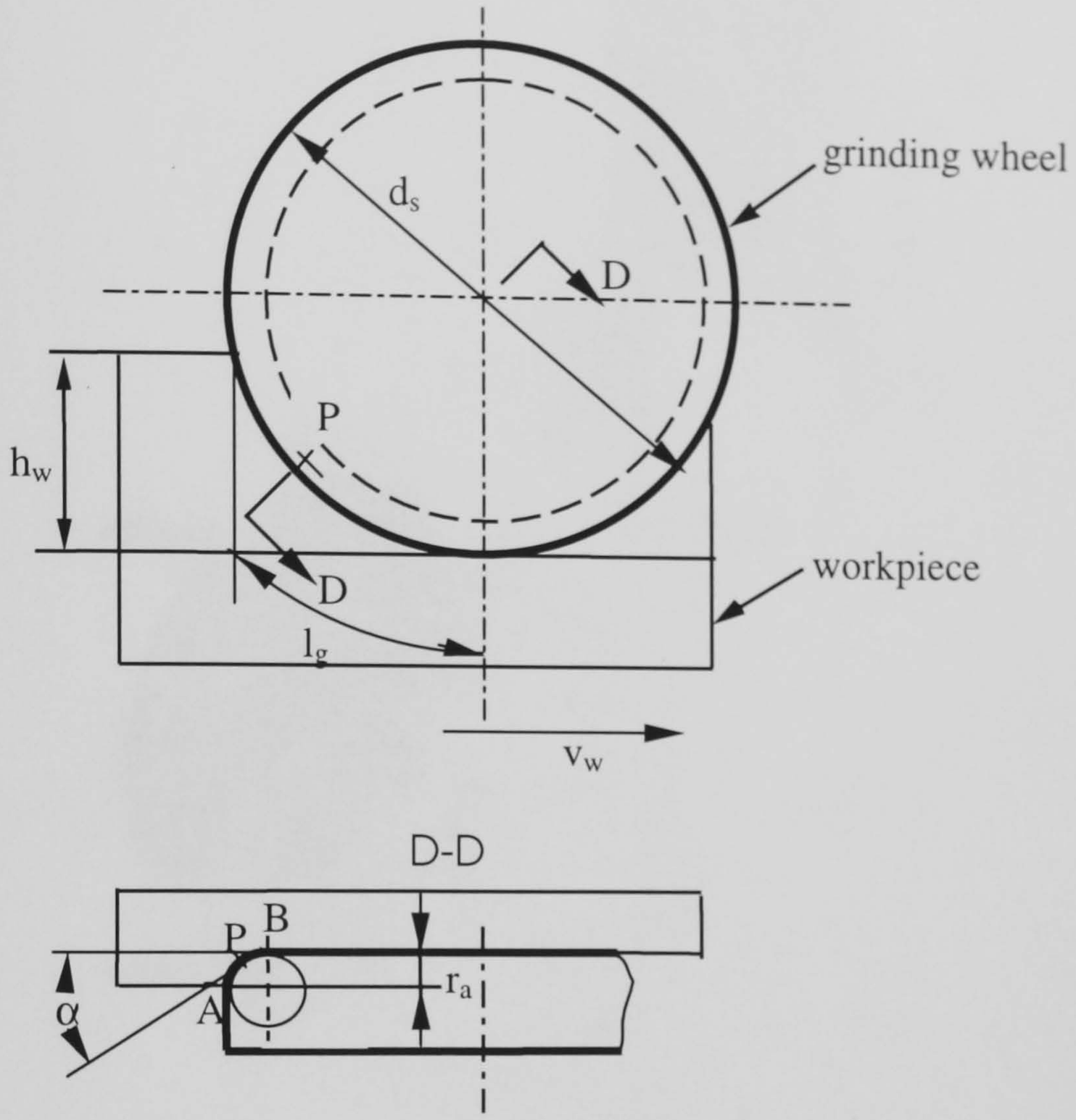

Figure 4.3 The geometric contact length in face grinding

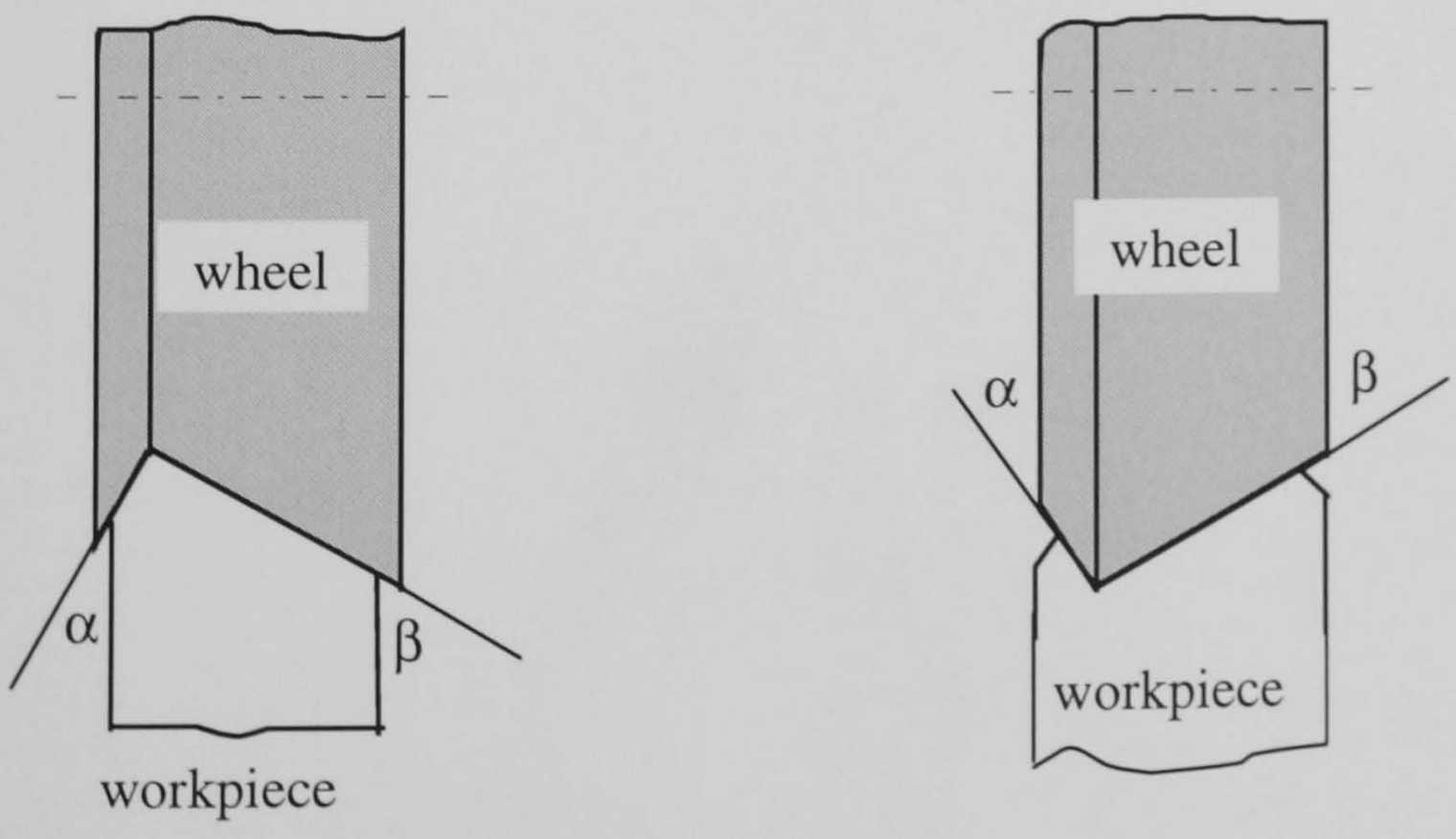

Figure 4.4 The inverted vee and vee form workpiece shapes

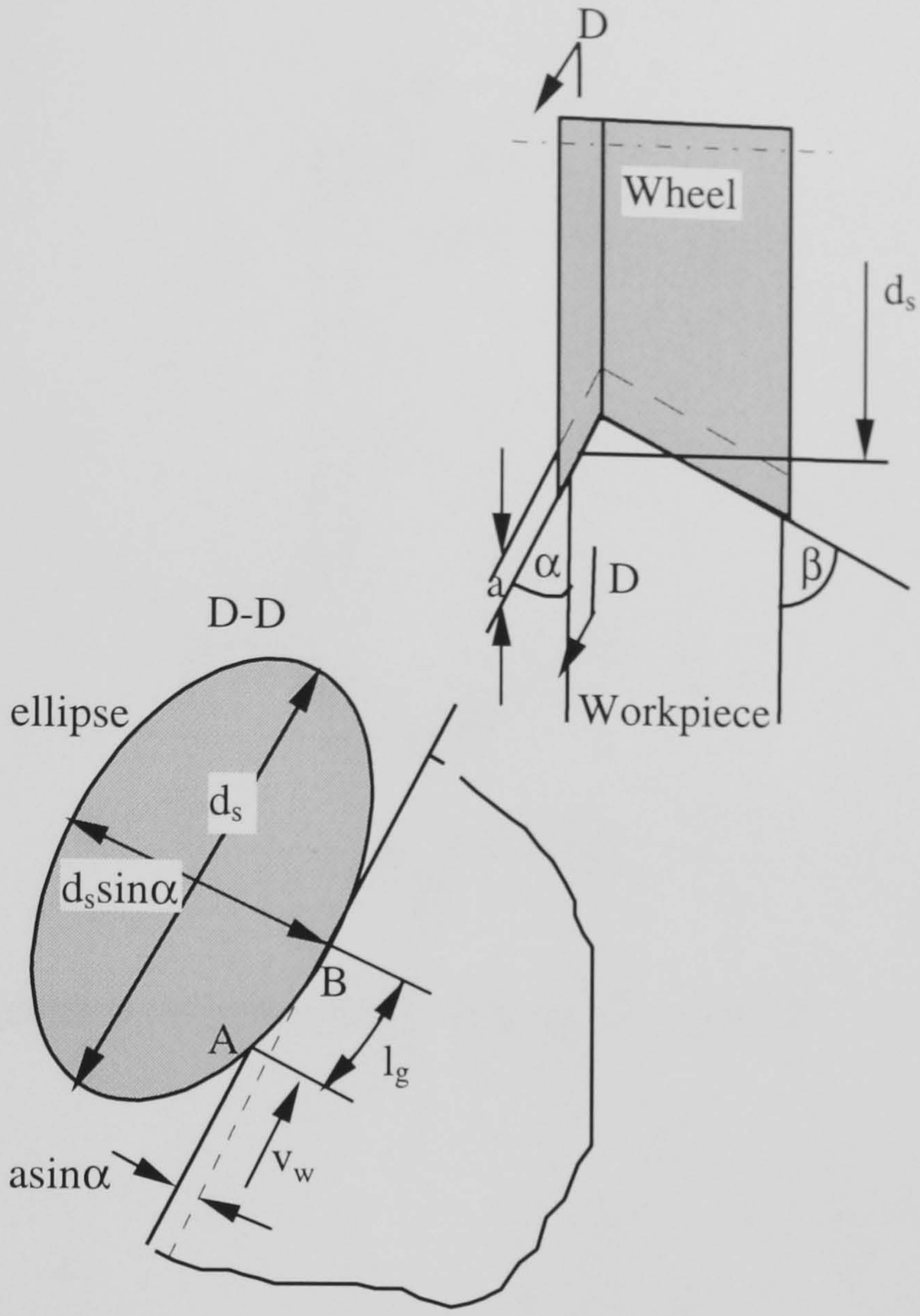

Figure 4.5 The geometric contact length for the inverted vee form

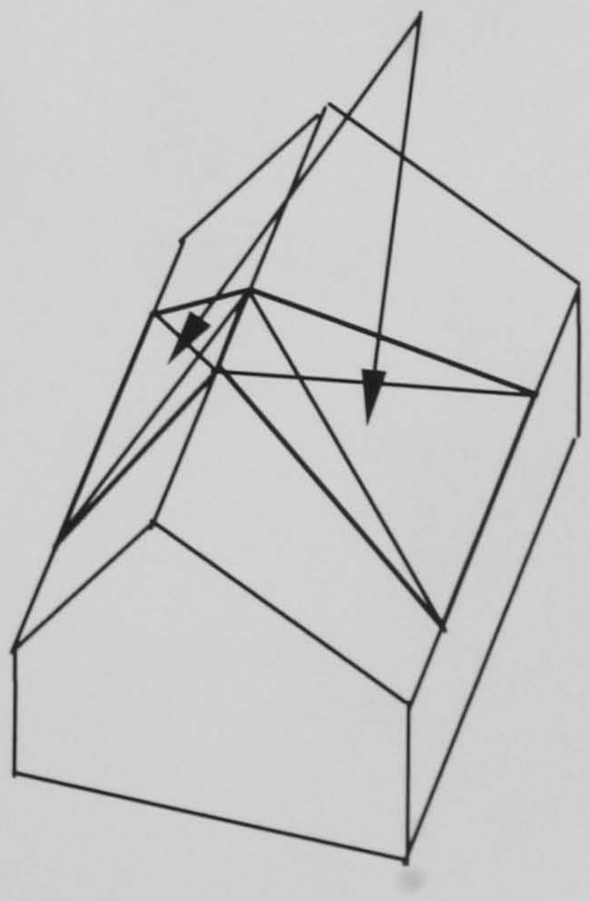

Figure 4.6 The contact area for the inverted vee form

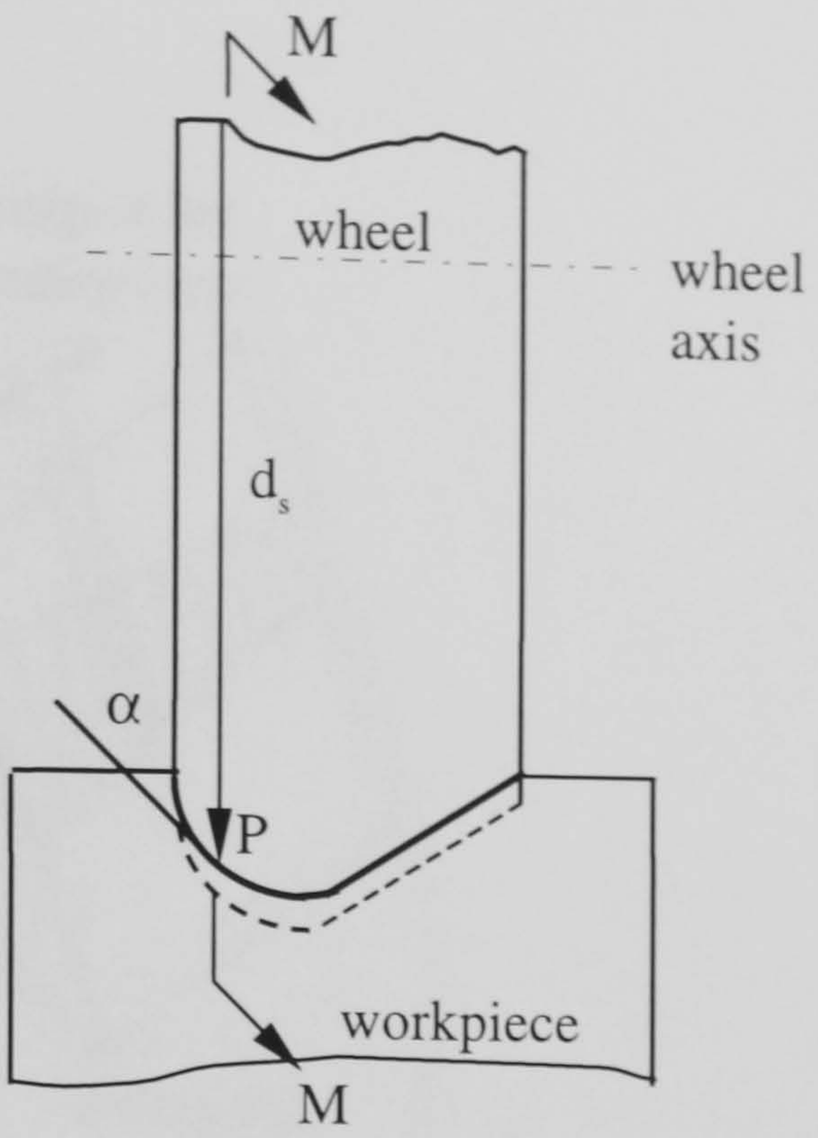

Figure 4.7 Flute form grinding and the profile angle α at the point P

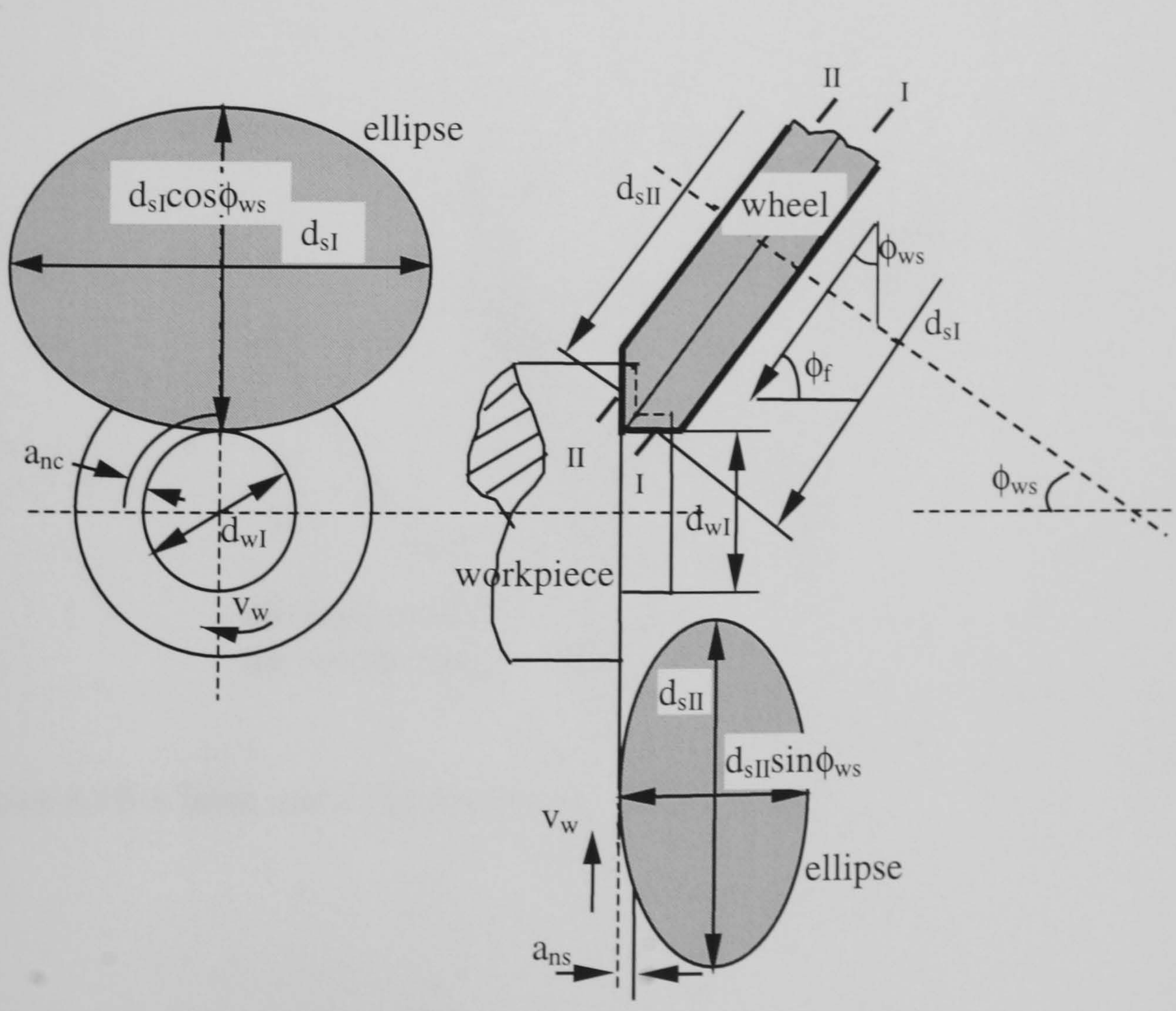

Figure 4.8 Cylindrical and shoulder face grinding with angle approach

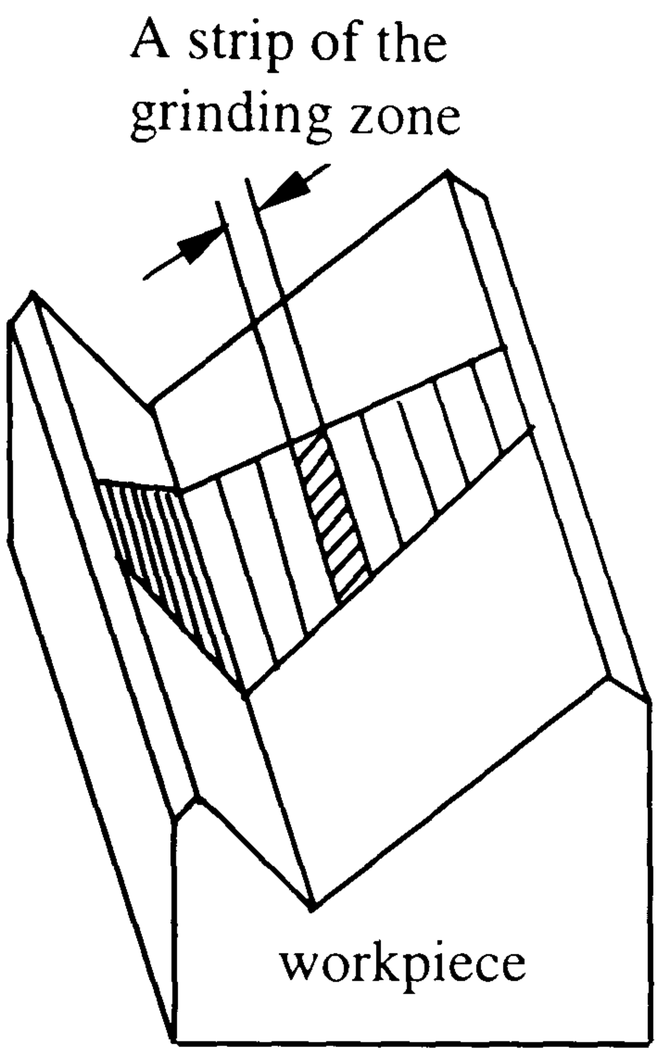

Figure 4.9 The grinding zone divided into strips

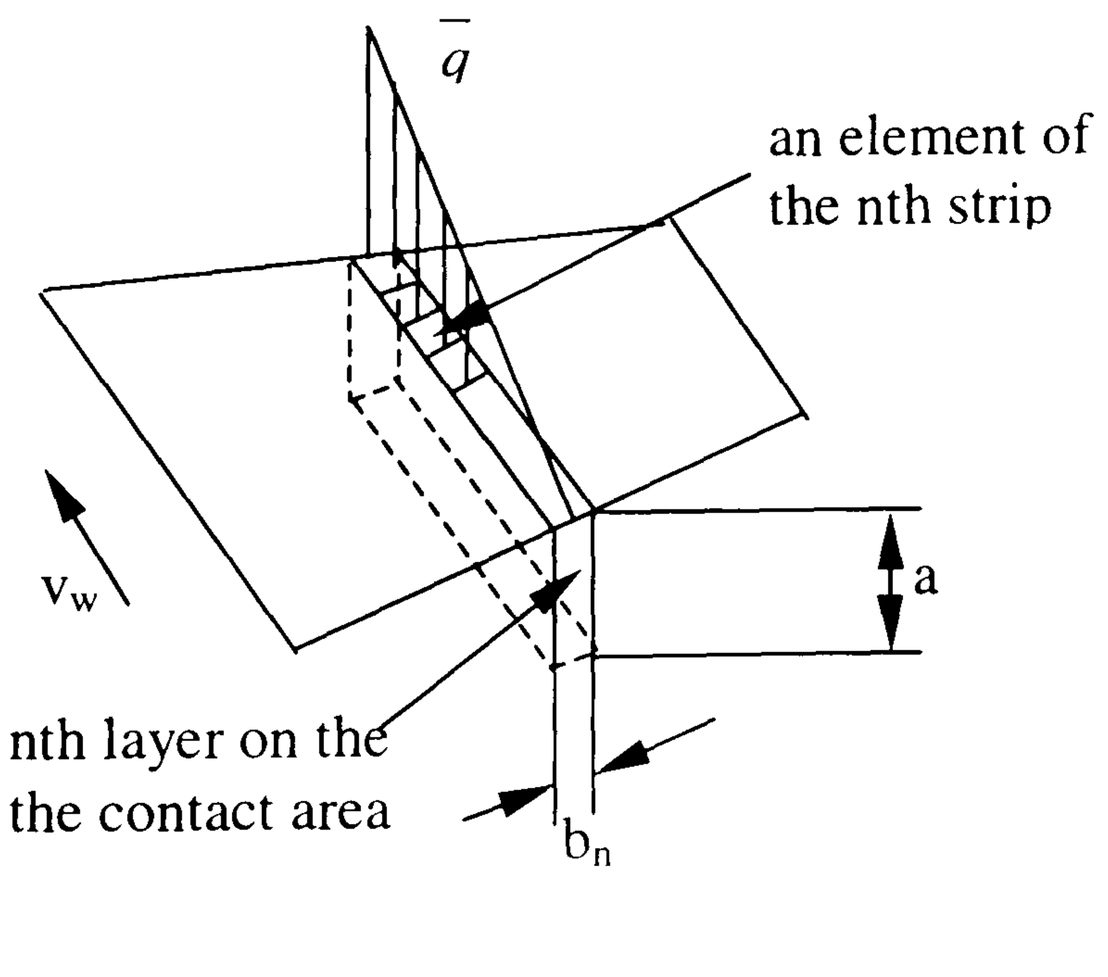

Figure 4.10 A layer under the contact area

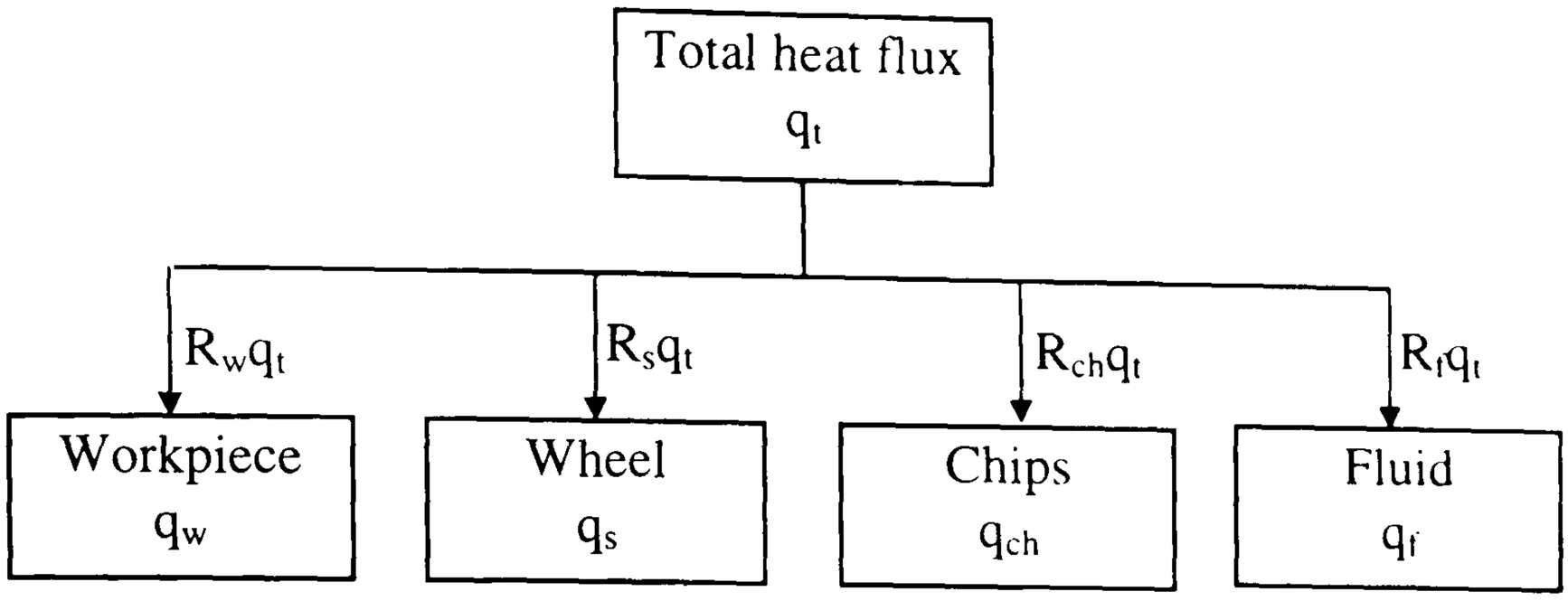

Figure 4.11 The heat flux partition in the grinding zone

$\kappa_w = 34.3 W/mK$ $\rho_w = 7815\ kg/m^3$ $c_w = 506\ J/kgK$

$\kappa_{ge} = 45 W/mK$ $v_s = 45 m/s$

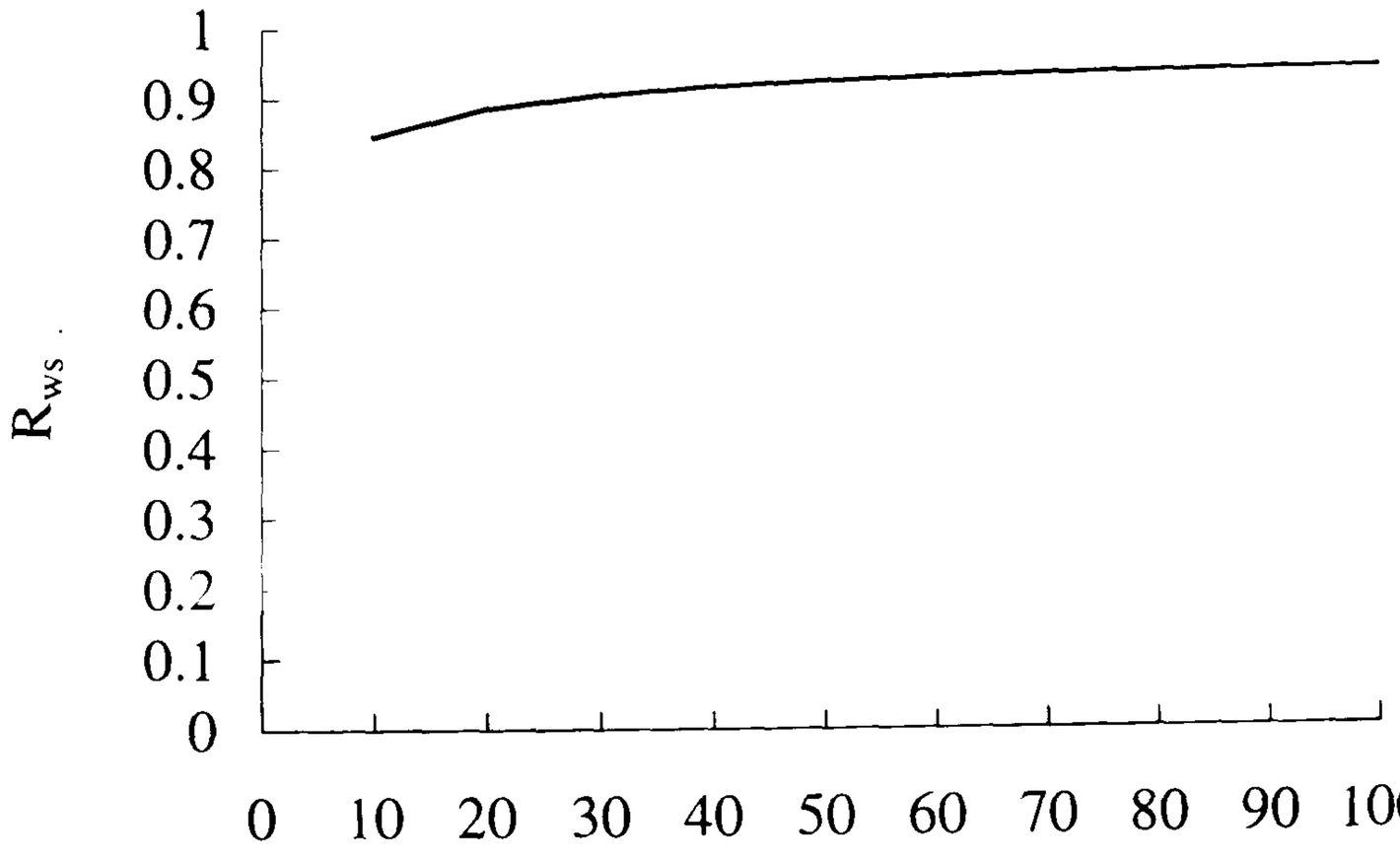

Figure 4.12 The variation of wheel-workpiece partition ratio with grain radius for alumina and steel

$\kappa_w = 34.3 W/mK$ $\rho_w = 7815\ kg/m^3$ $c_w = 506\ J/kgK$

$r_o = 15\mu m$ $v_s = 45 m/s$

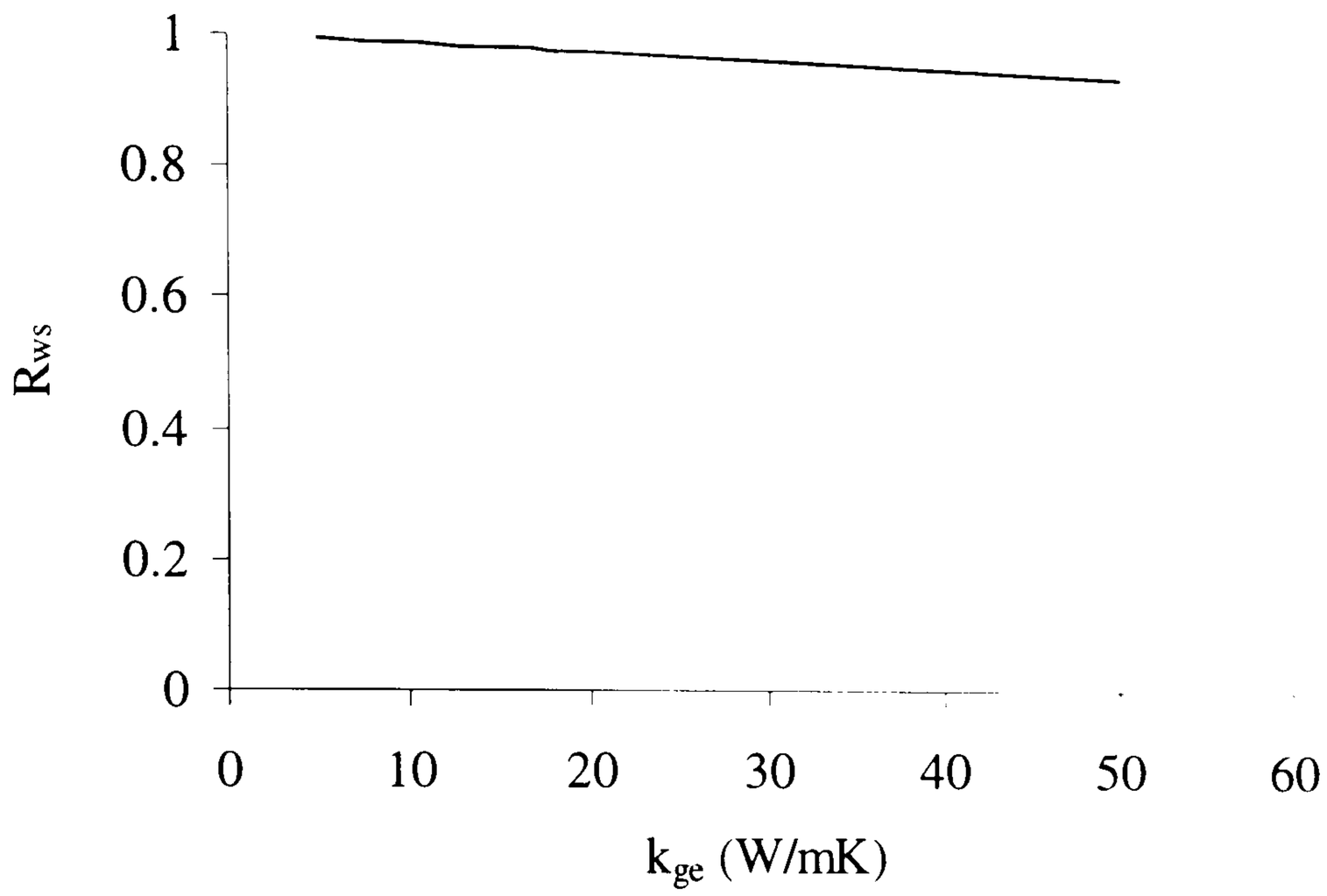

Figure 4.13 The variation of whee-workpiece partition ratio with grain thermal conductivity for alumina and steel

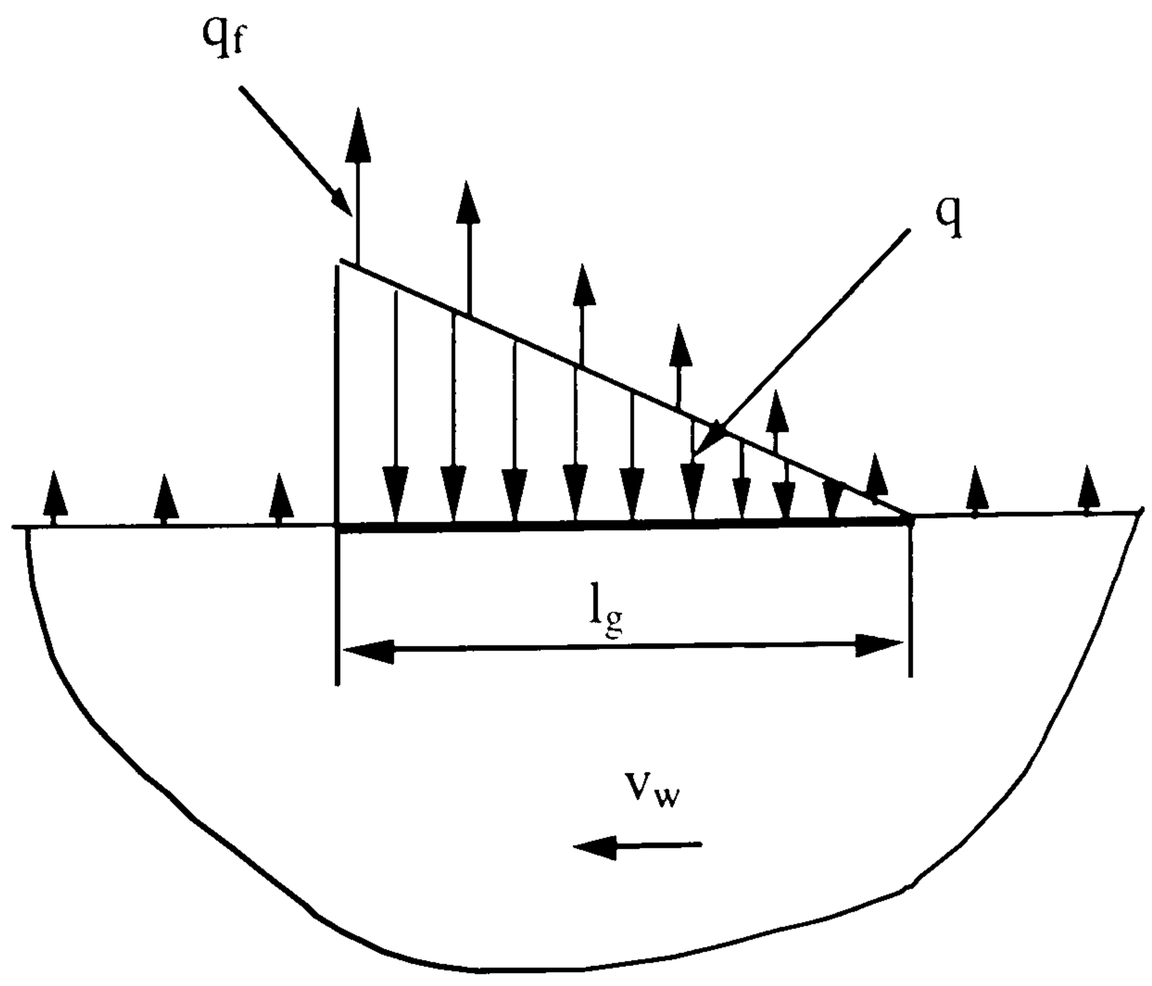

Figure 4.14 Uniform convective cooling on the workpiece surface

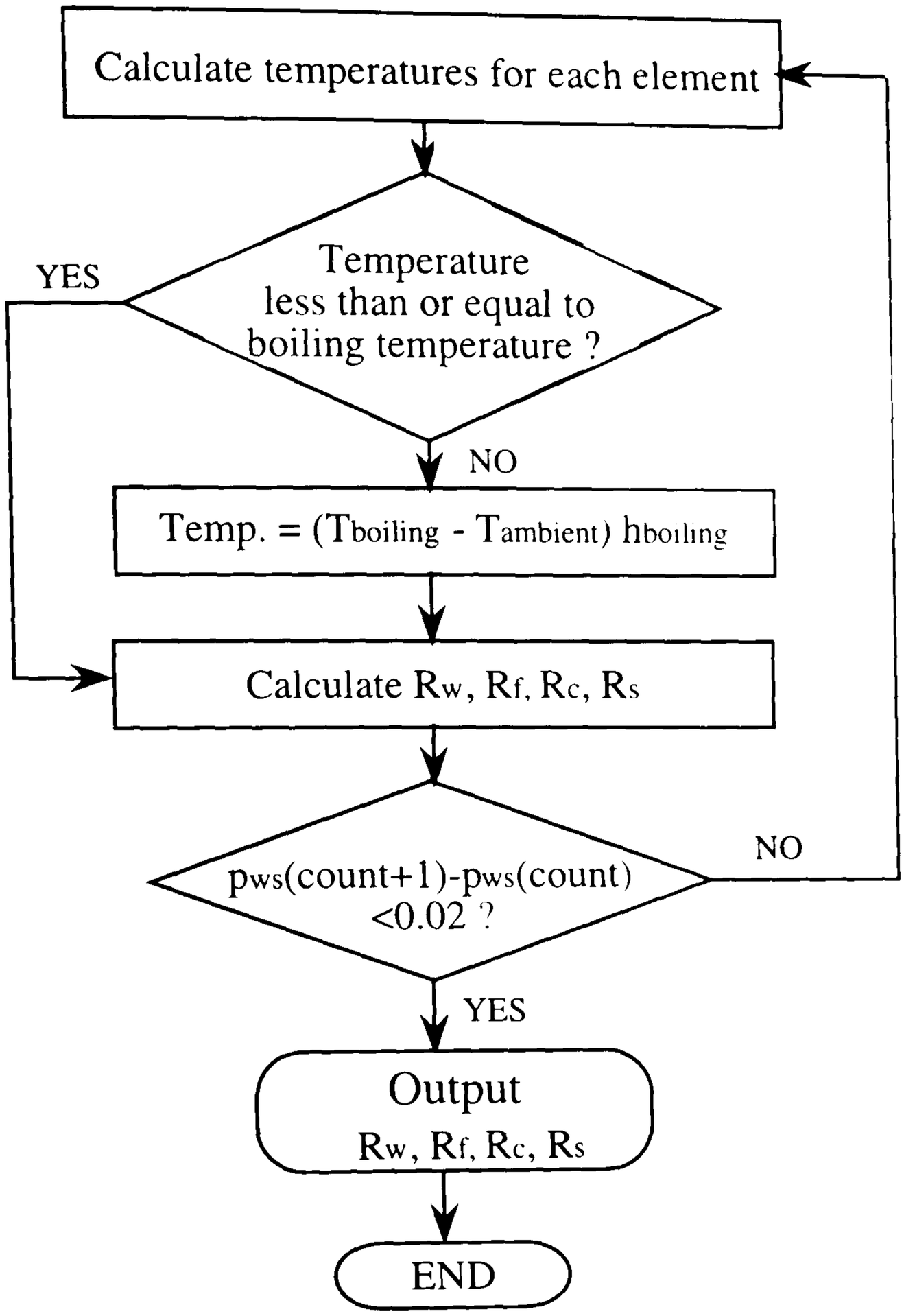

Figure 4.15 The flowchart for iterative calculation of workpiece partition ratio in wet grinding

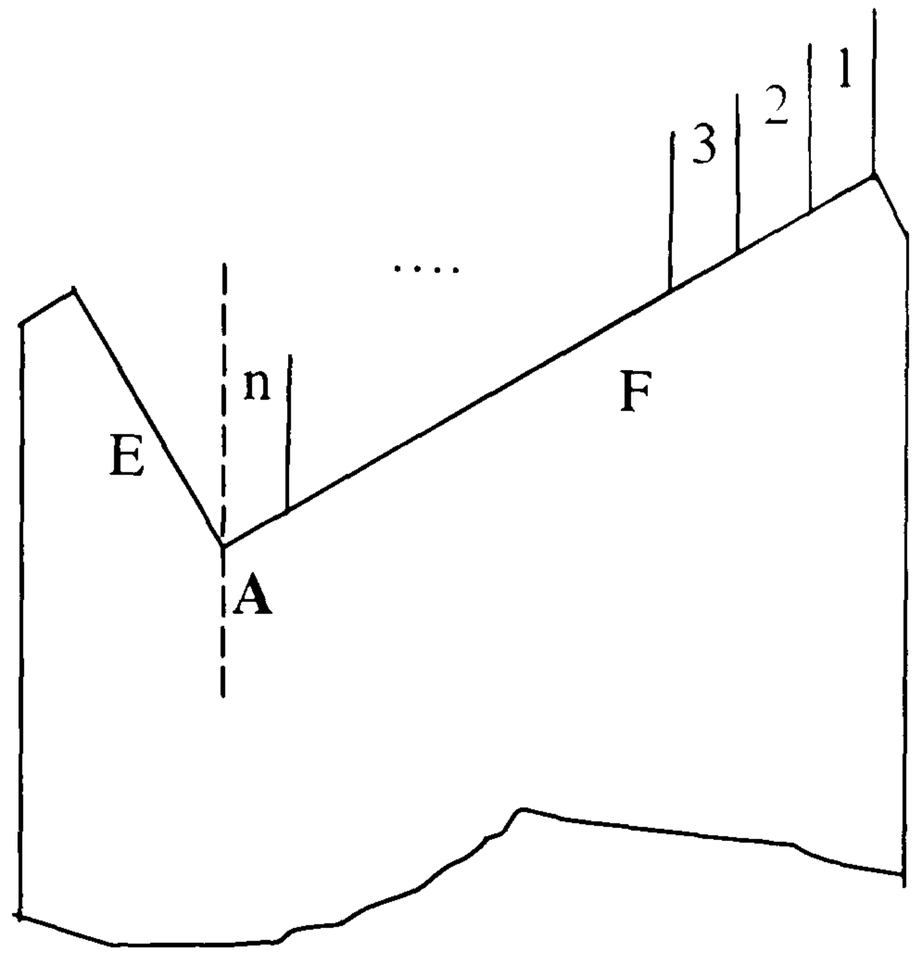

Figure 4.16 (a) The grinding contact area divided into strips

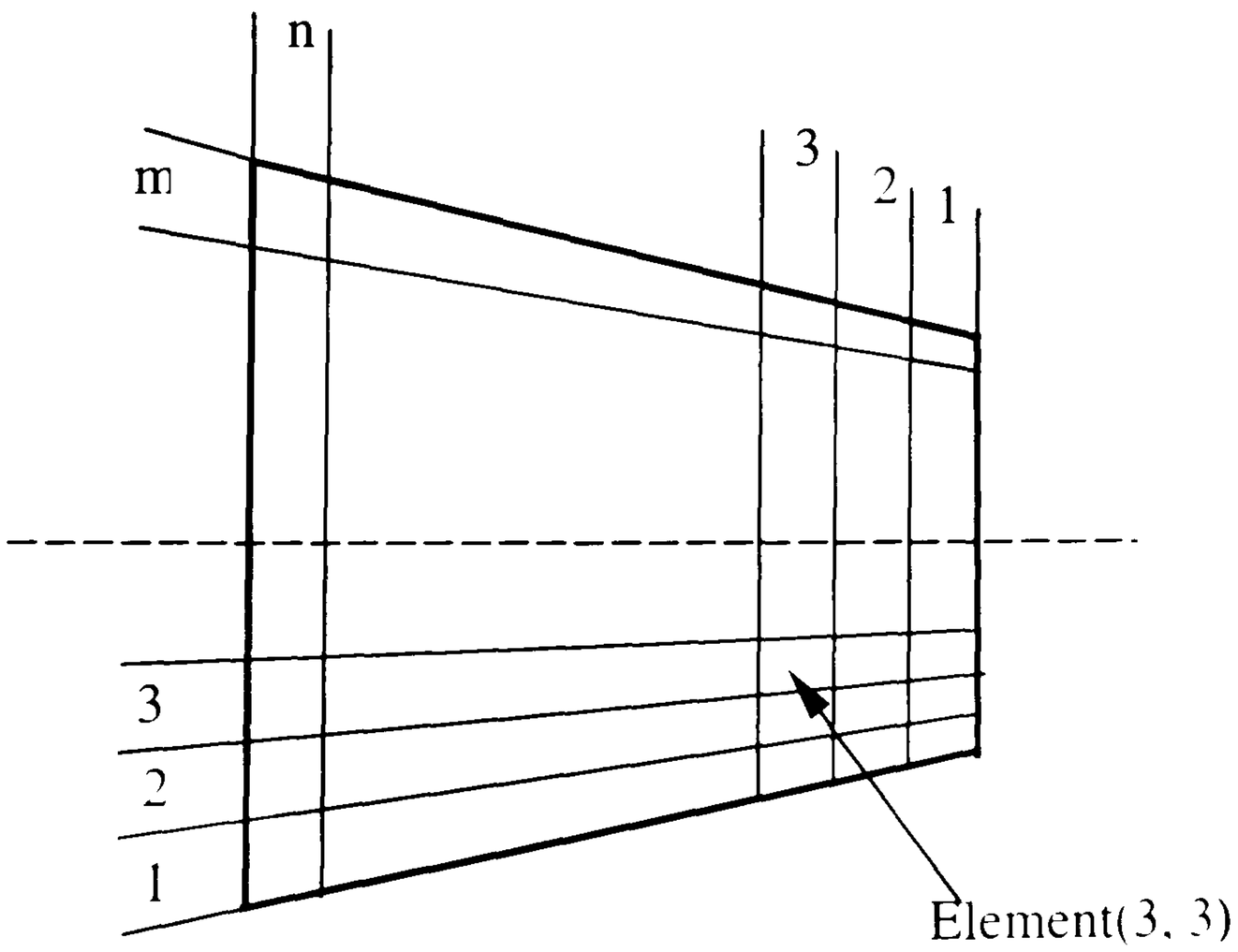

Figure 4.16 (b) The grinding contact area divided into a series of elements

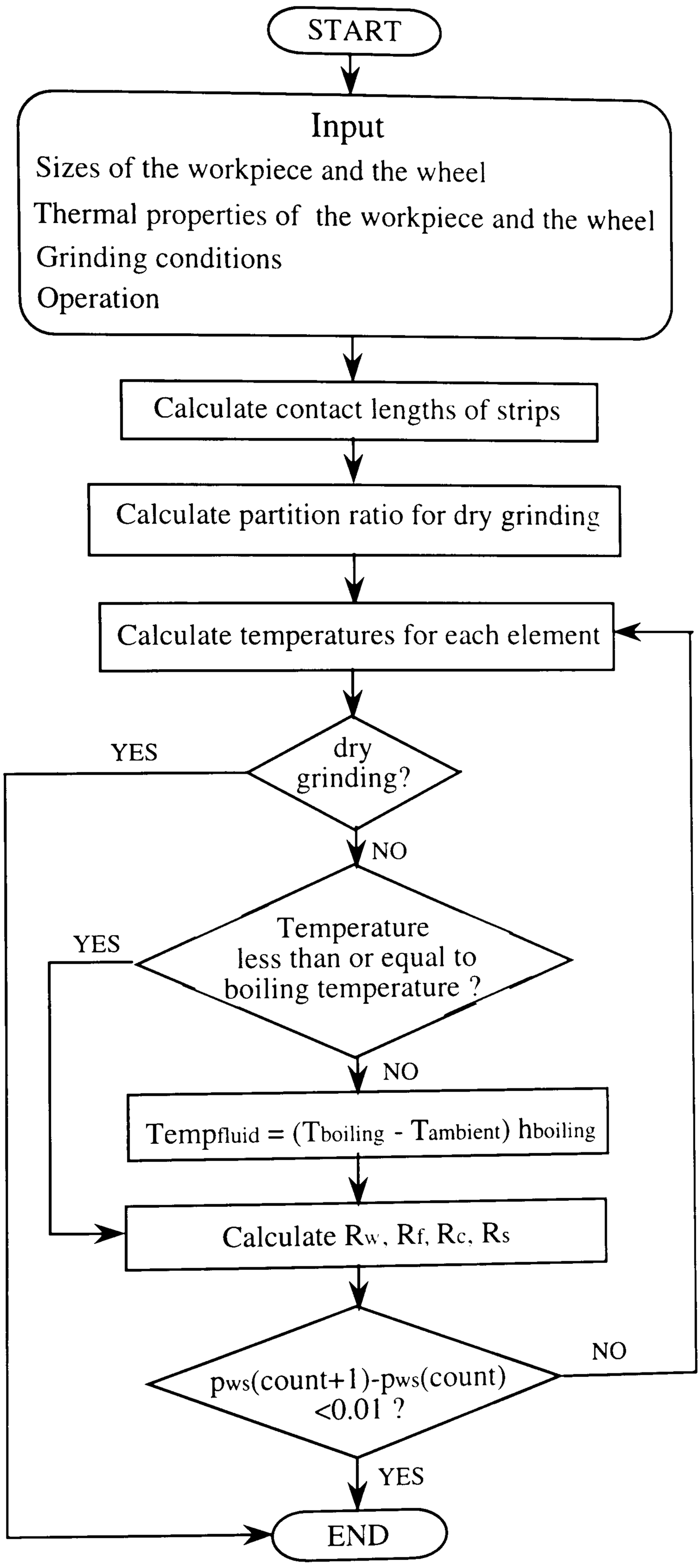

Figure 5.1 The flowchart of the program

Vee form

Wheel parameters:
d_s = 200 mm
v_s = 45 m/s

Sizes of workpiece:
flank1 = 10 mm
flank2 = 10 mm
angle1 = 60°
angle2 = 30°

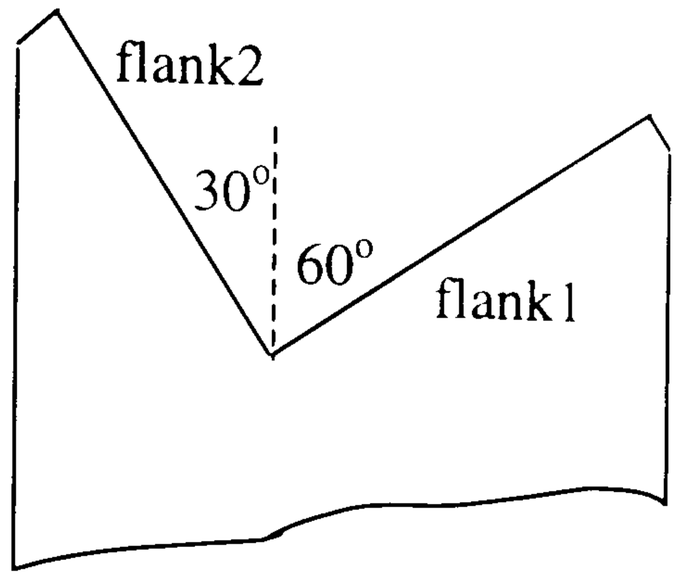

Grinding conditions:
v_w = 0.1 m/s;
power = 1000 W
a = 10 μm

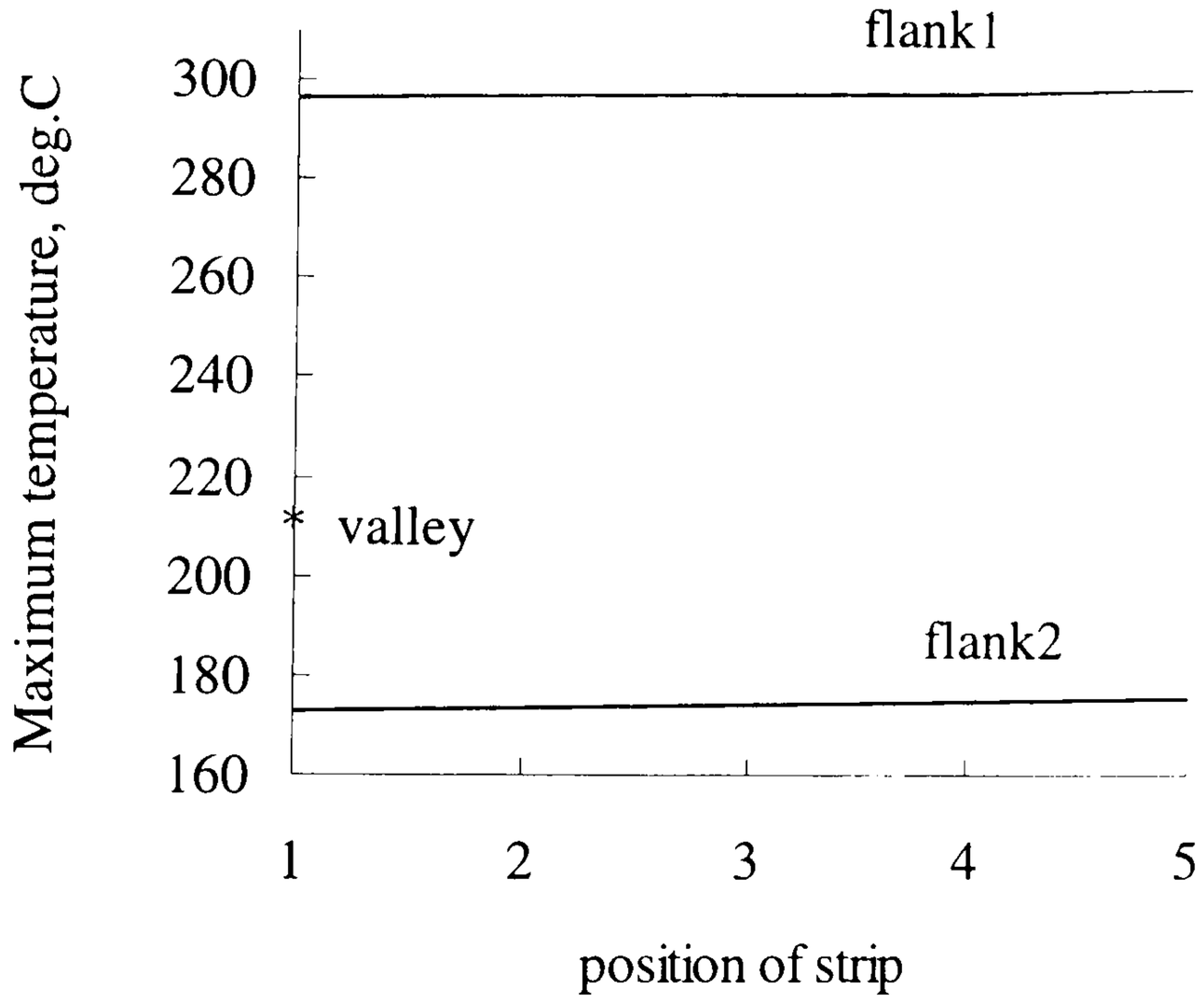

Figure 5.2 The maximum temperature for each strip in the grinding zone.

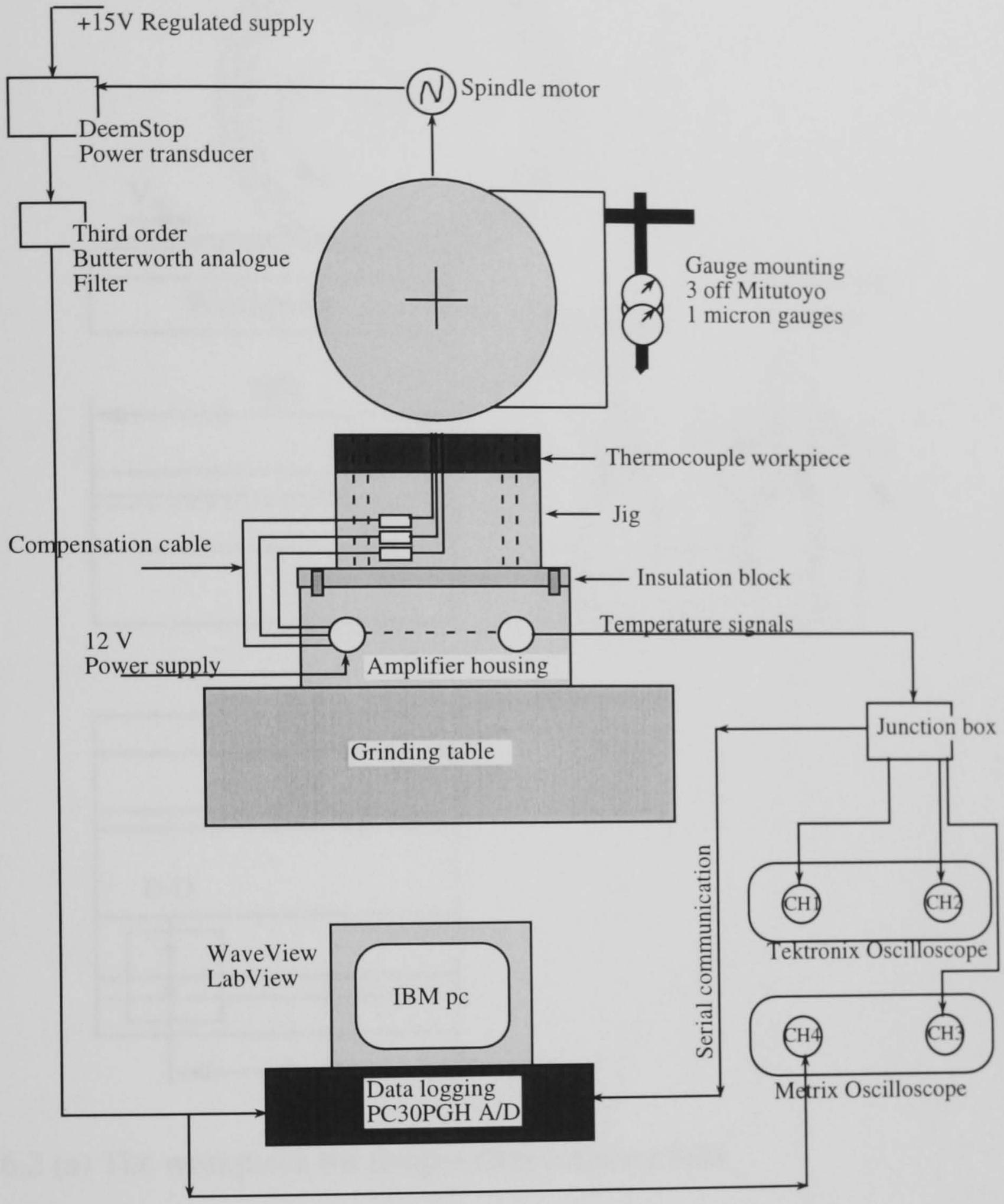

Figure 6.1 The experimental system

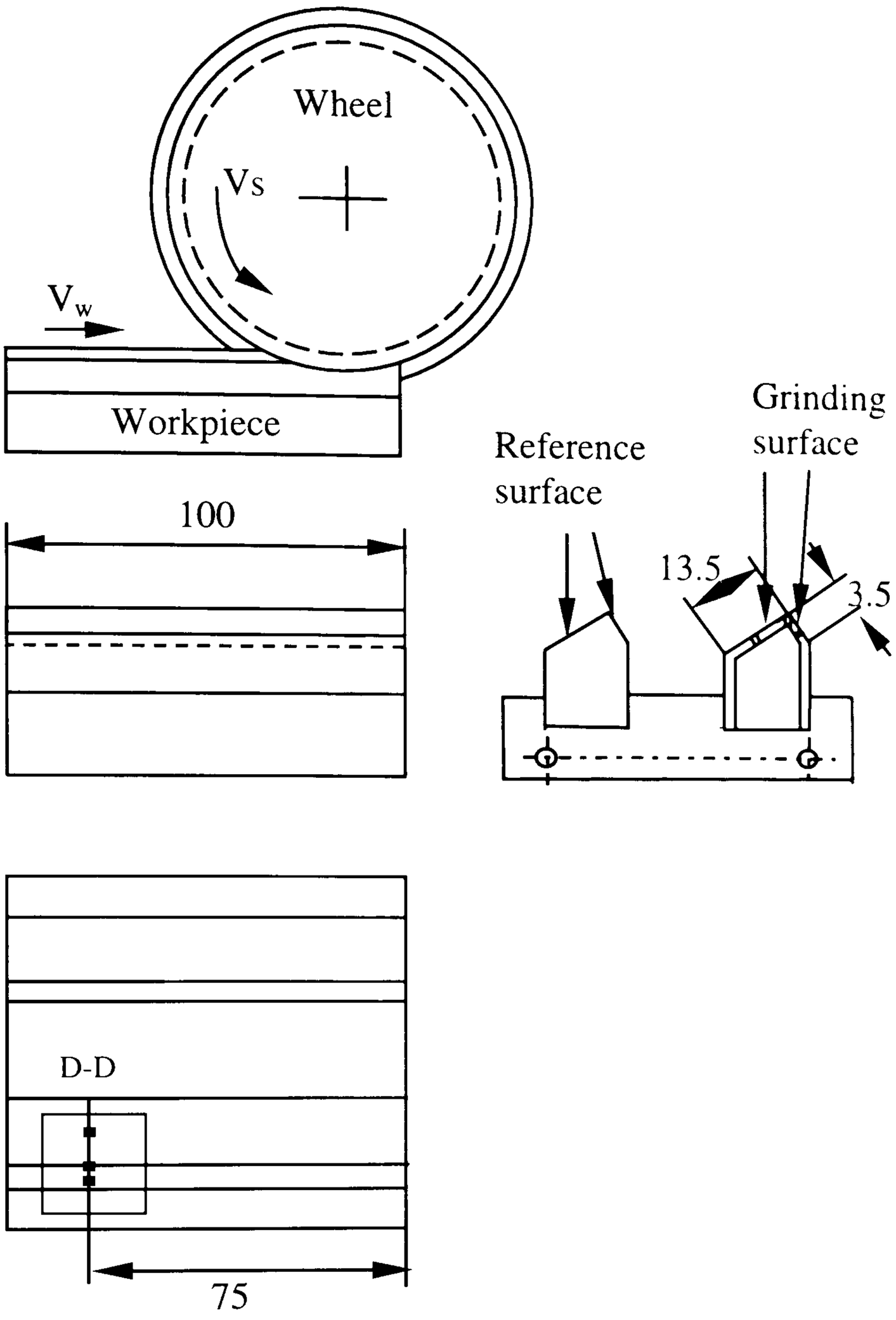

Figure 6.2 (a) The workpiece for temperature measurement

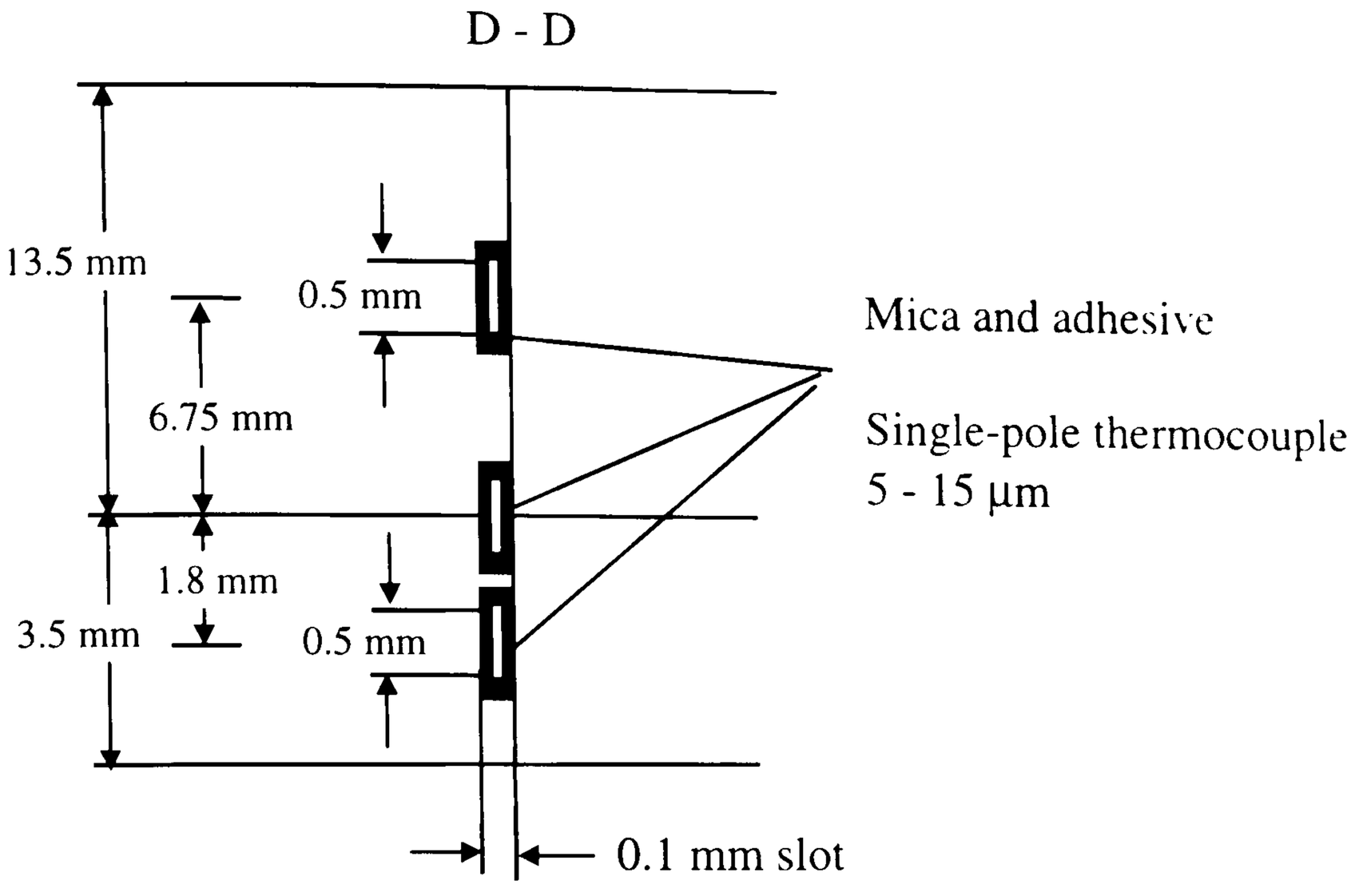

Figure 6.2 (b) The junction of thermocouple on the workpiece surface

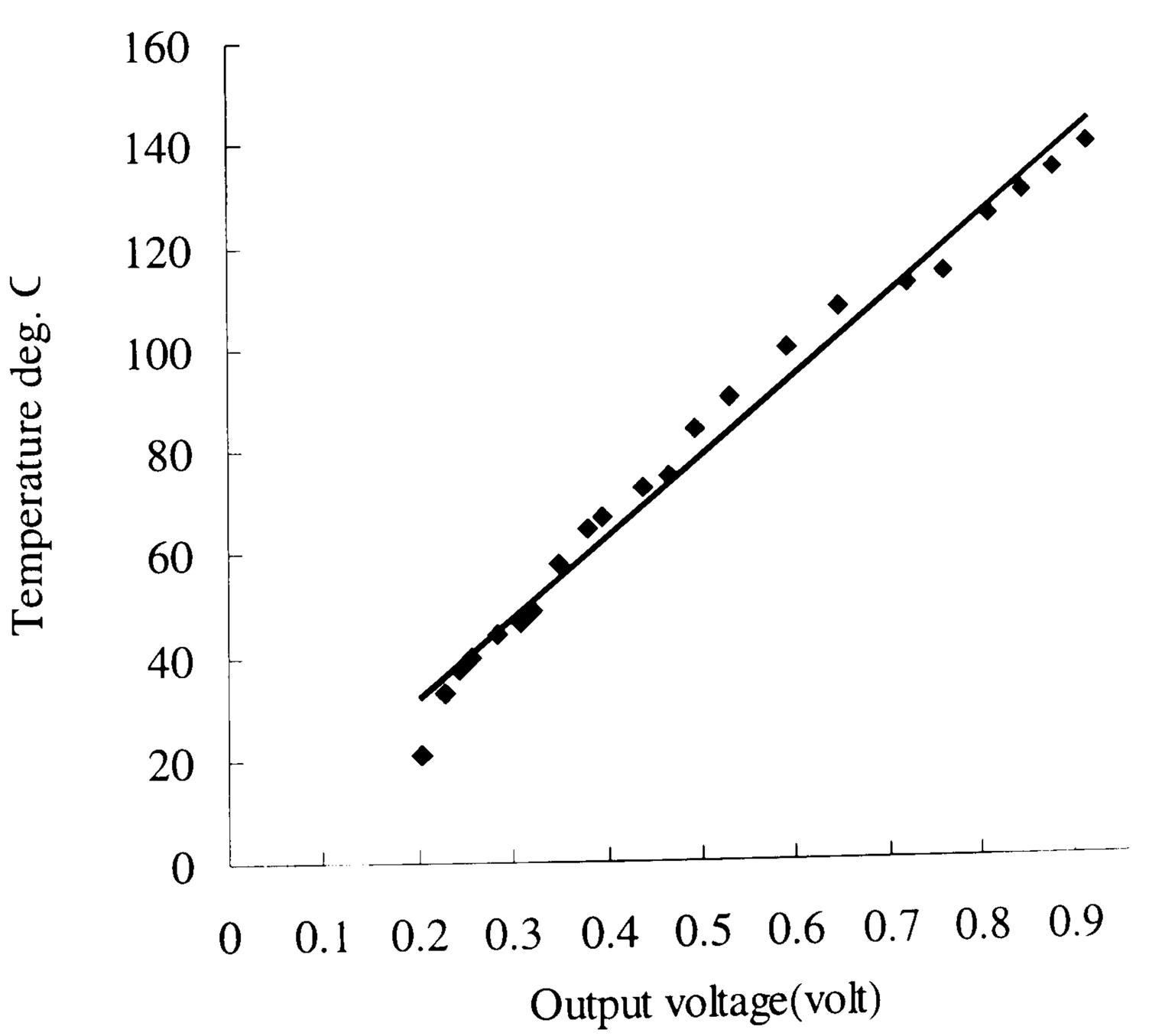

Figure 6.3 Calibration of the thermocouples

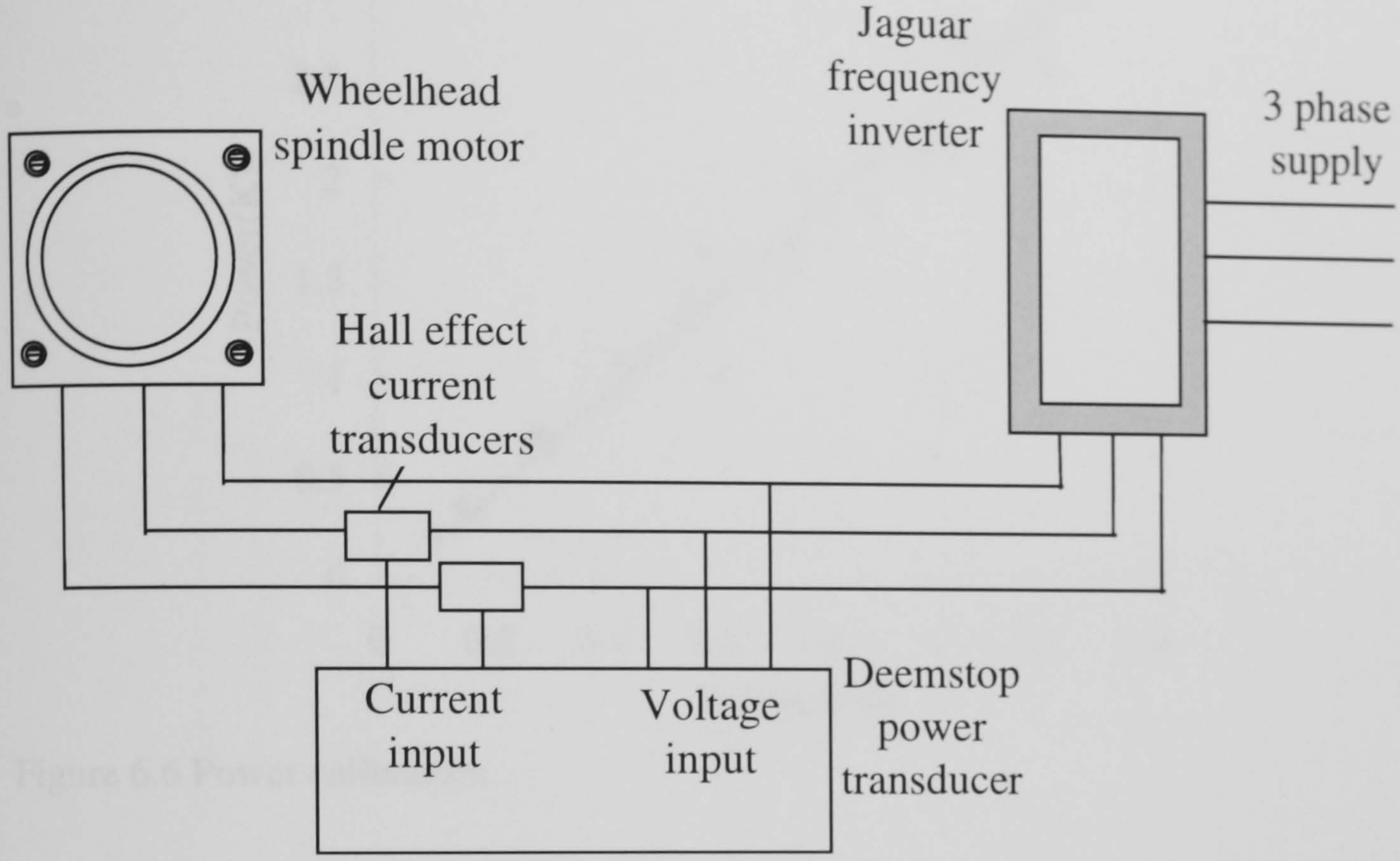

Figure 6.4 Schematic of the Deemstop power transducer installation

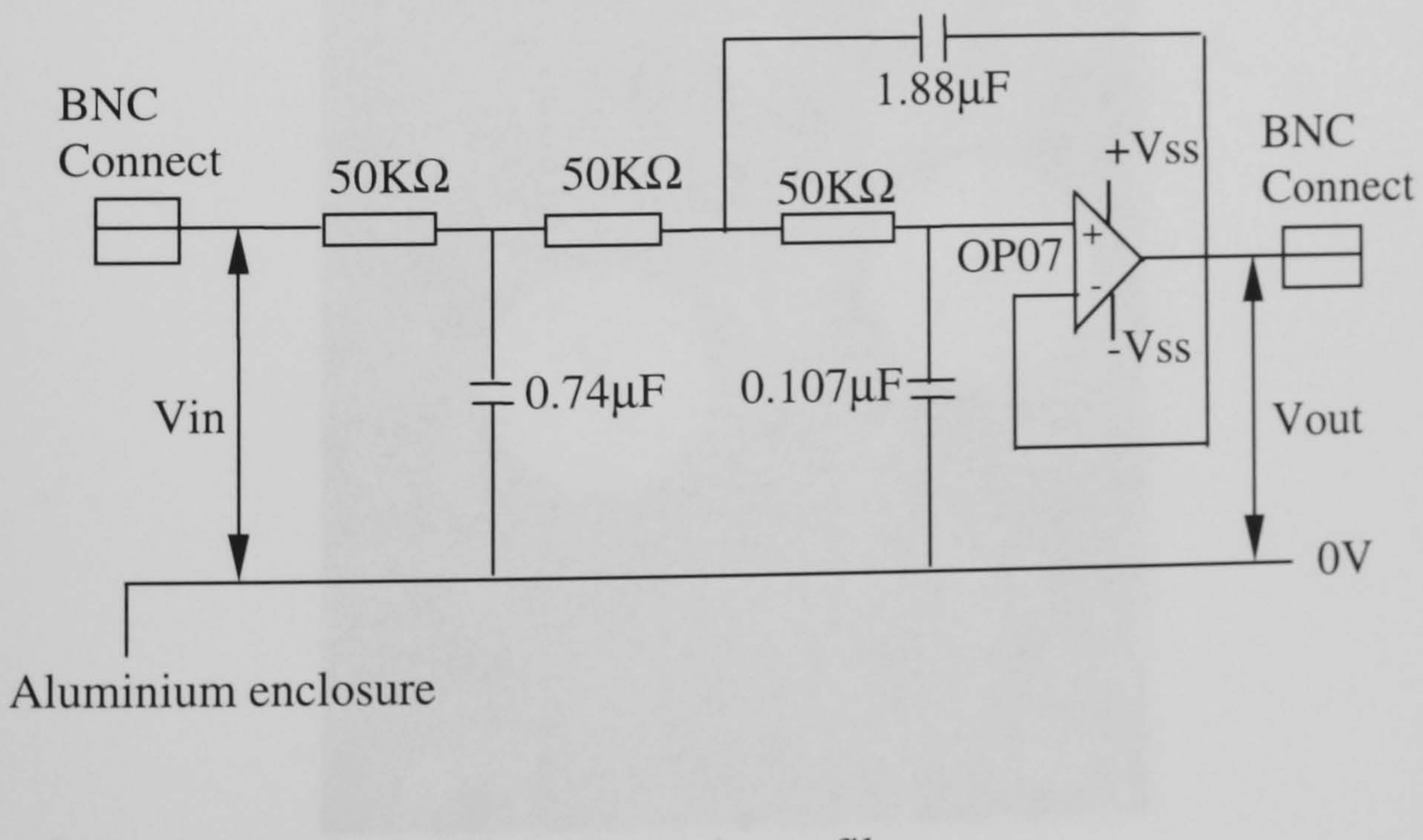

Figure 6.5 The third order Butterworth analogue filter

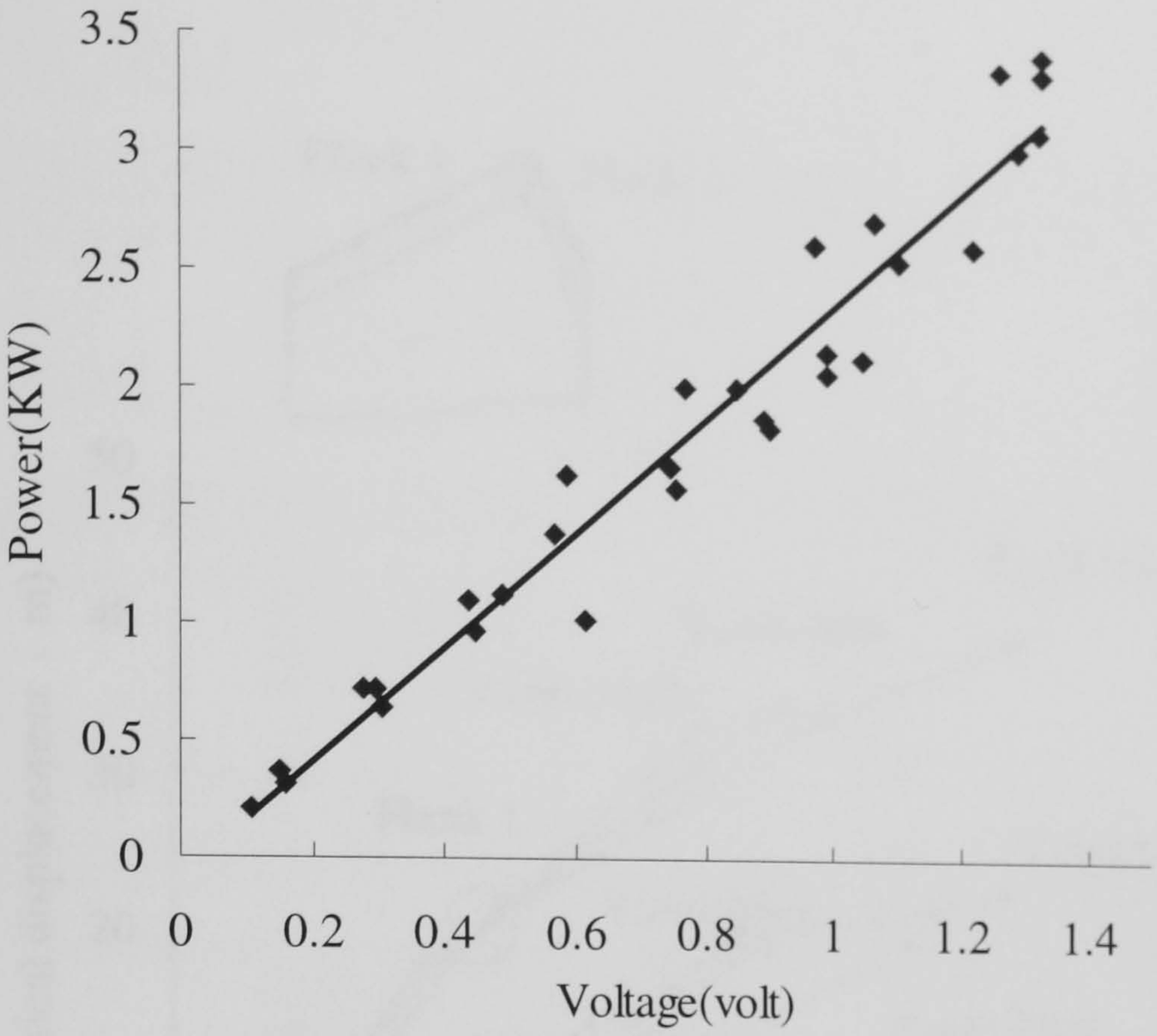

Figure 6.6 Power calibration

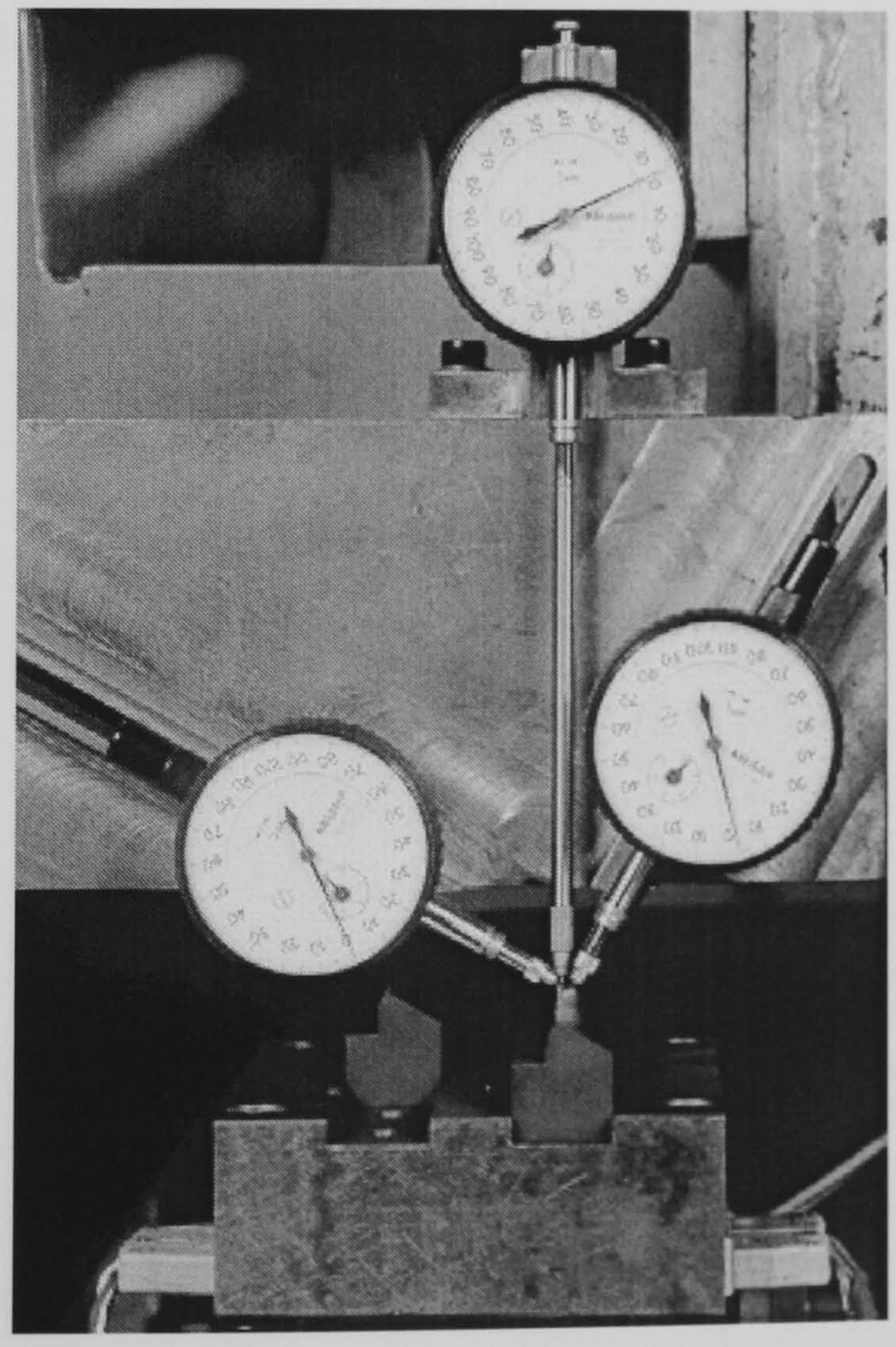

Figure 6.7 The subsystem for the measurement of the depth of cut

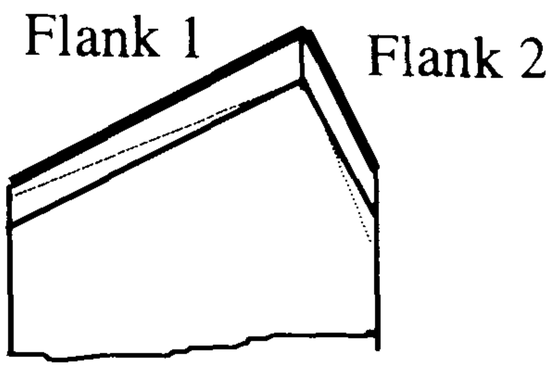

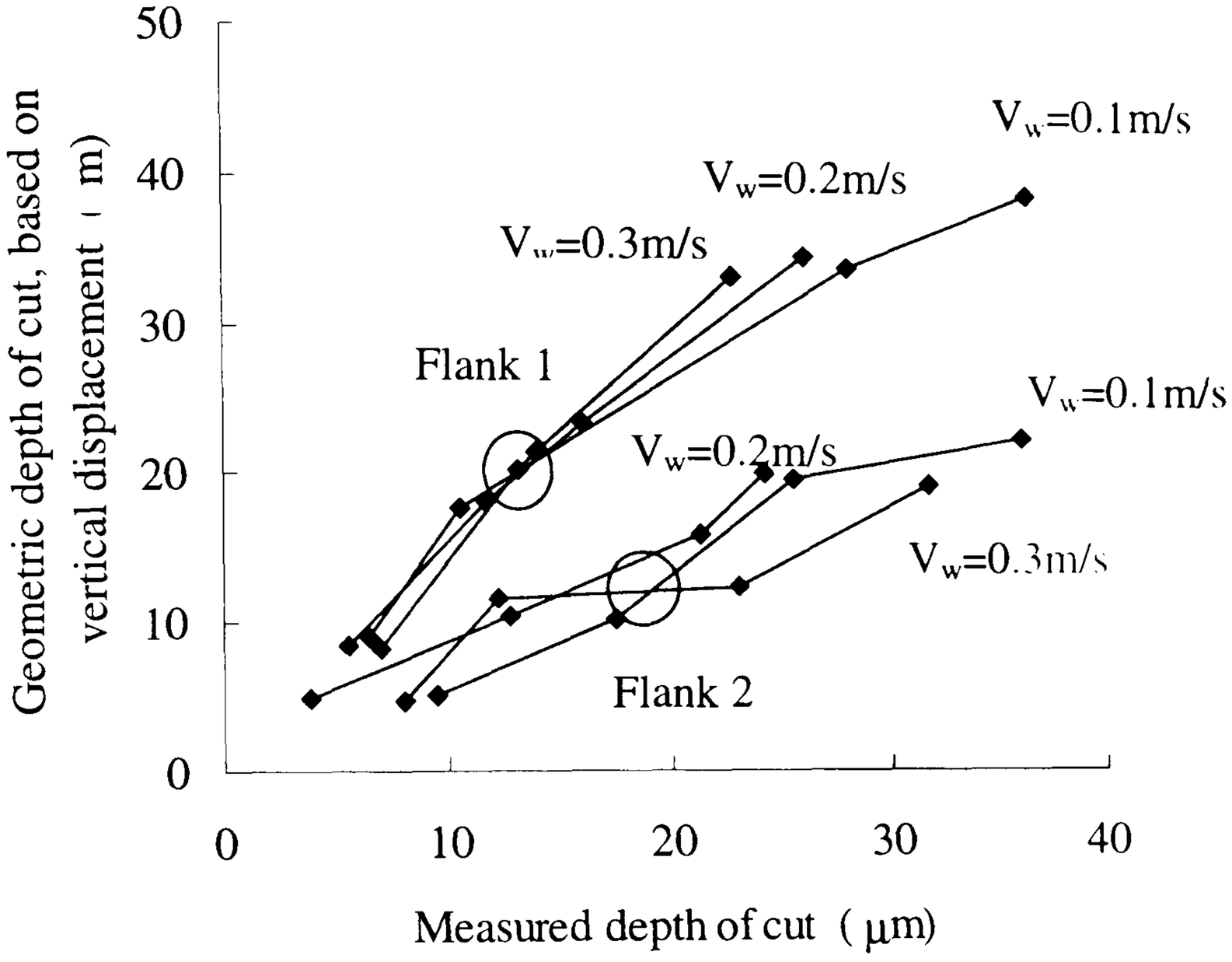

Figure 6.8 Measured values against expected values of the depth of cut

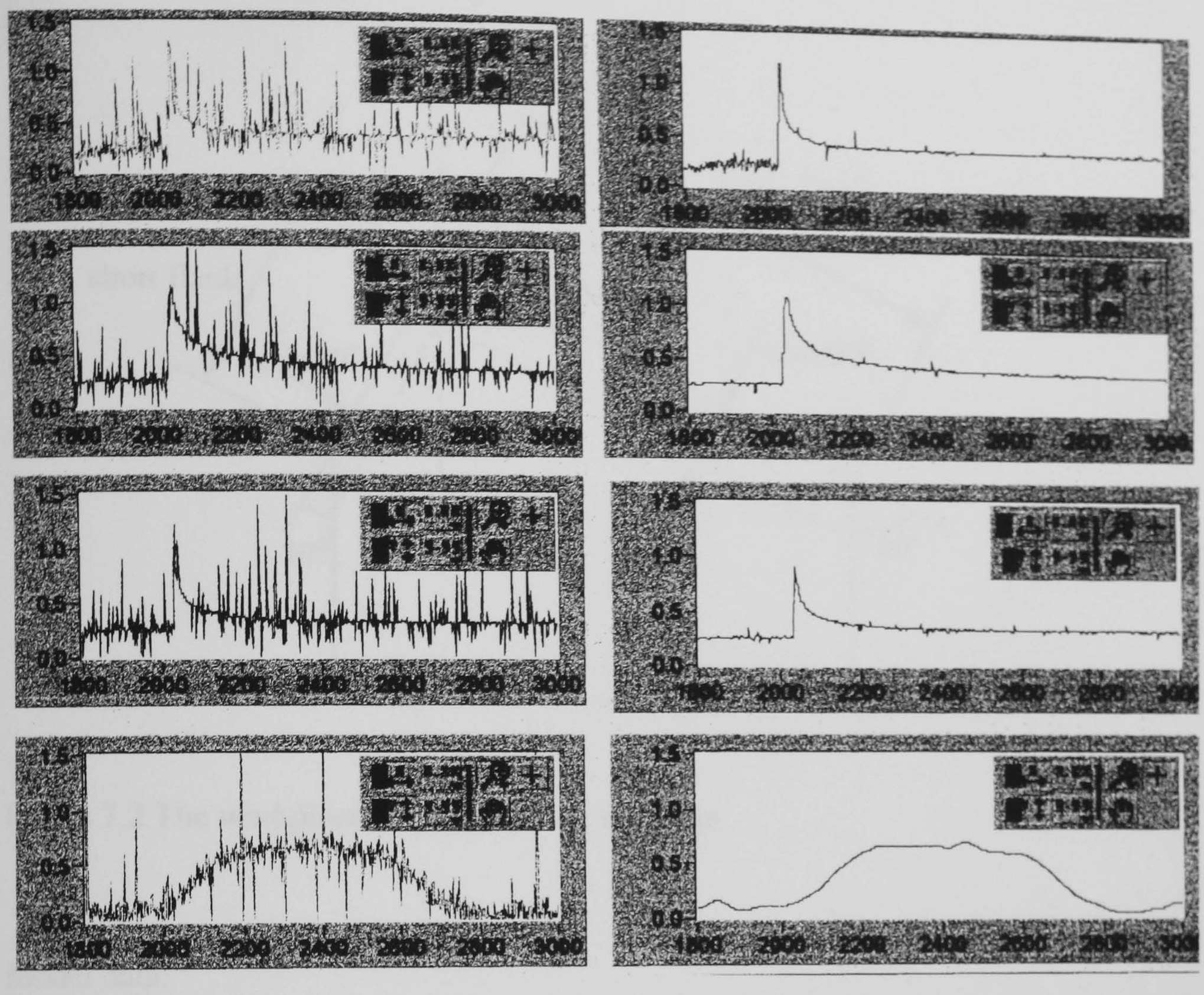

Figure 6.9 Typical outputs signals from LabView for the inverted vee form

Figure 7.1 A diamond roll dresser

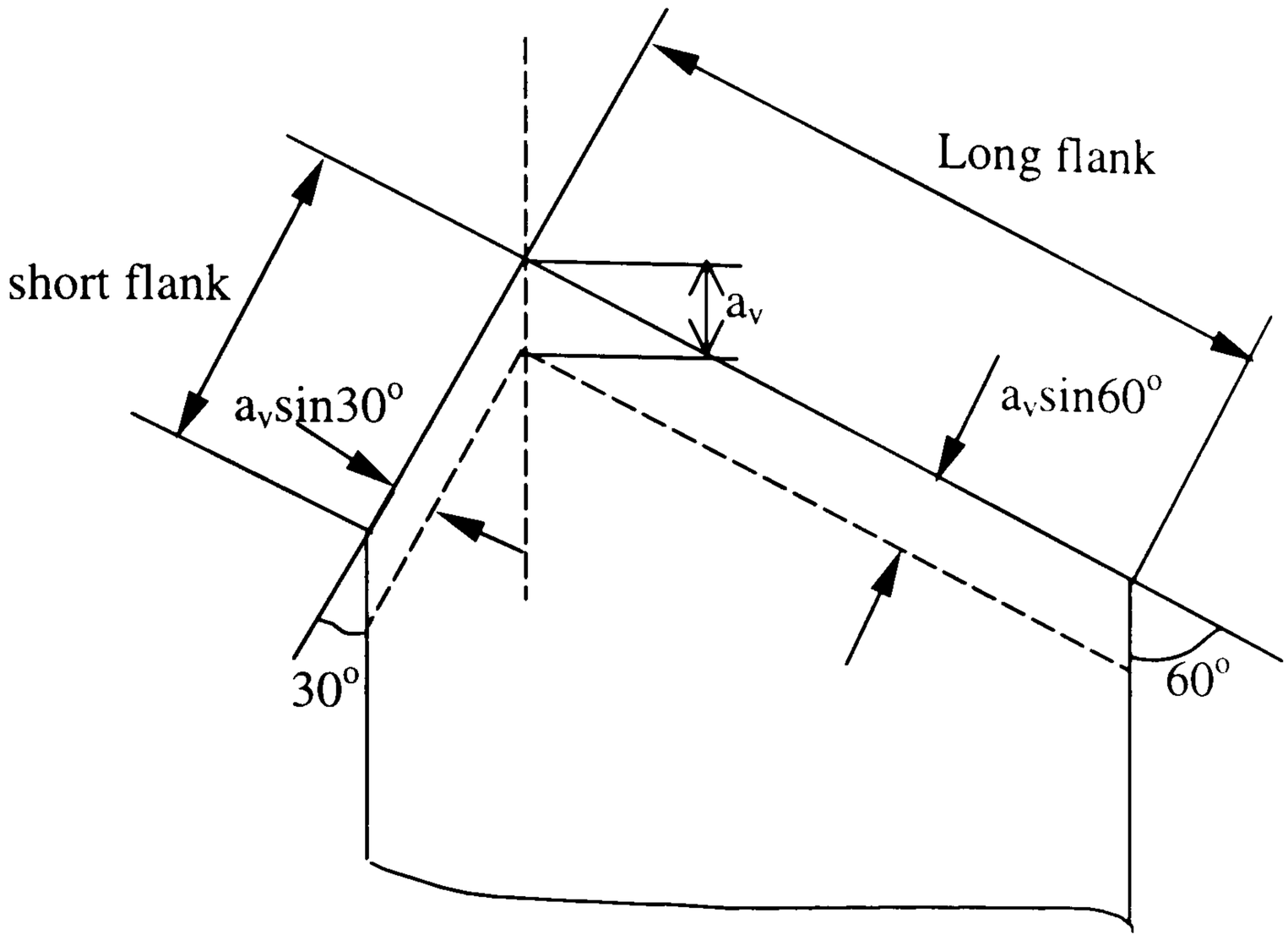

Figure 7.2 The workpiece for the inverted vee form

Model data:

Grinding power:	1000 W
Wheel diameter:	200 mm
Wheel speed:	45 m/s
Workpiece speed:	0.1 m/s
Material:	En31
Depth of cut:	10 μm

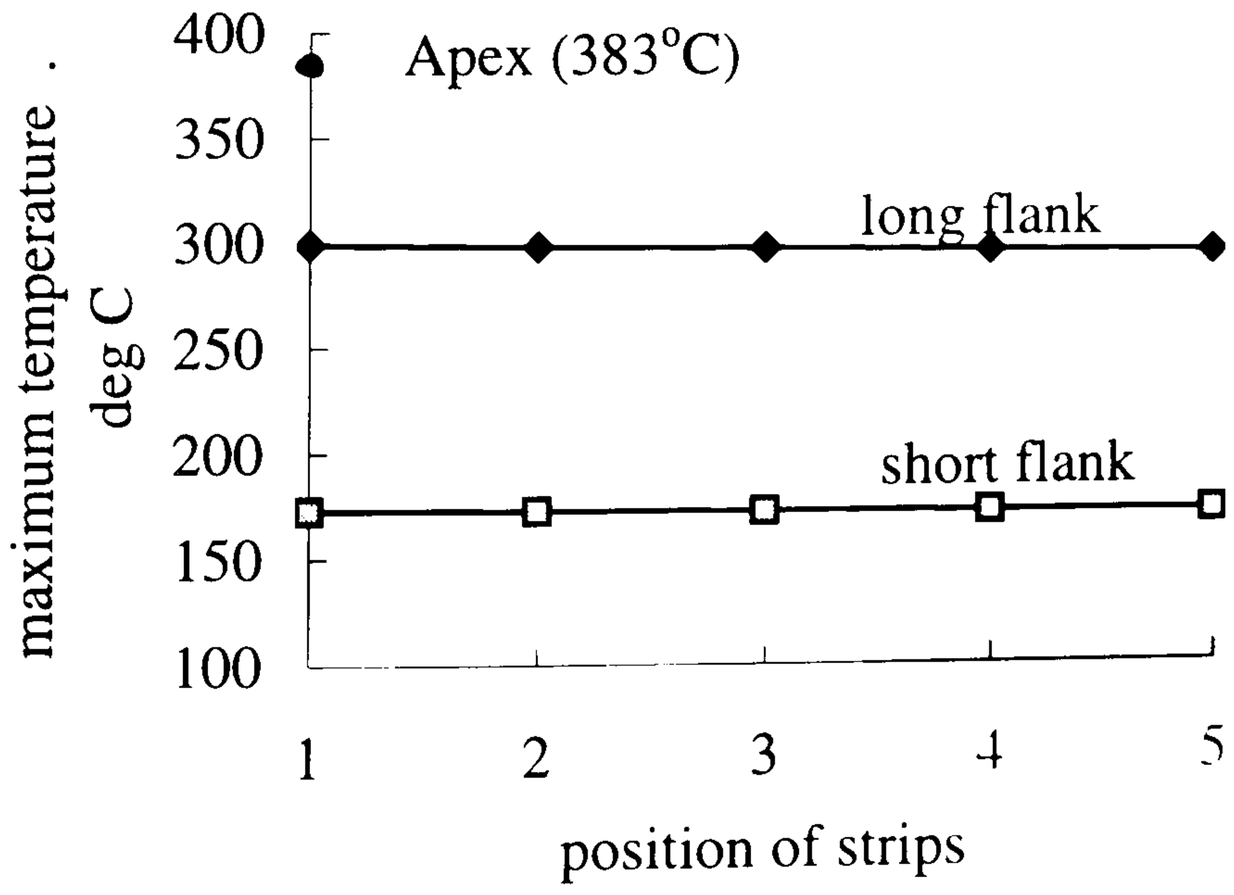

Figure 7.3 Theoretical maximum temperature distribution on the long and short flanks

Experimental data:

Machine	: Abwood (surface grinding)
Material	: En31
Wheel	: 77A601H8VLNAA
Wheel diameter	: 200 mm, max
Wheelspeed	: 46 m/s
Workspeed	: 0.1-0.3 m/s
Workpiece shape	: inverted vee form
Coolant	: dry

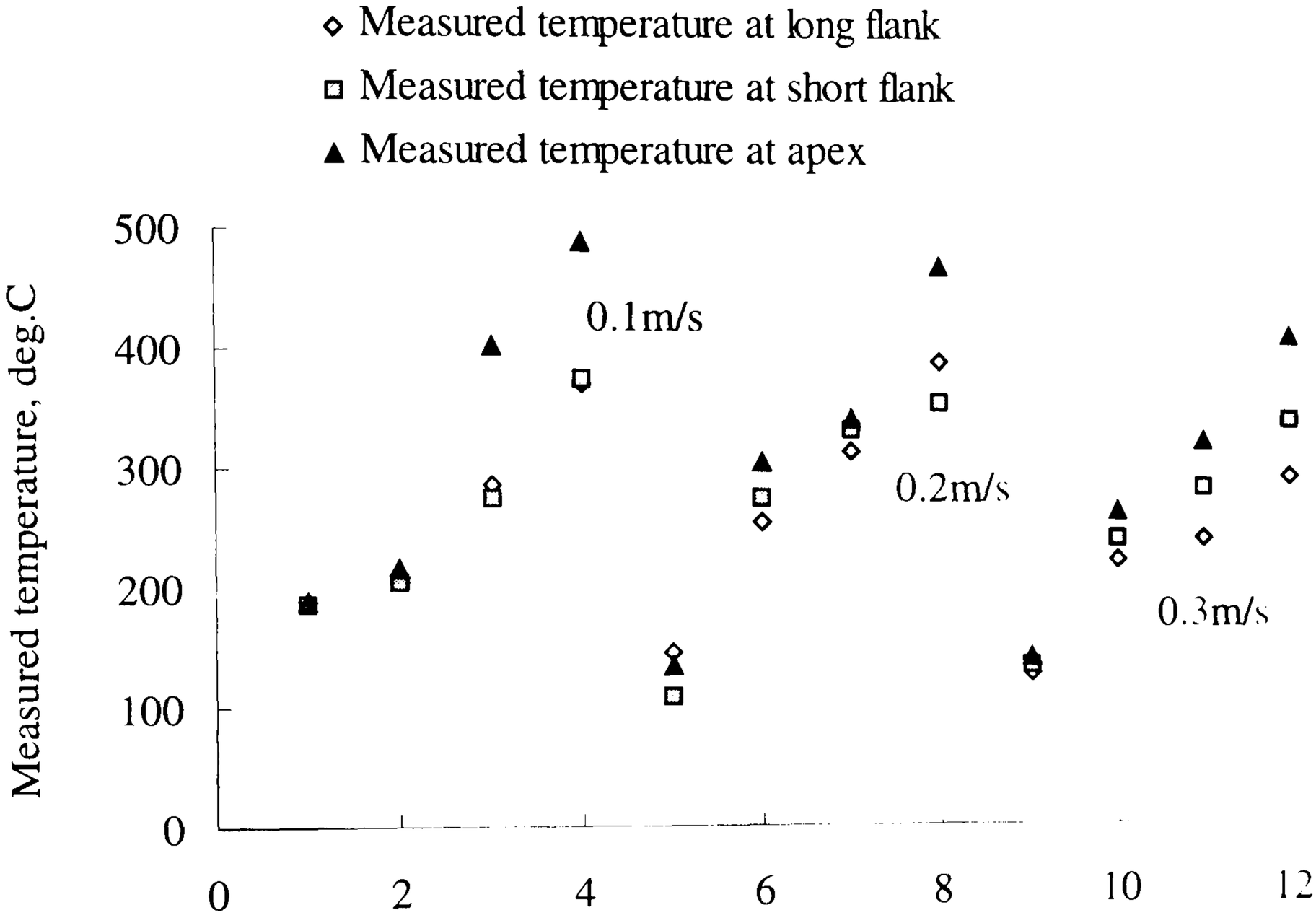

Figure 7.4 Measured temperature at the long flank, short flank and apex of the inverted vee form from experiments without coolant and varying depth of cut

Experimental data:

Machine	: Abwood (surface grinding)
Material	: En31
Wheel	: 77A601H8VLNAA
Wheel diameter	: 200 mm, max
Wheelspeed	: 46 m/s
Workspeed	: 0.1-0.3 m/s
Workpiece shape	: inverted vee form
Coolant	: dry

Model data:

$R_r = 10$ $r_o = 15\ \mu m$

$e_{ch} = 6\ J/mm^3$ $k_{ge} = 45\ W/mK$

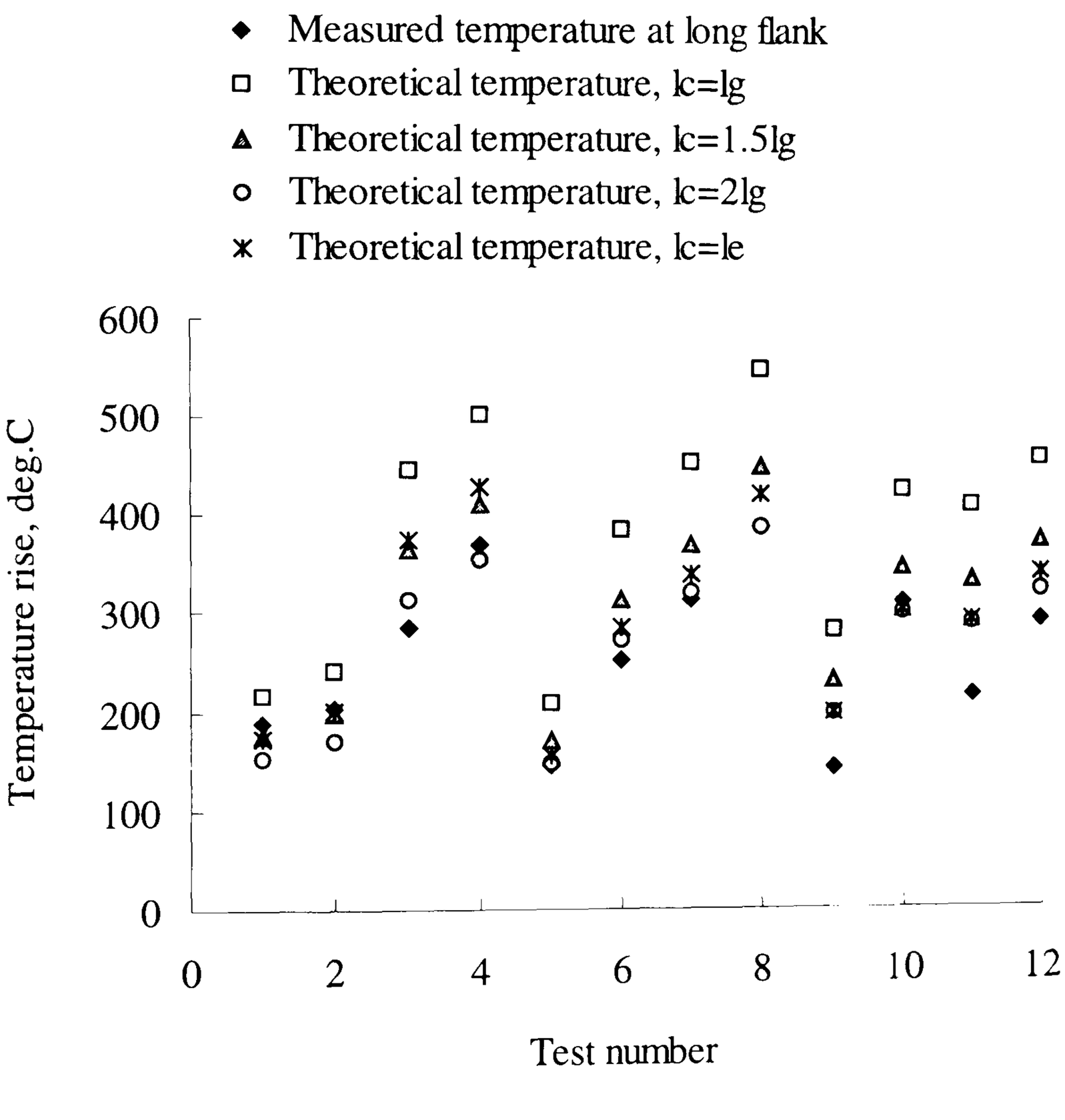

Figure 7.5 A comparison of measured temperature with predictions based on difference in contact lengths at the long flank of the inverted vee form

Experimental data:

Machine	: Abwood (surface grinding)
Material	: En31
Wheel	: 77A601H8VLNAA
Wheel diameter	: 200 mm, max
Wheelspeed	: 46 m/s
Workspeed	: 0.1-0.3 m/s
Workpiece shape	: inverted vee form
Coolant	: dry

Model data:

$R_r = 10$ $r_o = 15\ \mu m$

$e_{ch} = 6\ J/mm^3$ $k_{ge} = 45\ W/mK$

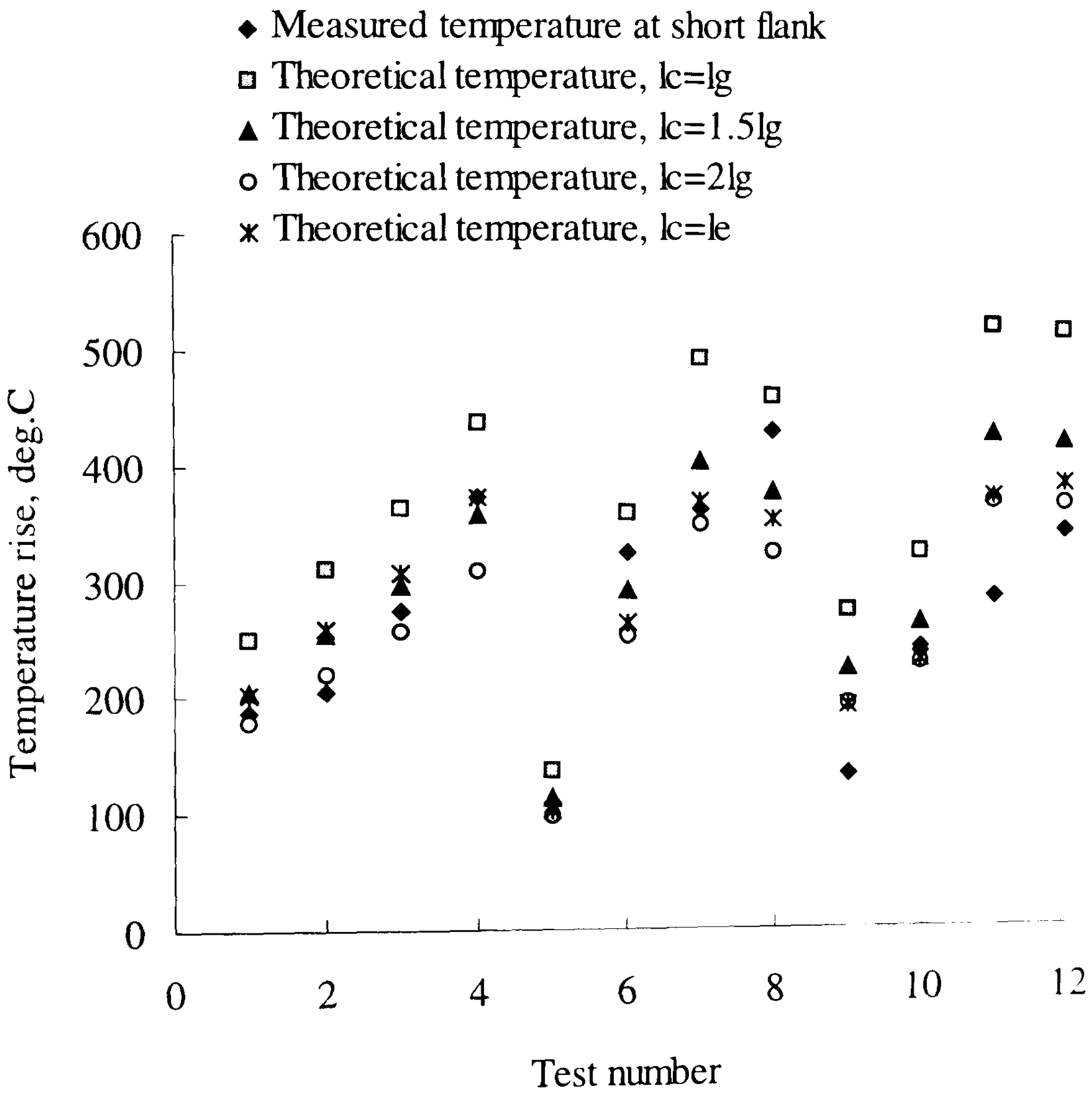

Figure 7.6 A comparison of measured temperature with predictions based on difference in contact lengths at the short flank of the inverted vee form

Experimental data:

Machine	: Abwood (surface grinding)
Material	: En31
Wheel	: 77A601H8VLNAA
Wheel diameter	: 200 mm, max
Wheelspeed	: 46 m/s
Workspeed	: 0.1-0.3 m/s
Workpiece shape	: inverted vee form
Coolant	: dry

Model data:

$R_r = 10$ $r_o = 15\ \mu m$

$e_{ch} = 6\ J/mm^3$ $k_{ge} = 45\ W/mK$

$sh_f = n$

◆ Measured temperature at apex
□ Theoretical temperature, lc=lg
△ Theoretical temperature, lc=1.5lg
○ Theoretical temperature, lc=2lg
✱ Theoretical temperature, lc=le

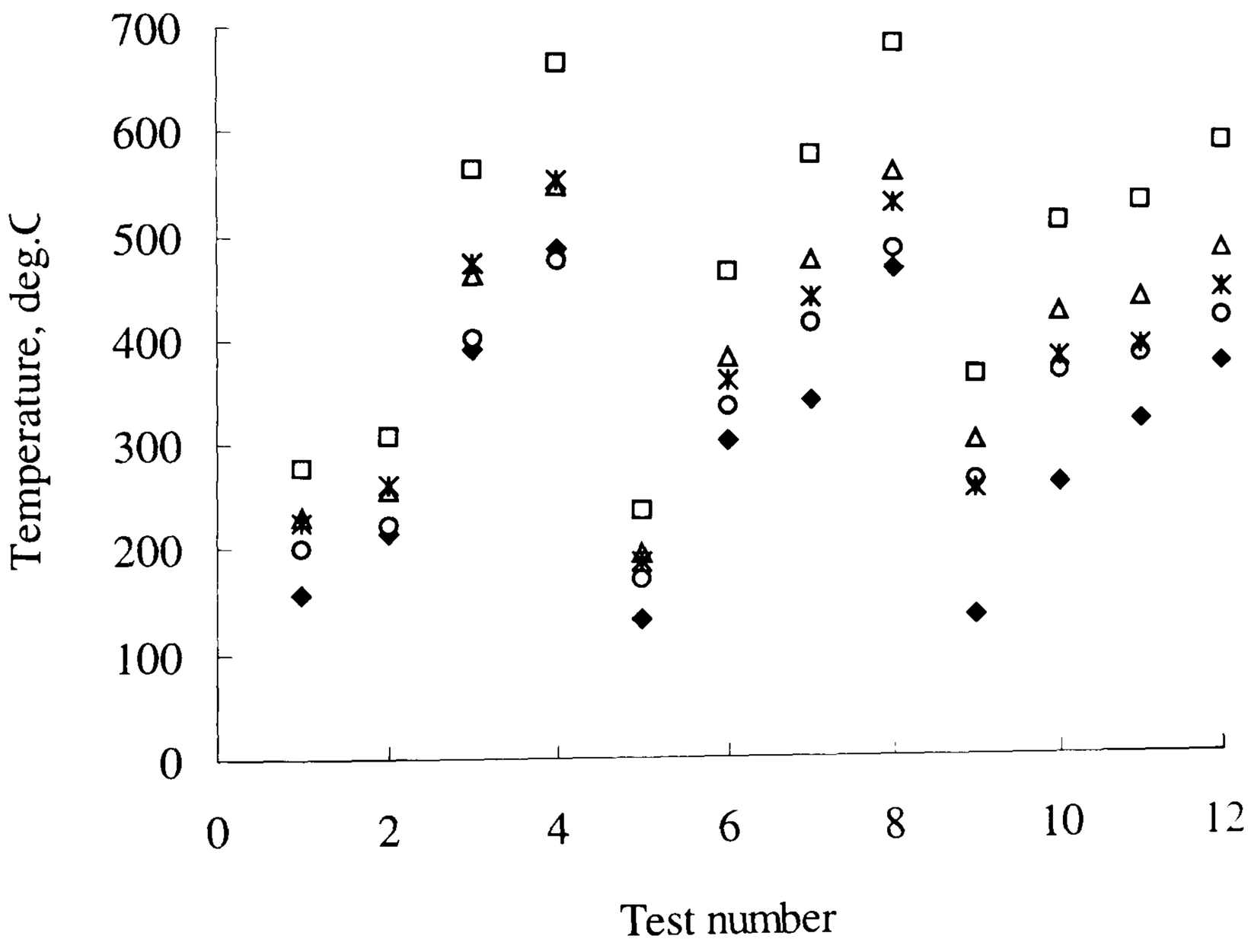

Figure 7.7 A comparison of measured temperature with predictions based on difference in contact lengths at the apex of the inverted vee form

Experimental data:

Machine	: Abwood (surface grinding)
Material	: En31
Wheel	: 77A601H8VLNAA
Wheel diameter	: 200 mm, max
Wheelspeed	: 46 m/s
Workspeed	: 0.1-0.3 m/s
Workpiece shape	: inverted vee form
Coolant	: dry

Model data:

$R_r = 10$ $r_o = 15\ \mu m$

$e_{ch} = 6\ J/mm^3$ $k_{ge} = 45\ W/mK$

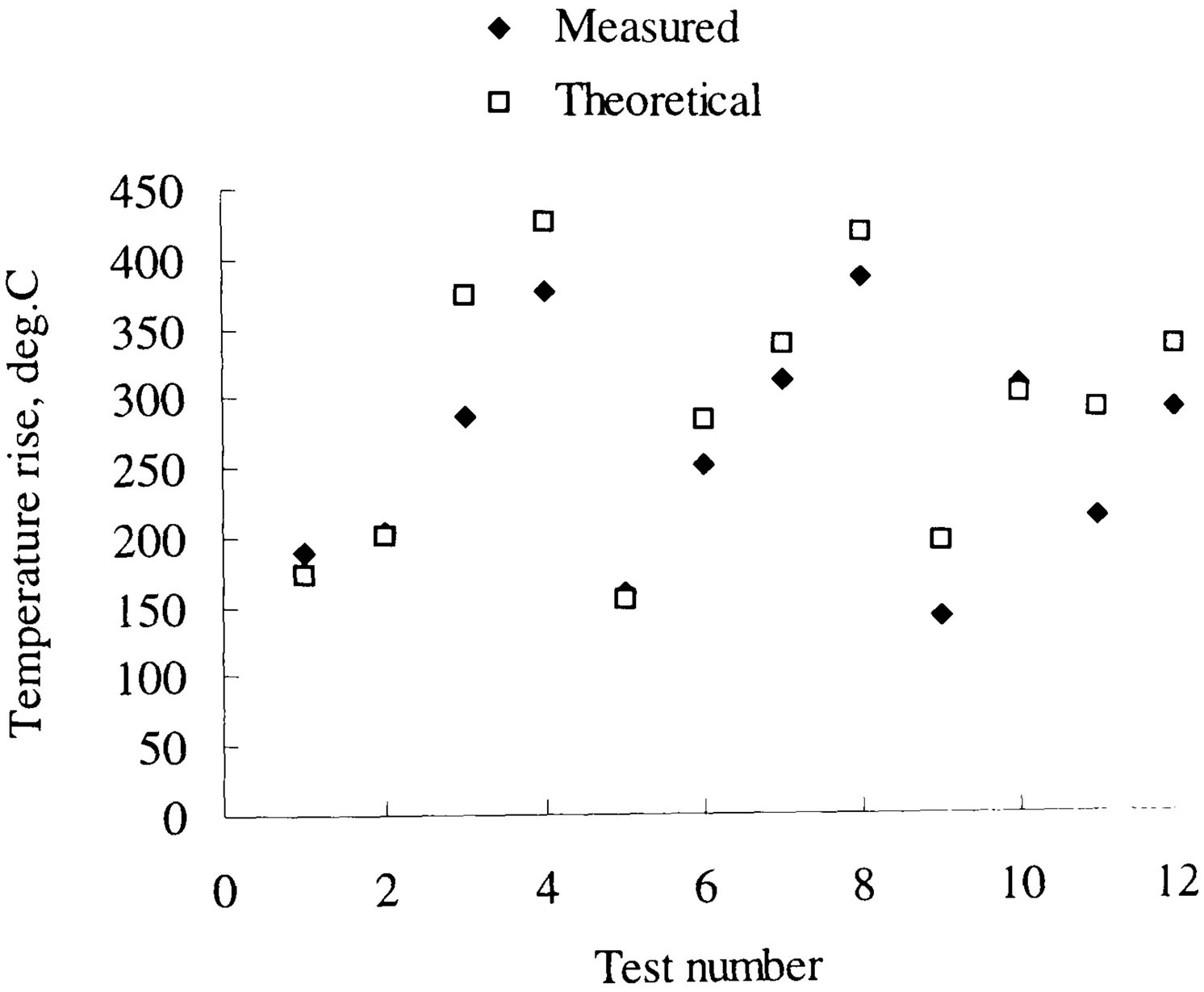

Figure 7.8 A comparison of measured and theoretical temperature using the real contact length model on the long flank of the inverted vee form in dry grinding

Experimental data:

Machine	: Abwood (surface grinding)
Material	: En31
Wheel	: 77A601H8VLNAA
Wheel diameter	: 200 mm, max
Wheelspeed	: 46 m/s
Workspeed	: 0.1-0.3 m/s
Workpiece shape	: inverted vee form
Coolant	: dry

Model data:

$R_r = 10$ $r_o = 15\ \mu m$

$e_{ch} = 6\ J/mm^3$ $k_{ge} = 45\ W/mK$

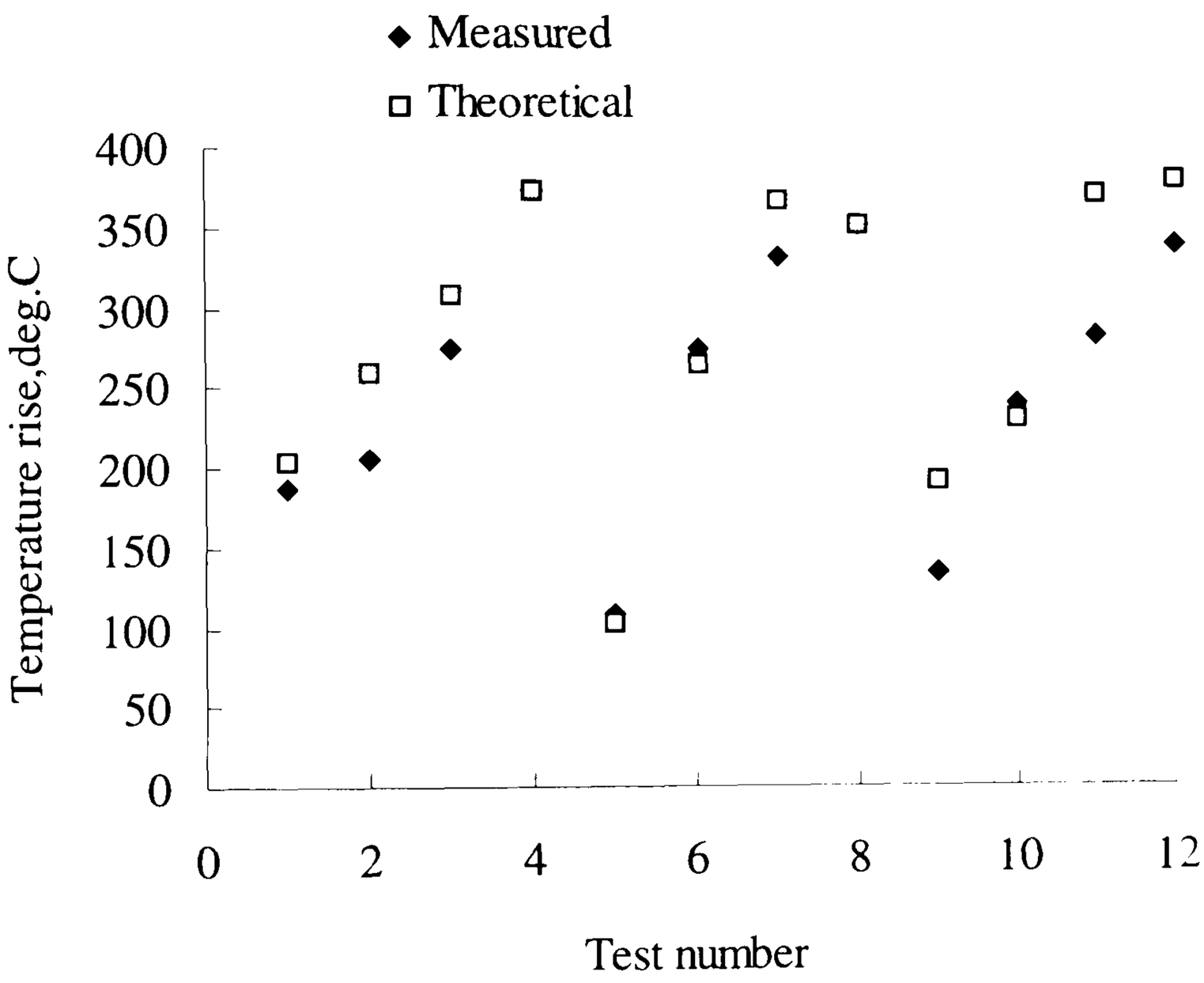

Figure 7.9 A comparison of measured and theoretical temperature using the real contact length model on the short flank of the inverted vee form in dry grinding

Experimental data:

Machine	: Abwood (surface grinding)
Material	: En31
Wheel	: 77A601H8VLNAA
Wheel diameter	: 200 mm, max
Wheelspeed	: 46 m/s
Workspeed	: 0.1-0.3 m/s
Workpiece shape	: inverted vee form
Coolant	: dry

Model data:

$R_r = 10$ $r_o = 15\ \mu m$

$e_{ch} = 6\ J/mm^3$ $k_{ge} = 45\ W/mK$

$sh_f = n$

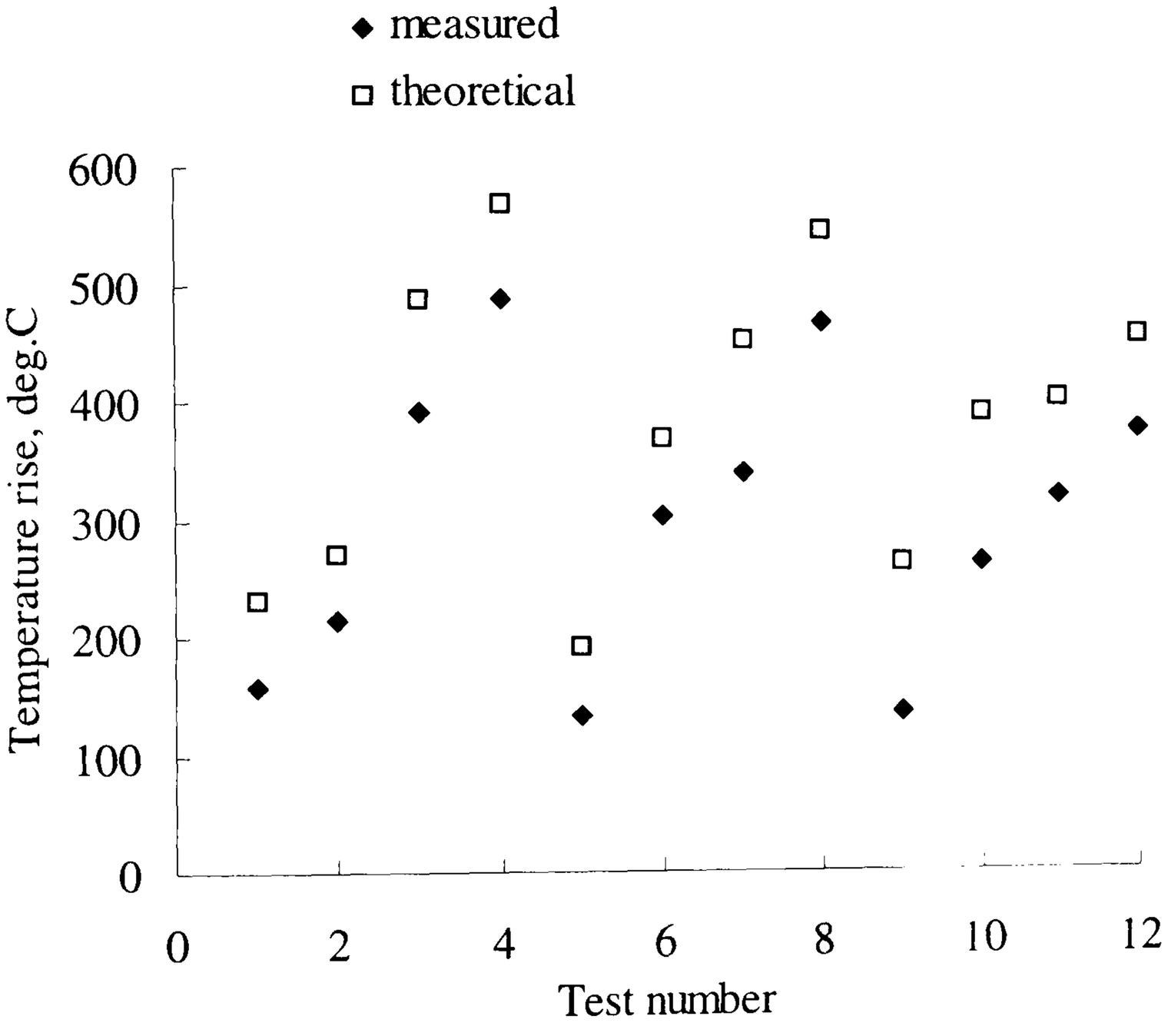

Figure 7.10 A comparison of measured and theoretical temperature using the real contact length model on the apex of the inverted vee form in dry grinding

Experimental data:

Machine	: Abwood (surface grinding)
Material	: En31
Wheel	: 77A601H8VLNAA
Wheel diameter	: 200 mm, max
Wheelspeed	: 46 m/s
Workspeed	: 0.1m/s
Workpiece shape	: inverted vee form
Coolant	: dry

Model data:

$R_r = 10$ $r_o = 15\ \mu m$

$e_{ch} = 6\ J/mm^3$ $k_{ge} = 45\ W/mK$

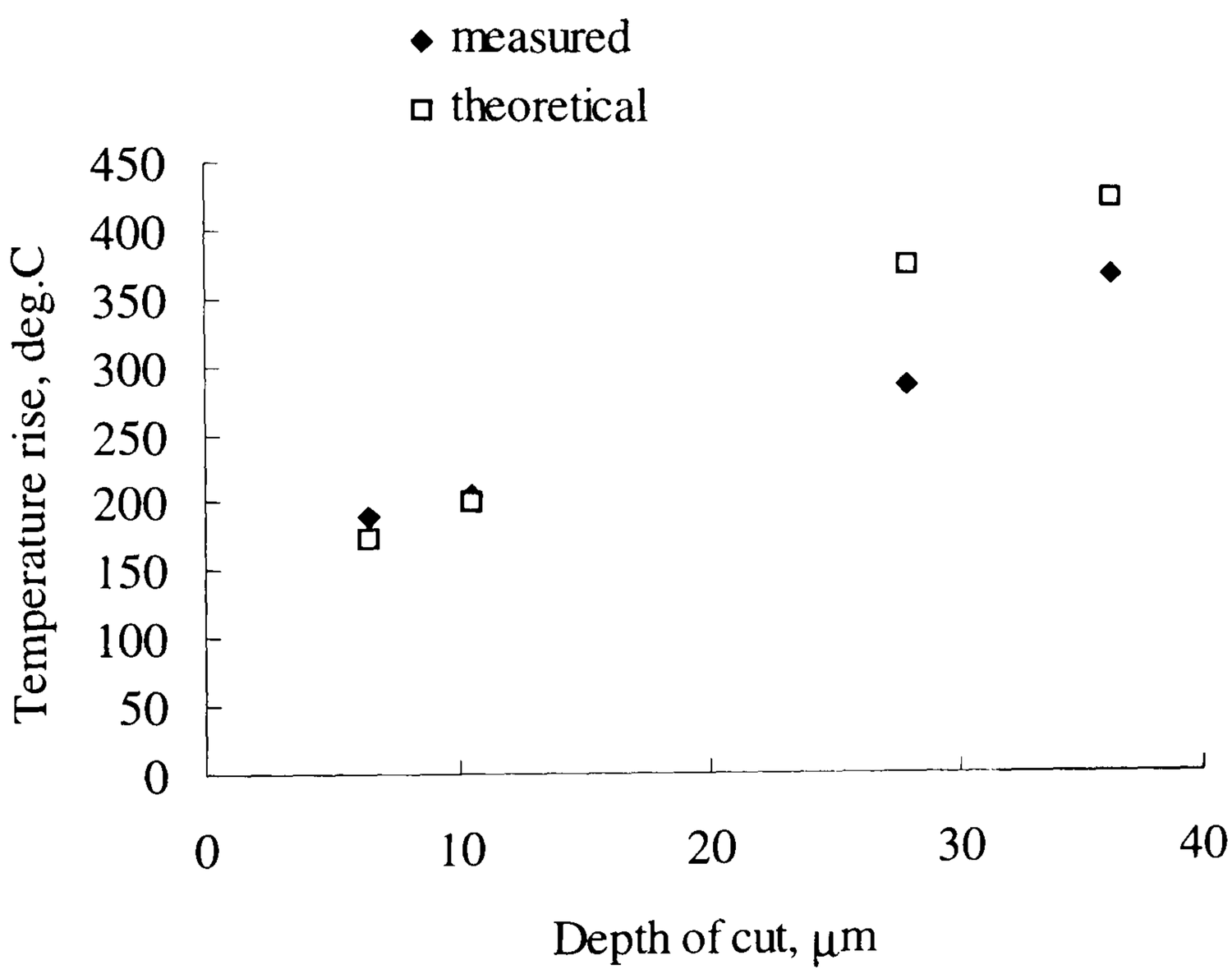

Figure 7.11 A comparison of measured temperature with predicted temperature against depth of cut at 0.1 m/s workspeed on the long flank of the inverted vee

Experimental data:

Machine	: Abwood (surface grinding)
Material	: En31
Wheel	: 77A601H8VLNAA
Wheel diameter	: 200 mm, max
Wheelspeed	: 46 m/s
Workspeed	: 0.2 m/s
Workpiece shape	: inverted vee form
Coolant	: dry

Model data:

$R_r = 10$ $r_o = 15\ \mu m$

$e_{ch} = 6\ J/mm^3$ $k_{ge} = 45\ W/mK$

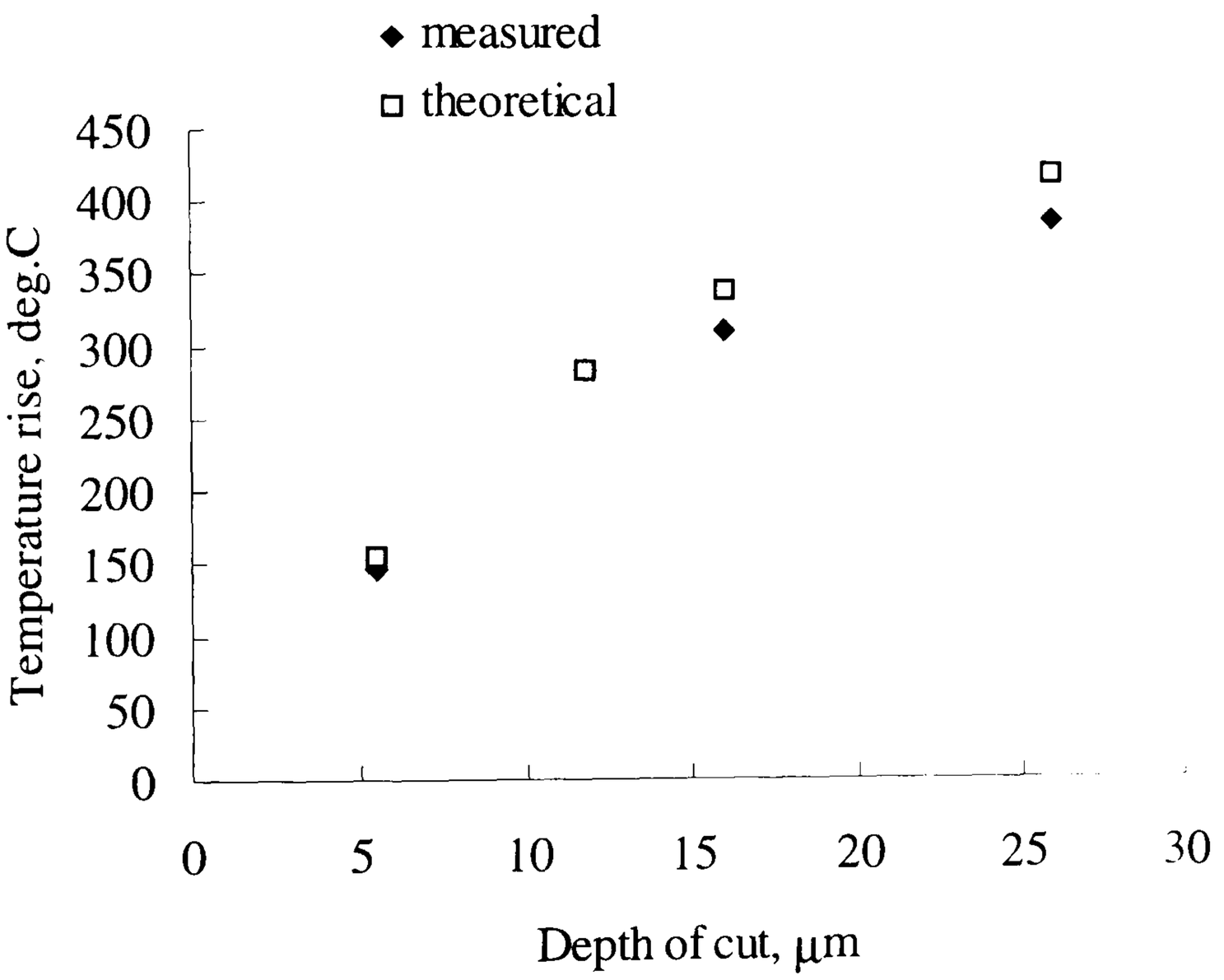

Figure 7.12 A comparison of measured temperature with predicted temperature against depth of cut at 0.2 m/s workspeed on the long flank of the inverted vee

Experimental data:

Machine	: Abwood (surface grinding)
Material	: En31
Wheel	: 77A601H8VLNAA
Wheel diameter	: 200 mm, max
Wheelspeed	: 46 m/s
Workspeed	: 0.3 m/s
Workpiece shape	: inverted vee form
Coolant	: dry

Model data:

$R_r = 10$ $r_o = 15\ \mu m$

$e_{ch} = 6\ J/mm^3$ $k_{ge} = 45\ W/mK$

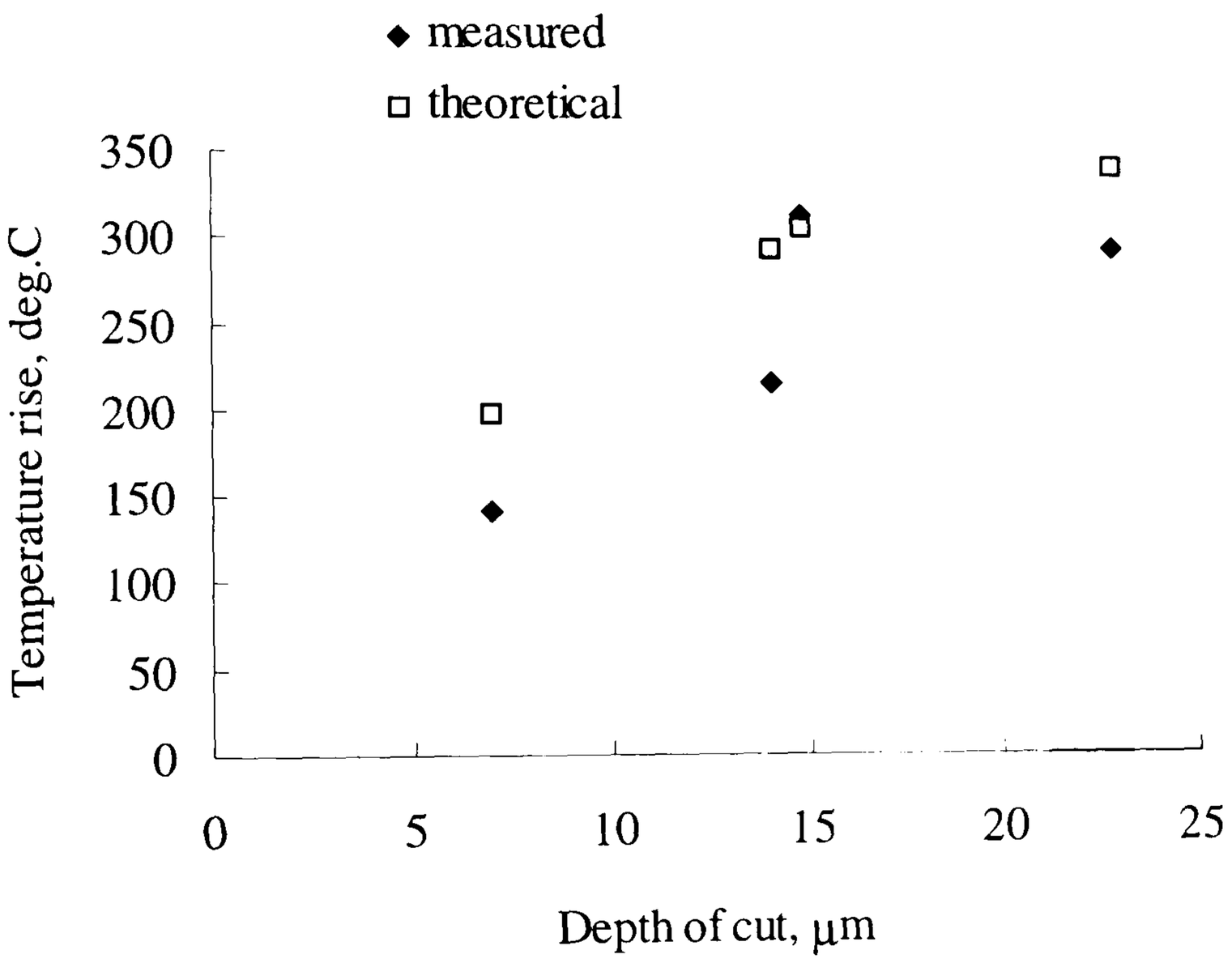

Figure 7.13 A comparison of measured temperature with predicted temperature against depth of cut at workspeed of 0.3 m/s on the long flank of the inverted vee

Experimental data:

Machine	: Abwood (surface grinding)
Material	: En31
Wheel	: 77A601H8VLNAA
Wheel diameter	: 200 mm, max
Wheelspeed	: 46 m/s
Workspeed	: 0.1 m/s
Workpiece shape	: inverted vee form
Coolant	: dry

Model data:

$R_r = 10$ $r_o = 15\ \mu m$

$e_{ch} = 6\ J/mm^3$ $k_{ge} = 45\ W/mK$

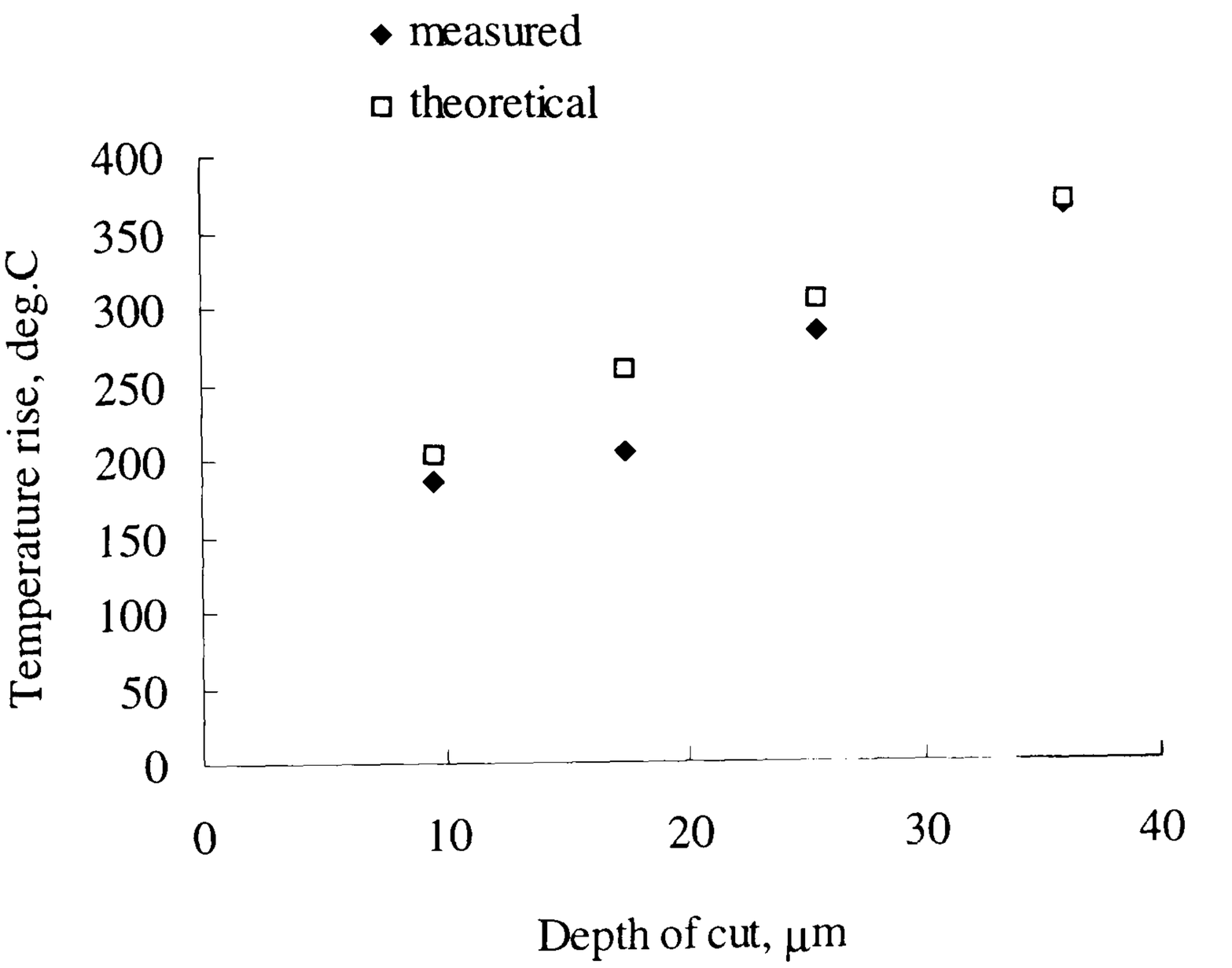

Figure 7.14 A comparison of measured temperature with predicted temperature against depth of cut at workspeed of 0.1 m/s on the short flank of the inverted vee

Experimental data:

Machine	: Abwood (surface grinding)
Material	: En31
Wheel	: 77A601H8VLNAA
Wheel diameter	: 200 mm. max
Wheelspeed	: 46 m/s
Workspeed	: 0.2 m/s
Workpiece shape	: inverted vee form
Coolant	: dry

Model data:

$R_r = 10$ $r_o = 15\ \mu m$

$e_{ch} = 6\ J/mm^3$ $k_{ge} = 45\ W/mK$

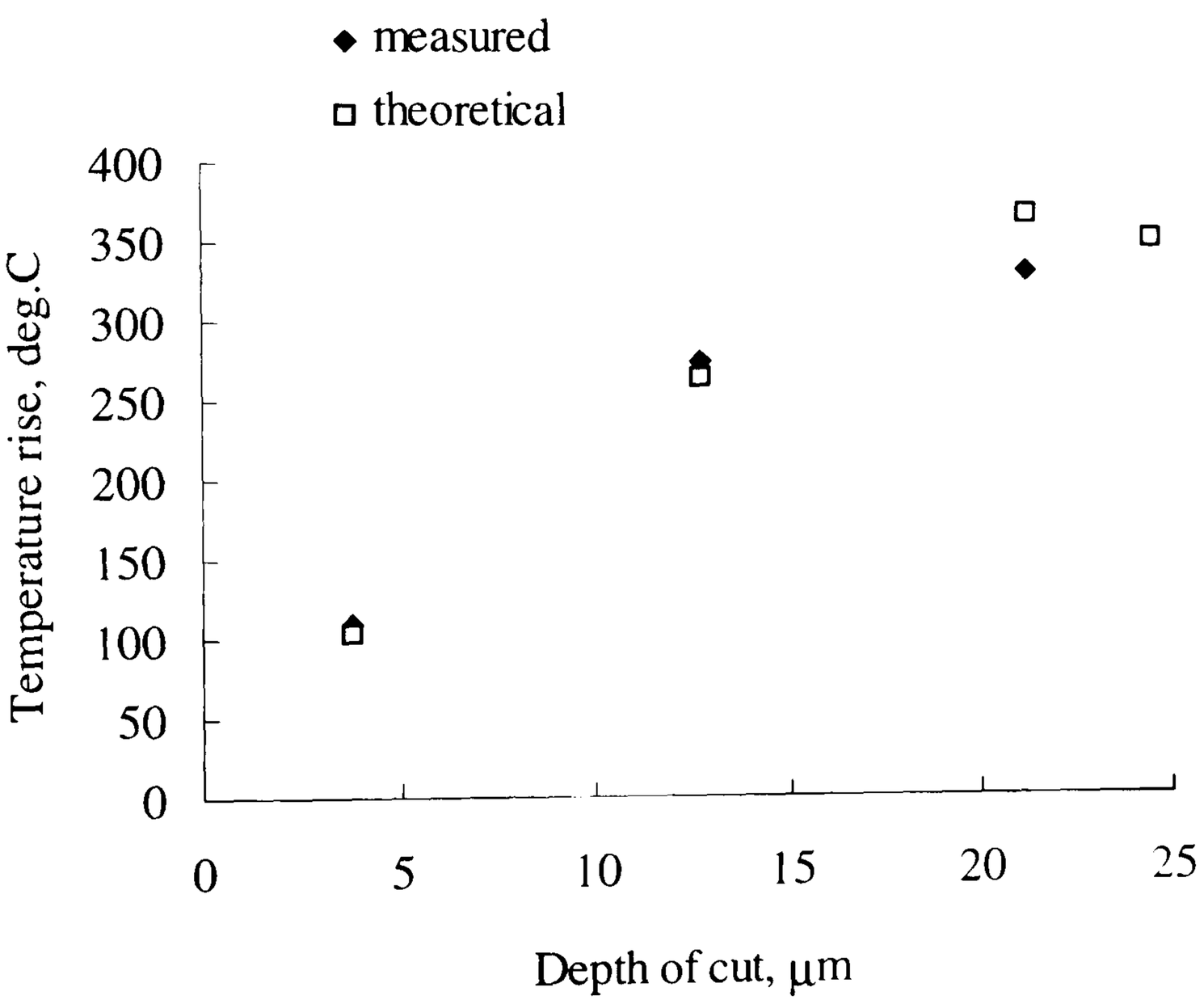

Figure 7.15 A comparison of measured temperature with predicted temperature against depth of cut at 0.2 m/s workspeed on the short flank of the inverted vee

Experimental data:

Machine	: Abwood (surface grinding)
Material	: En31
Wheel	: 77A601H8VLNAA
Wheel diameter	: 200 mm, max
Wheelspeed	: 46 m/s
Workspeed	: 0.3 m/s
Workpiece shape	: inverted vee form
Coolant	: dry

Model data:

$R_r = 10$ $r_o = 15\ \mu m$

$e_{ch} = 6\ J/mm^3$ $k_{ge} = 45\ W/mK$

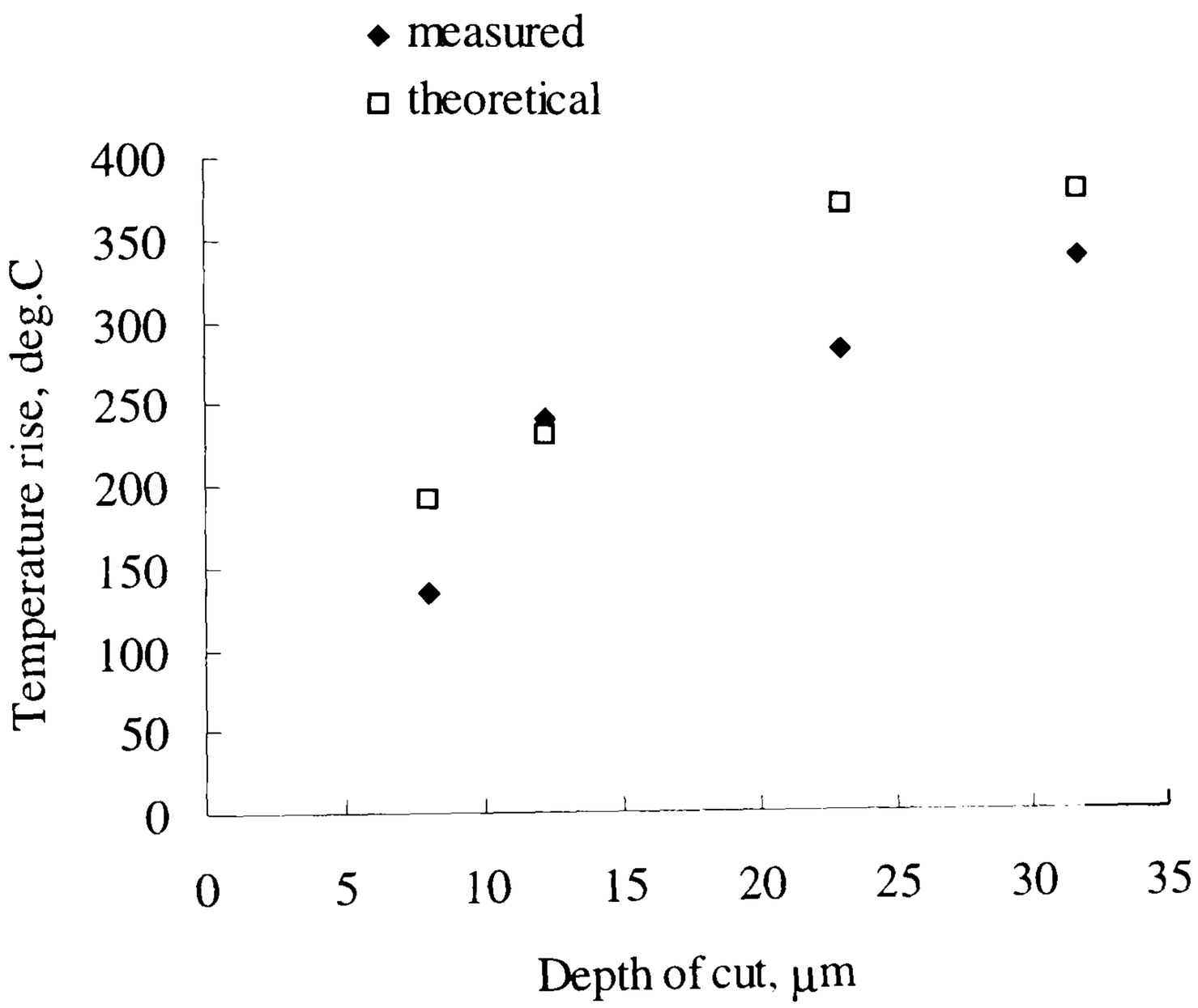

Figure 7.16 A comparison of measured temperature with predicted temperature against depth of cut at 0.3 m/s workspeed on the short flank of the inverted vee

Experimental data:

Machine	: Abwood (surface grinding)
Material	: En31
Wheel	: 77A601H8VLNAA
Wheel diameter	: 200 mm, max
Wheelspeed	: 46 m/s
Workspeed	: 0.1 m/s
Workpiece shape	: inverted vee form
Coolant	: dry

Model data:

$R_r = 10$ $r_o = 15\ \mu m$

$e_{ch} = 6\ J/mm^3$ $k_{ge} = 45\ W/mK$

$sh_f = n$

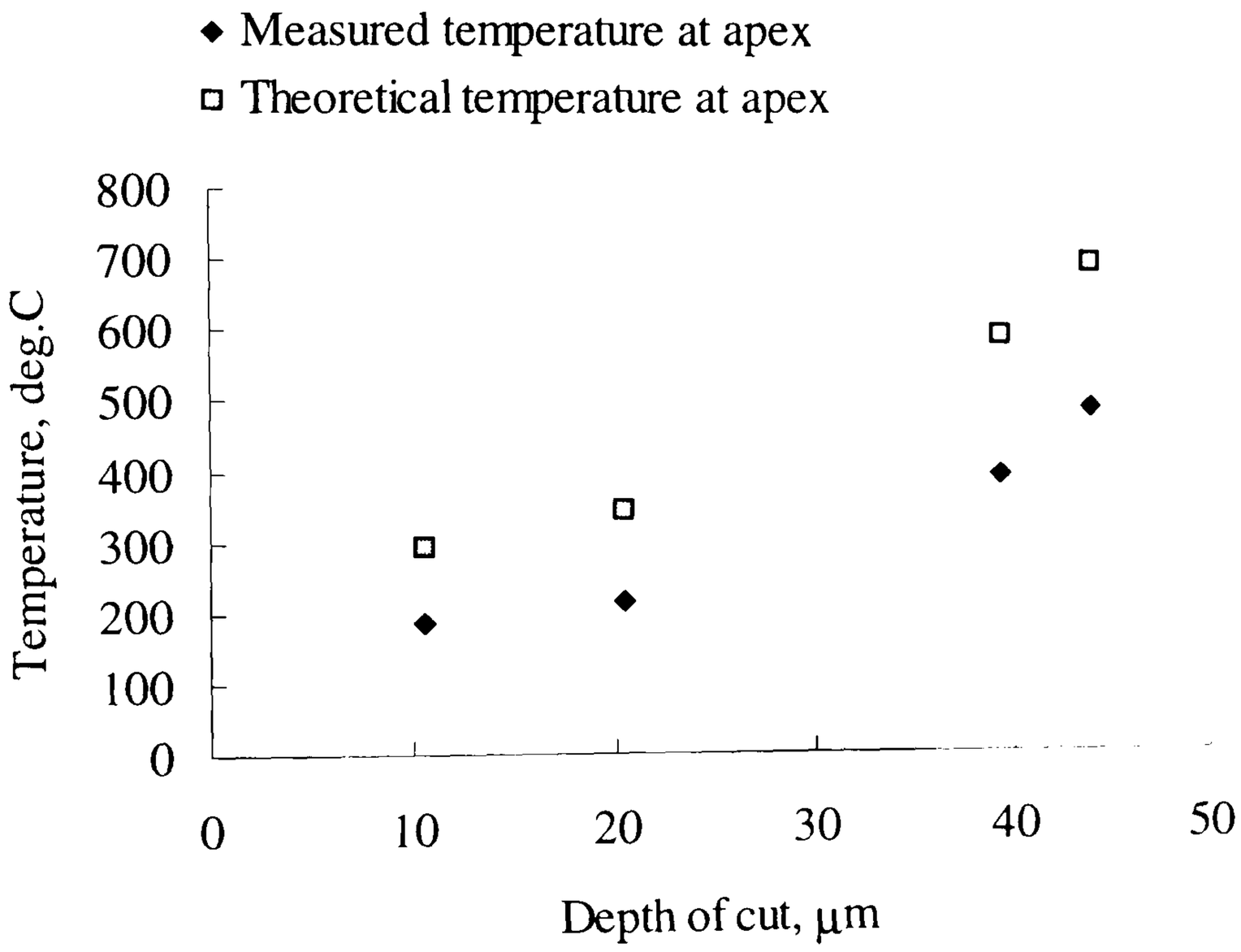

Figure 7.17 A comparison of measured temperature with predicted temperature against depth of cut at 0.1 m/s workspeed on the apex of the inverted vee

Experimental data:

Machine	: Abwood (surface grinding)
Material	: En31
Wheel	: 77A601H8VLNAA
Wheel diameter	: 200 mm. max
Wheelspeed	: 46 m/s
Workspeed	: 0.2 m/s
Workpiece shape	: inverted vee form
Coolant	: dry

Model data:

$R_r = 10$ $r_o = 15\ \mu m$

$e_{ch} = 6\ J/mm^3$ $k_{ge} = 45\ W/mK$

$sh_f = n$

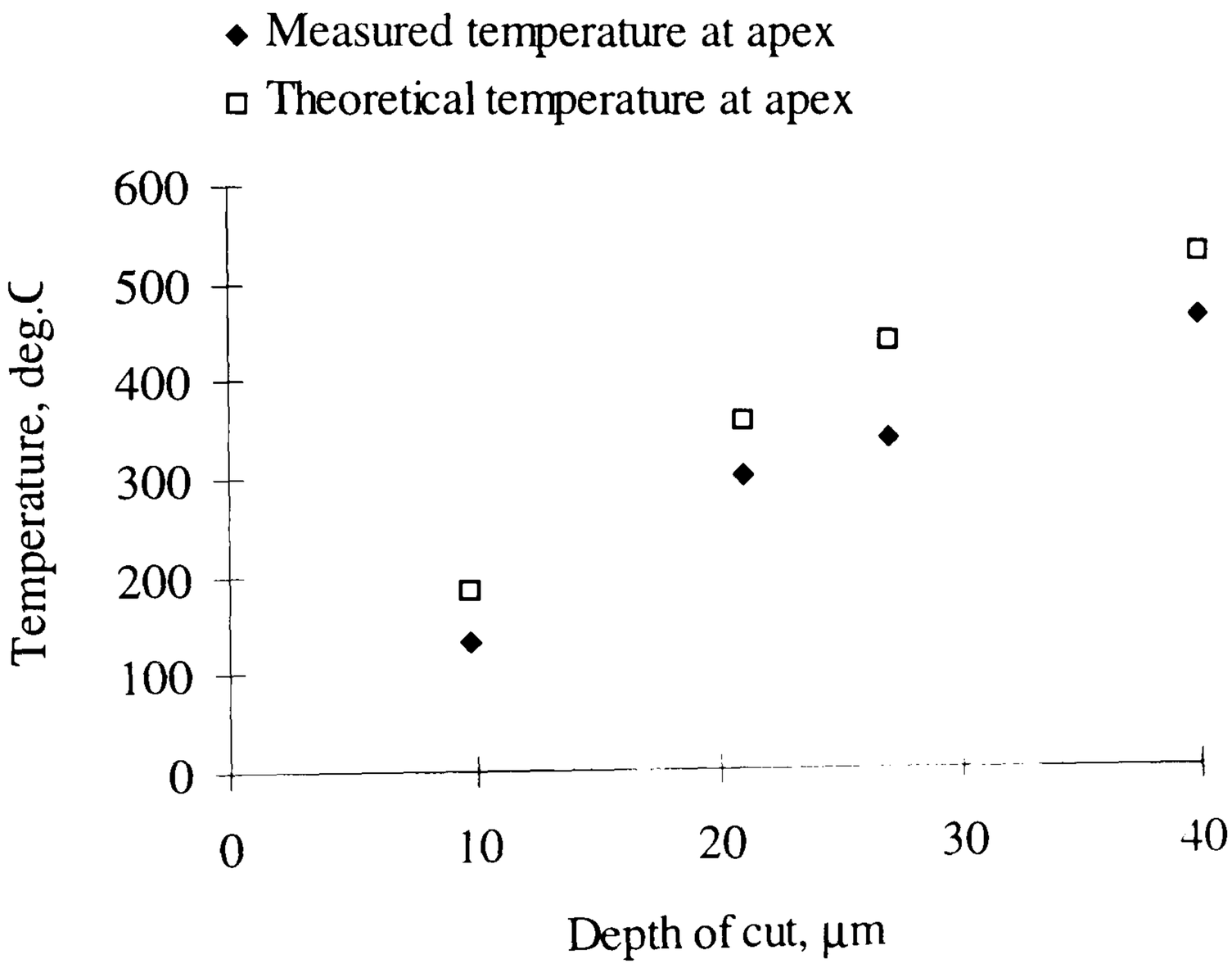

Figure 7.18 A comparison of measured temperature with predicted temperature against depth of cut at 0.2 m/s workspeed on the apex of the inverted vee

Experimental data:

Machine	: Abwood (surface grinding)
Material	: En31
Wheel	: 77A601H8VLNAA
Wheel diameter	: 200 mm, max
Wheelspeed	: 46 m/s
Workspeed	: 0.3 m/s
Workpiece shape	: inverted vee form
Coolant	: dry

Model data:

$R_r = 10$ $r_o = 15\ \mu m$

$e_{ch} = 6\ J/mm^3$ $k_{ge} = 45\ W/mK$

$sh_f = n$

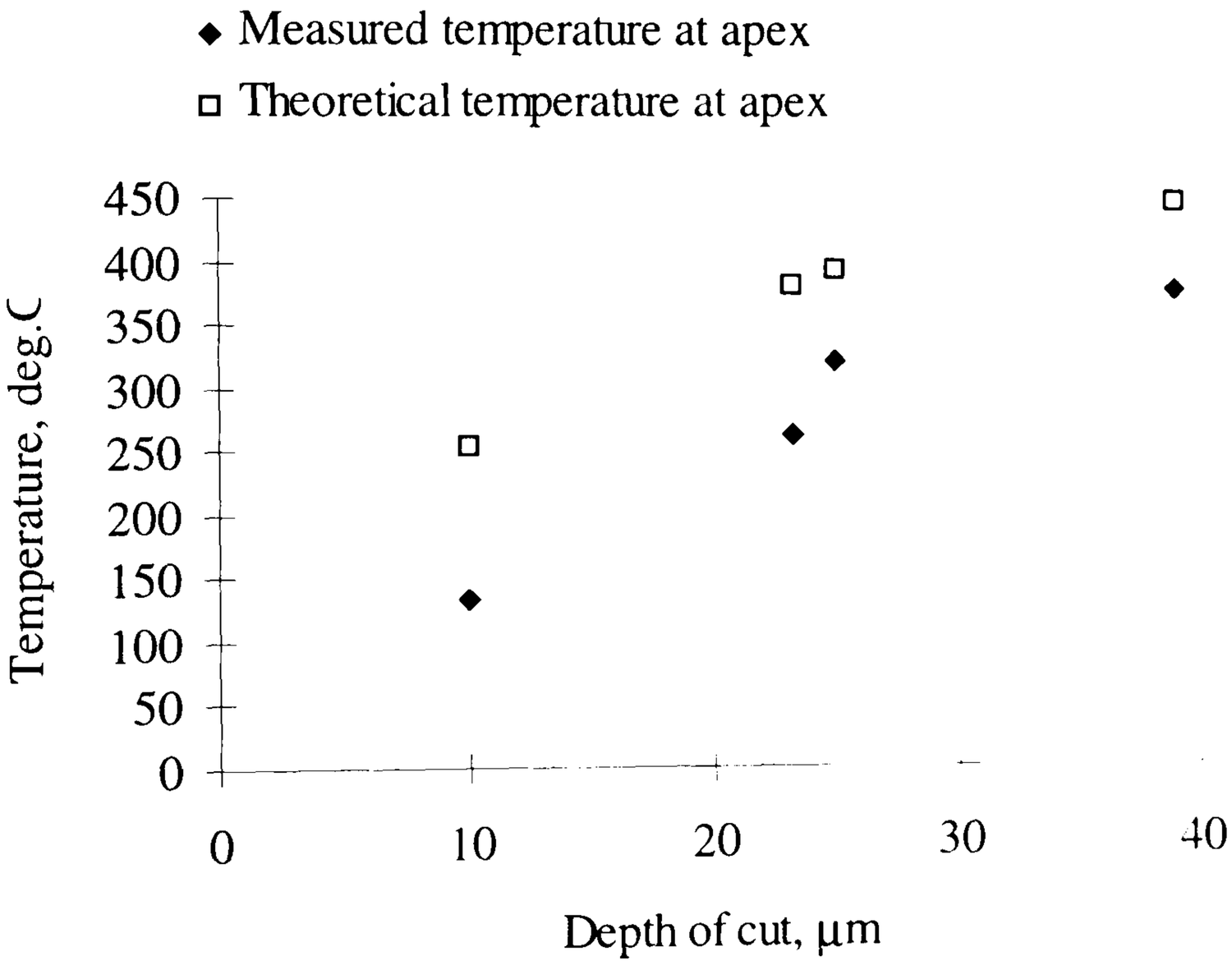

Figure 7.19 A comparison of measured temperature with predicted temperature against depth of cut at 0.3 m/s workspeed on the apex of the inverted vee

Experimental data:

Machine	: Abwood (surface grinding)
Material	: En31
Wheel	: 77A601H8VLNAA
Wheel diameter	: 200 mm, max.
Wheelspeed	: 46 m/s
Workspeed	: 0.1 - 0.3 m/s
Workpiece shape	: inverted vee form
Coolant	: dry

Model data:

$R_r = 10$ $r_o = 15\ \mu m$

$e_{ch} = 6\ J/mm^3$ $k_{ge} = 45\ W/mK$

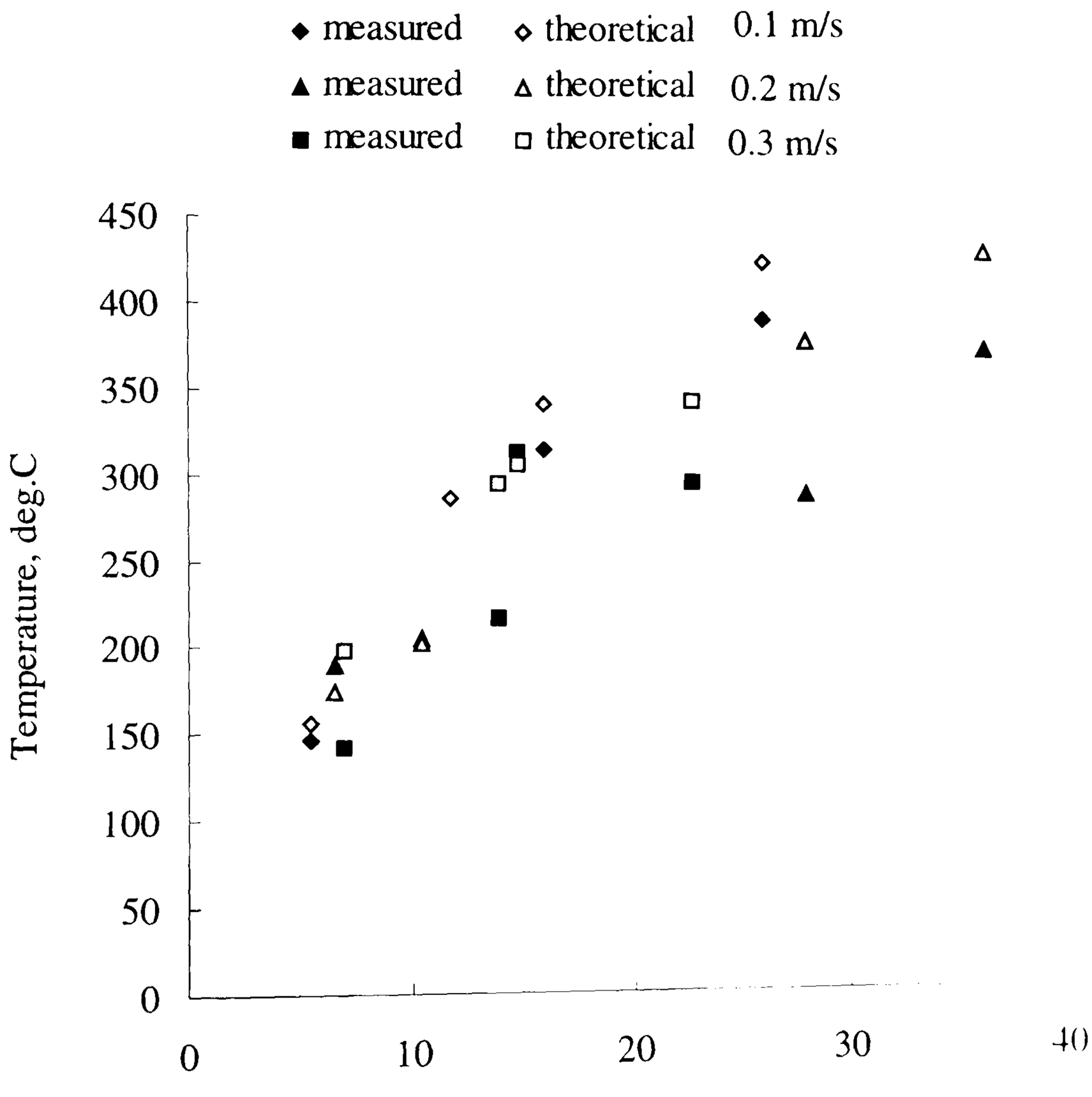

Figure 7.20 Comparison of measured and predicted temperature against depth of cut for different workpiece speeds at the long flank of the inverted vee form in dry grinding

Experimental data:

Machine	: Abwood (surface grinding)
Material	: En31
Wheel	: 77A601H8VLNAA
Wheel diameter	: 200 mm, max
Wheelspeed	: 46 m/s
Workspeed	: 0.1 - 0.3 m/s
Workpiece shape	: inverted vee form
Coolant	: dry

Model data:

$R_r = 10$ $r_o = 15\ \mu m$

$e_{ch} = 6\ J/mm^3$ $k_{ge} = 45\ W/mK$

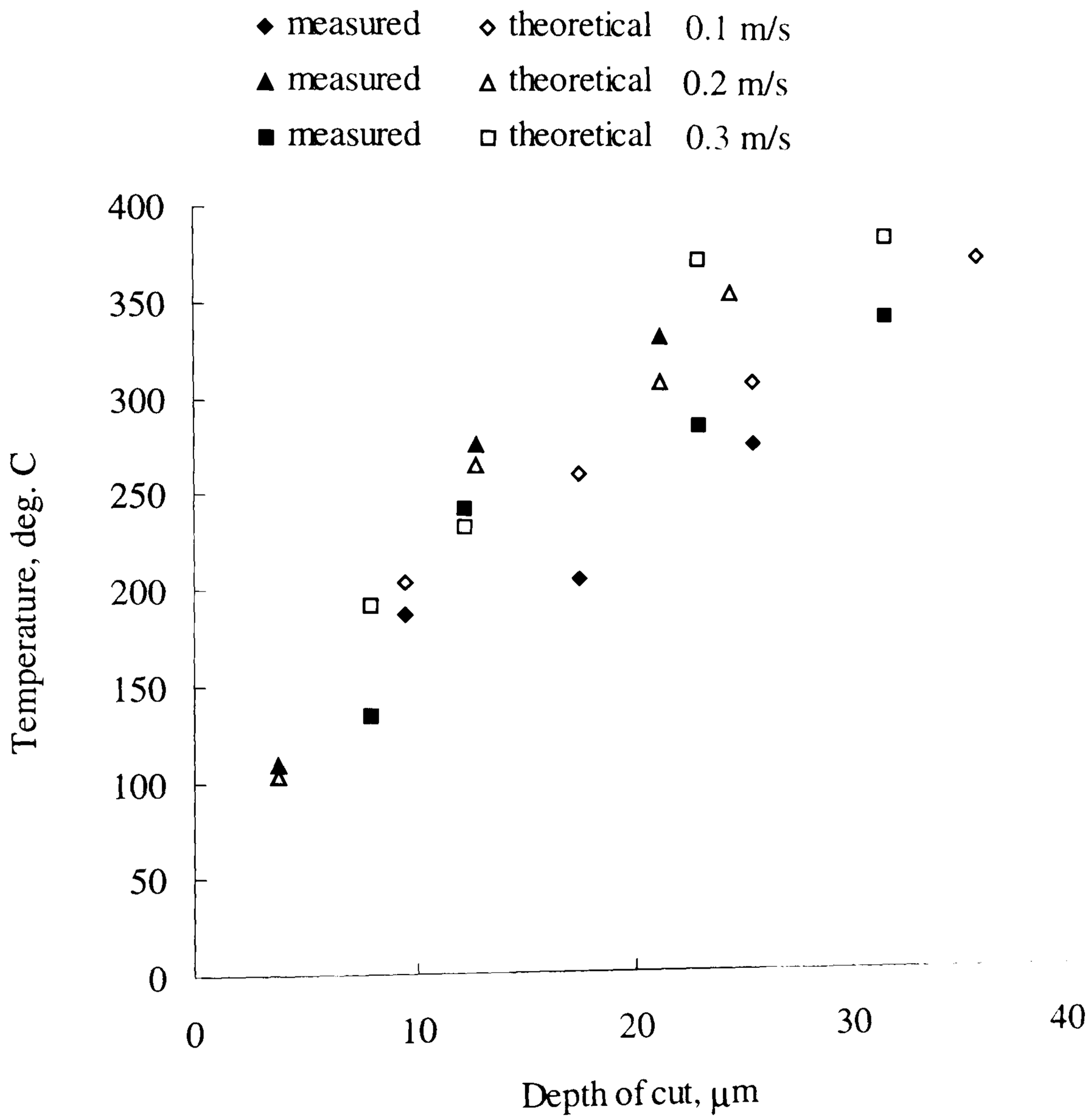

Figure 7.21 Comparison of measured and predicted temperature against depth of cut for different workpiece speeds at the short flank of the inverted vee form in dry grinding

Experimental data:

Machine	: Abwood (surface grinding)
Material	: En31
Wheel	: 77A601H8VLNAA
Wheel diameter	: 200 mm, max
Wheelspeed	: 46 m/s
Workspeed	: 0.1 - 0.3 m/s
Workpiece shape	: inverted vee form
Coolant	: dry

Model data:

$R_r = 10$ $r_o = 15\ \mu m$

$e_{ch} = 6\ J/mm^3$ $k_{ge} = 45\ W/mK$

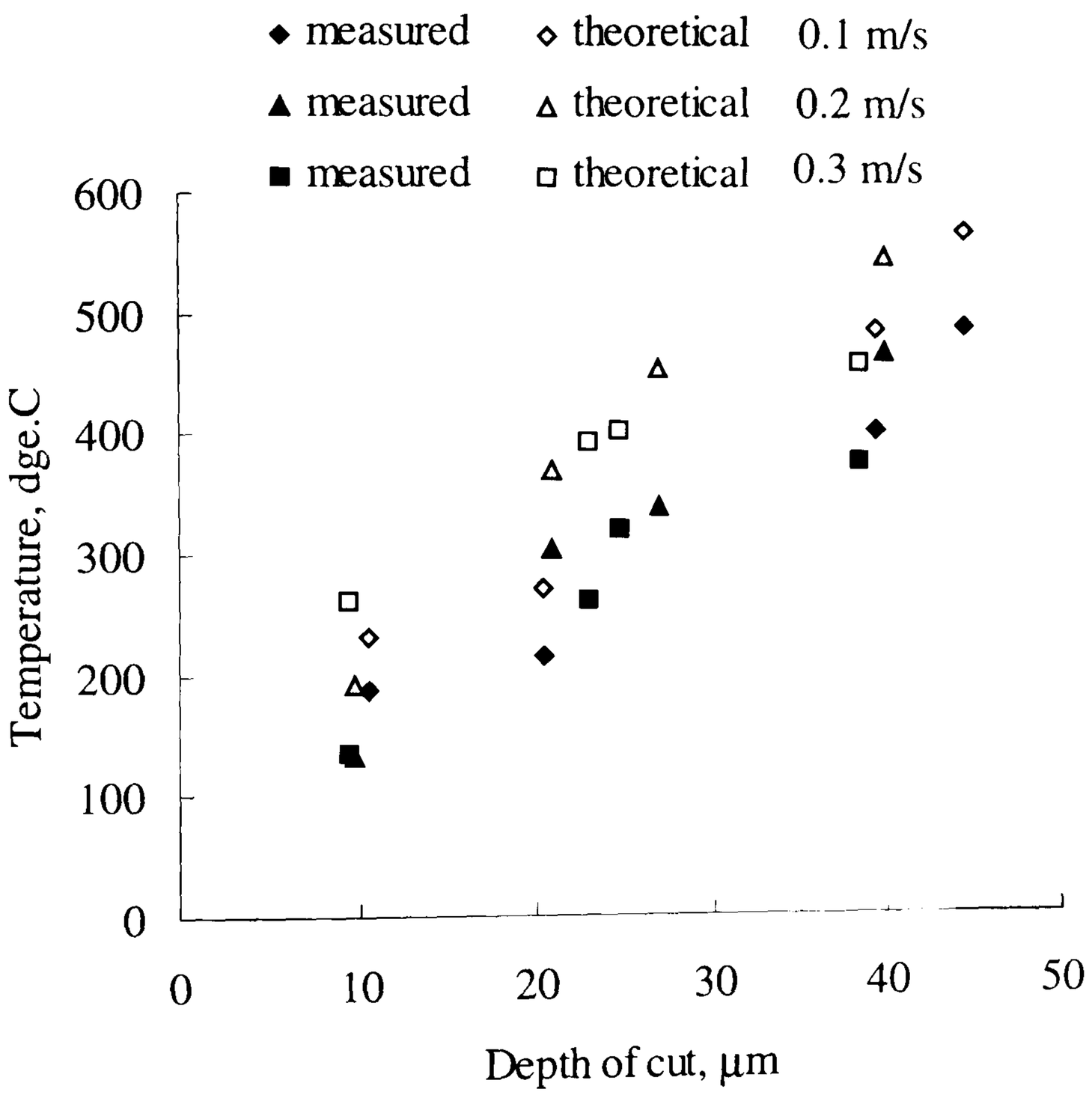

Figure 7.22 Comparison of measured and predicted temperature against depth of cut for different workpiece speeds at the apex of the inverted vee form in dry grinding

Experimental data:

Machine	: Abwood (surface grinding)
Material	: En31
Wheel	: 77A601H8VLNAA
Wheel diameter	: 200 mm, max
Wheelspeed	: 46 m/s
Workspeed	: 0.1 - 0.3 m/s
Workpiece shape	: inverted vee form
Coolant	: dry

Model data:

$R_r = 10$ $r_o = 15\ \mu m$

$e_{ch} = 6\ J/mm^3$ $k_{ge} = 45\ W/mK$

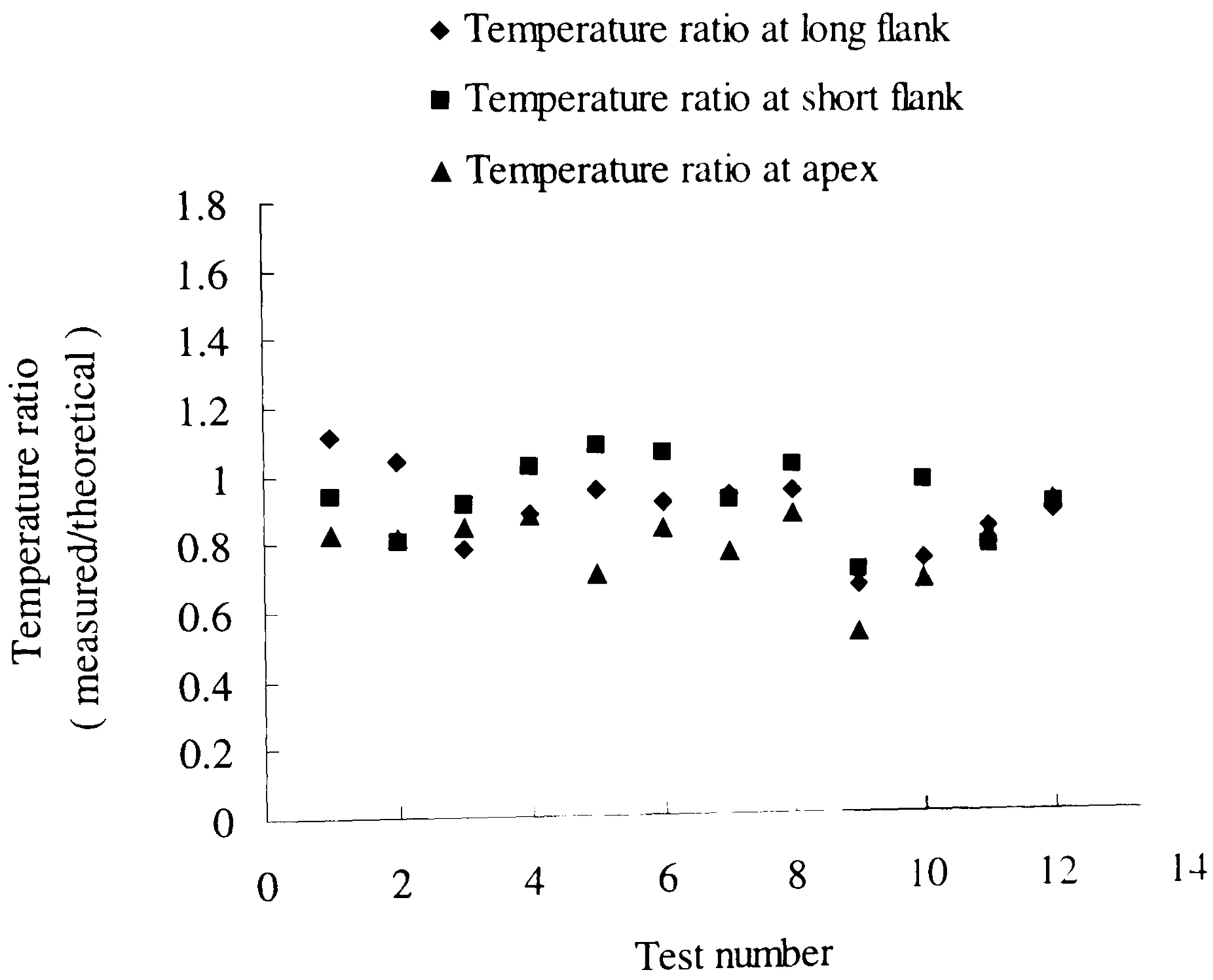

Figure 7.23 Temperature ratios for the long flank, short flank and the apex of the inverted vee form

Experimental data:

Machine	: Abwood (surface grinding)
Material	: En31
Wheel	: 77A601H8VLNAA
Wheel diameter	: 200 mm, max
Wheelspeed	: 46 m/s
Workspeed	: 0.1 - 0.3 m/s
Workpiece shape	: inverted vee form
Coolant	: dry

Model data:

$R_r = 10$ $r_o = 15\ \mu m$

$e_{ch} = 6\ J/mm^3$ $k_{ge} = 45\ W/mK$

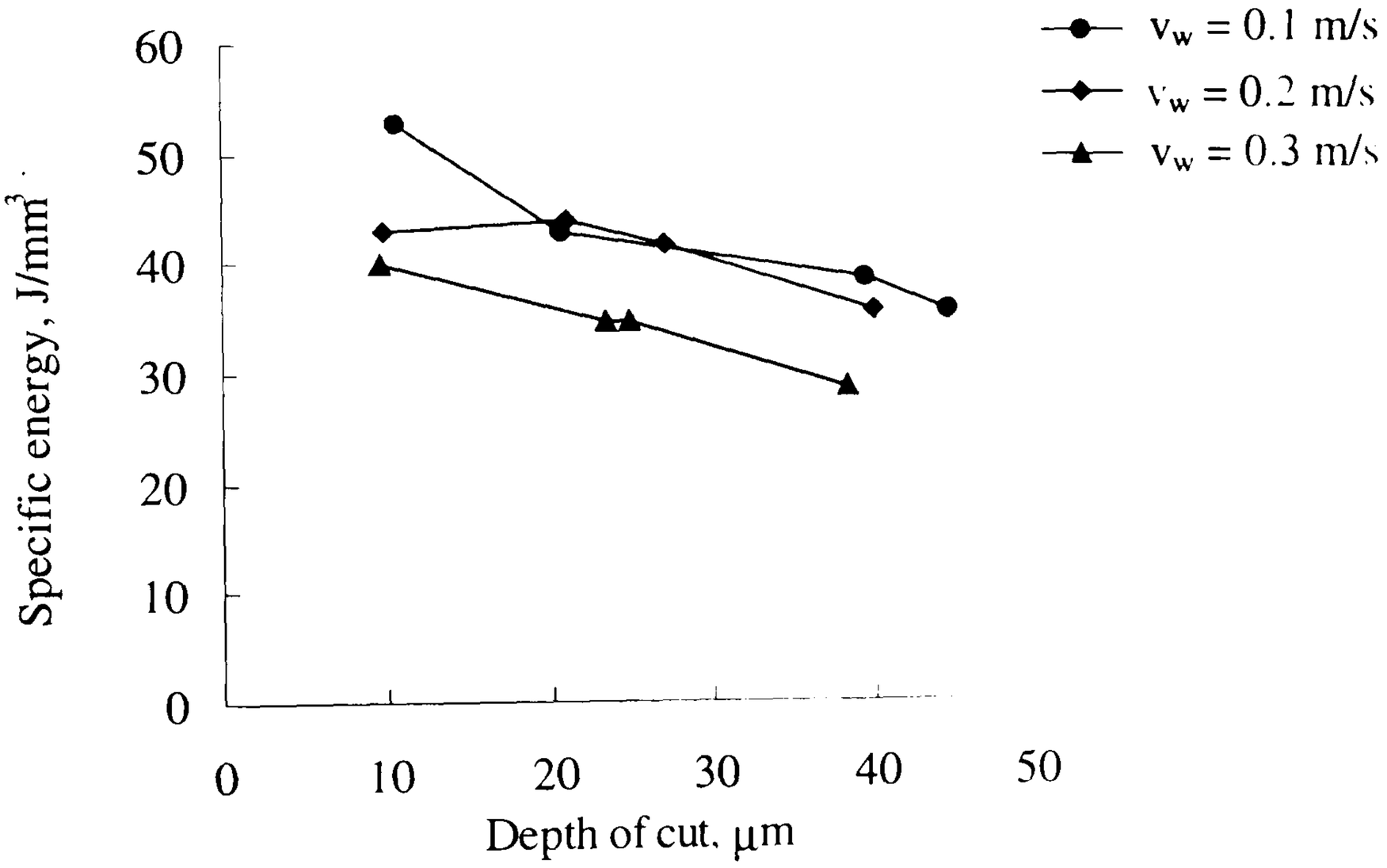

Figure 7.24. A comparison of the specific energy without coolant for different workpiece speeds for the inverted vee form

Experimental data:

Machine	: Abwood (surface grinding)
Material	: En31
Wheel	: 77A601H8VLNAA
Wheel diameter	: 200 mm, max
Wheelspeed	: 46 m/s
Workspeed	: 0.1-0.3 m/s
Workpiece shape	: inverted vee form
Coolant	: dry

Model data:

$R_r = 10$ $r_o = 15\ \mu m$

$e_{ch} = 6\ J/mm^3$ $k_{ge} = 45\ W/mK$

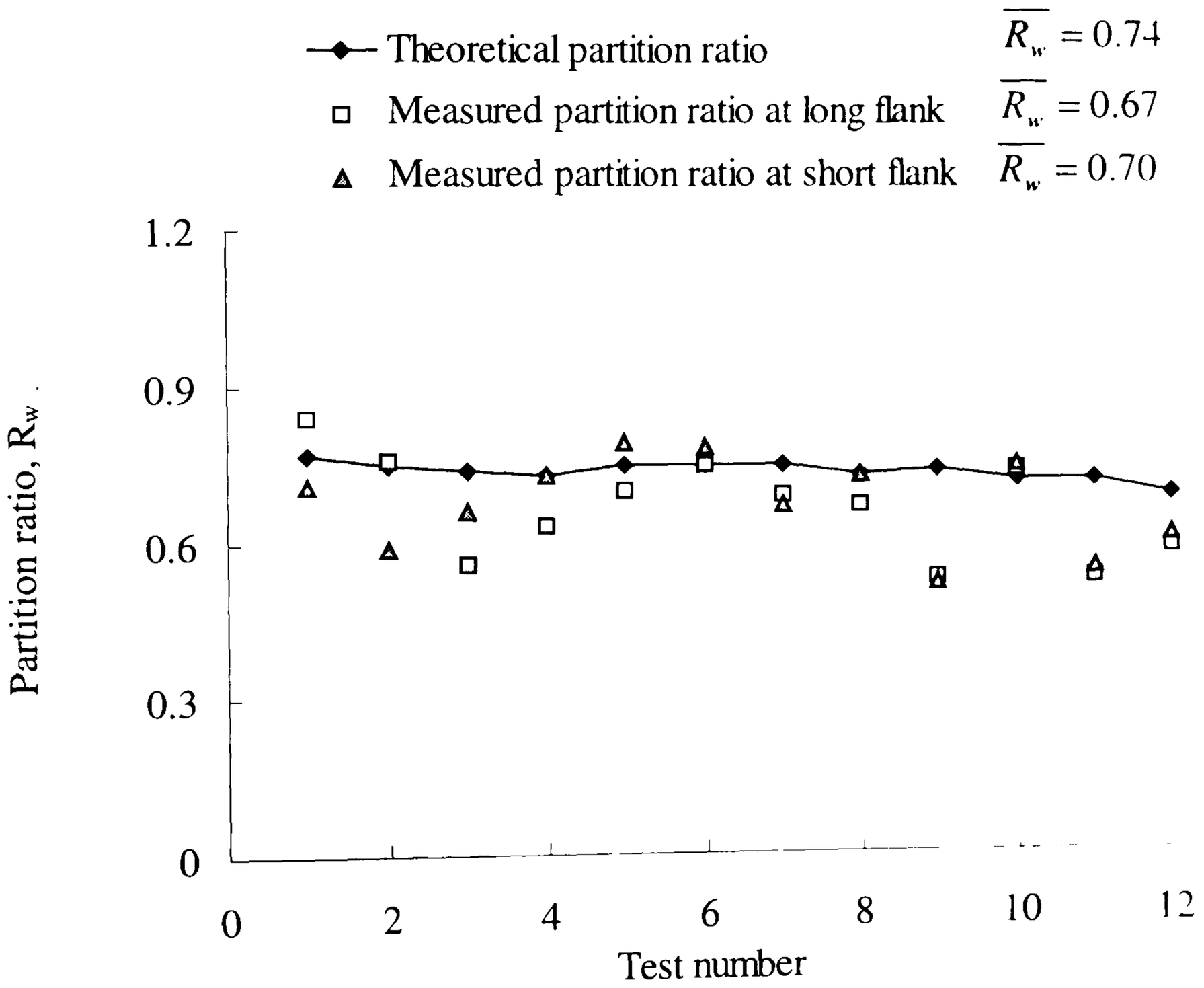

Figure 7.25. A comparison between theoretical and measured partition ratio without fluid for the inverted vee form

Experimental data:

Machine	: Abwood (surface grinding)
Material	: En31
Wheel	: 77A601H8VLNAA
Wheel diameter	: 200 mm. max
Wheelspeed	: 46 m/s
Workspeed	: 0.1-0.3 m/s
Workpiece shape	: inverted vee form
Coolant	: wet

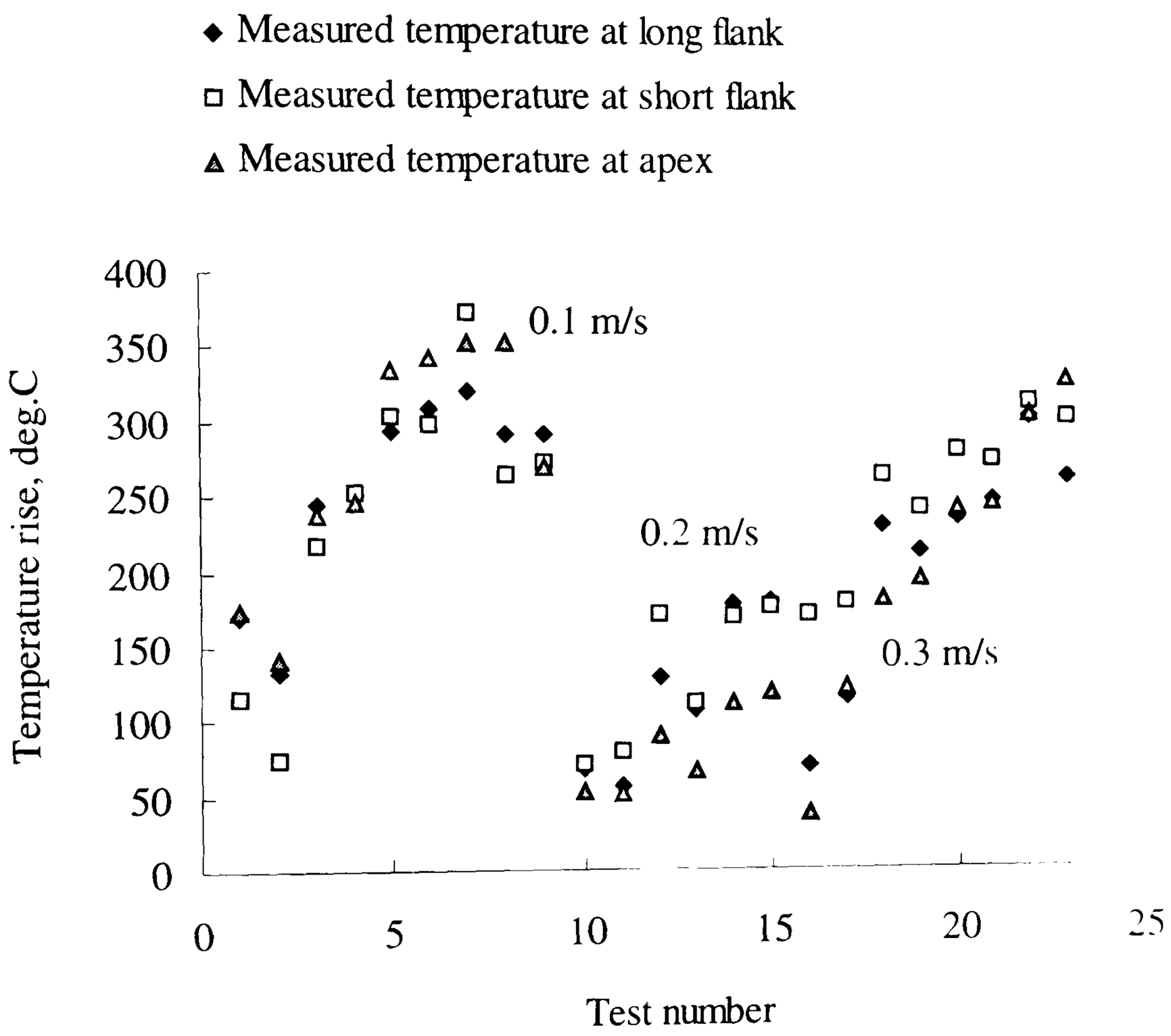

Figure 7.26 Measured temperature at long flank, short flank and apex of inverted vee form in wet grinding with various depths of cut

Experimental data:

Machine	: Abwood (surface grinding)
Material	: En31
Wheel	: 77A601H8VLNAA
Wheel diameter	: 200 mm, max
Wheelspeed	: 46 m/s
Workspeed	: 0.1 m/s
Workpiece shape	: inverted vee form
Coolant	: wet

Model data:

$R_r = 10$ $r_o = 15\ \mu m$

$e_{ch} = 6\ J/mm^3$ $k_{ge} = 45\ W/mK$

$h_c = 500$, 6000, and 10,000 W/m^2K

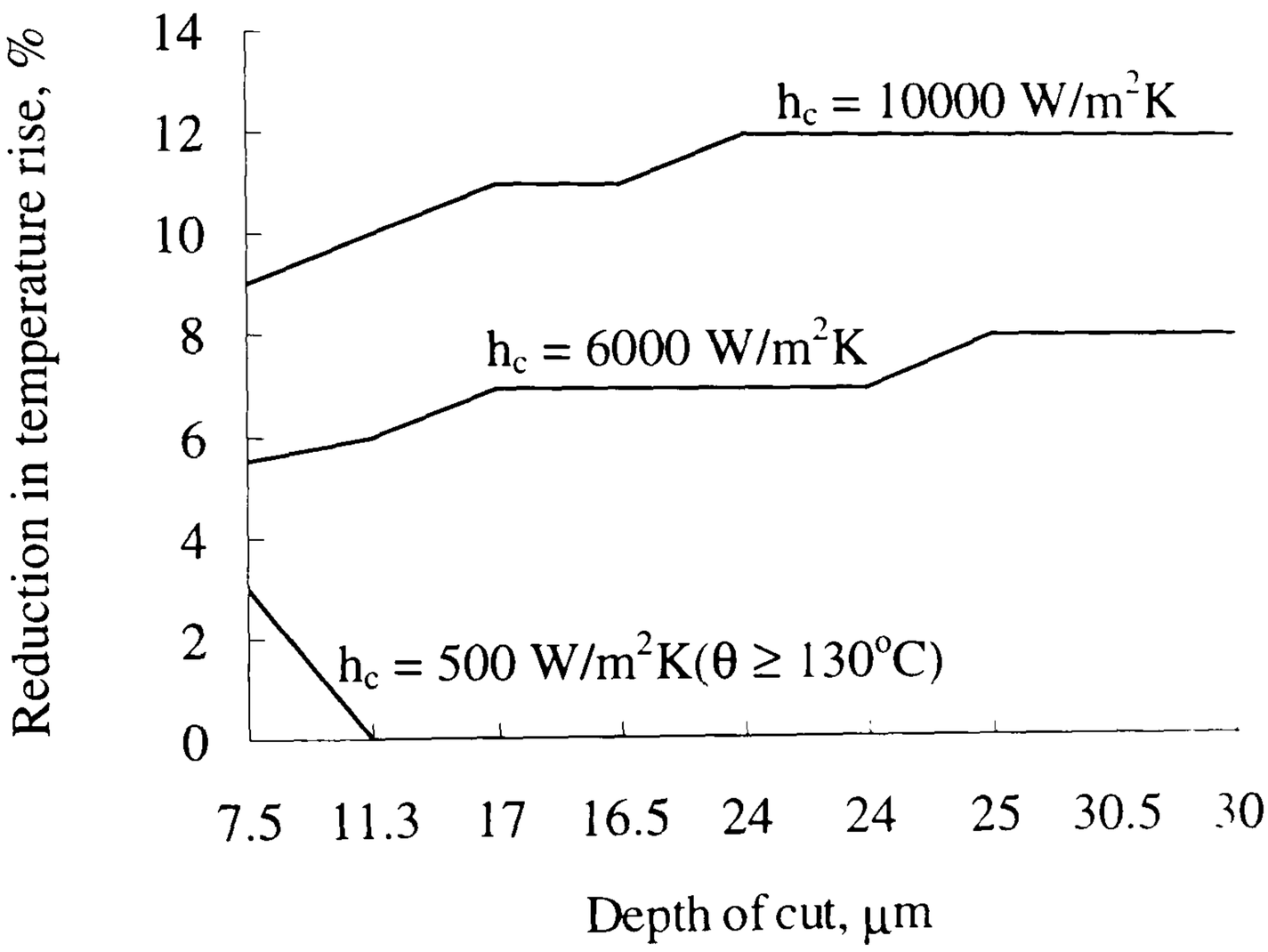

Figure 7.27 Reduction in maximum predicted temperature against depth of cut on the long flank of the inverted vee form due to different convection coefficients at $v_w = 0.1$ m/s

Experimental data:

Machine	: Abwood (surface grinding)
Material	: En31
Wheel	: 77A601H8VLNAA
Wheel diameter	: 200 mm, max
Wheelspeed	: 46 m/s
Workspeed	: 0.1 m/s
Workpiece shape	: inverted vee form
Coolant	: wet

Model data:

$R_r = 10$ $r_o = 15\ \mu m$

$e_{ch} = 6\ J/mm^3$ $k_{ge} = 45\ W/mK$

$h_c = 500$, 6000, and 10,000 W/m^2K

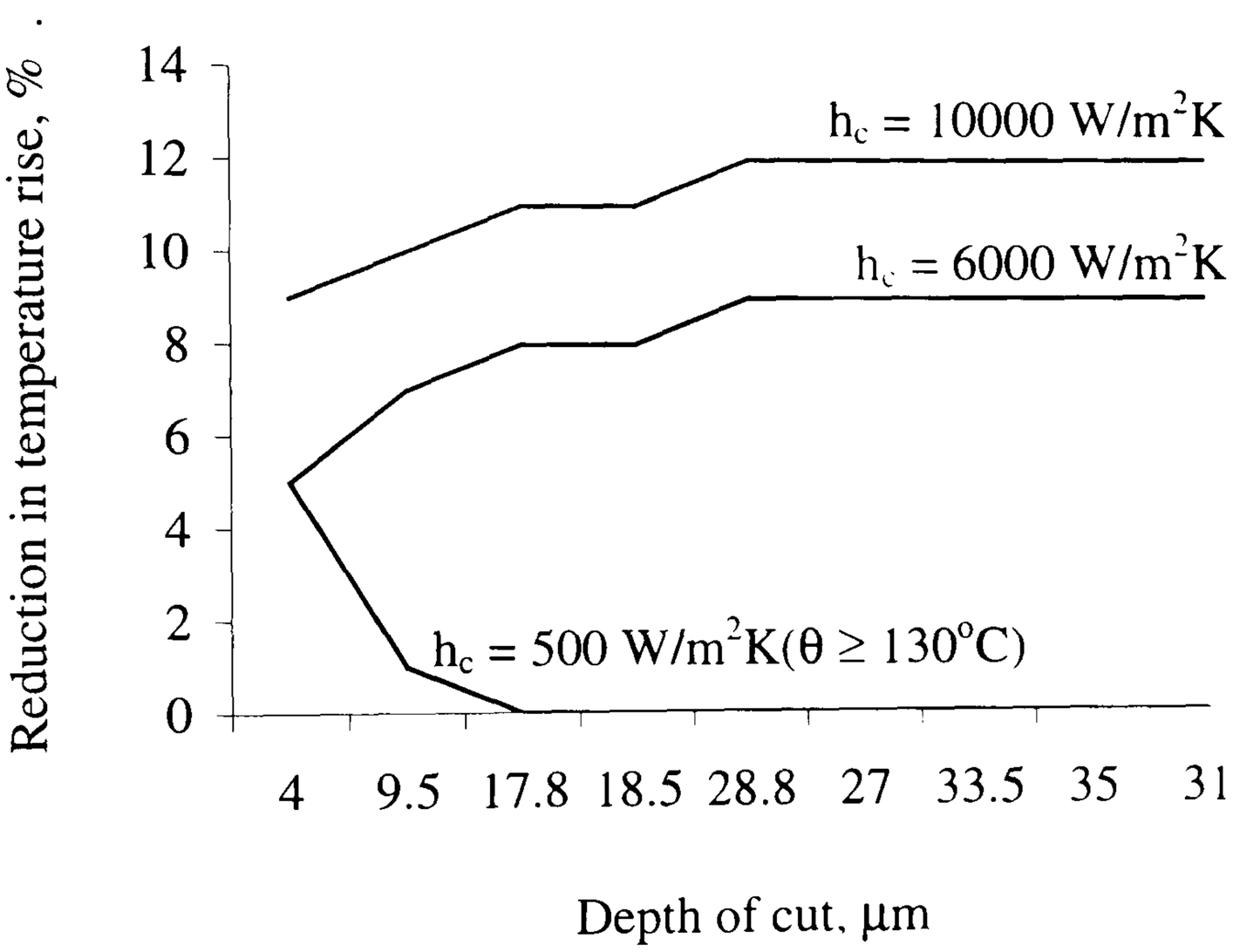

Figure 7.28 Reduction in maximum predicted temperature against depth of cut on the short flank of the inverted vee form due to different convection coefficients at $v_w = 0.1$ m/s

Experimental data:

Machine	: Abwood (surface grinding)
Material	: En31
Wheel	: 77A601H8VLNAA
Wheel diameter	: 200 mm, max
Wheelspeed	: 46 m/s
Workspeed	: 0.1 m/s
Workpiece shape	: inverted vee form
Coolant	: wet

Model data:

$R_r = 10$	$r_o = 15\ \mu m$
$e_{ch} = 6\ J/mm^3$	$k_{ge} = 45\ W/mK$
$h_c = 500$, 6000, and 10,000 W/m^2K	$sh_f = n$

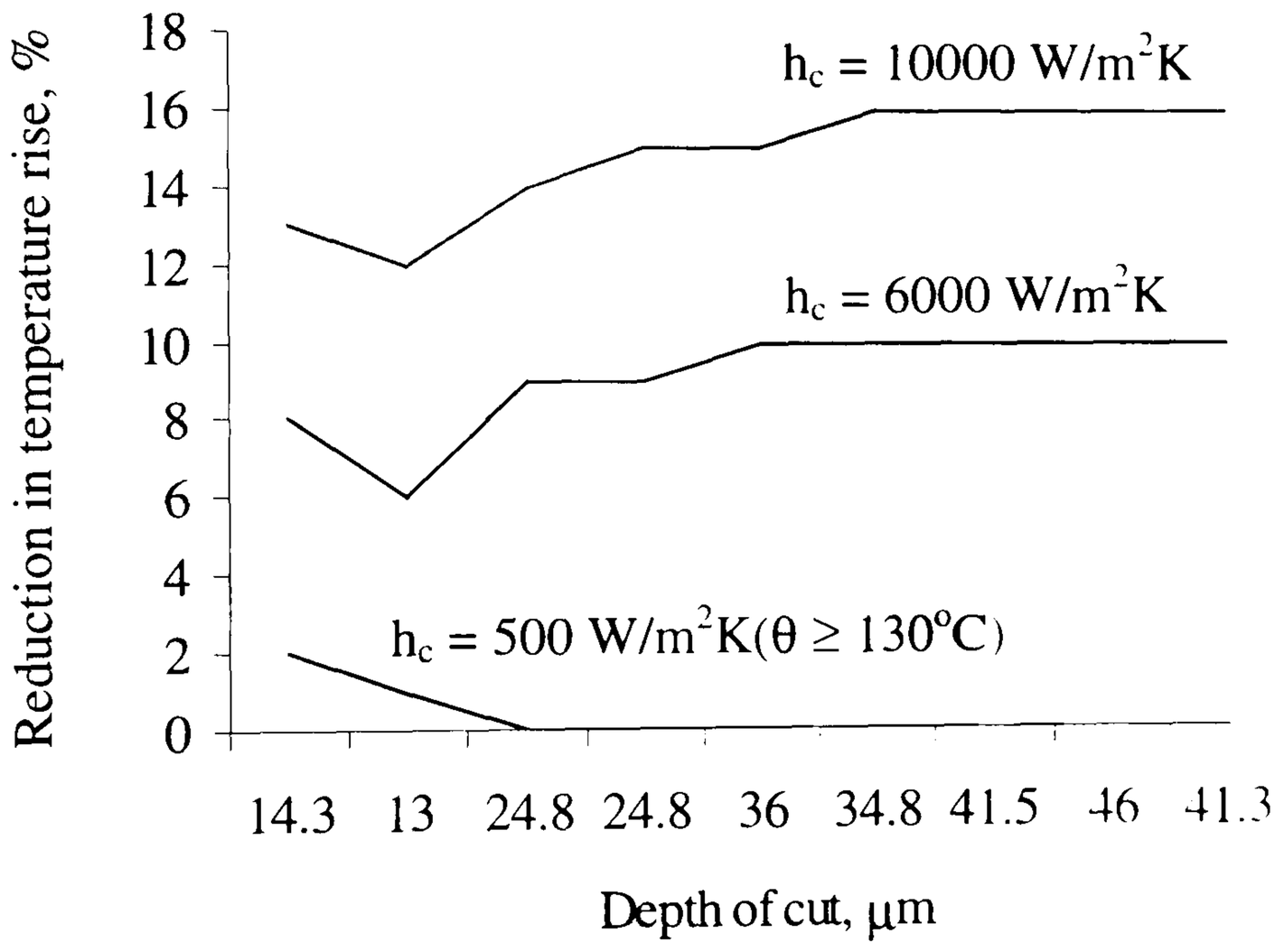

Figure 7.29 Reduction in maximum predicted temperature against depth of cut on the apex of the inverted vee form due to different convection coefficients at $v_w = 0.1$ m/s

Experimental data:

Machine	: Abwood (surface grinding)
Material	: En31
Wheel	: 77A601H8VLNAA
Wheel diameter	: 200 mm, max
Wheelspeed	: 46 m/s
Workspeed	: 0.1 m/s
Workpiece shape	: inverted vee form
Coolant	: wet

Model data:

$R_r = 10$ $r_o = 15\ \mu m$

$e_{ch} = 6\ J/mm^3$ $k_{ge} = 45\ W/mK$

$h_c = 500$, 6000, and 10,000 W/m^2K $sh_f = n$

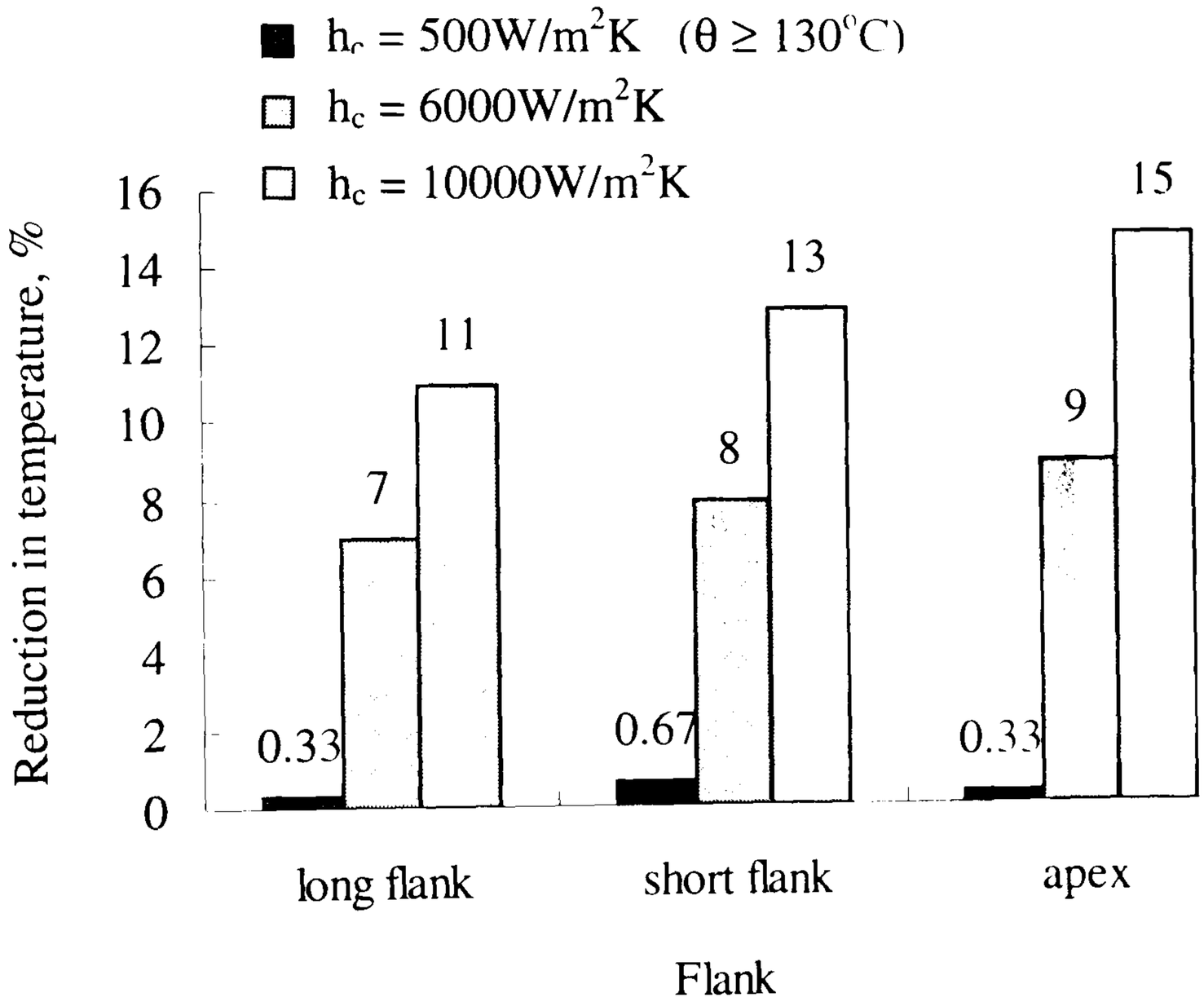

Figure 7.30 Reduction in predicted temperatures with different convection coefficients on the inverted vee form at $v_w = 0.1$ m/s

Experimental data:

Machine	: Abwood (surface grinding)
Material	: En31
Wheel	: 77A601H8VLNAA
Wheel diameter	: 200 mm, max
Wheelspeed	: 46 m/s
Workspeed	: 0.1-0.3 m/s
Workpiece shape	: inverted vee form
Coolant	: wet

Model data:

$R_r = 10$ $r_o = 15\ \mu m$

$e_{ch} = 6\ J/mm^3$ $k_{ge} = 45\ W/mK$

$h_c = 500\ W/m^2K$

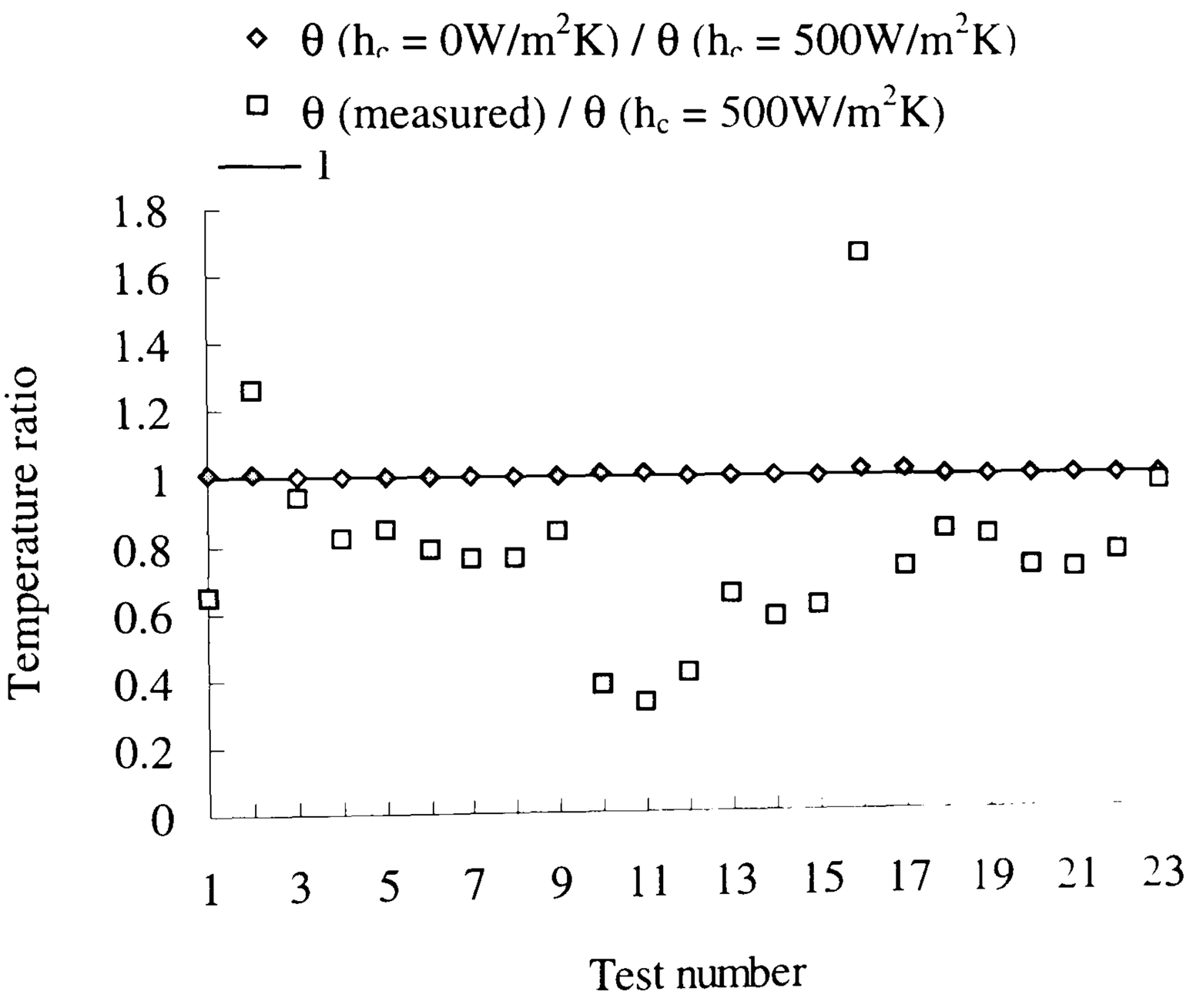

Figure 7.31 Ratios of measured and predicted temperature at long flank for different conditions

Experimental data:

Machine	: Abwood (surface grinding)
Material	: En31
Wheel	: 77A601H8VLNAA
Wheel diameter	: 200 mm, max
Wheelspeed	: 46 m/s
Workspeed	: 0.1-0.3 m/s
Workpiece shape	: inverted vee form
Coolant	: wet

Model data:

$R_r = 10$ $\quad r_o = 15\ \mu m$

$e_{ch} = 6\ J/mm^3$ $\quad k_{ge} = 45\ W/mK$

$h_c = 500\ W/m^2K$

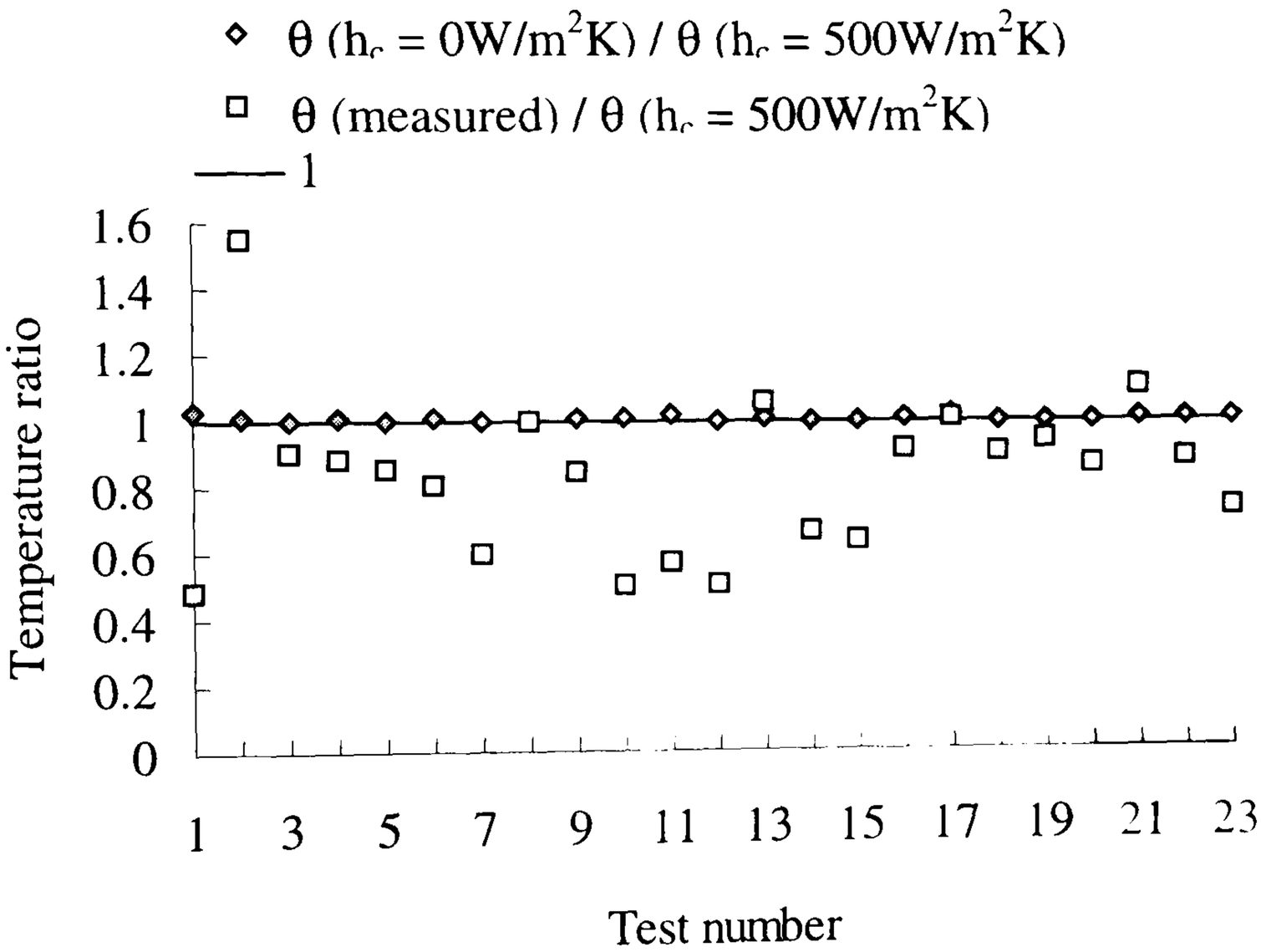

Figure 7.32 Ratio of measured and predicted temperature on the short flank for different grinding conditions

Experimental data:

Machine	: Abwood (surface grinding)
Material	: En31
Wheel	: 77A601H8VLNAA
Wheel diameter	: 200 mm, max
Wheelspeed	: 46 m/s
Workspeed	: 0.1-0.3 m/s
Workpiece shape	: inverted vee form
Coolant	: wet

Model data:

$R_r = 10$
$e_{ch} = 6\ J/mm^3$
$h_c = 500\ W/m^2K$
$r_o = 15\ \mu m$
$k_{ge} = 45\ W/mK$

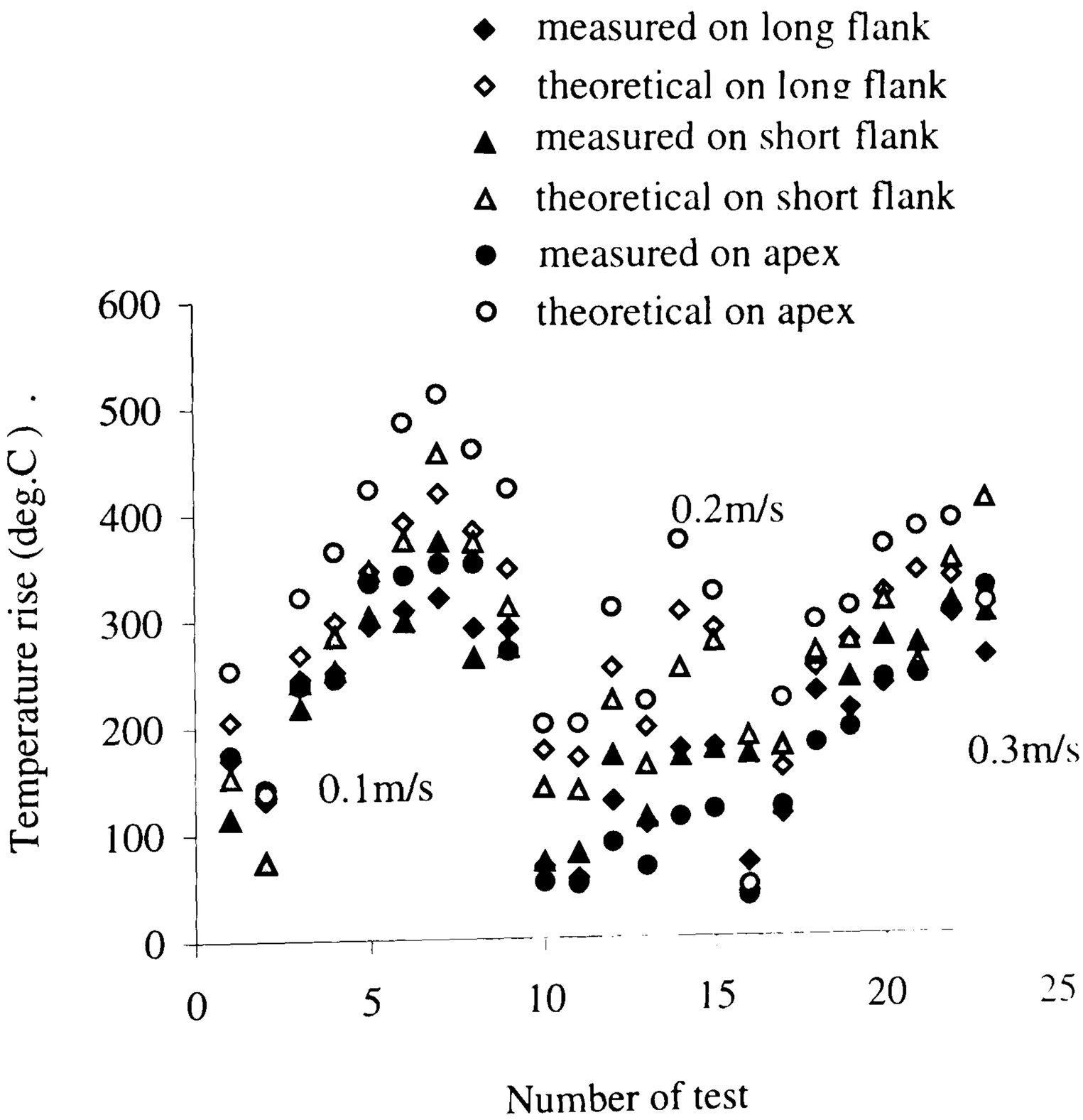

Figure 7.33 Comparison of the measured and predicted temperature for $h_c = 500\ W/m^2K$

Experimental data:

Machine	: Abwood (surface grinding)
Material	: En31
Wheel	: 77A601H8VLNAA
Wheel diameter	: 200 mm, max
Wheelspeed	: 46 m/s
Workspeed	: 0.1-0.3 m/s
Workpiece shape	: inverted vee form
Coolant	: wet

Model data:

$R_r = 10$ $r_o = 15\ \mu m$

$e_{ch} = 6\ J/mm^3$ $k_{ge} = 45\ W/mK$

$h_c = 6000\text{-}10000\ W/m^2K$

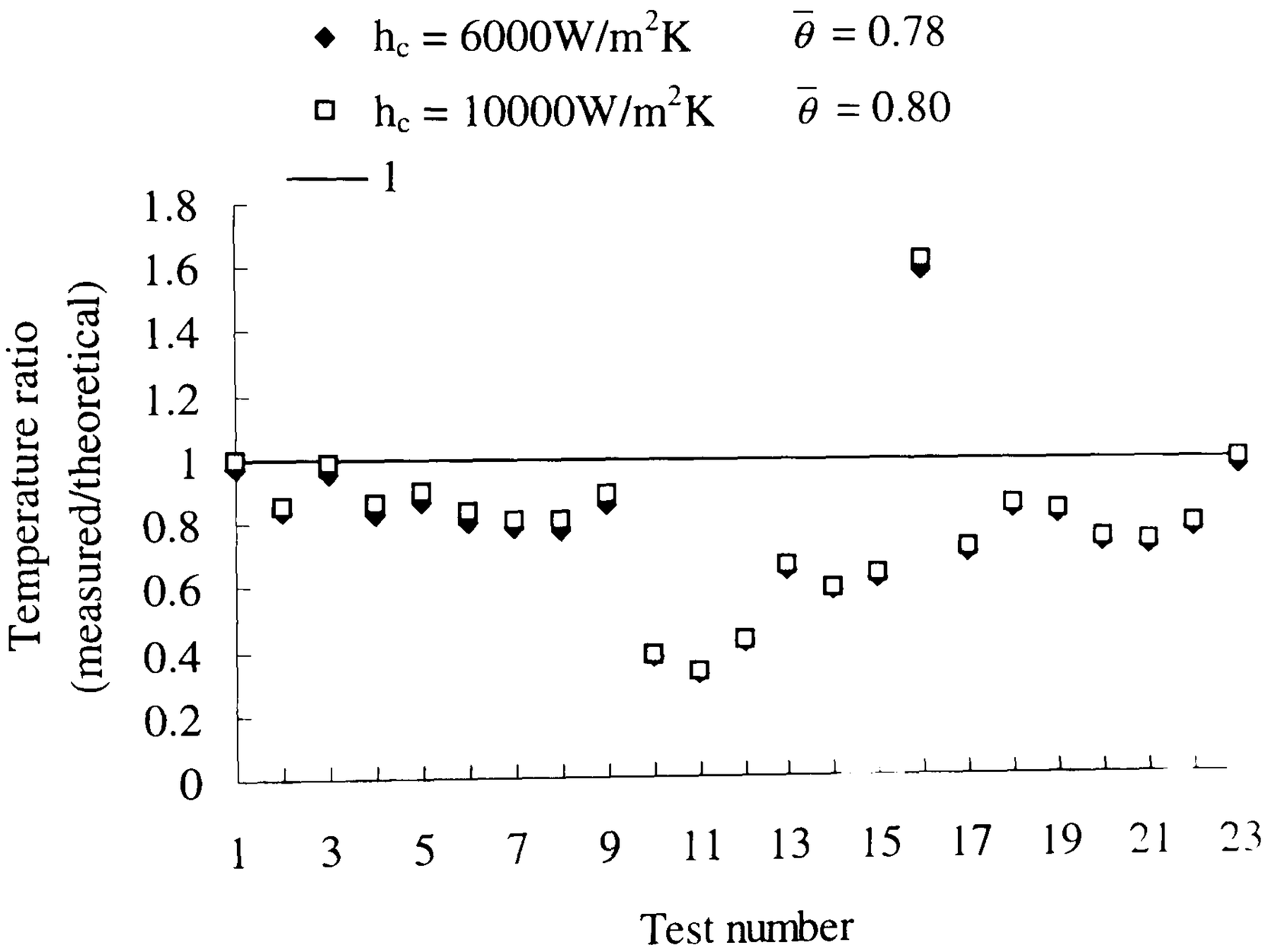

Figure 7.34 Ratio of measured and predicted temperature on the long flank of the inverted vee form for different convection coefficients

Experimental data:

Machine	: Abwood (surface grinding)
Material	: En31
Wheel	: 77A601H8VLNAA
Wheel diameter	: 200 mm, max
Wheelspeed	: 46 m/s
Workspeed	: 0.1-0.3 m/s
Workpiece shape	: inverted vee form
Coolant	: wet

Model data:

$R_r = 10$ $r_o = 15\ \mu m$

$e_{ch} = 6\ J/mm^3$ $k_{ge} = 45\ W/mK$

$h_c = 6000\text{-}10000\ W/m^2K$

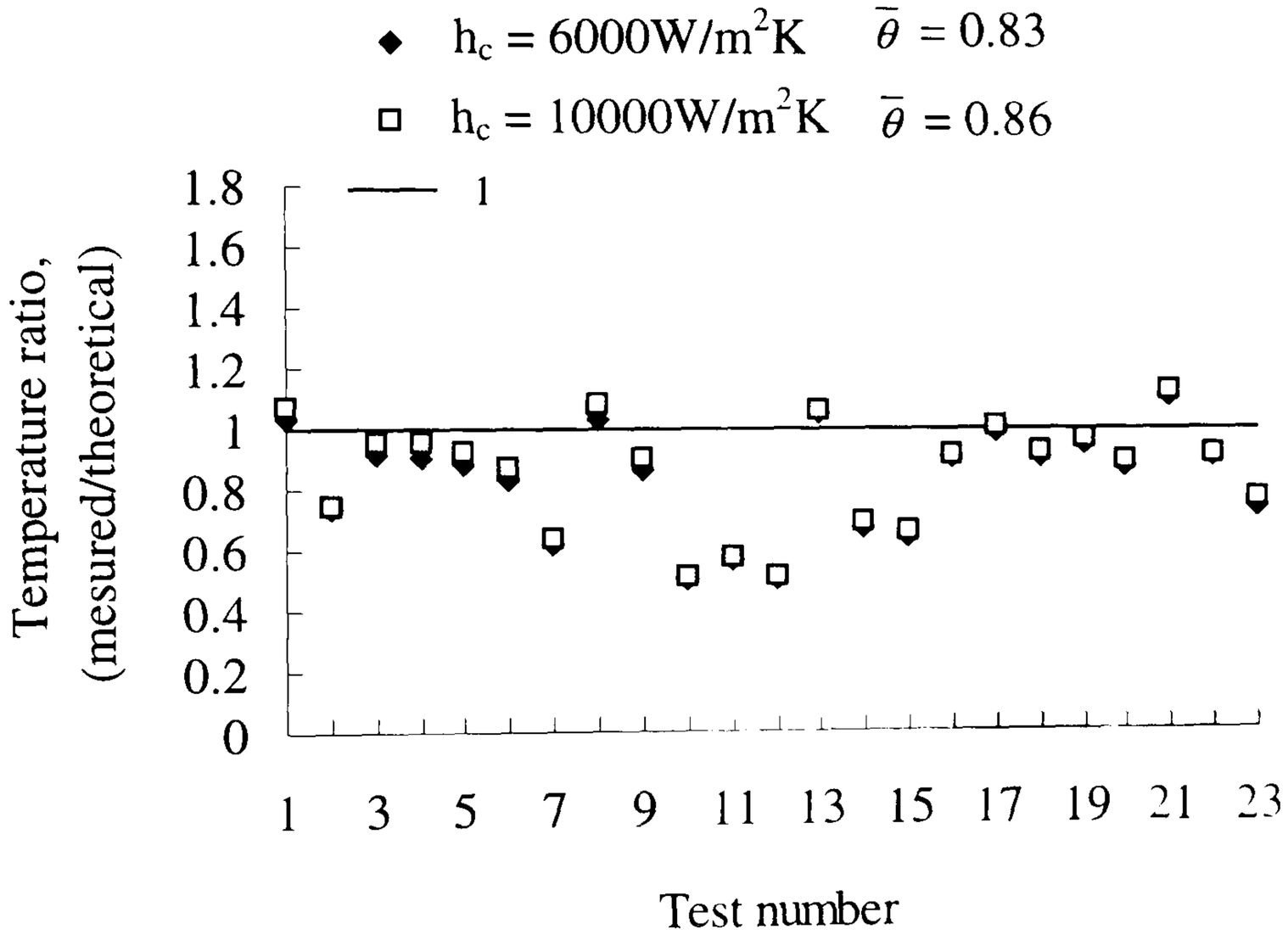

Figure 7.35 Ratio of measured and predicted temperature on the short flank of the inverted vee form for different convection coefficients

Experimental data:

Machine	: Abwood (surface grinding)
Material	: En31
Wheel	: 77A601H8VLNAA
Wheel diameter	: 200 mm, max
Wheelspeed	: 46 m/s
Workspeed	: 0.1-0.3 m/s
Workpiece shape	: inverted vee form
Coolant	: wet

Model data:

$R_r = 10$ $\quad r_o = 15\ \mu m$

$e_{ch} = 6\ J/mm^3$ $\quad k_{ge} = 45\ W/mK$

$h_c = 10000\ W/m^2K$

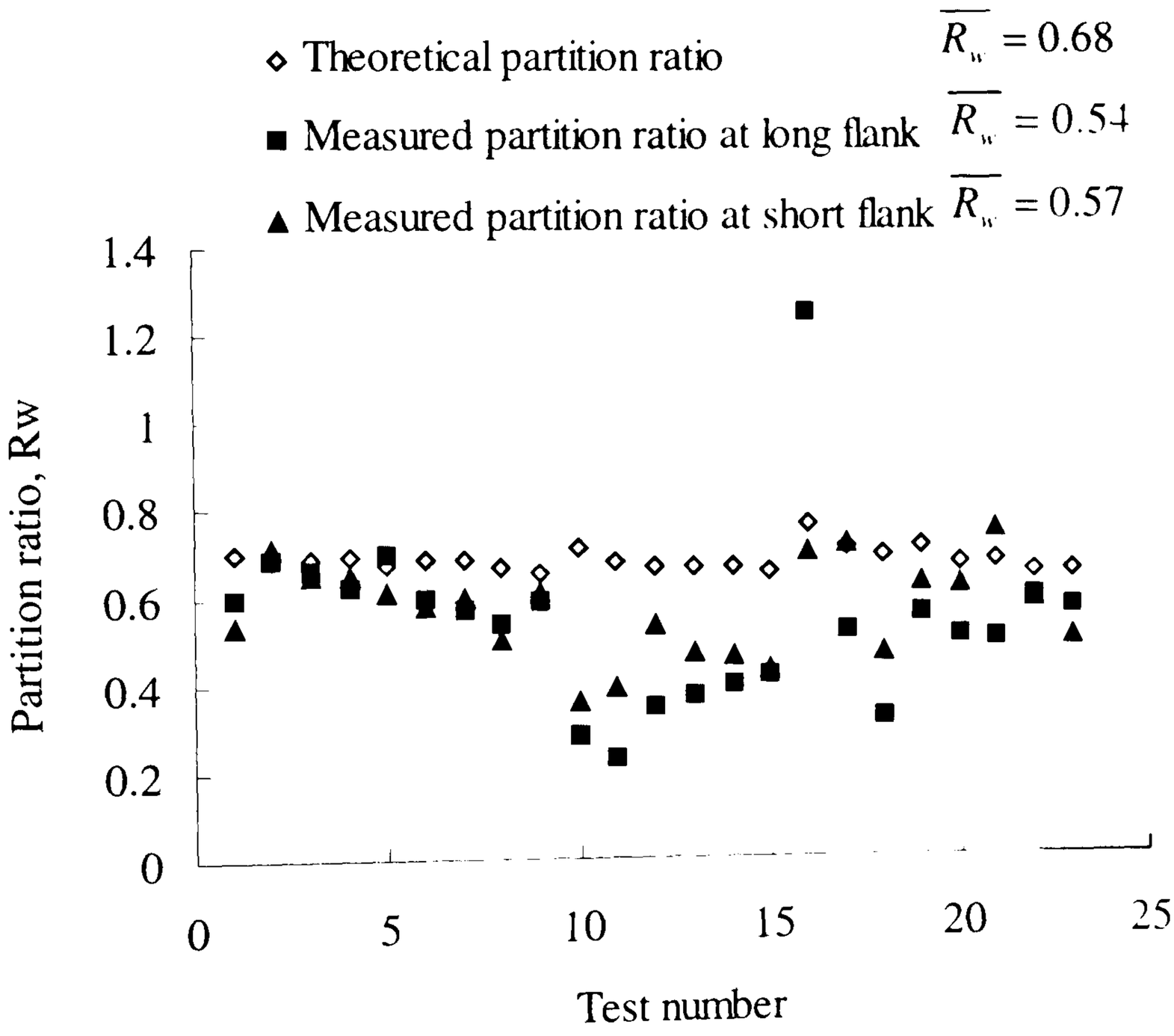

Figure 7.36 Predicted and measured partition ratios with fluid for the inverted vee form

Experimental data:

Machine	: Abwood (surface grinding)
Material	: En31
Wheel	: 77A601H8VLNAA
Wheel diameter	: 200 mm, max
Wheelspeed	: 46 m/s
Workspeed	: 0.1-0.3 m/s
Workpiece shape	: inverted vee form
Coolant	: dry

Model data:

$R_r = 10$ $\quad r_o = 15\ \mu m$

$e_{ch} = 6\ J/mm^3$ $\quad k_{ge} = 45\ W/mK$

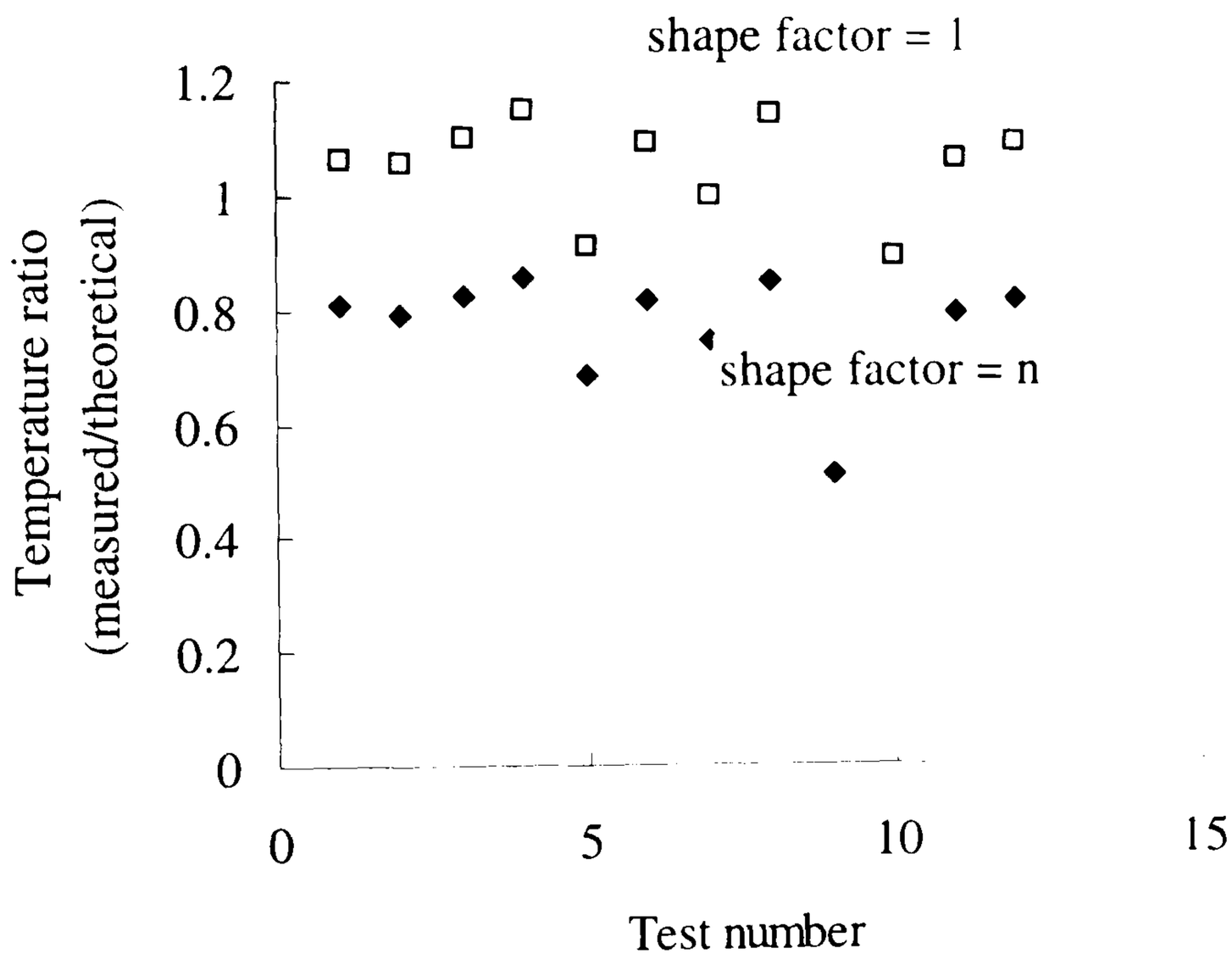

Figure 7.37 Ratio of the measured and predicted temperature for a sharp edge shape factor, n and a plane surface shape factor , 1 in dry inverted vee form grinding

Experimental data:

Machine	: Abwood (surface grinding)
Material	: En31
Wheel	: 77A601H8VLNAA
Wheel diameter	: 200 mm, max
Wheelspeed	: 46 m/s
Workspeed	: 0.1-0.3 m/s
Workpiece shape	: inverted vee form
Coolant	: wet

Model data:

$R_r = 10$
$e_{ch} = 6$ J/mm^3
$h_c = 10000$ W/m^{2}K
$r_o = 15$ µm
$k_{ge} = 45$ W/mK

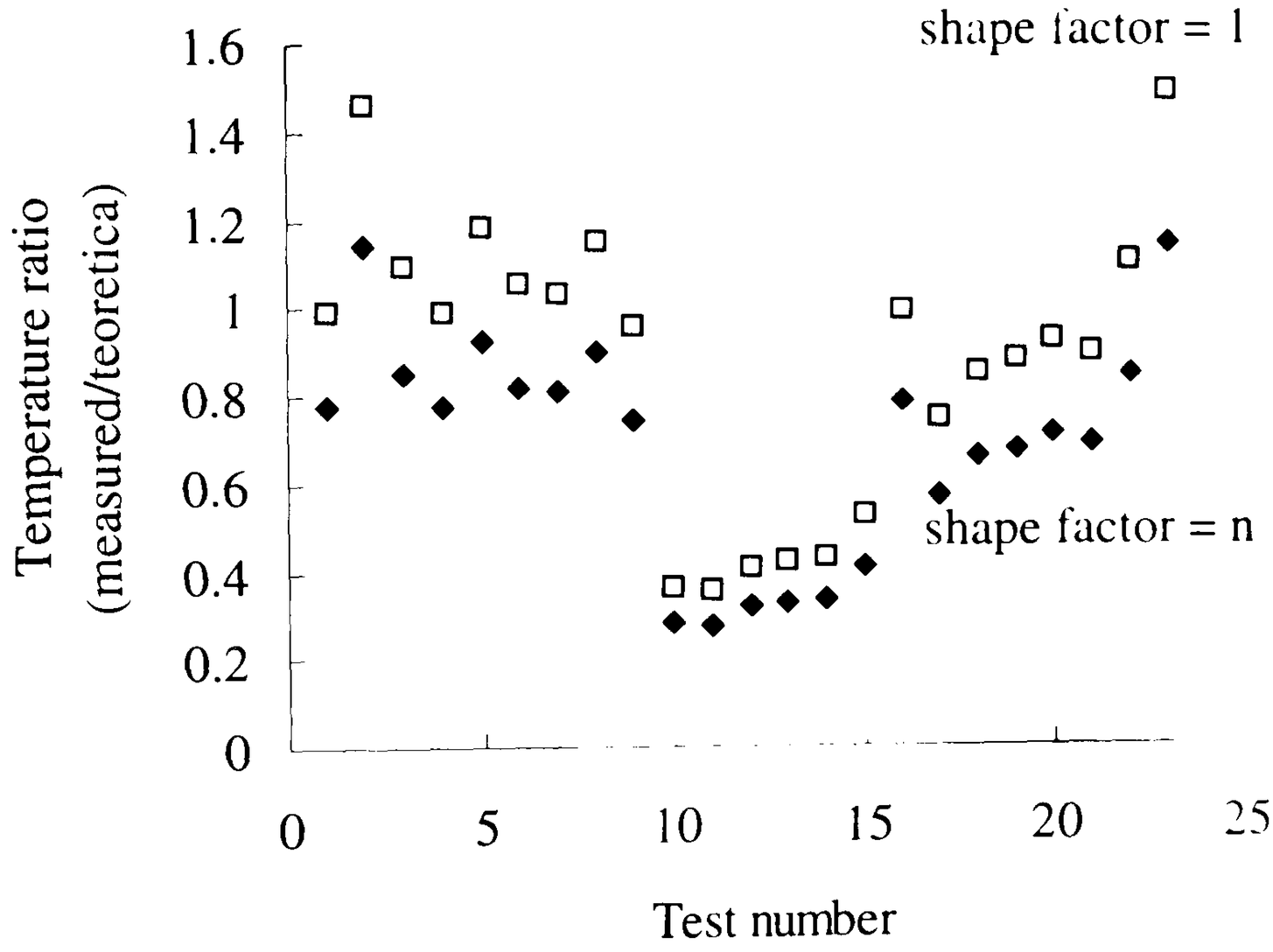

Figure 7.38 Ratio of the measured and predicted temperature for a sharp edge shape factor, n and a plane surface shape factor , 1 in wet inverted vee form grinding

Experimental data:

Machine	: Abwood (surface grinding)
Material	: En31
Wheel	: 77A601H8VLNAA
Wheel diameter	: 200 mm, max
Wheelspeed	: 46 m/s
Workspeed	: 0.1-0.3 m/s
Workpiece shape	: inverted vee form
Coolant	: wet and dry

Model data:

$R_r = 10$ $r_o = 15\ \mu m$

$e_{ch} = 6\ J/mm^3$ $k_{ge} = 45\ W/mK$

$h_c = 10000\ W/m^2K$

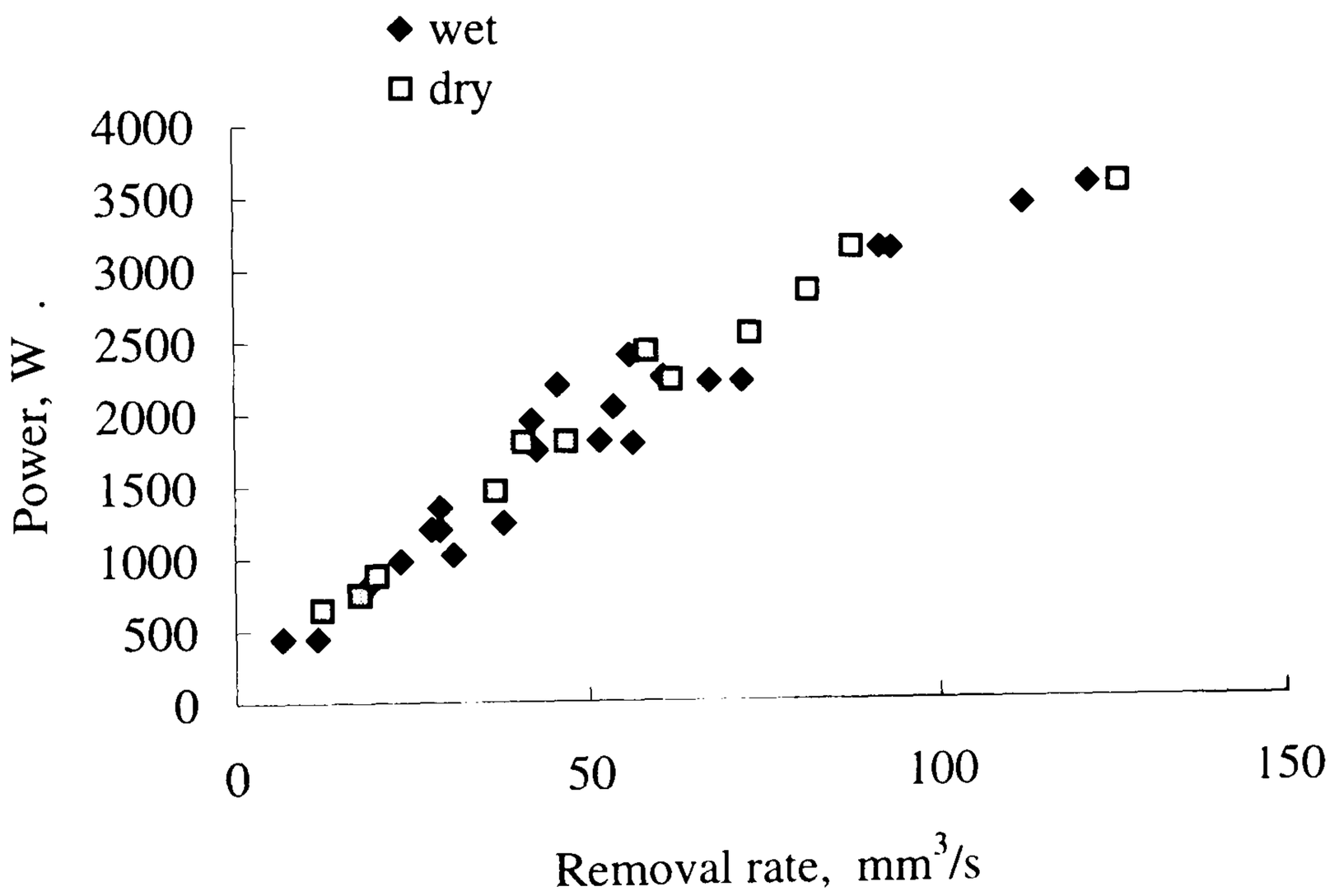

Figure 7.39 Grinding power for dry and wet grinding of the inverted vee form grinding

Experimental data:

Machine	: Abwood (surface grinding)
Material	: En31
Wheel	: 77A601H8VLNAA
Wheel diameter	: 200 mm, max
Wheelspeed	: 46 m/s
Workspeed	: 0.1 m/s
Workpiece shape	: inverted vee form
Coolant	: wet and dry

Model data:

$R_r = 10$ $r_o = 15\ \mu m$

$e_{ch} = 6\ J/mm^3$ $k_{ge} = 45\ W/mK$

$h_c = 10000\ W/m^2K$

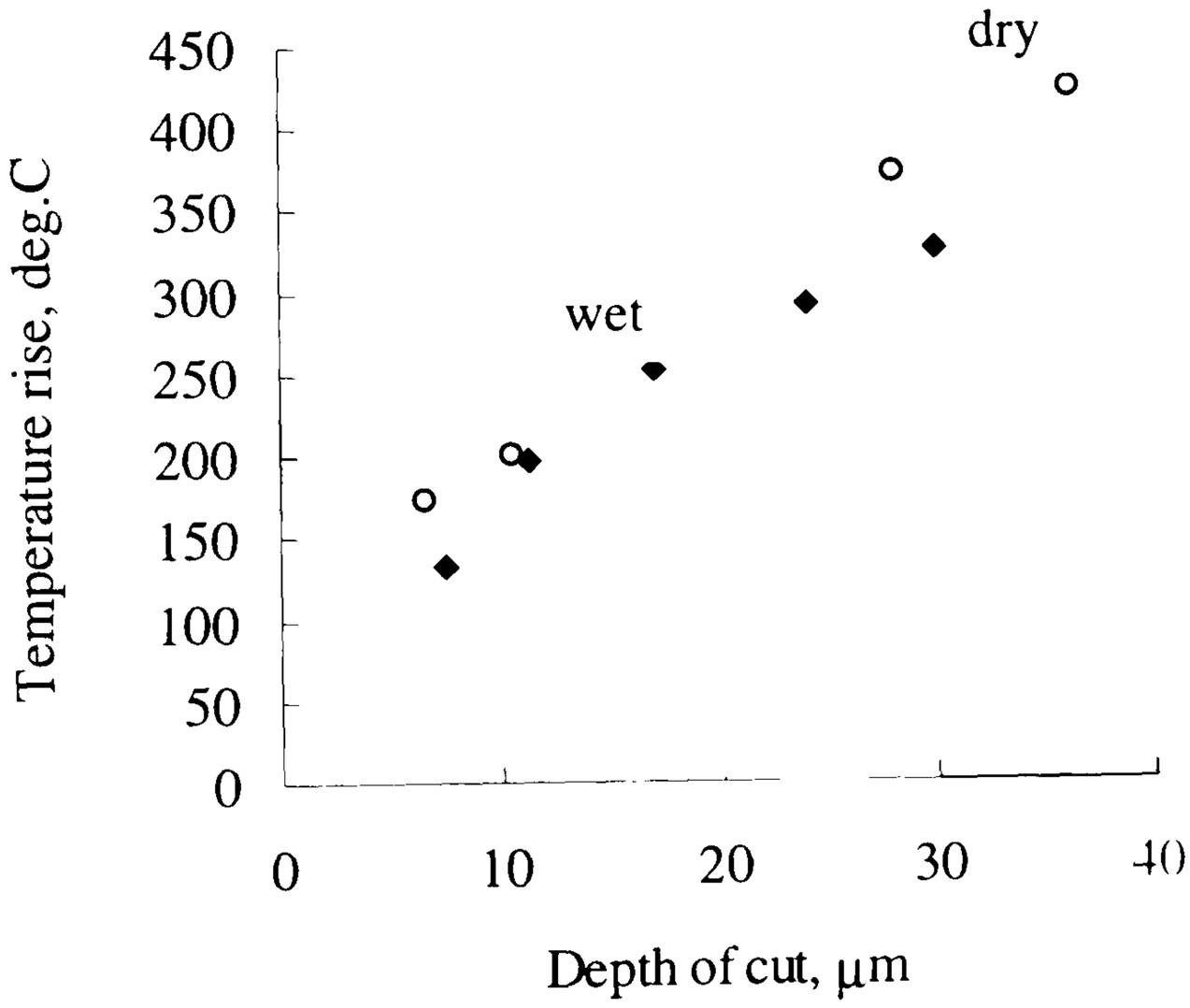

Figure 7.40 Theoretical temperature rise for dry and wet grinding on the long flank of the inverted vee form at $v_w = 0.1$ m/s

Experimental data:

Machine	: Abwood (surface grinding)
Material	: En31
Wheel	: 77A601H8VLNAA
Wheel diameter	: 200 mm, max
Wheelspeed	: 46 m/s
Workspeed	: 0.1 m/s
Workpiece shape	: inverted vee form
Coolant	: wet and dry

Model data:

$R_r = 10$ $\quad r_o = 15\ \mu m$

$e_{ch} = 6\ J/mm^3$ $\quad k_{ge} = 45\ W/mK$

$h_c = 10000\ W/m^2K$

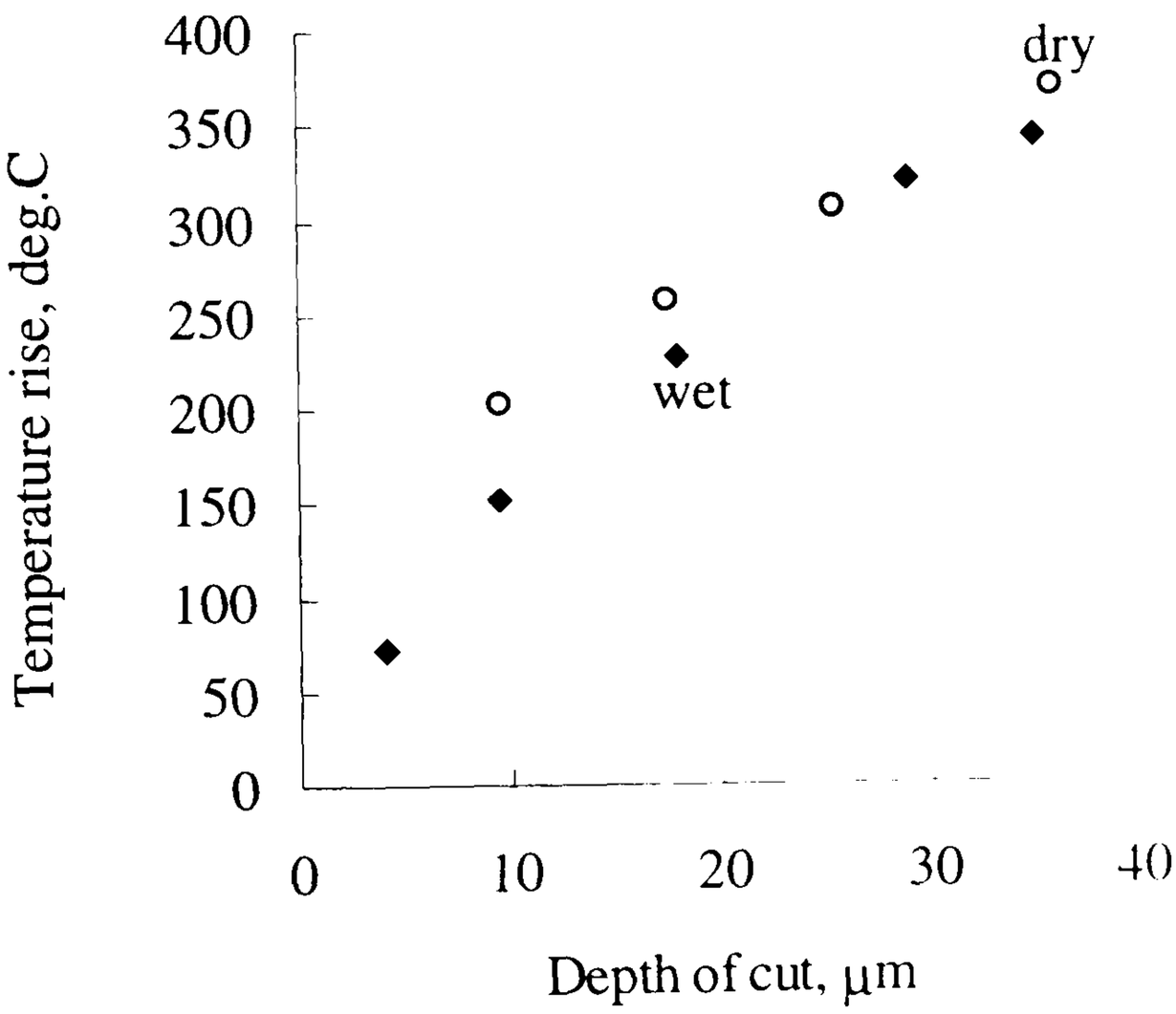

Figure 7.41 Theoretical temperature rise for dry and wet grinding on the short flank of the inverted vee form at $v_w = 0.1$ m/s

Experimental data:

Machine	: Abwood (surface grinding)
Material	: En31
Wheel	: 77A601H8VLNAA
Wheel diameter	: 200 mm, max
Wheelspeed	: 46 m/s
Workspeed	: 0.2 m/s
Workpiece shape	: inverted vee form
Coolant	: wet and dry

Model data:

$R_r = 10$ $r_o = 15\ \mu m$

$e_{ch} = 6\ J/mm^3$ $k_{ge} = 45\ W/mK$

$h_c = 10000\ W/m^2K$

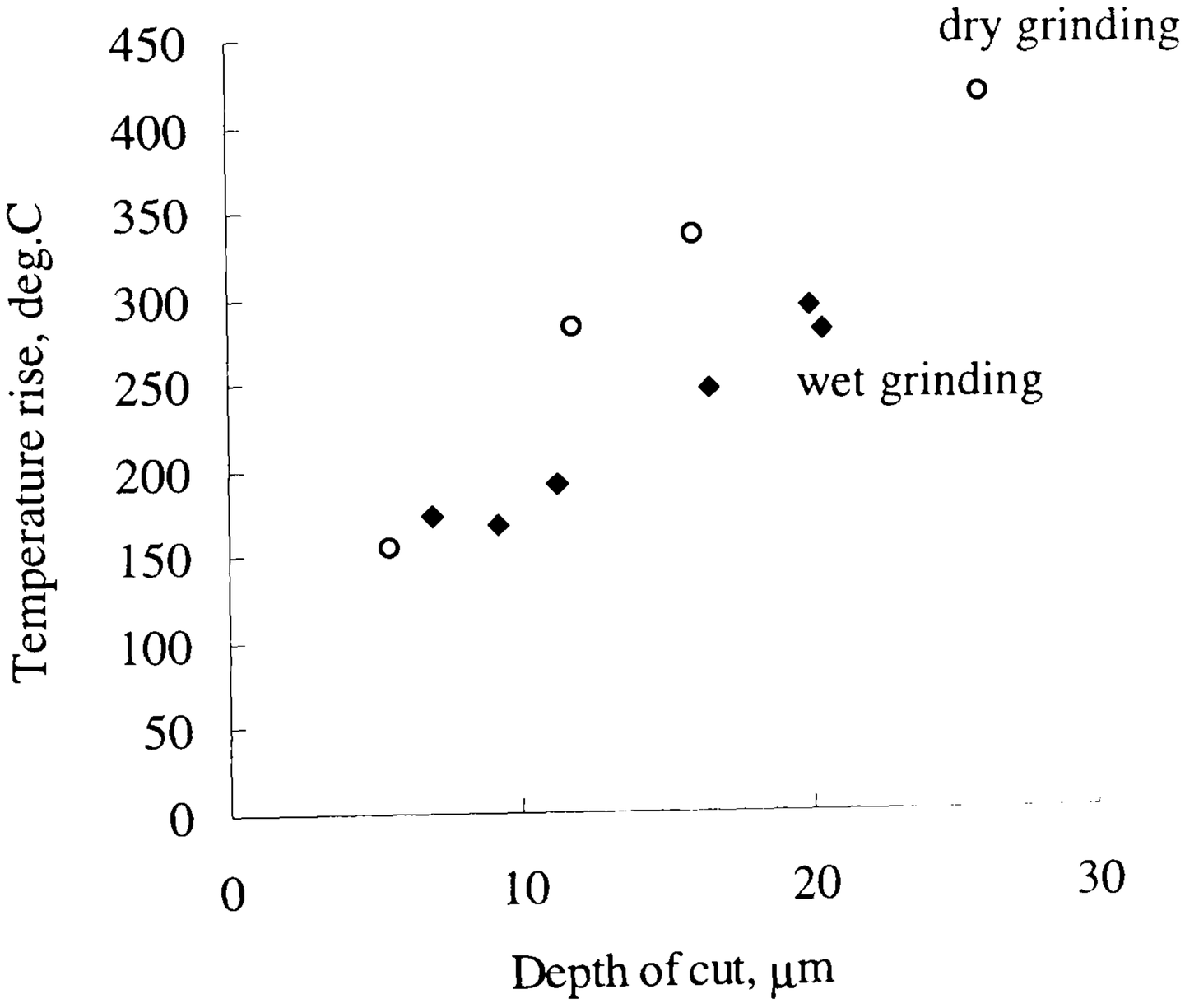

Figure 7.42 Theoretical temperature rise for dry and wet grinding on the long flank of the inverted vee form at $v_w = 0.2$ m/s

Experimental data:

Machine	: Abwood (surface grinding)
Material	: En31
Wheel	: 77A601H8VLNAA
Wheel diameter	: 200 mm, max
Wheelspeed	: 46 m/s
Workspeed	: 0.2 m/s
Workpiece shape	: inverted vee form
Coolant	: wet and dry

Model data:

$R_r = 10$
$e_{ch} = 6\ J/mm^3$
$h_c = 10000\ W/m^2K$
$r_o = 15\ \mu m$
$k_{ge} = 45\ W/mK$

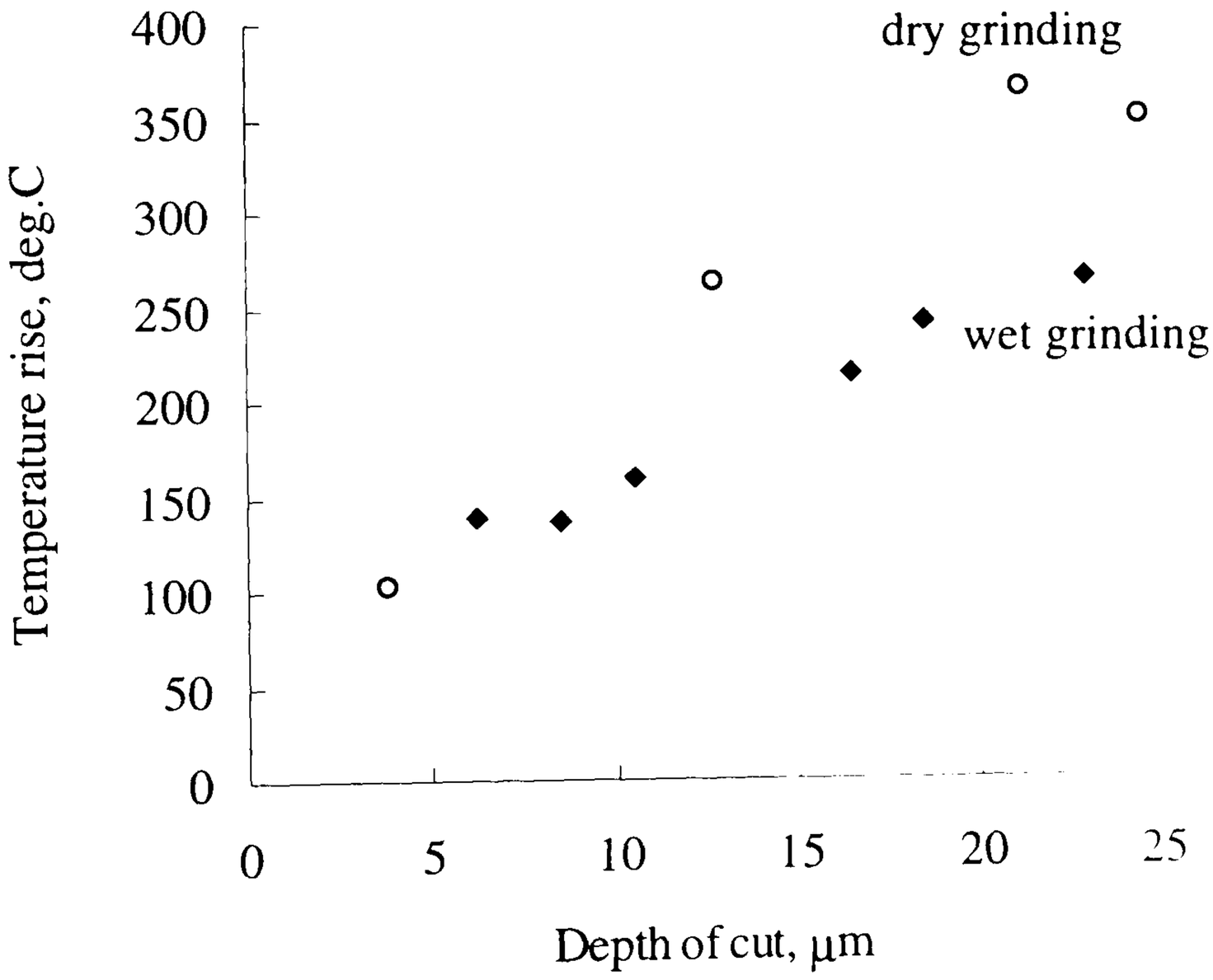

Figure 7.43 Theoretical temperature rise for dry and wet grinding on the short flank of the inverted vee form at $v_w = 0.2$ m/s

Experimental data:

Machine	: Abwood (surface grinding)
Material	: En31
Wheel	: 77A601H8VLNAA
Wheel diameter	: 200 mm, max
Wheelspeed	: 46 m/s
Workspeed	: 0.2 m/s
Workpiece shape	: inverted vee form
Coolant	: wet and dry

Model data:

$R_r = 10$
$e_{ch} = 6\ J/mm^3$
$h_c = 10000\ W/m^2K$
$r_o = 15\ \mu m$
$k_{ge} = 45\ W/mK$

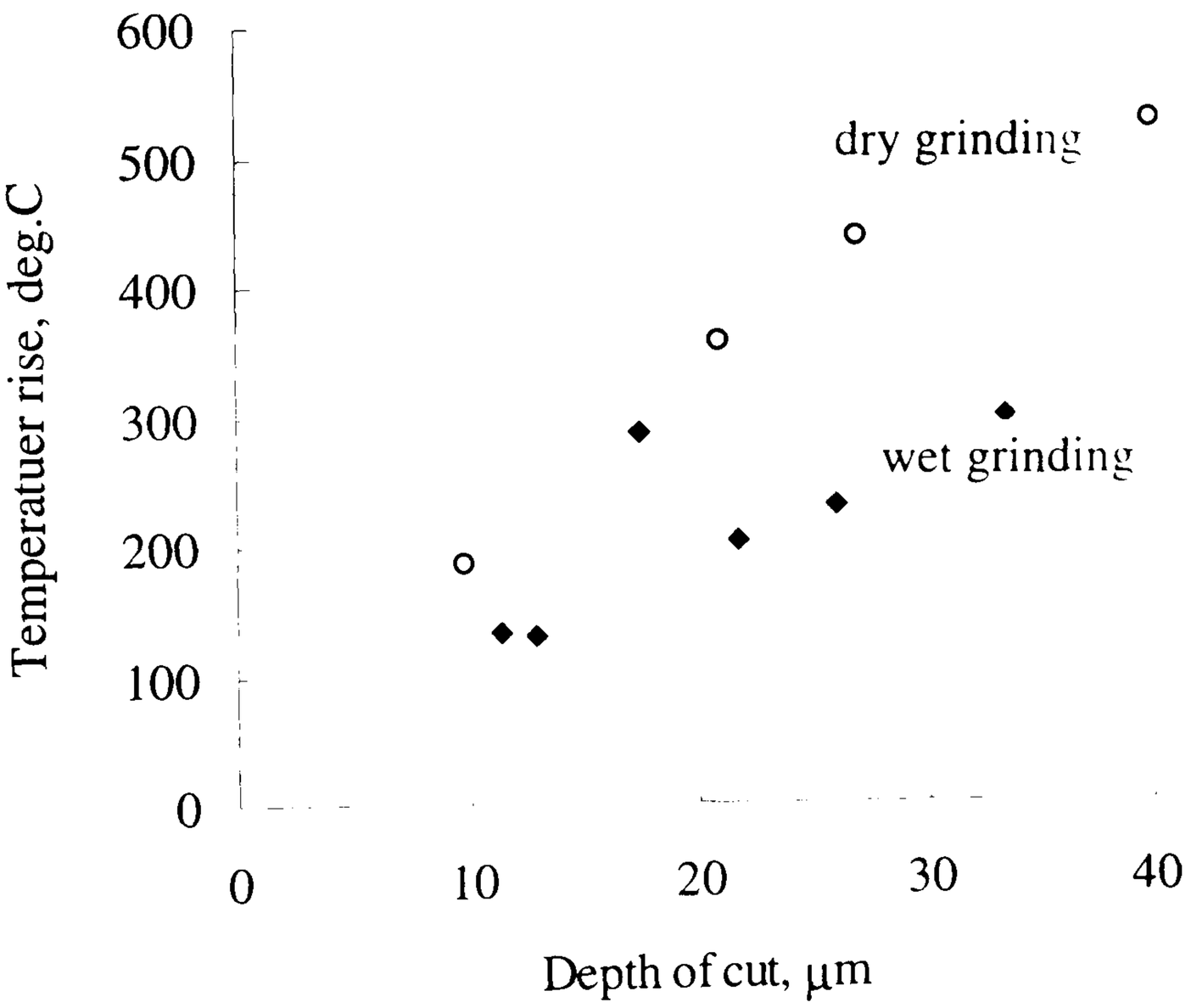

Figure 7.44 Theoretical temperature rise for dry and wet grinding at the apex of the inverted vee form at $v_w = 0.2$ m/s

Experimental data:

Machine	: Abwood (surface grinding)
Material	: En31
Wheel	: 77A601H8VLNAA
Wheel diameter	: 200 mm, max
Wheelspeed	: 46 m/s
Workspeed	: 0.1 m/s
Workpiece shape	: inverted vee form
Coolant	: wet and dry

Model data:

$R_r = 10$ $\quad r_o = 15\ \mu m$

$e_{ch} = 6\ J/mm^3$ $\quad k_{ge} = 45\ W/mK$

$h_c = 10000\ W/m^2K$

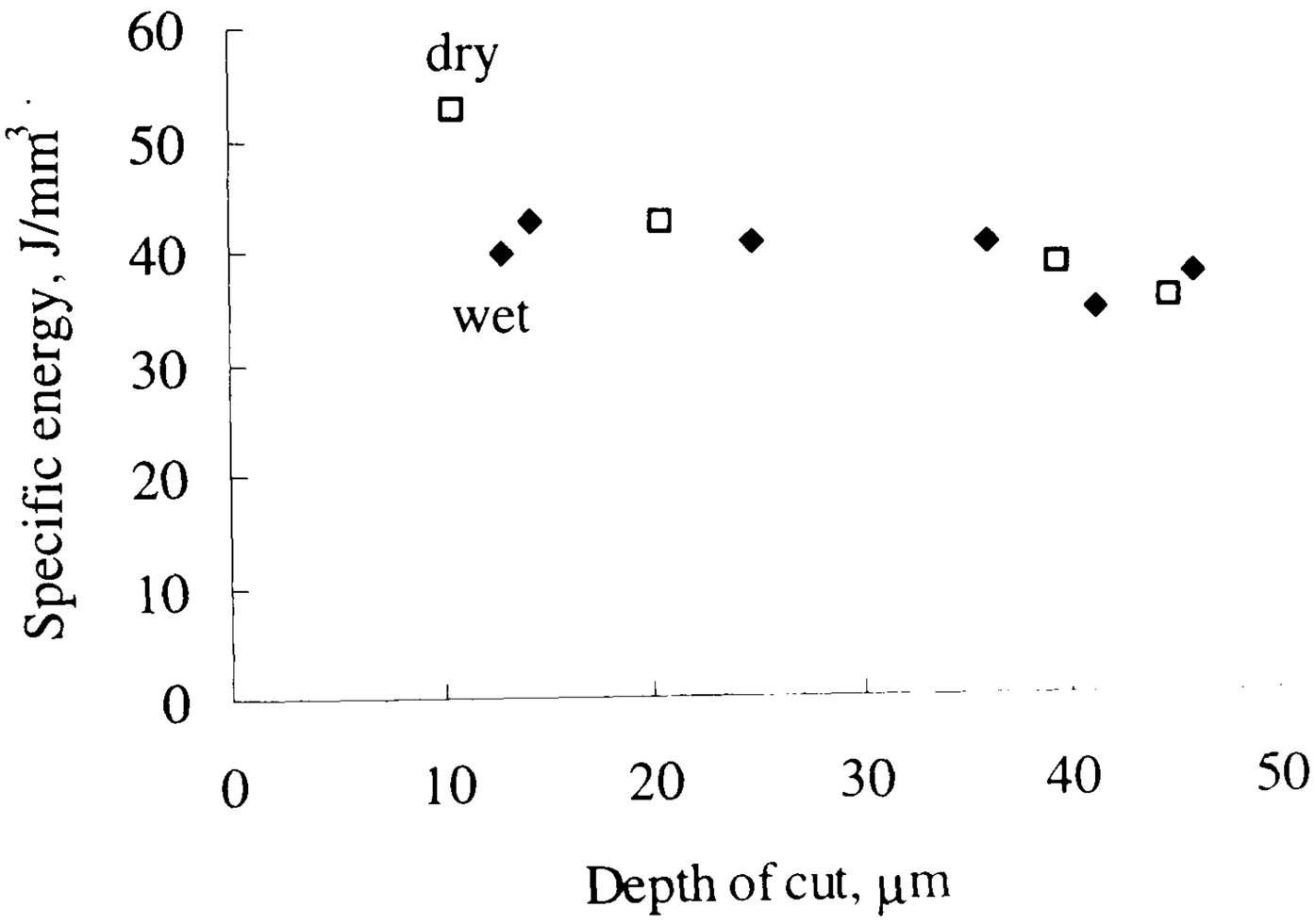

Figure 7.45 Specific energy for dry grinding and wet grinding at workspeed $v_w = 0.1$ m/s for the inverted vee form

Experimental data:

Machine	: Abwood (surface grinding)
Material	: En31
Wheel	: 77A601H8VLNAA
Wheel diameter	: 200 mm, max
Wheelspeed	: 46 m/s
Workspeed	: 0.2m/s
Workpiece shape	: inverted vee form
Coolant	: wet and dry

Model data:

$R_r = 10$ $r_o = 15\ \mu m$

$e_{ch} = 6\ J/mm^3$ $k_{ge} = 45\ W/mK$

$h_c = 10000\ W/m^2K$

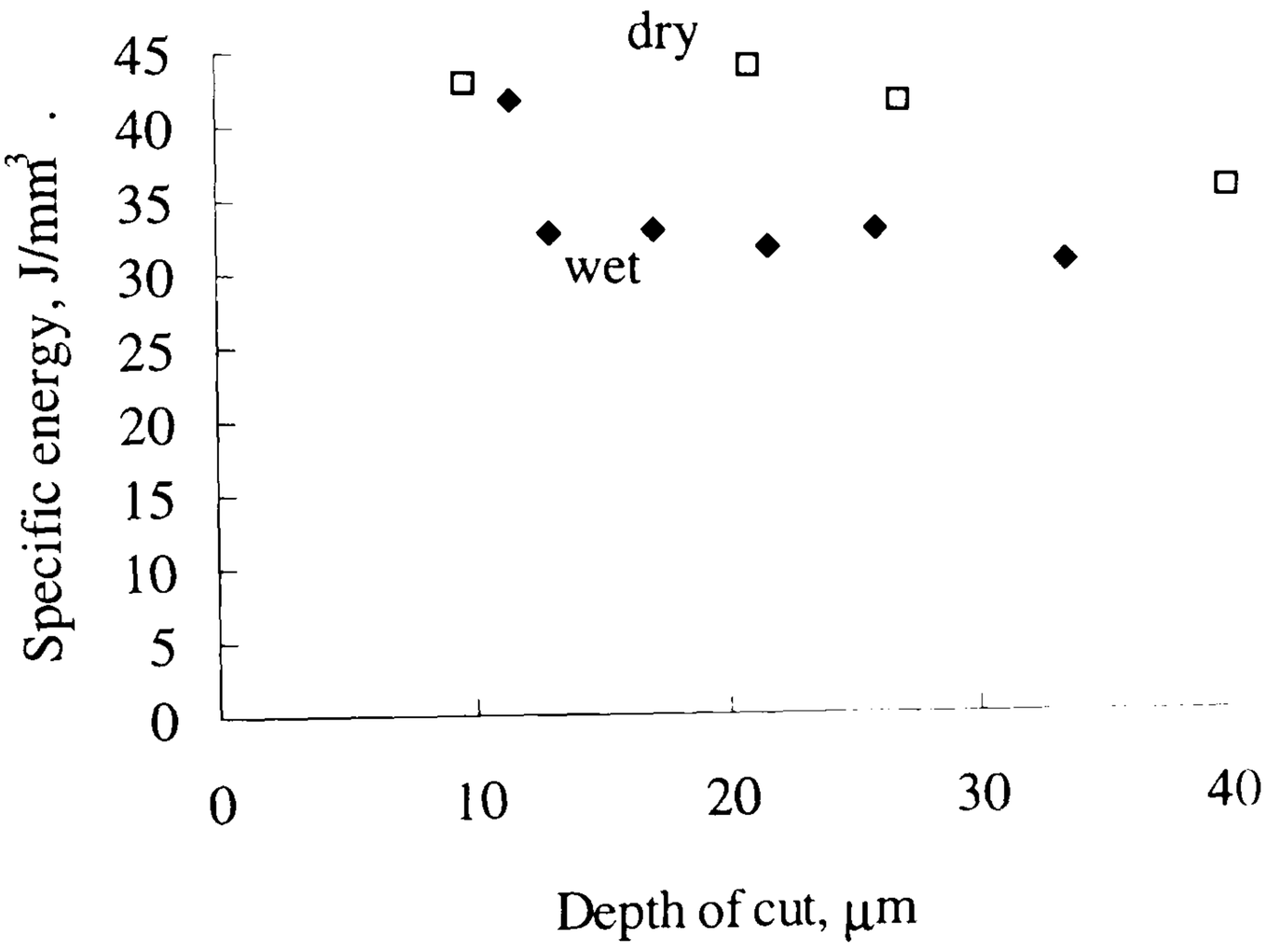

Figure 7. 46 Specific energy for dry grinding and wet grinding at a workspeed $v_w = 0.2$ m/s for the inverted vee form

Experimental data:

Machine	: Abwood (surface grinding)
Material	: En31
Wheel	: 77A601H8VLNAA
Wheel diameter	: 200 mm. max
Wheelspeed	: 46 m/s
Workspeed	: 0.1-0.3 m/s
Workpiece shape	: inverted vee form
Coolant	: wet and dry

Model data :

$R_r = 10$ $r_o = 15\ \mu m$

$e_{ch} = 6\ J/mm^3$ $h_c = 10{,}000\ W/m^2K$

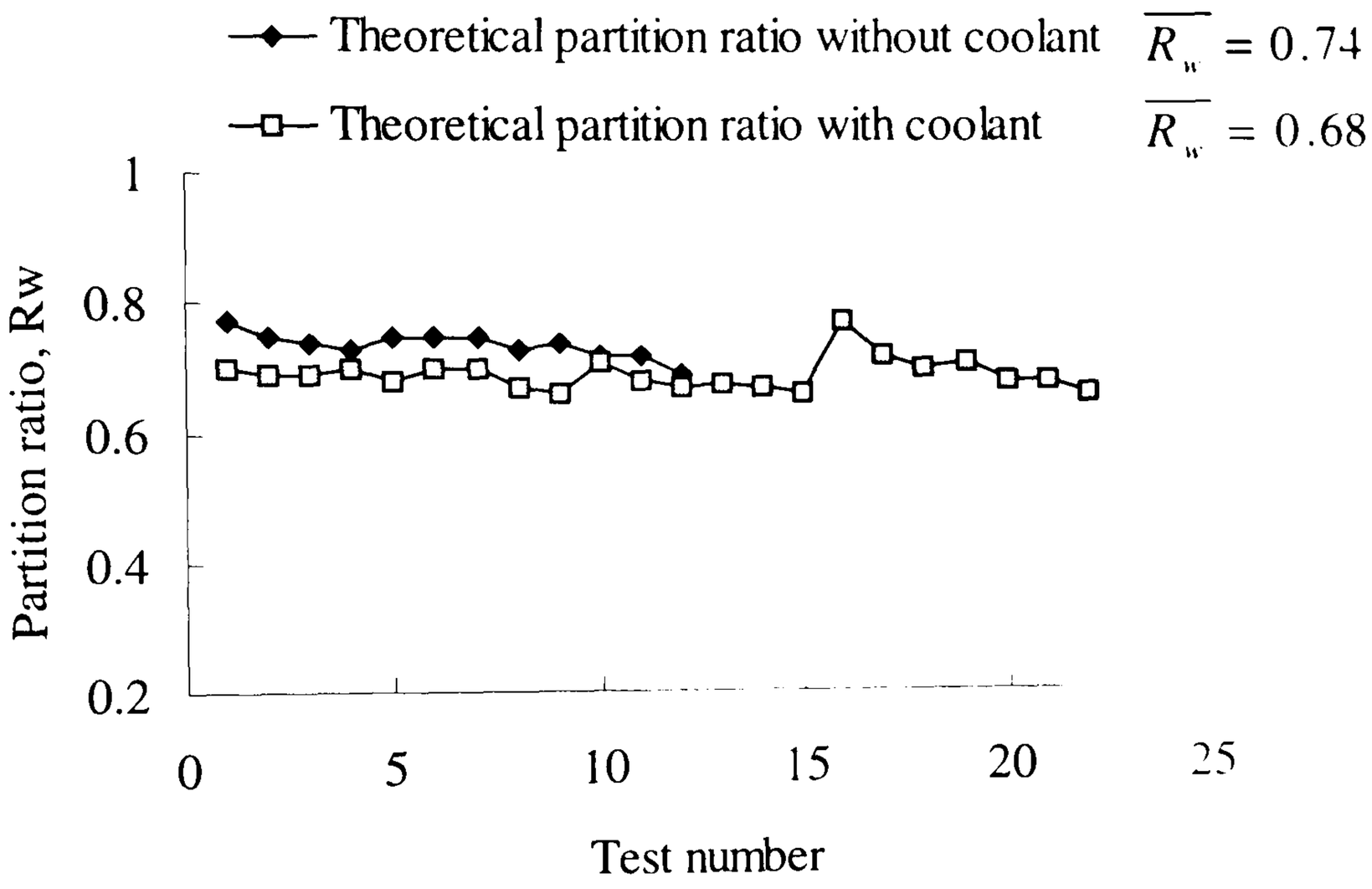

Figure 7.47 Theoretical partition ratio with and without coolant for the inverted vee form

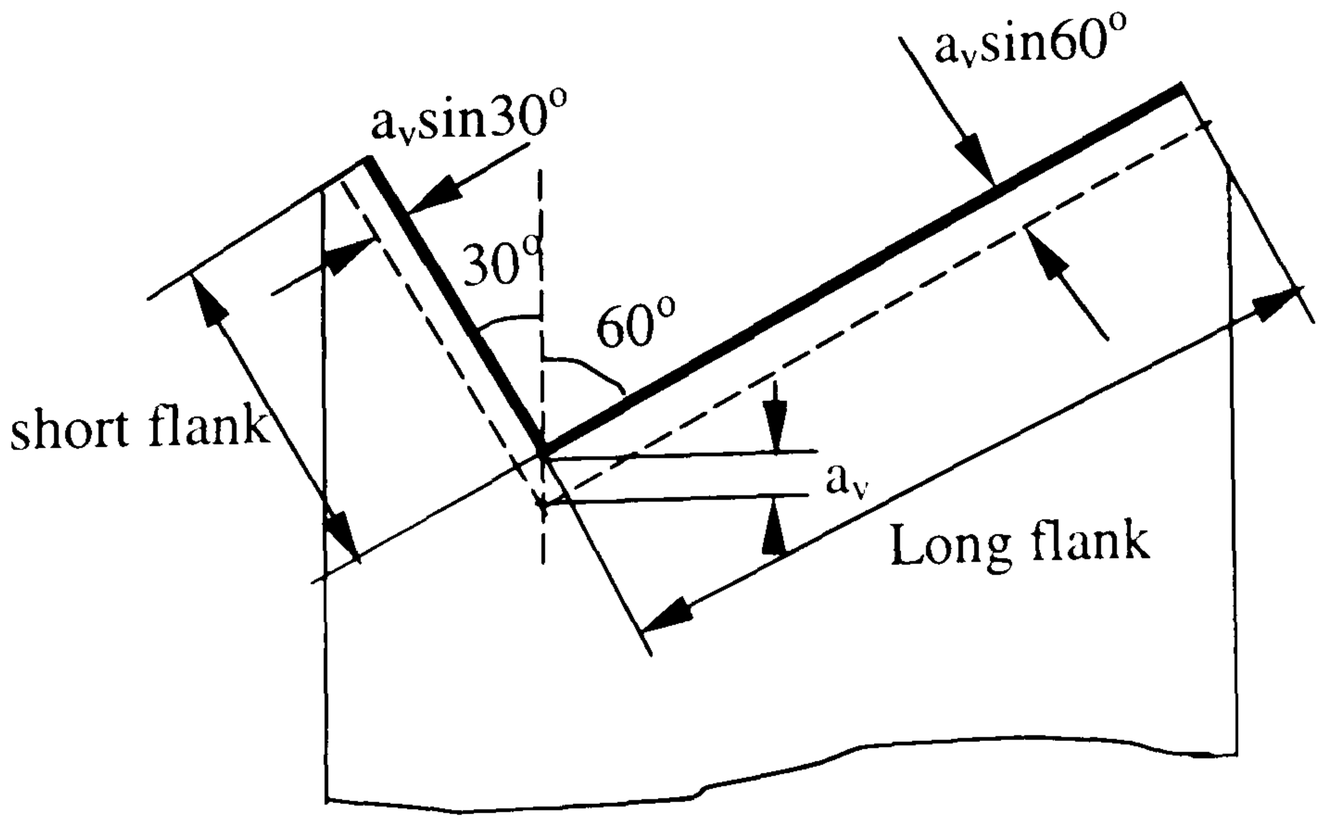

Figure 7.48 The workpiece of vee form

Experimental data:

Machine	: Abwood (surface grinding)
Material	: En31
Wheel	: 77A601H8VLNAA
Wheel diameter	: 200 mm, max
Wheelspeed	: 46 m/s
Workspeed	: 0.1-0.2 m/s
Workpiece shape	: vee form
Coolant	: dry

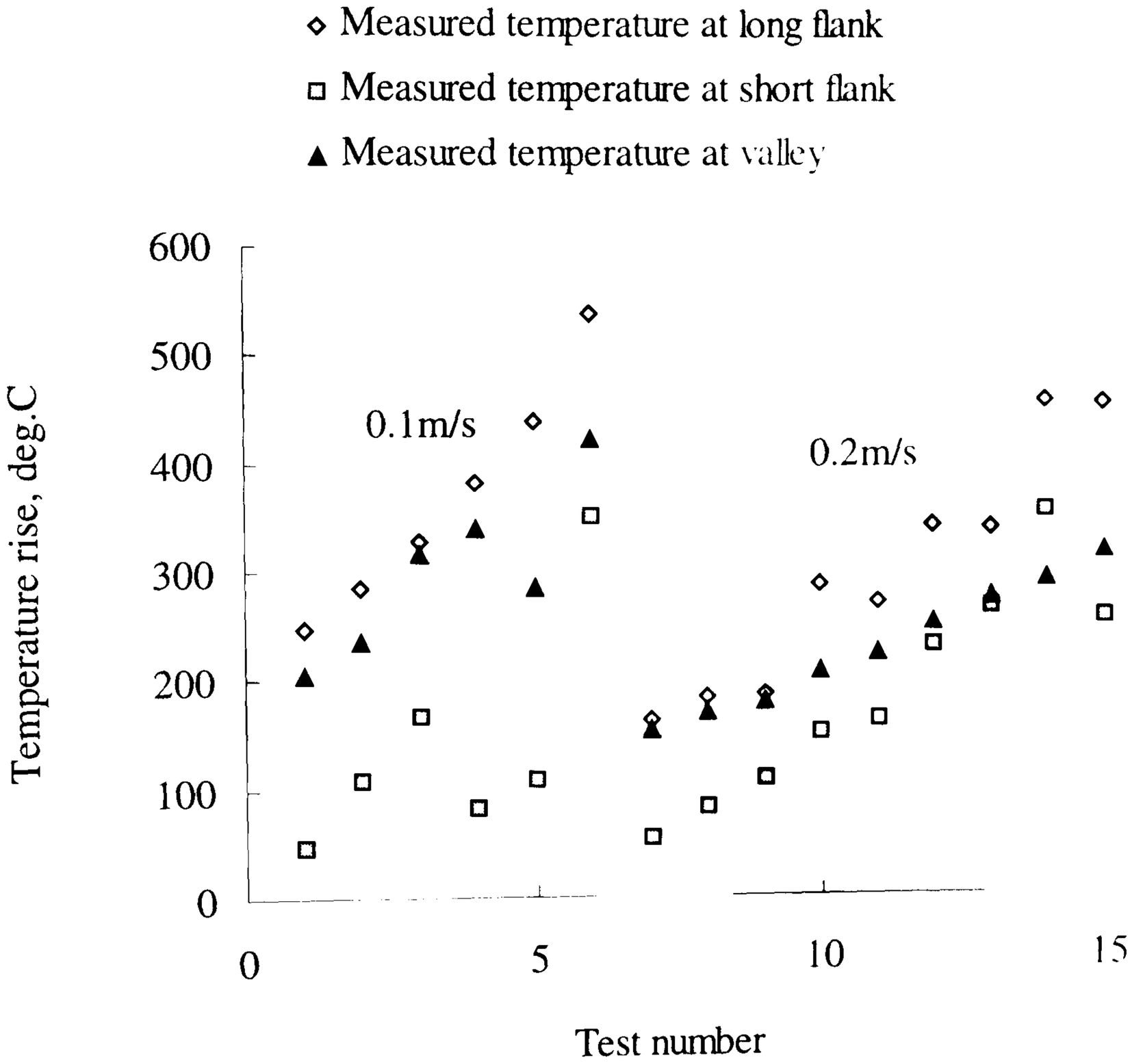

Figure 7.49 Measured temperatures for dry vee form grinding at workspeeds 0.1-0.2 m/s and different depths of cut

Experimental data:

Machine	: Abwood (surface grinding)
Material	: En31
Wheel	: 77A601H8VLNAA
Wheel diameter	: 200 mm, max
Wheelspeed	: 46 m/s
Workspeed	: 0.1 m/s
Workpiece shape	: vee form
Coolant	: dry

Model data :

$R_r = 10$	$r_o = 15\ \mu m$
$\kappa_g = 45$ W/mK	$e_{ch} = 6$ J/mm^3

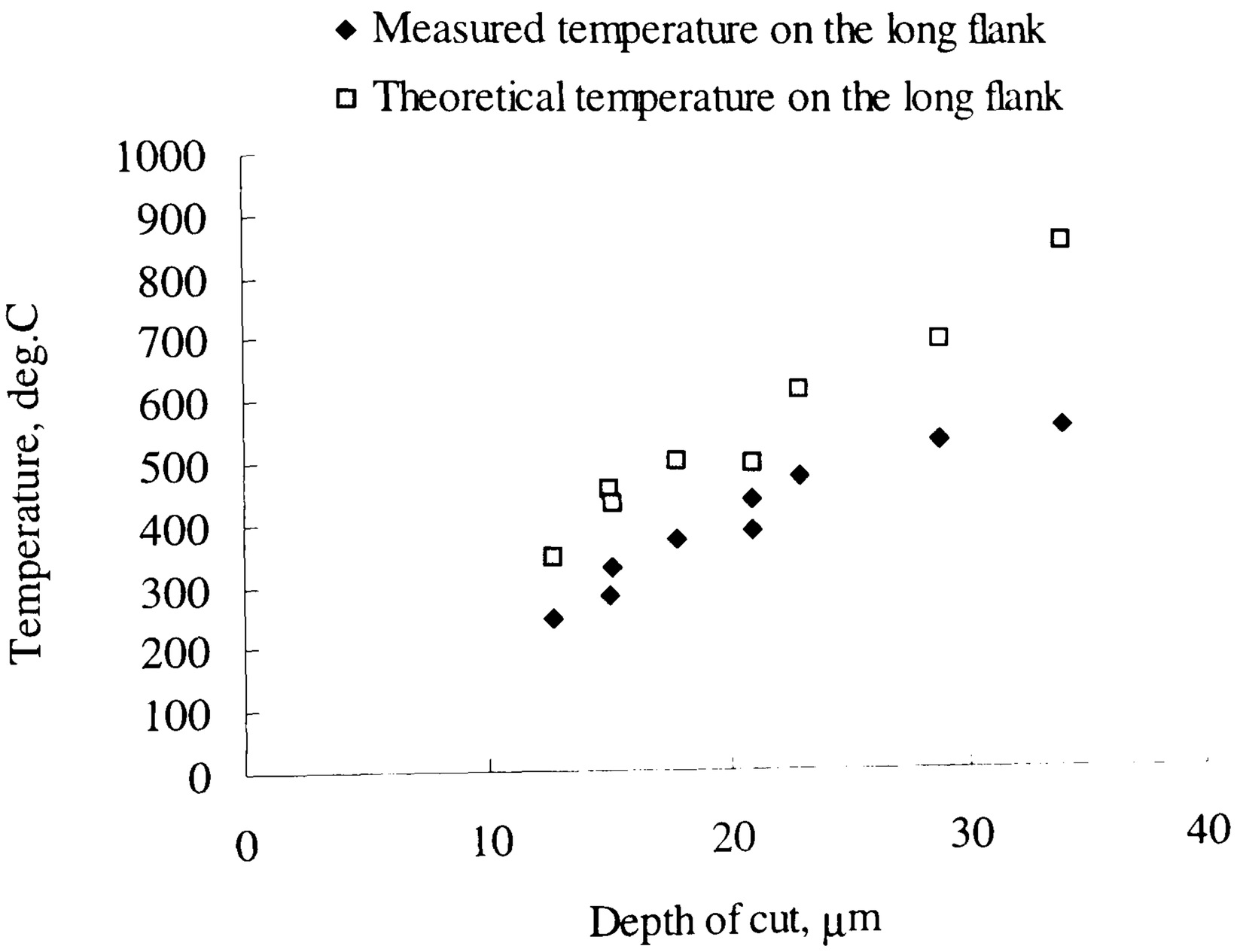

Figure 7.50 Measured and predicted temperatures against depth of cut for the long flank in dry vee form grinding at 0.1m/s

Experimental data:

Machine	: Abwood (surface grinding)
Material	: En31
Wheel	: 77A601H8VLNAA
Wheel diameter	: 200 mm, max
Wheelspeed	: 46 m/s
Workspeed	: 0.2 m/s
Workpiece shape	: vee form
Coolant	: dry

Model data :

$R_r = 10$ $\quad r_o = 15\ \mu m$

$\kappa_g = 45\ W/mK$ $\quad e_{ch} = 6\ J/mm^3$

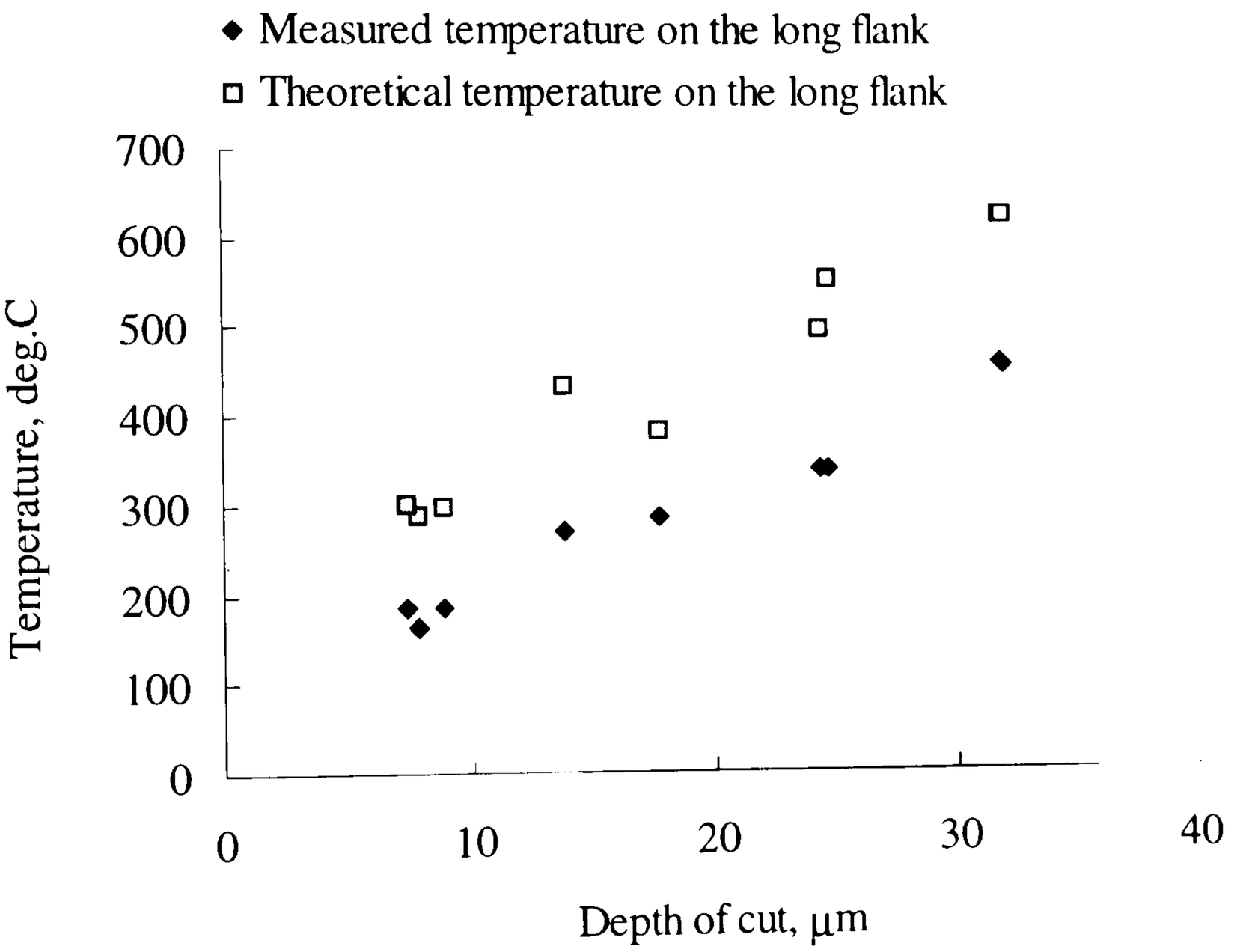

Figure 7.51 Measured and predicted temperatures against depth of cut for the long flank in dry vee form grinding at 0.2m/s

Experimental data:

Machine	: Abwood (surface grinding)
Material	: En31
Wheel	: 77A601H8VLNAA
Wheel diameter	: 200 mm, max
Wheelspeed	: 46 m/s
Workspeed	: 0.1 m/s
Workpiece shape	: vee form
Coolant	: dry

Model data :

$R_r = 10$	$r_o = 15\ \mu m$
$\kappa_g = 45$ W/mK	$e_{ch} = 6$ J/mm^3

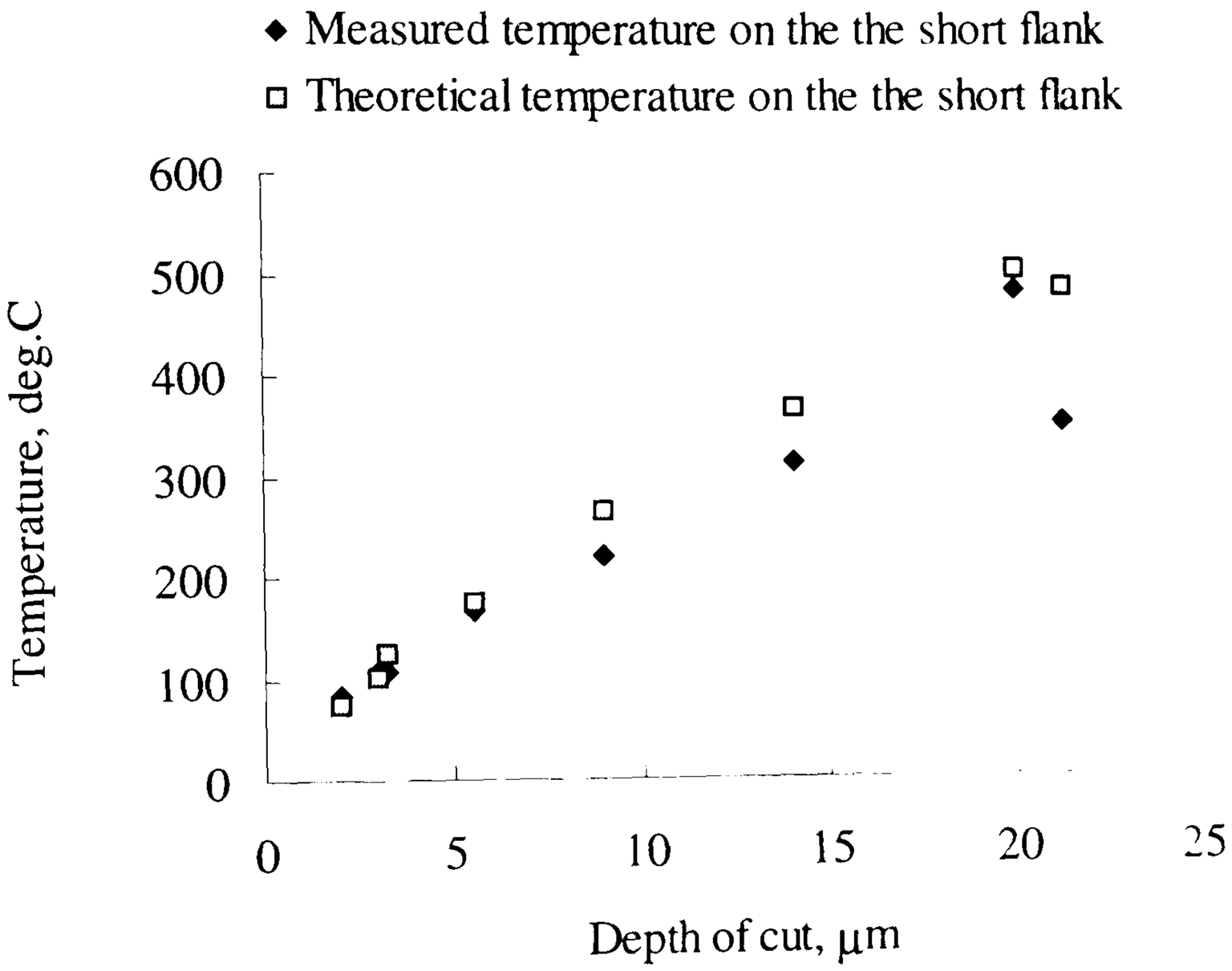

Figure 7.52 Measured and predicted temperature against depth of cut for the short flank in dry vee form grinding at 0.1m/s

Experimental data:

Machine	: Abwood (surface grinding)
Material	: En31
Wheel	: 77A601H8VLNAA
Wheel diameter	: 200 mm, max
Wheelspeed	: 46 m/s
Workspeed	: 0.2 m/s
Workpiece shape	: vee form
Coolant	: dry

Model data :

$R_r = 10$ $r_o = 15\ \mu m$

$\kappa_g = 45$ W/mK $e_{ch} = 6$ J/mm^3

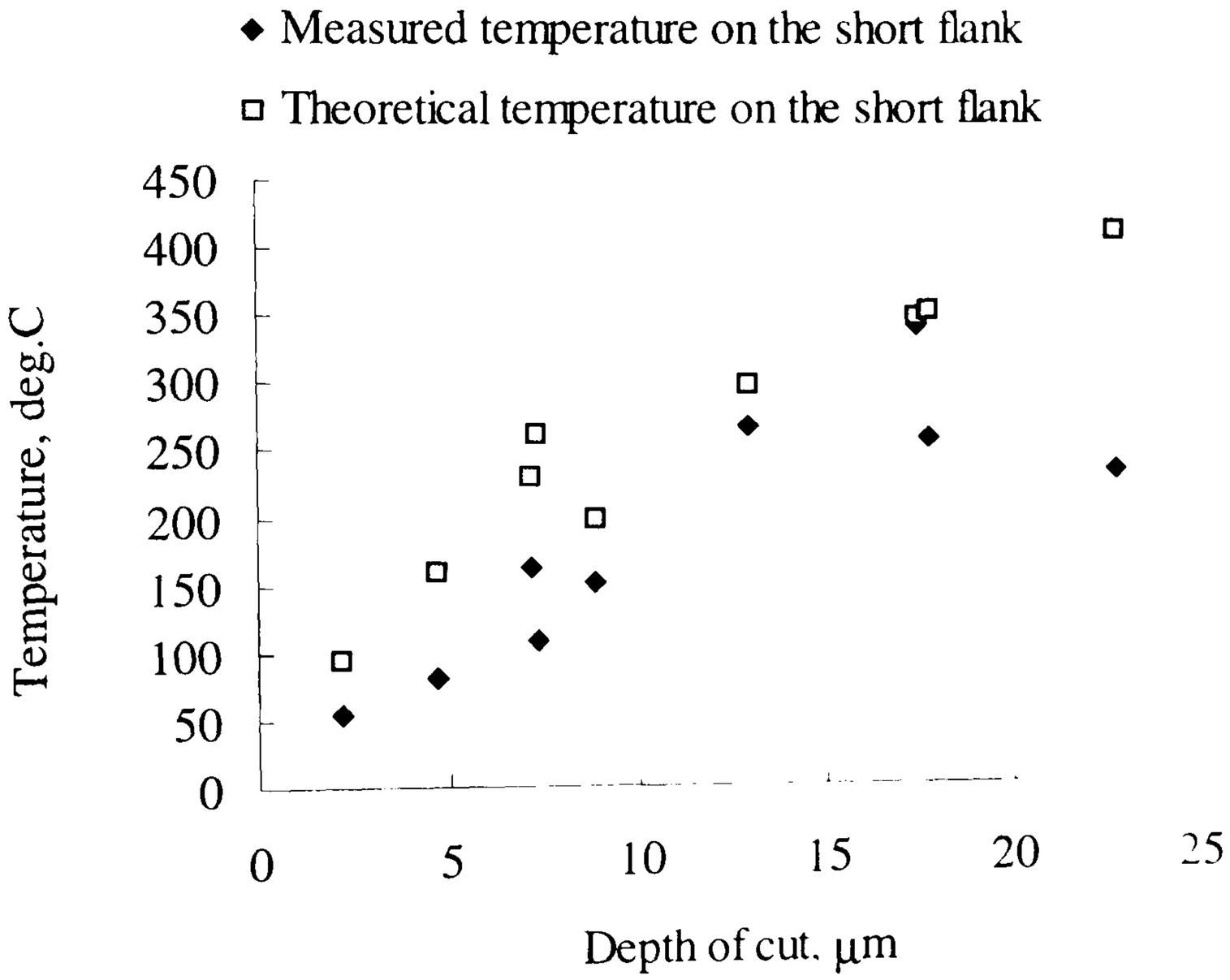

Figure 7.53 Measured and predicted temperature against depth of cut for the short flank in dry vee form grinding at 0.2m/s

Experimental data:

Machine	: Abwood (surface grinding)
Material	: En31
Wheel	: 77A601H8VLNAA
Wheel diameter	: 200 mm. max
Wheelspeed	: 46 m/s
Workspeed	: 0.1-0.2 m/s
Workpiece shape	: vee form
Coolant	: dry

Model data :

$R_r = 10$ $r_o = 15\ \mu m$

$\kappa_g = 45$ W/mK $e_{ch} = 6$ J/mm^3

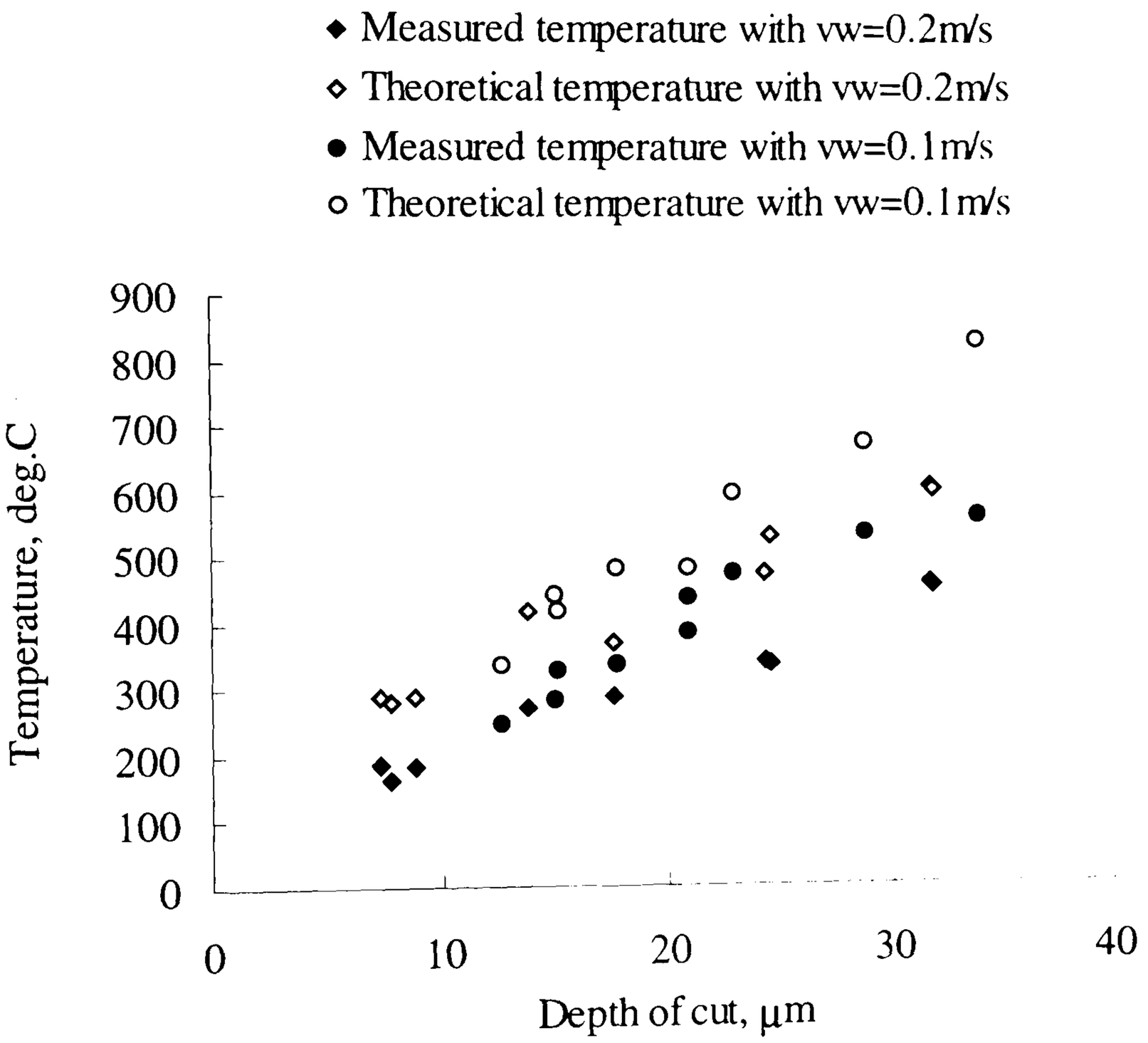

Figure 7.54 Measured and predicted temperature for different workspeeds for the long flank in dry vee form grinding

Experimental data:

Machine	: Abwood (surface grinding)
Material	: En31
Wheel	: 77A601H8VLNAA
Wheel diameter	: 200 mm, max
Wheelspeed	: 46 m/s
Workspeed	: 0.1-0.2 m/s
Workpiece shape	: vee form
Coolant	: dry

Model data :

$R_r = 10$ $\quad r_o = 15\ \mu m$

$\kappa_g = 45$ W/mK $\quad e_{ch} = 6$ J/mm^3

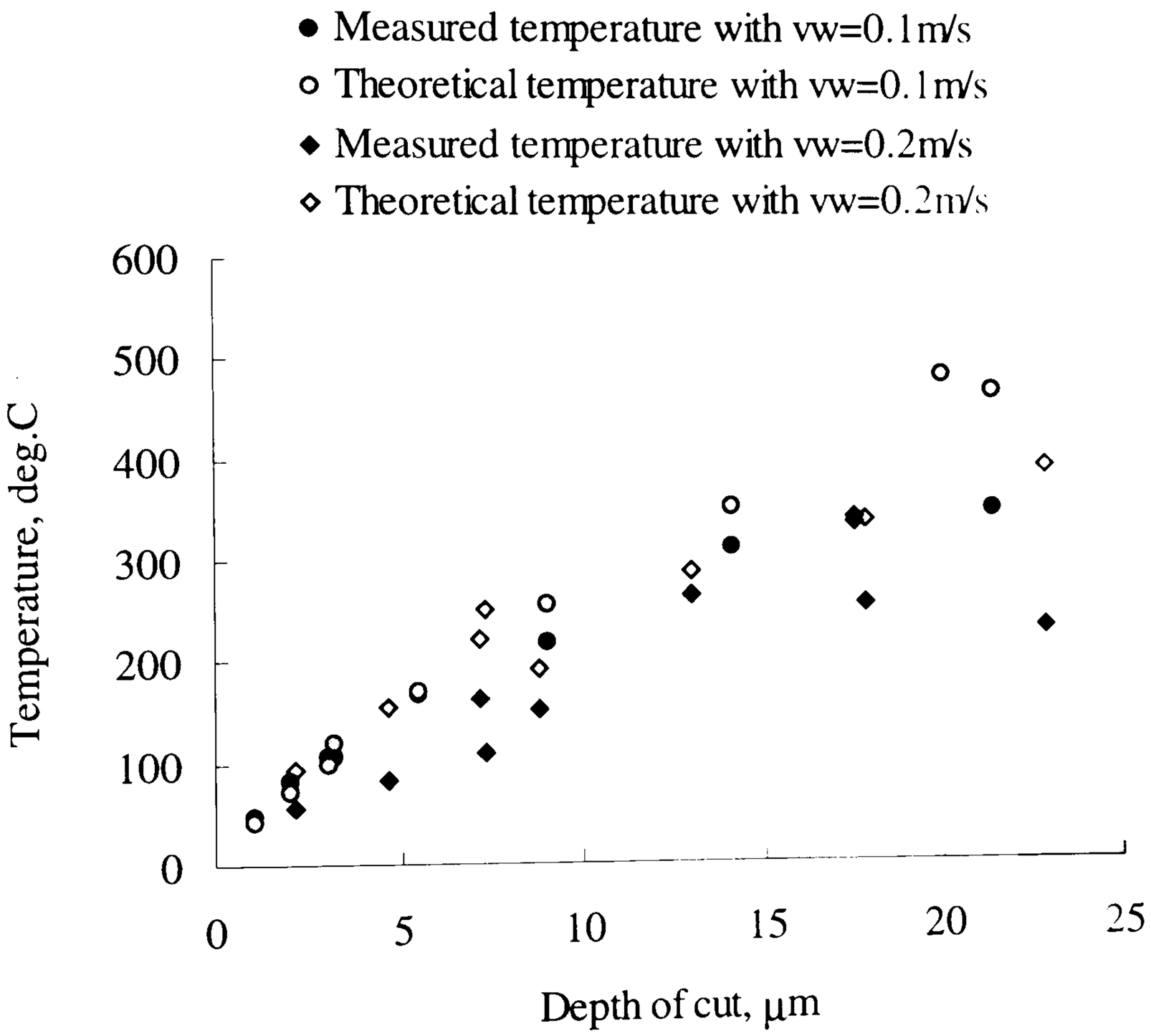

Figure 7.55 Measured and predicted temperature for different workspeeds for the short flank in dry vee form grinding

Experimental data:

Machine	: Abwood (surface grinding)
Material	: En31
Wheel	: 77A601H8VLNAA
Wheel diameter	: 200 mm, max
Wheelspeed	: 46 m/s
Workspeed	: 0.2 m/s
Workpiece shape	: vee form
Coolant	: dry

Model data :

$R_r = 10$ $\quad r_o = 15\ \mu m$

$\kappa_g = 45$ W/mK $\quad e_{ch} = 6$ J/mm^3

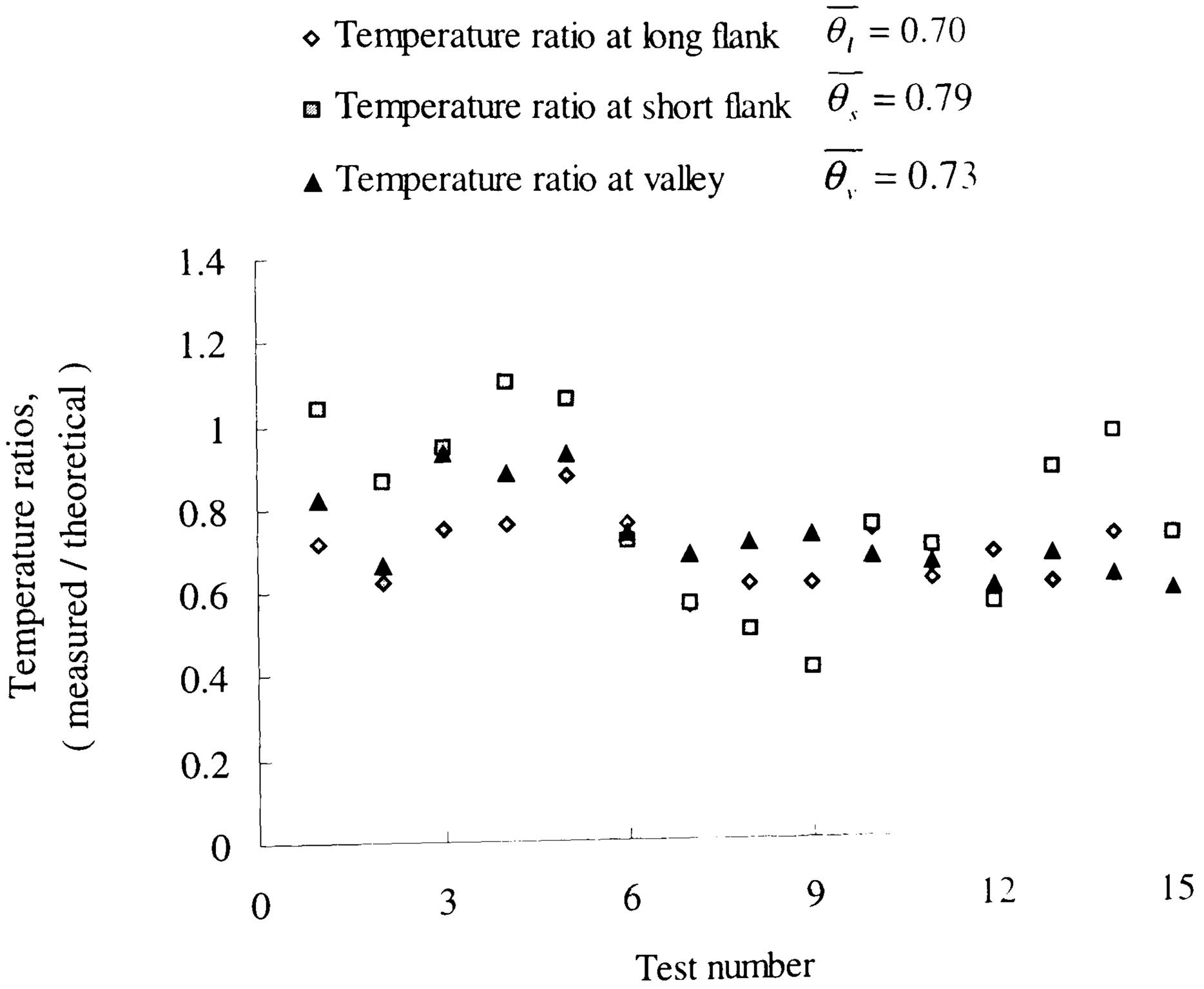

Figure 7.56 Ratio of measured and predicted temperature at the long flank, short flank and valley in dry vee form grinding

Experimental data:

Machine	: Abwood (surface grinding)
Material	: En31
Wheel	: 77A601H8VLNAA
Wheel diameter	: 200 mm, max
Wheelspeed	: 46 m/s
Workspeed	: 0.1-0.2 m/s
Workpiece shape	: vee form
Coolant	: dry

Model data :

$R_r = 10$ $\quad r_o = 15\ \mu m$

$\kappa_g = 45$ W/mK $\quad e_{ch} = 6$ J/mm^3

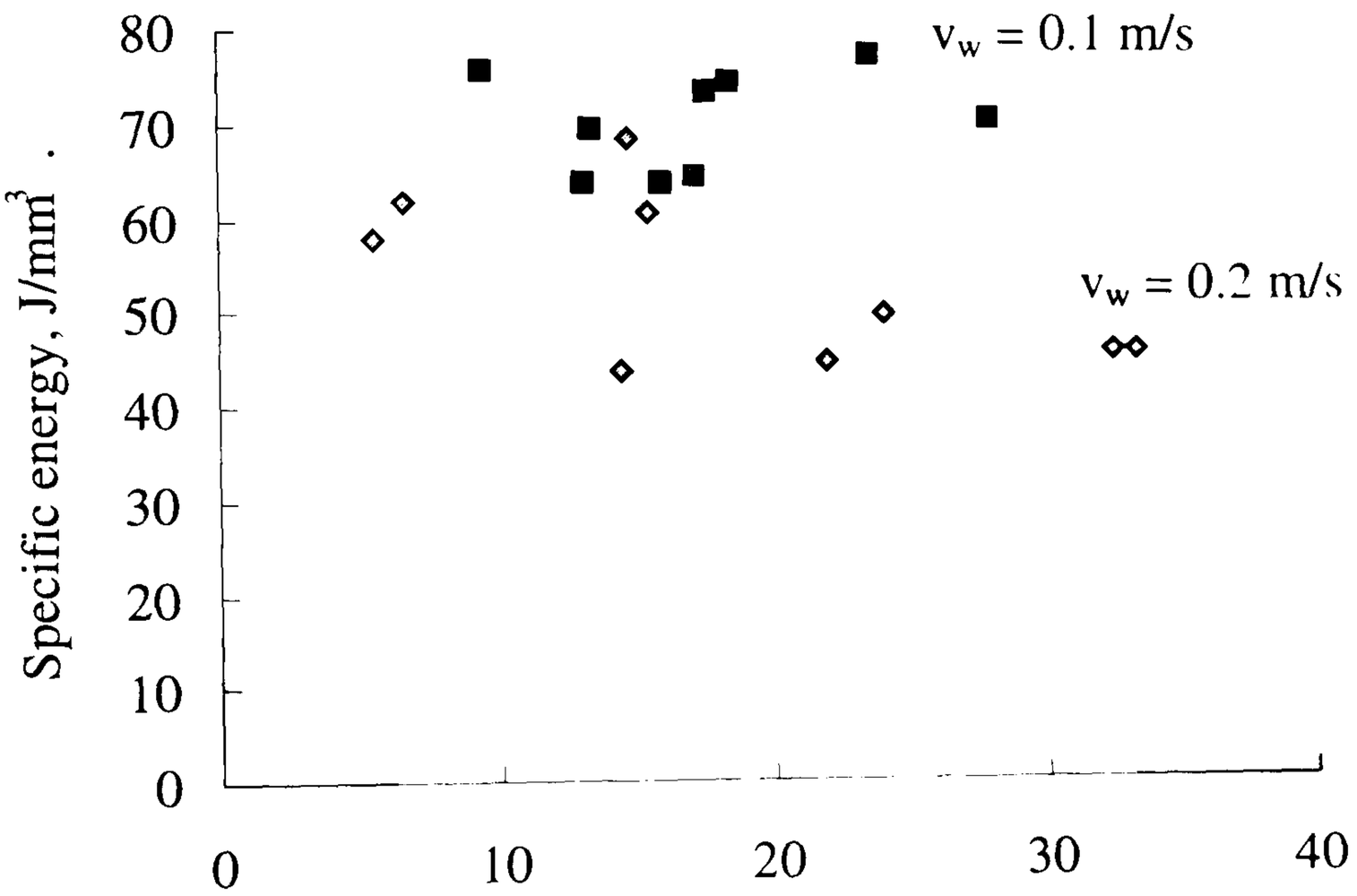

Figure 7.57 Specific energy with different workspeeds in dry vee form grinding

Experimental data:

Machine	: Abwood (surface grinding)
Material	: En31
Wheel	: 77A601H8VLNAA
Wheel diameter	: 200 mm, max
Wheelspeed	: 46 m/s
Workspeed	: 0.1-0.2 m/s
Workpiece shape	: vee form
Coolant	: dry

Model data :

$R_r = 10$ $r_o = 15\ \mu m$

$\kappa_g = 45$ W/mK $e_{ch} = 6$ J/mm^3

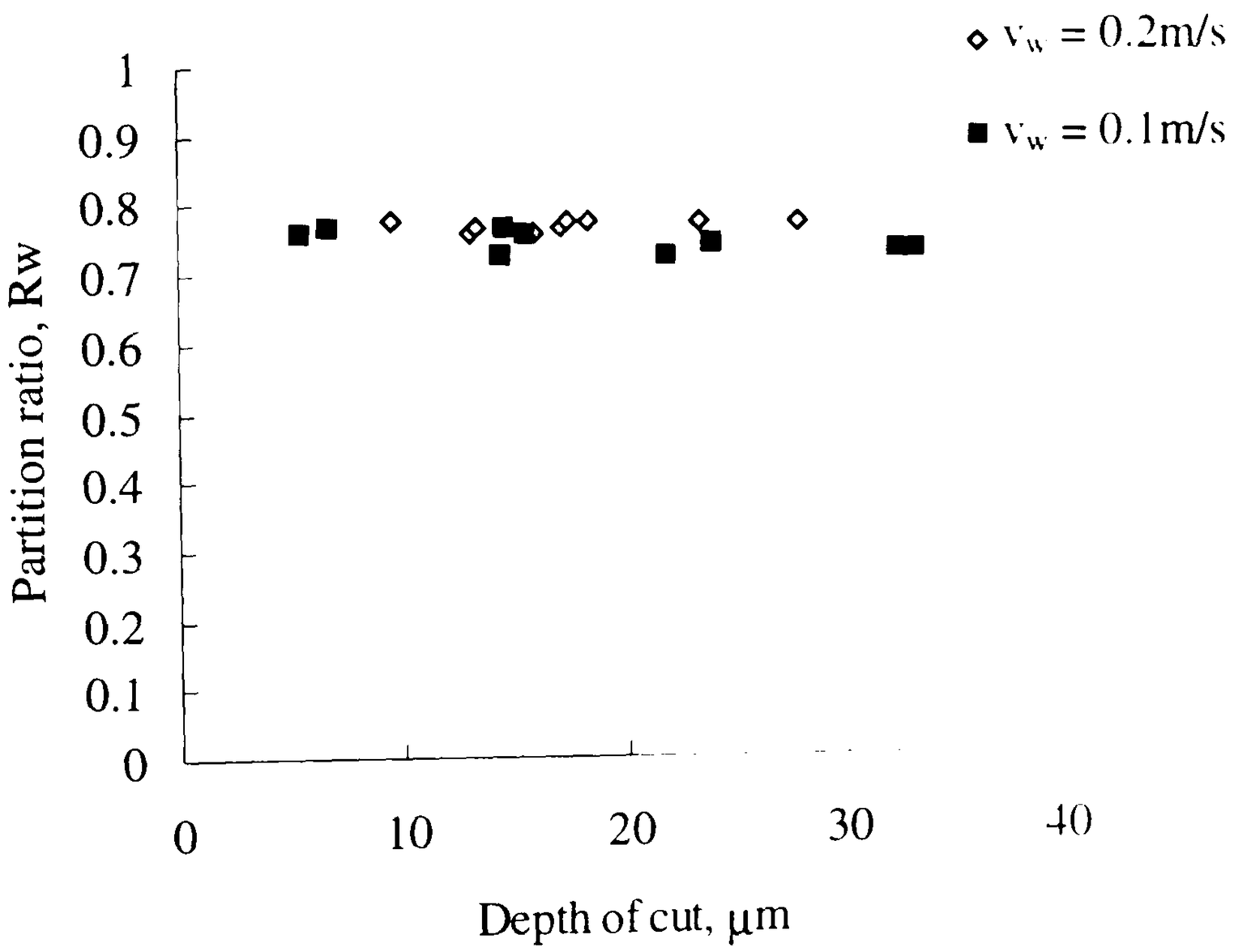

Figure 7.58 Theoretical partition ratio for different workspeeds in dry vee form grinding

Experimental data:

Machine	: Abwood (surface grinding)
Material	: En31
Wheel	: 77A601H8VLNAA
Wheel diameter	: 200 mm, max
Wheelspeed	: 46 m/s
Workspeed	: 0.1-0.2 m/s
Workpiece shape	: vee form
Coolant	: dry

Model data :

$R_r = 10$ $\quad r_o = 15\ \mu m$

$\kappa_g = 45$ W/mK $\quad e_{ch} = 6$ J/mm^3

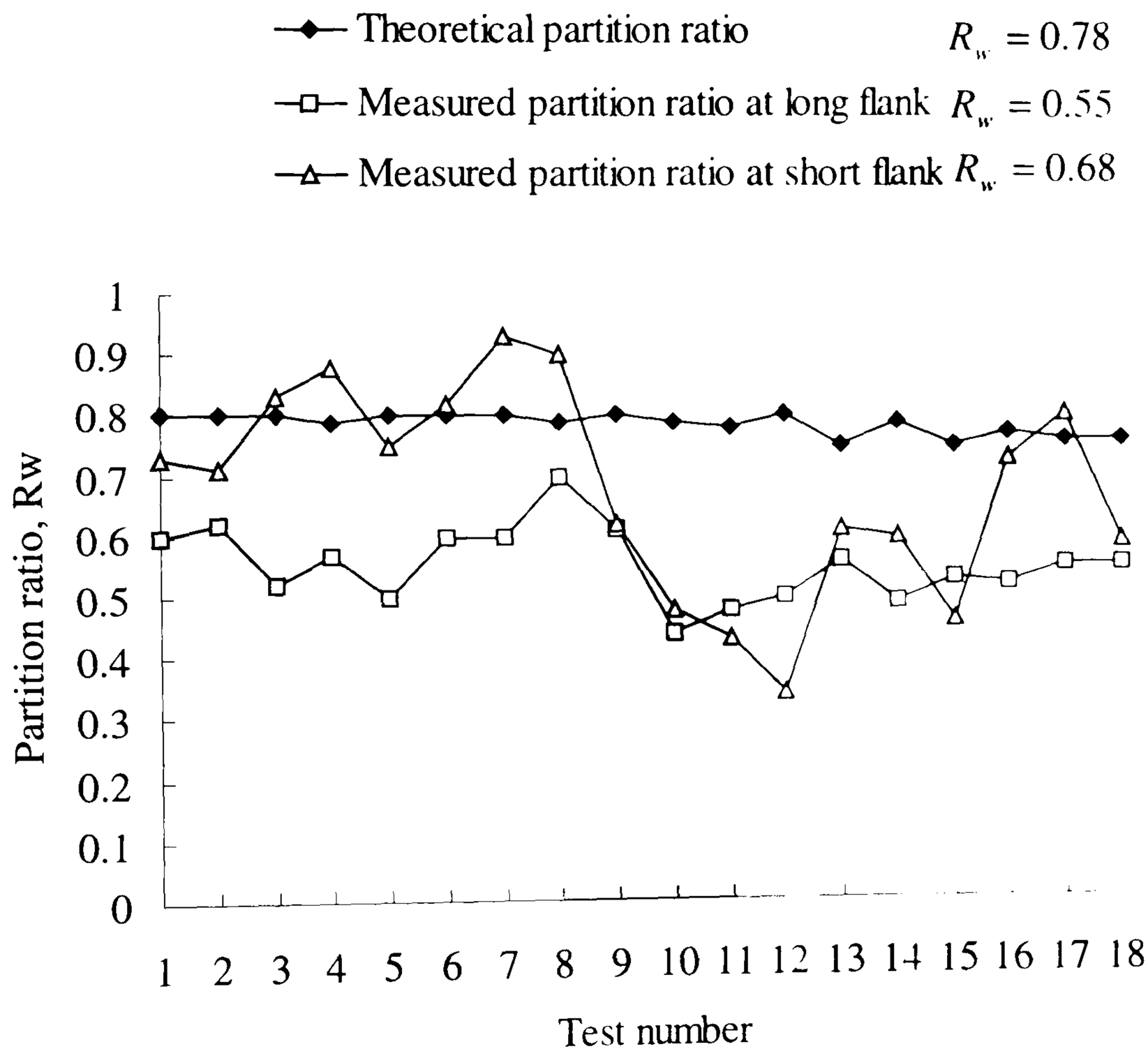

Figure 7.59 Measured and predicted partition ratios based on experimental data for dry vee form grinding

Experimental data:

Machine	: Abwood (surface grinding)
Material	: En31
Wheel	: 77A601H8VLNAA
Wheel diameter	: 200 mm, max
Wheelspeed	: 46 m/s
Workspeed	: 0.2-0.3 m/s
Workpiece shape	: vee form
Coolant	: wet

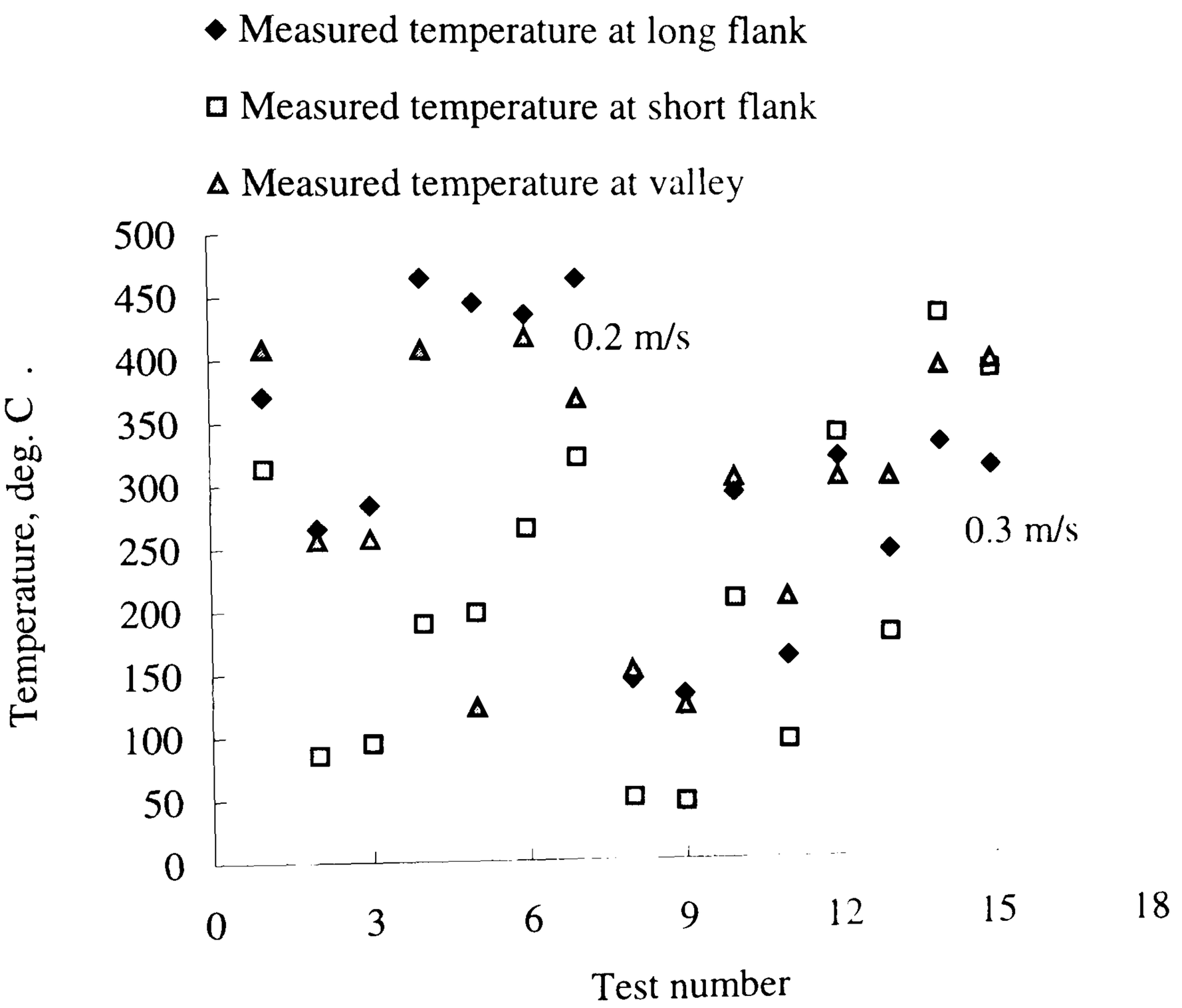

Figure 7.60 Measured temperature at the long flank, short flank and valley of vee form for wet grinding

Experimental data:

Machine	: Abwood (surface grinding)
Material	: En31
Wheel	: 77A601H8VLNAA
Wheel diameter	: 200 mm, max
Wheelspeed	: 46 m/s
Workspeed	: 0.2-0.3 m/s
Workpiece shape	: vee form
Coolant	: wet

Model data :

$R_r = 10$ $r_o = 15\ \mu m$

$\kappa_g = 45\ W/mK$ $e_{ch} = 6\ J/mm^3$

$h_c = 10000\ W/m^2K$

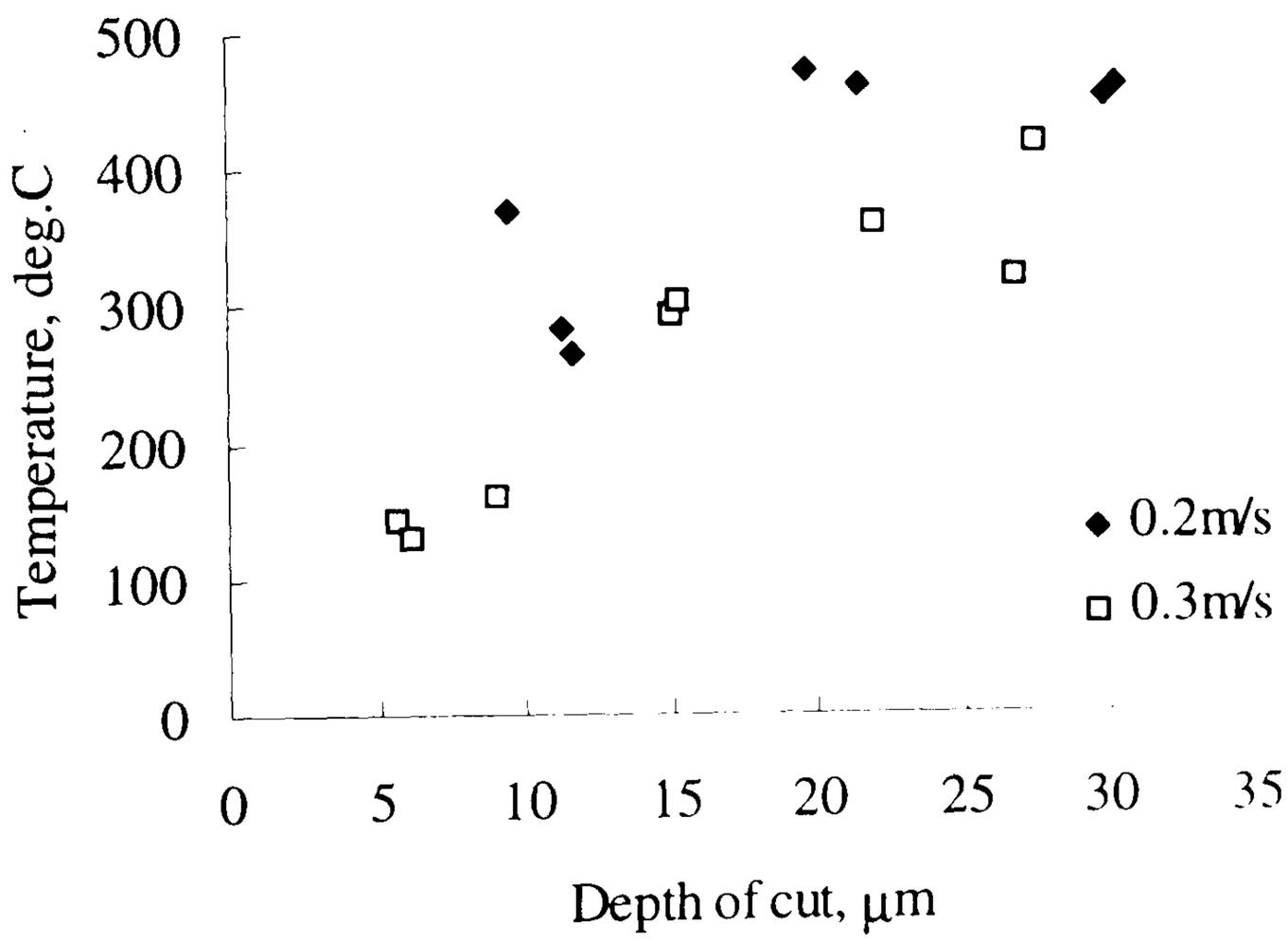

Figure 7.61 Temperatures against depth of cut with different workspeeds on the long flank of the vee form in wet grinding

Experimental data:

Machine	: Abwood (surface grinding)
Material	: En31
Wheel	: 77A601H8VLNAA
Wheel diameter	: 200 mm, max
Wheelspeed	: 46 m/s
Workspeed	: 0.2-0.3 m/s
Workpiece shape	: vee form
Coolant	: wet

Model data :

$R_r = 10$ $\quad r_o = 15\ \mu m$

$\kappa_g = 45\ W/mK$ $\quad e_{ch} = 6\ J/mm^3$

$h_c = 10000\ W/m^2K$

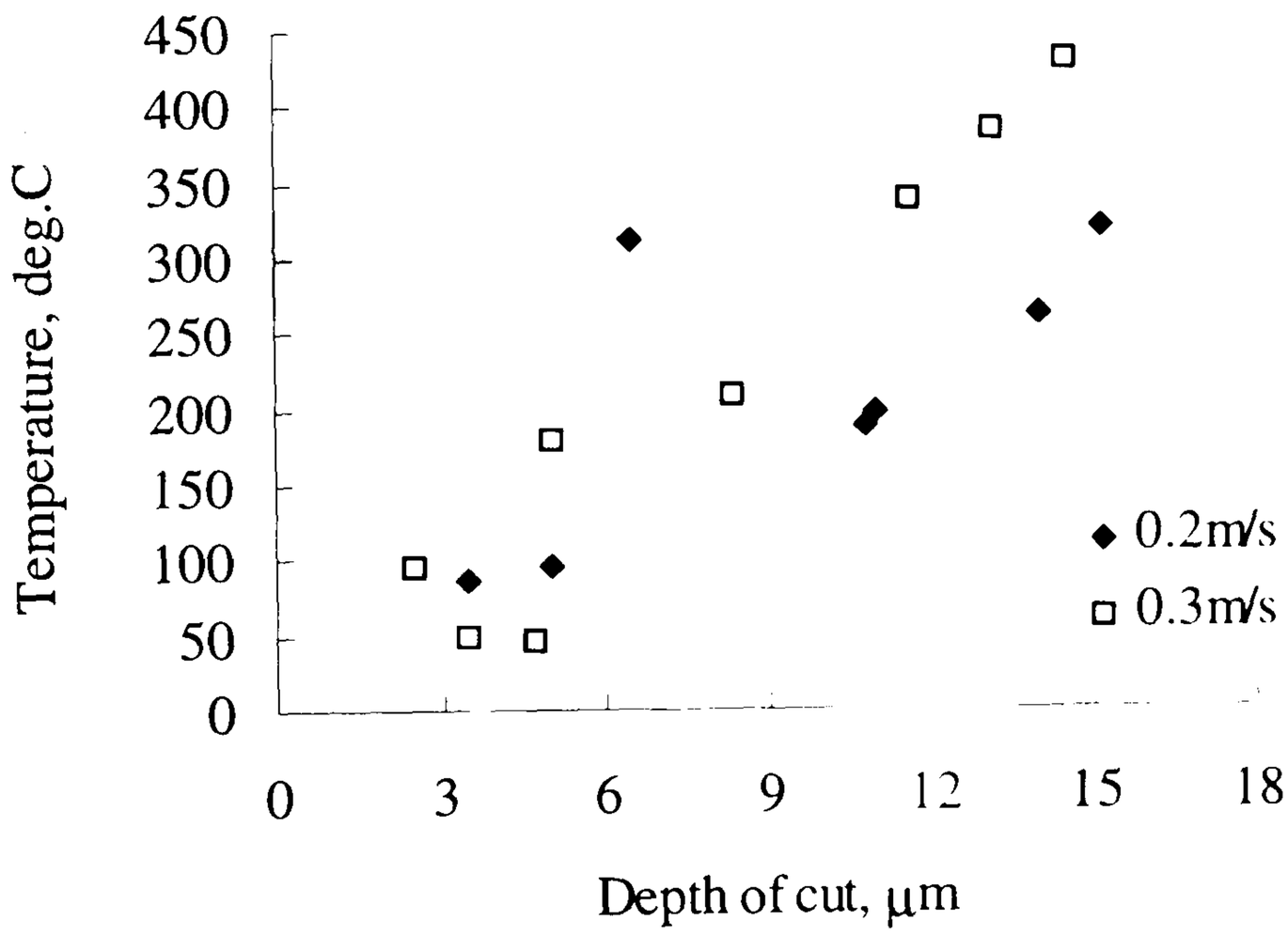

Figure 7.62 Temperature against depth of cut for different workspeeds on the short flank in wet vee form grinding

Experimental data:

Machine	: Abwood (surface grinding)
Material	: En31
Wheel	: 77A601H8VLNAA
Wheel diameter	: 200 mm. max
Wheelspeed	: 46 m/s
Workspeed	: 0.2-0.3 m/s
Workpiece shape	: vee form
Coolant	: wet

Model data :

$R_r = 10$ $\quad r_o = 15\ \mu m$

$\kappa_g = 45\ W/mK$ $\quad e_{ch} = 6\ J/mm^3$

$h_c = 10000\ W/m^2K$

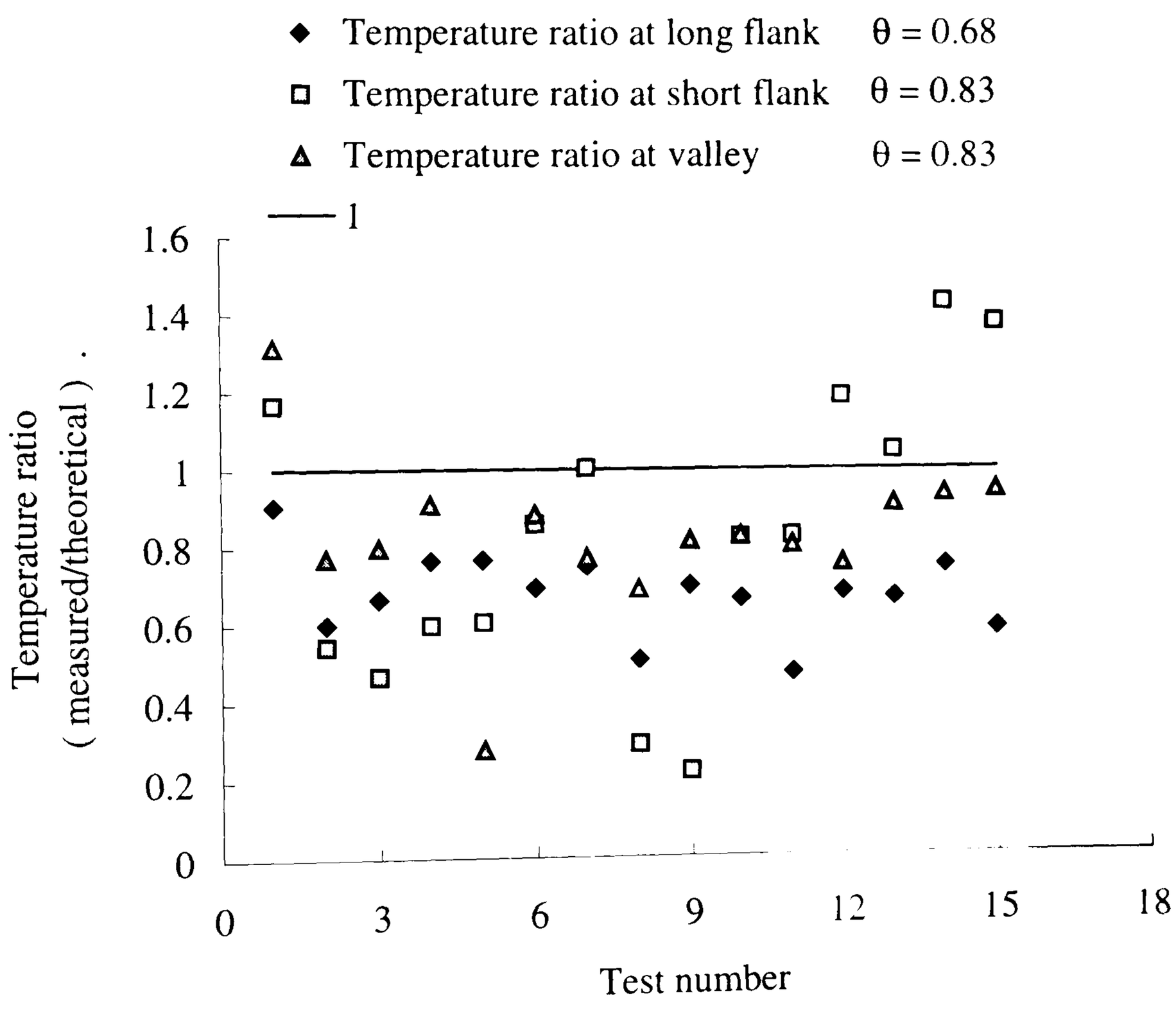

Figure 7.63 Ratio between measured and predicted temperature on the long flank, short flank and valley in wet vee form grinding

Experimental data:

Machine	: Abwood (surface grinding)
Material	: En31
Wheel	: 77A601H8VLNAA
Wheel diameter	: 200 mm, max
Wheelspeed	: 46 m/s
Workspeed	: 0.2-0.3 m/s
Workpiece shape	: vee form
Coolant	: wet

Model data :

$R_r = 10$ $r_o = 15\ \mu m$

$\kappa_g = 45\ W/mK$ $e_{ch} = 6\ J/mm^3$

$h_c = 10000\ W/m^2K$

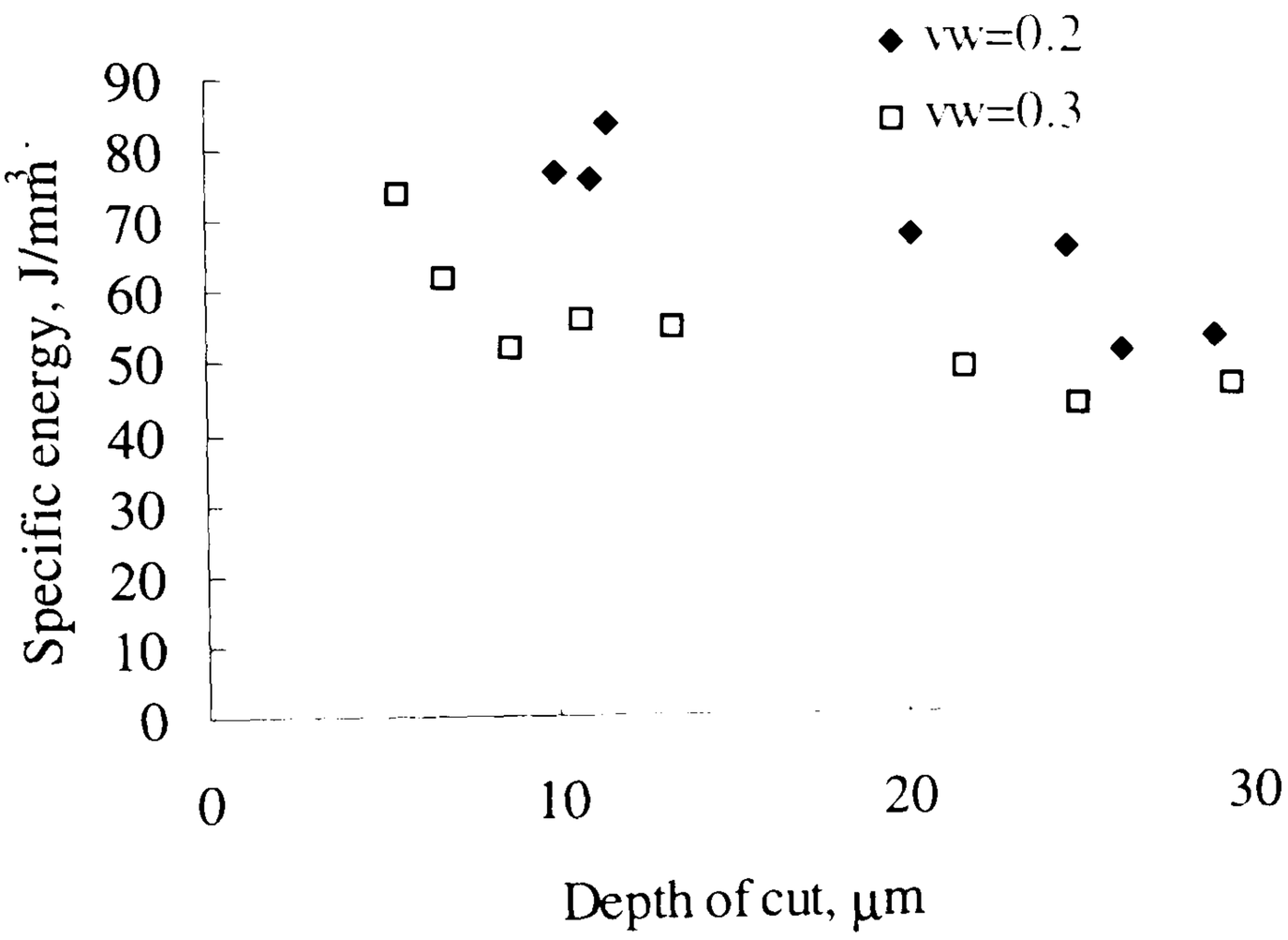

Figure 7.64 Specific energy for different workspeeds in wet vee form grinding

Experimental data:

Machine	: Abwood (surface grinding)
Material	: En31
Wheel	: 77A601H8VLNAA
Wheel diameter	: 200 mm, max
Wheelspeed	: 46 m/s
Workspeed	: 0.2-0.3 m/s
Workpiece shape	: vee form
Coolant	: wet

Model data :

$R_r = 10$ $r_o = 15\ \mu m$

$\kappa_g = 45$ W/mK $e_{ch} = 6$ J/mm^3

$h_c = 10000$ W/m^{2}K

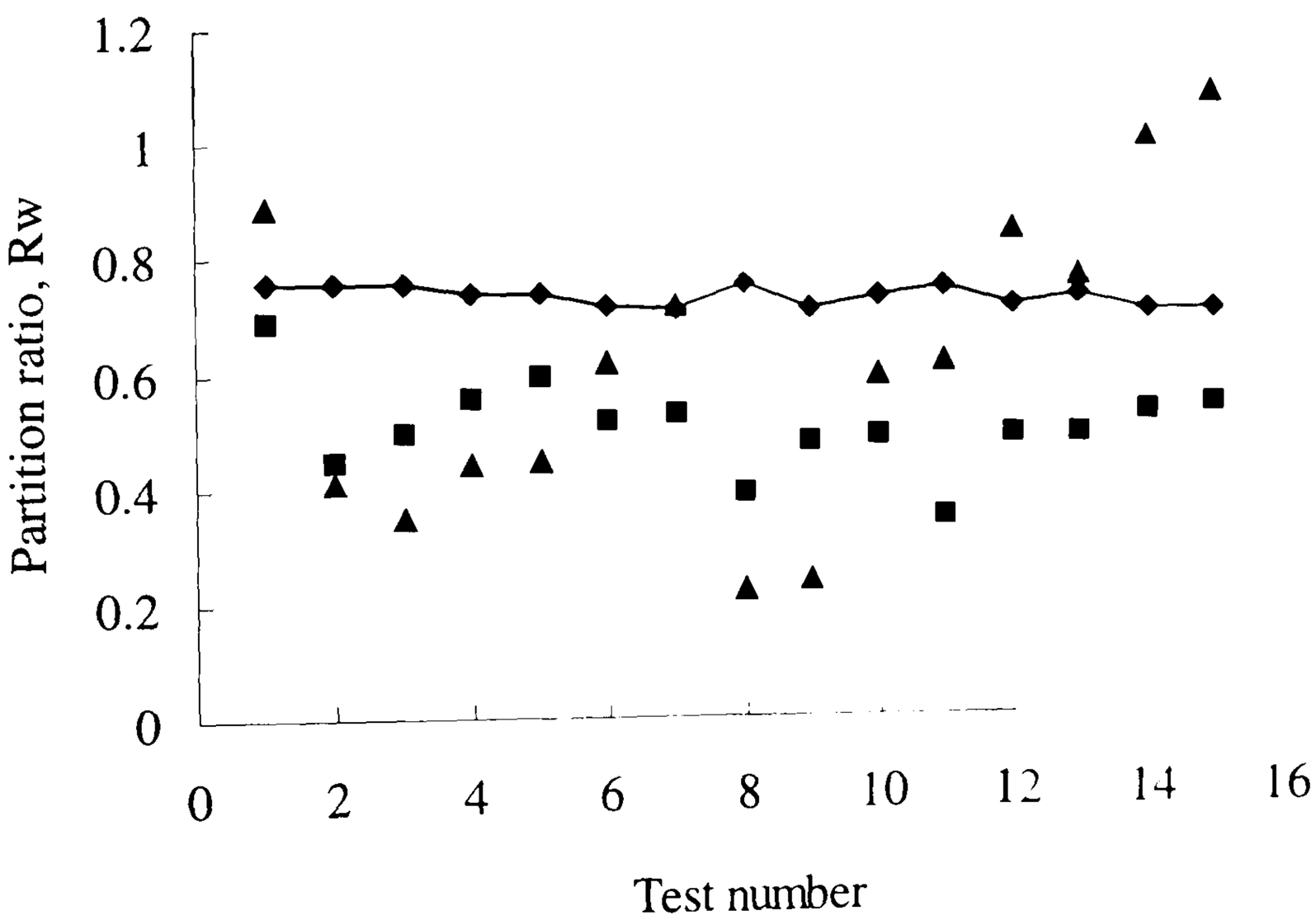

Figure 7.65 Measured and theoretical partition ratios based on experimental data for wet vee form grinding

Experimental data:

Machine	: Abwood (surface grinding)
Material	: En31
Wheel	: 77A601H8VLNAA
Wheel diameter	: 200 mm, max
Wheelspeed	: 46 m/s
Workspeed	: 0.2-0.3 m/s
Workpiece shape	: vee form
Coolant	: wet

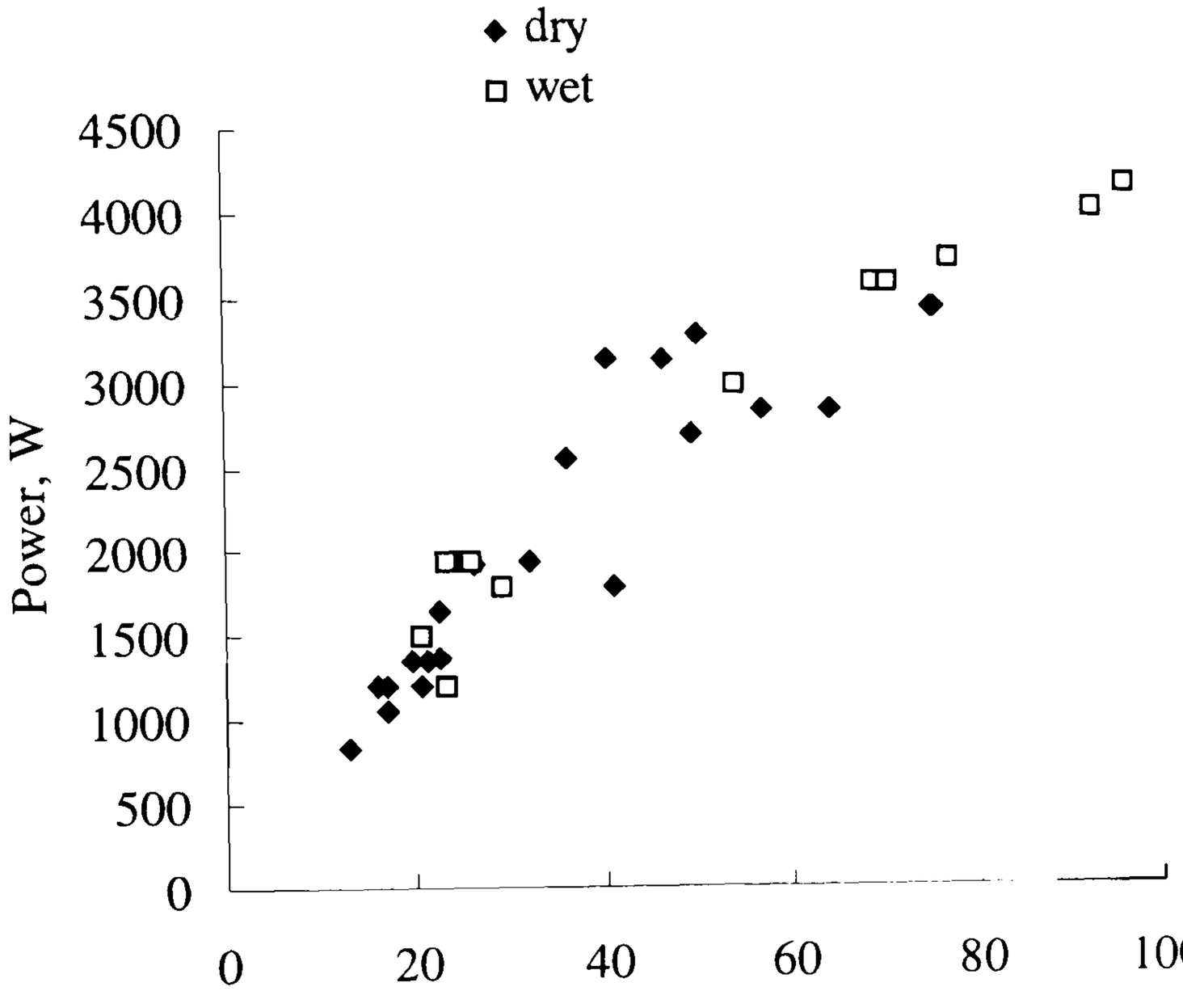

Figure 7.66 Grinding power against removal rate for wet and dry grinding for the vee form

Experimental data:

Machine	: Abwood (surface grinding)
Material	: En31
Wheel	: 77A601H8VLNAA
Wheel diameter	: 200 mm, max
Wheelspeed	: 46 m/s
Workspeed	: 0.1-0.3 m/s
Workpiece shape	: vee form
Coolant	: dry and wet

Model data :

$R_r = 10$ $r_o = 15\ \mu m$

$\kappa_g = 45$ W/mK $e_{ch} = 6$ J/mm^3

$h_c = 10000$ W/m^{2}K

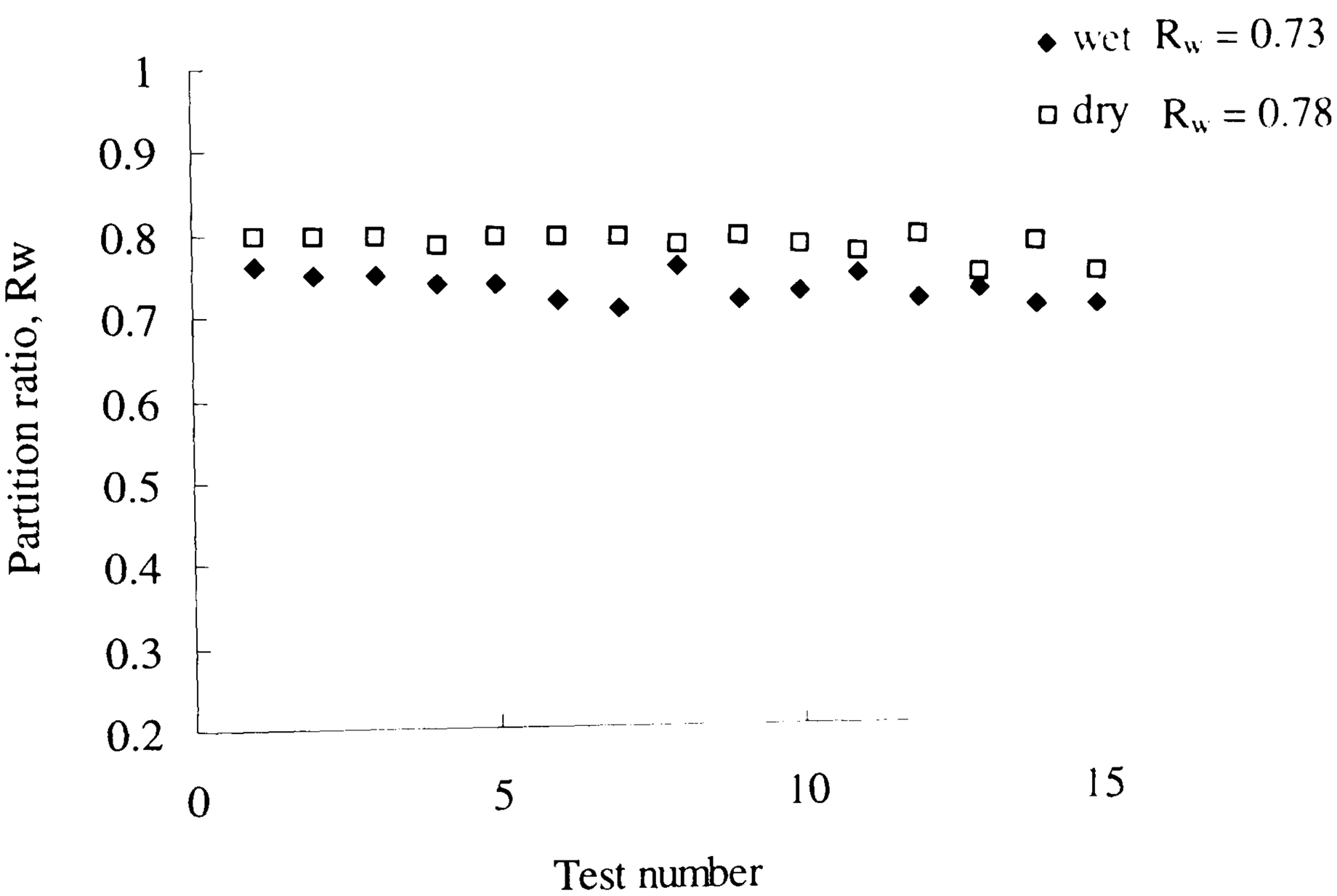

Figure 7.67 Predicted partition ratios for dry and wet vee form grinding

Experimental data:

Machine	: Abwood (surface grinding)
Material	: En31
Wheel	: 77A601H8VLNAA
Wheel diameter	: 200 mm, max
Wheelspeed	: 46 m/s
Workspeed	: 0.1 m/s
Workpiece shape	: inverted vee form
Coolant	: dry

Model data :

$R_r = 10$ $r_o = 15\ \mu m$

$\kappa_g = 45$ W/mK $e_{ch} = 6$ J/mm^3

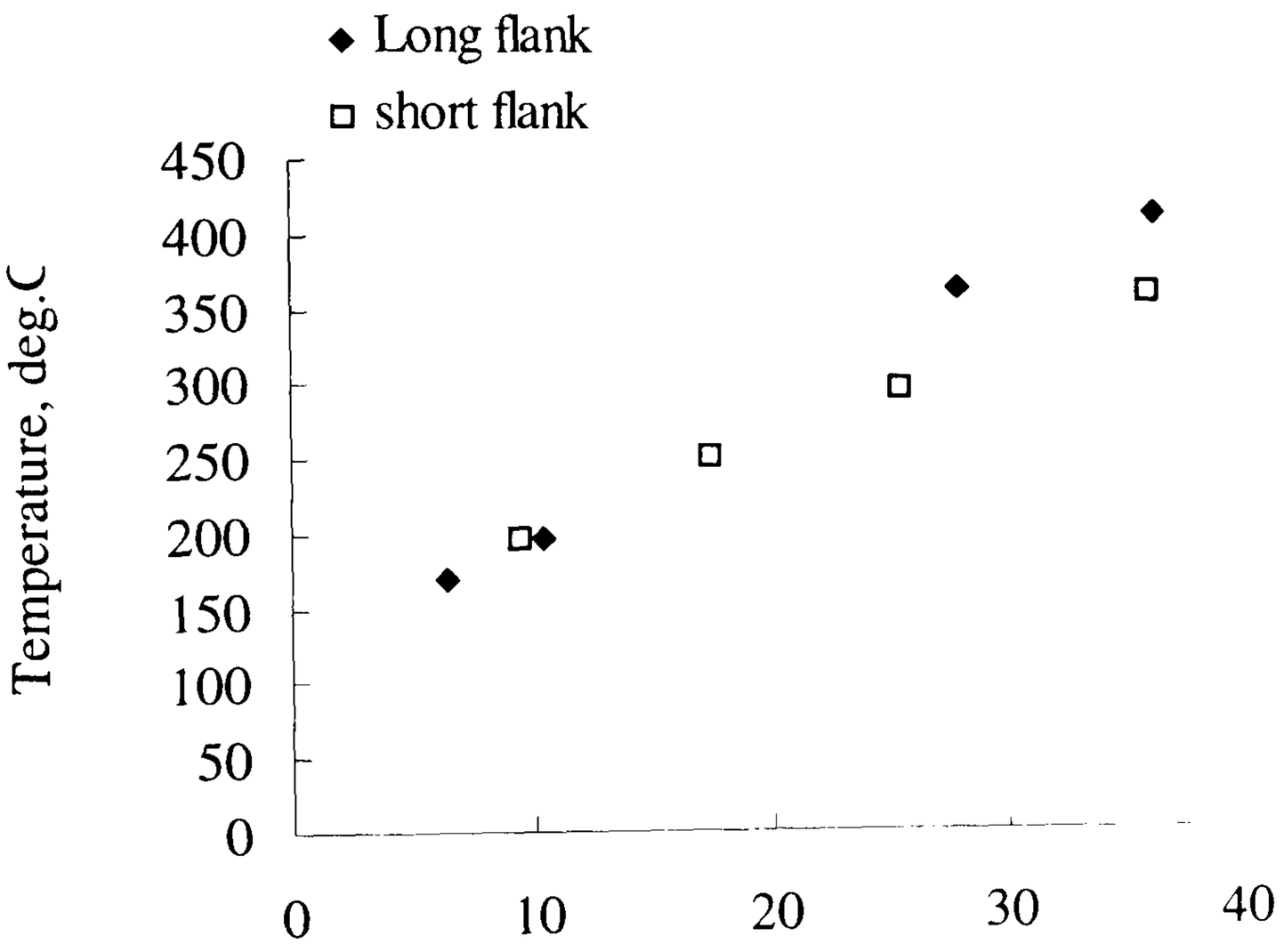

Figure 7.68 A comparison of the temperatures on the long flank and on the short flank of the inverted vee form at a workspeed, $v_w = 0.1$ m/s

Experimental data:

Machine	: Abwood (surface grinding)
Material	: En31
Wheel	: 77A601H8VLNAA
Wheel diameter	: 200 mm. max
Wheelspeed	: 46 m/s
Workspeed	: 0.1 m/s
Workpiece shape	: inverted vee form
Coolant	: dry

Model data :

$R_r = 10$ $r_o = 15\ \mu m$

$\kappa_g = 45$ W/mK $e_{ch} = 6$ J/mm^3

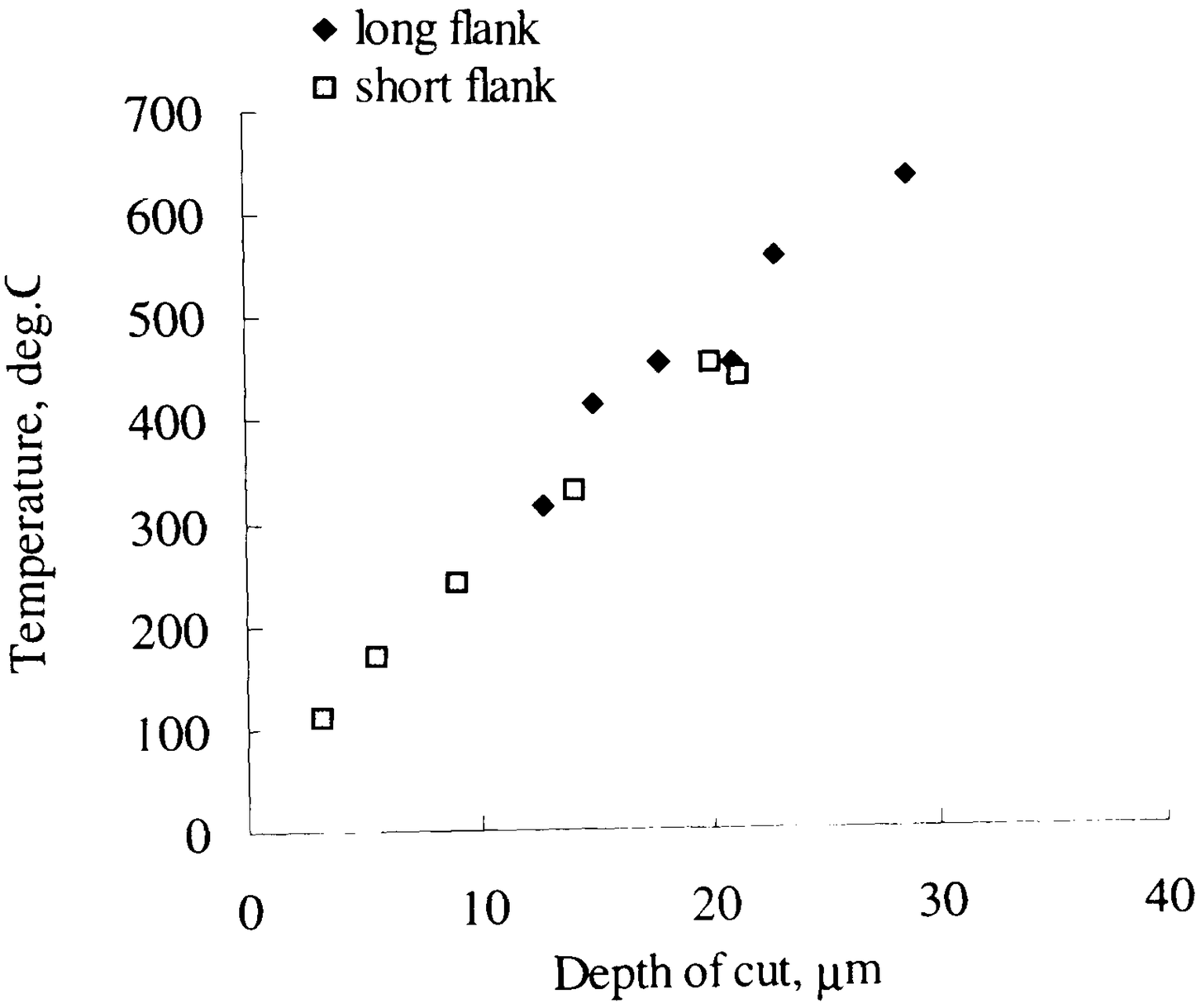

Figure 7.69 A comparison of the temperatures on the long flank and on the short flank of the inverted vee form at a workspeed, $v_w = 0.1$ m/s

Experimental data:

Machine	: Abwood (surface grinding)
Material	: En31
Wheel	: 77A601H8VLNAA
Wheel diameter	: 200 mm, max
Wheelspeed	: 46 m/s
Workspeed	: 0.2 m/s
Workpiece shape	: inverted vee form
Coolant	: dry

Model data :

$R_r = 10$ $r_o = 15\ \mu m$

$\kappa_g = 45$ W/mK $e_{ch} = 6$ J/mm^3

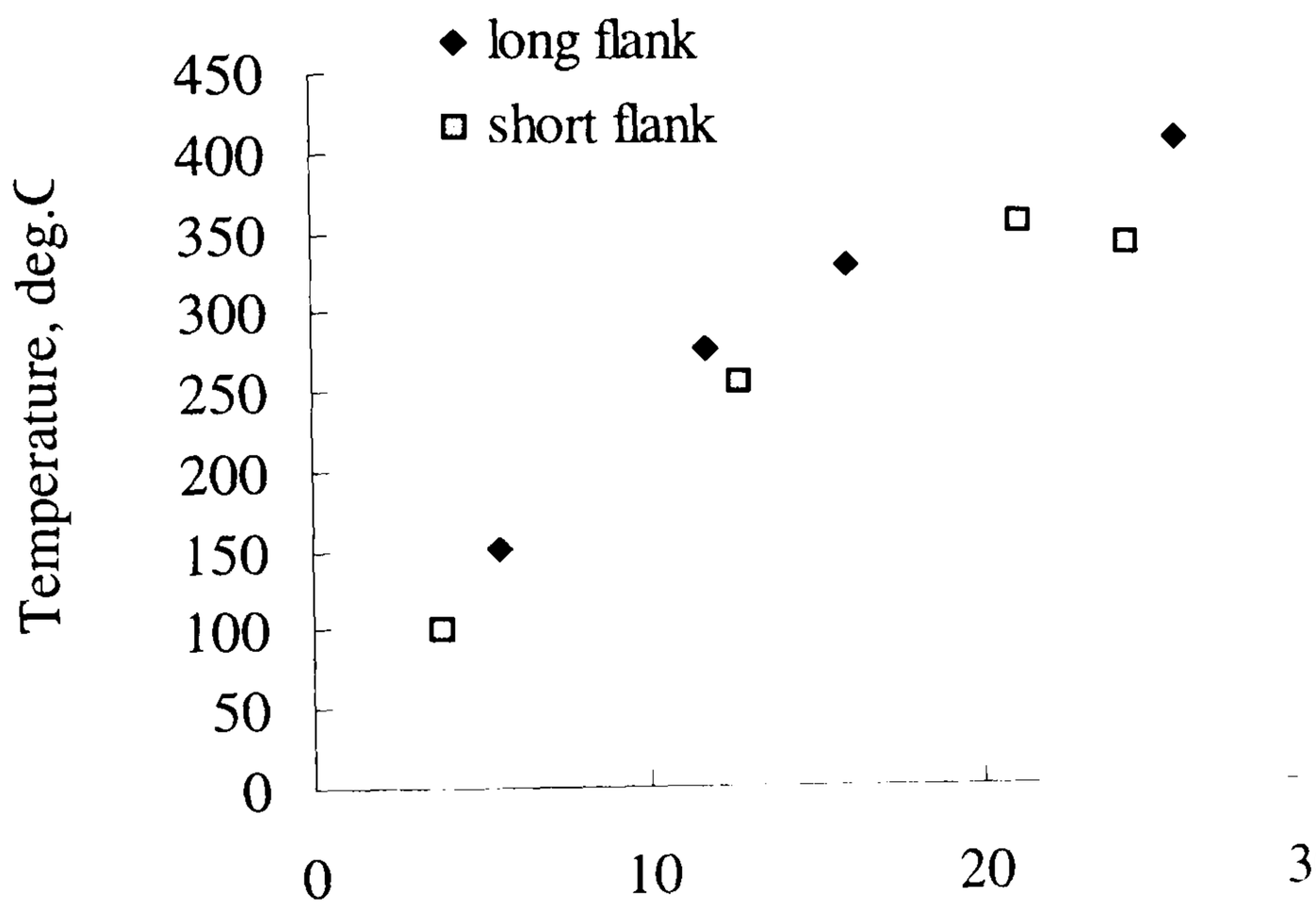

Figure 7.70 Measured temperatures on the long and short flanks of the inverted vee form at a workspeed of $v_w = 0.2$ m/s

Experimental data:

Machine	: Abwood (surface grinding)
Material	: En31
Wheel	: 77A601H8VLNAA
Wheel diameter	: 200 mm. max
Wheelspeed	: 46 m/s
Workspeed	: 0.2 m/s
Workpiece shape	: inverted vee form
Coolant	: dry

Model data :

$R_r = 10$ $r_o = 15\ \mu m$

$\kappa_g = 45$ W/mK $e_{ch} = 6$ J/mm^3

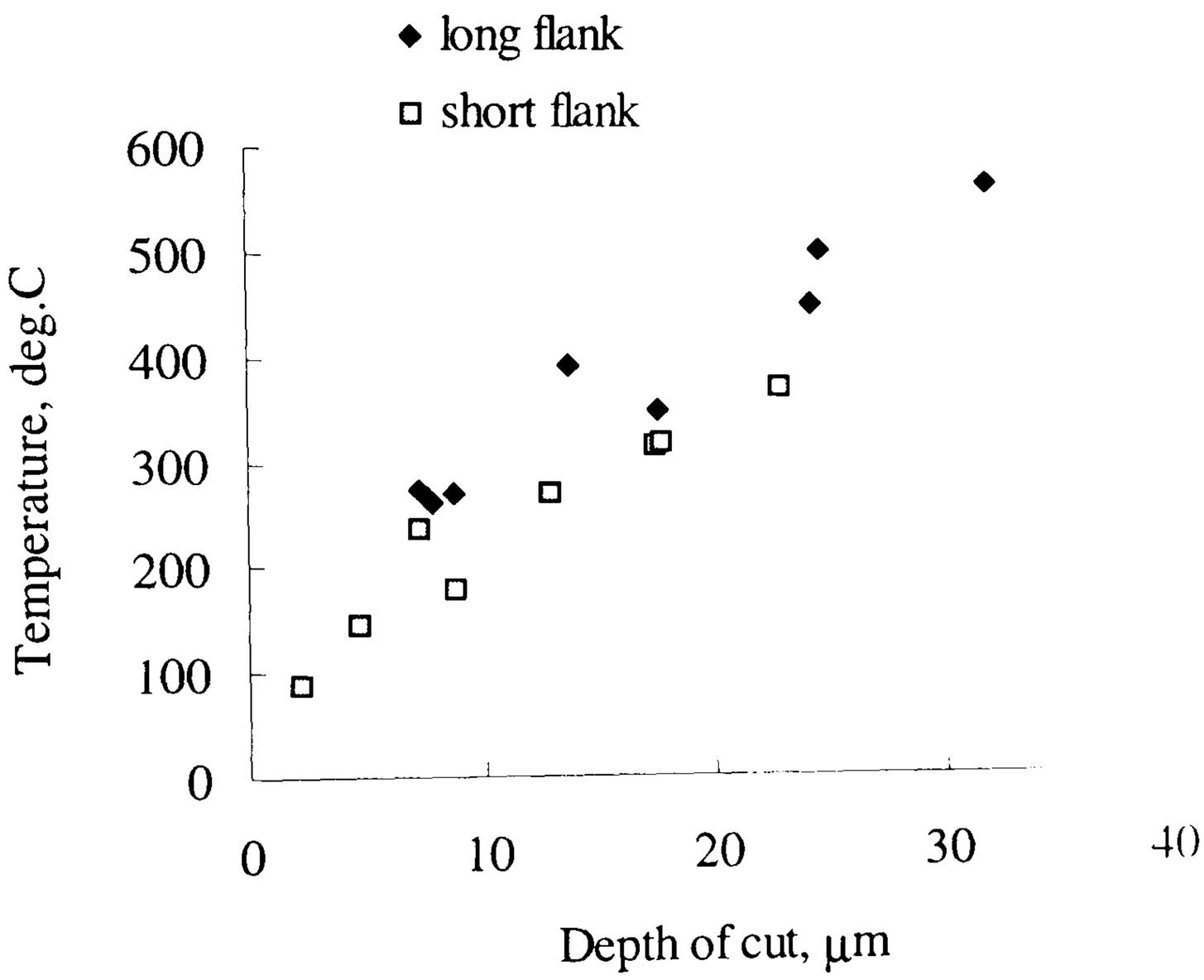

Figure 7.71 Measured temperatures on the long and short flanks of the inverted vee form at a workspeed of $v_w = 0.2$ m/s

Experimental data:

Machine	: Abwood (surface grinding)
Material	: En31
Wheel	: 77A601H8VLNAA
Wheel diameter	: 200 mm, max
Wheelspeed	: 46 m/s
Workspeed	: 0.1 m/s
Workpiece shape	: vee form and inverted vee form
Coolant	: dry

Model data :

$R_r = 10$ $\quad r_o = 15\ \mu m$

$\kappa_g = 45$ W/mK $\quad e_{ch} = 6$ J/mm^3

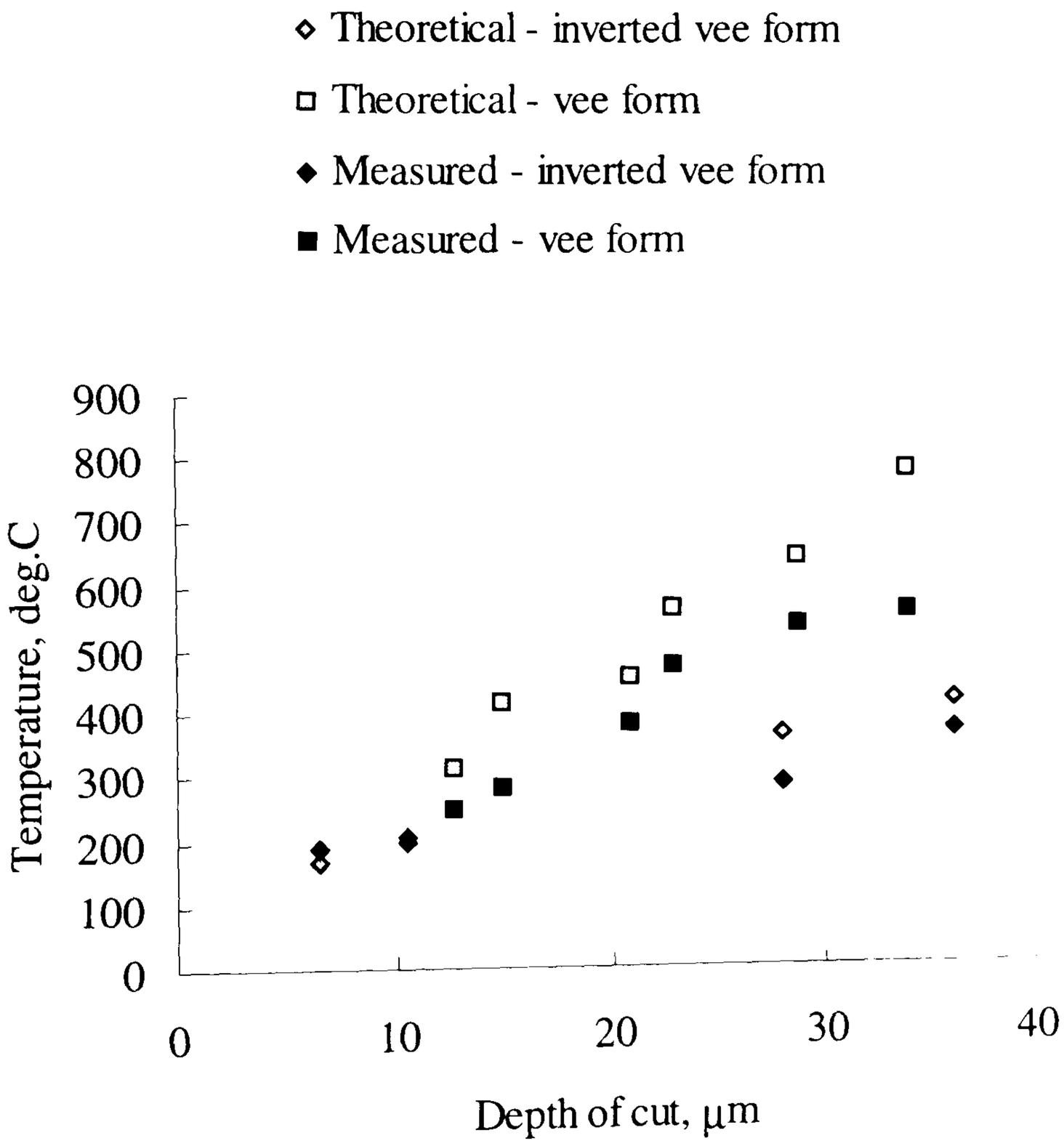

Figure 7.72 Measured and predicted temperatures for the long flank of the inverted vee form and the vee form at a workspeed of $v_w = 0.1$ m/s

Experimental data:

Machine	: Abwood (surface grinding)
Material	: En31
Wheel	: 77A601H8VLNAA
Wheel diameter	: 200 mm, max
Wheelspeed	: 46 m/s
Workspeed	: 0.1 m/s
Workpiece shape	: vee form and inverted vee form
Coolant	: dry

Model data :

$R_r = 10$ $r_o = 15\ \mu m$

$\kappa_g = 45$ W/mK $e_{ch} = 6$ J/mm^3

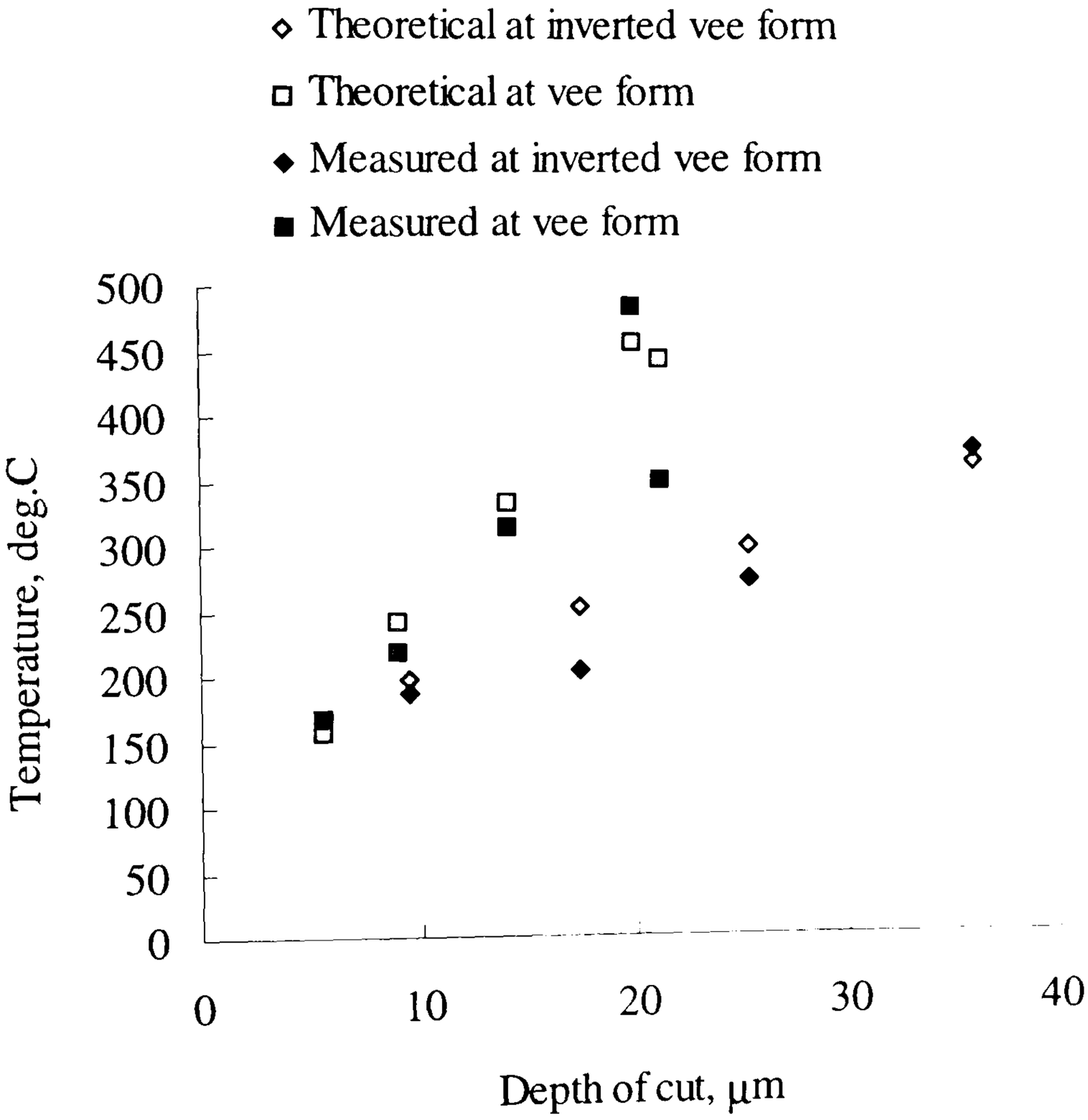

Figure 7.73 Measured and predicted temperatures for the short flank of the inverted vee form and the vee form at a workspeed of $v_w = 0.1$ m/s

Experimental data:

Machine	: Abwood (surface grinding)
Material	: En31
Wheel	: 77A601H8VLNAA
Wheel diameter	: 200 mm, max
Wheelspeed	: 46 m/s
Workspeed	: 0.1-0.3 m/s
Workpiece shape	: vee form and inverted vee form
Coolant	: dry

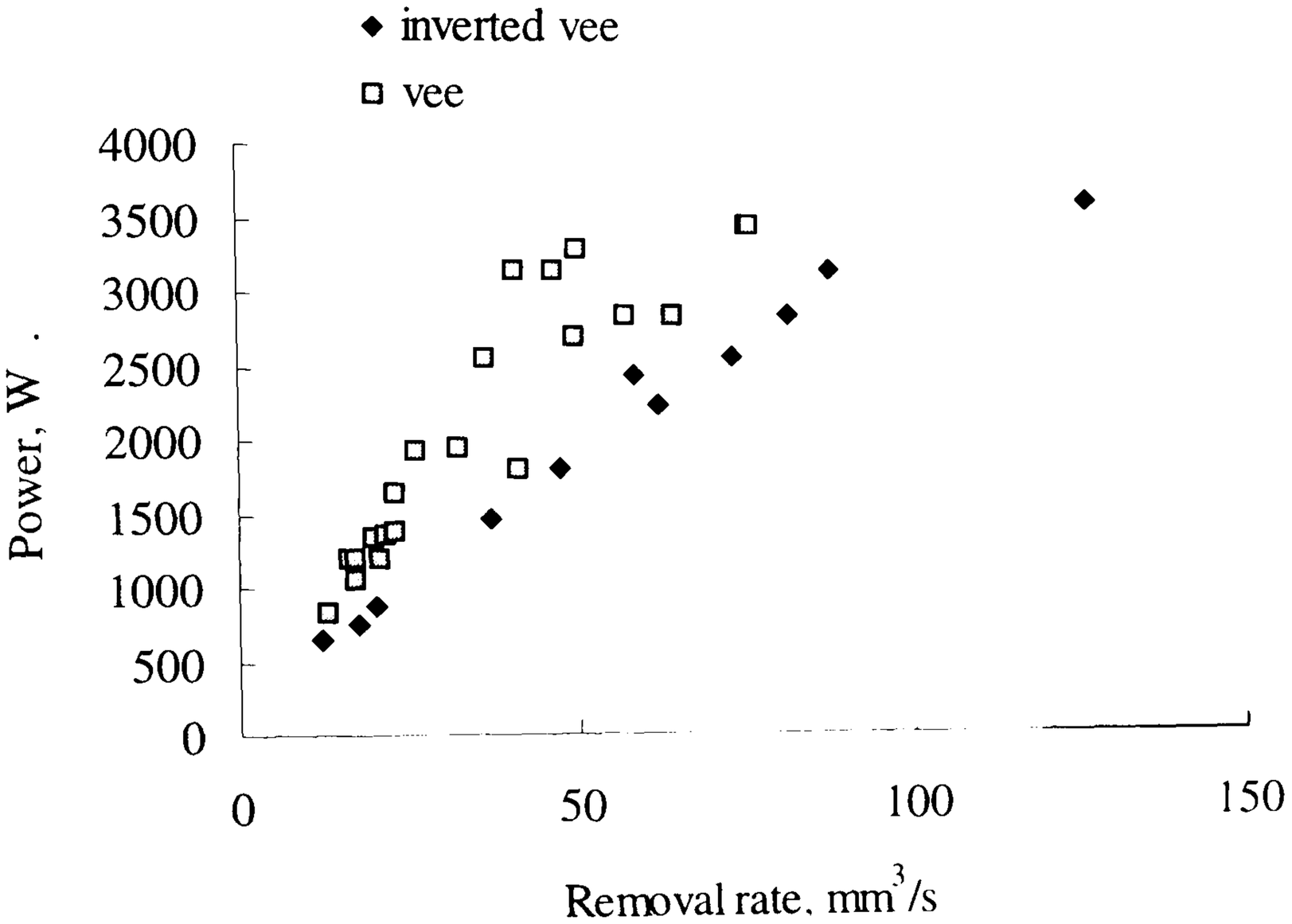

Figure 7.74 Grinding power against removal rate for the inverted vee form and vee form in dry grinding

Experimental data:

Machine	: Abwood (surface grinding)
Material	: En31
Wheel	: 77A601H8VLNAA
Wheel diameter	: 200 mm. max
Wheelspeed	: 46 m/s
Workspeed	: 0.1-0.3 m/s
Workpiece shape	: inverted vee form and vee form
Coolant	: wet

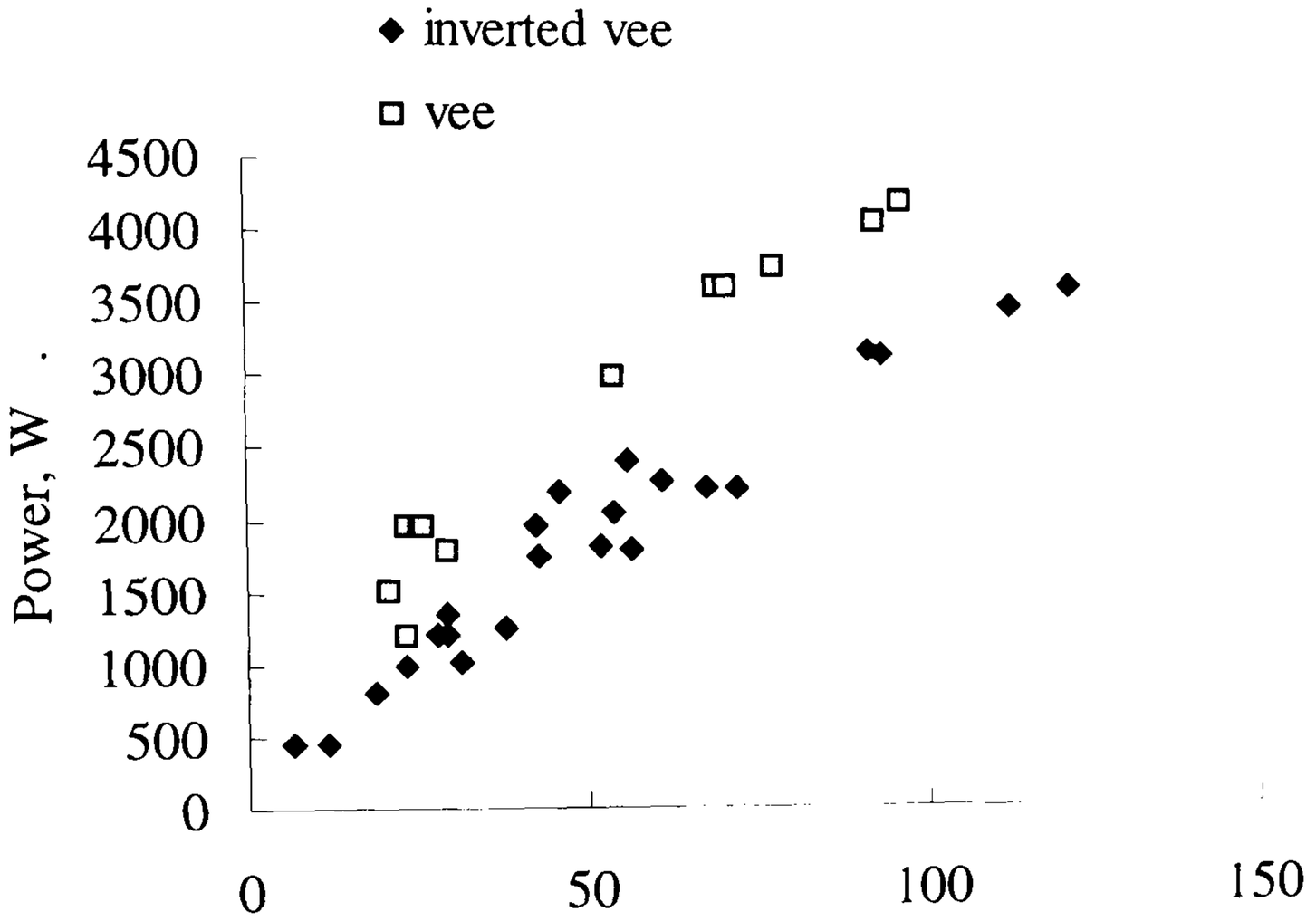

Figure 7.75 Grinding power against removal rate for wet inverted vee and vee form grinding

Experimental data:

Machine	: Abwood (surface grinding)
Material	: En31
Wheel	: CBN
Wheel diameter	: 200 mm, max
Wheelspeed	: 46 m/s
Workspeed	: 0.1 m/s
Workpiece shape	: vee form
Coolant	: dry

Model data :

$R_r = 10$ $\quad r_o = 15\ \mu m$

$\kappa_g = 260$ W/mK $\quad e_{ch} = 6$ J/mm^3

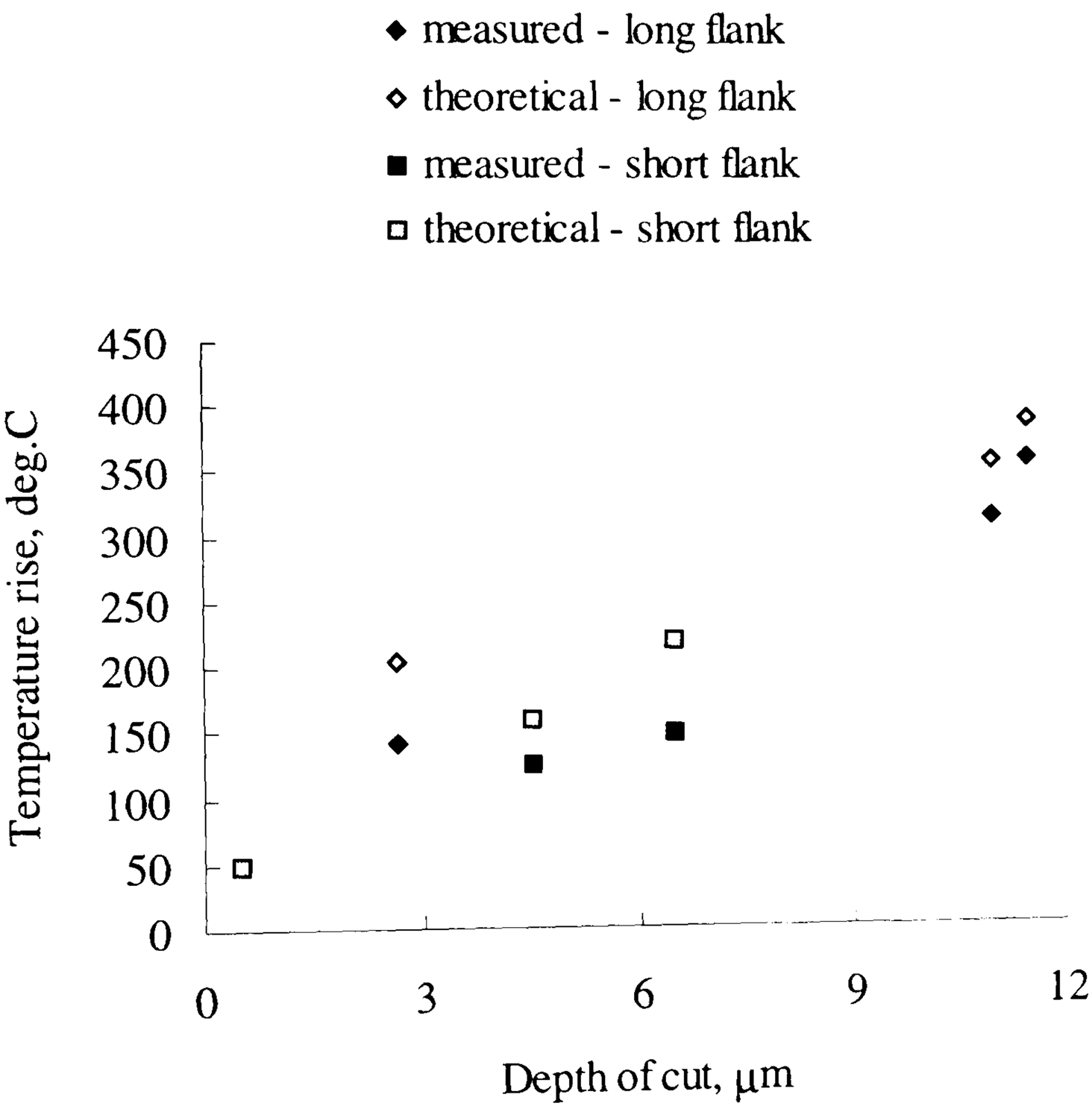

Figure 7.76 Measured and predicted temperature for the vee form with the CBN grinding wheel, $v_w = 0.1$ m/s

Experimental data:

Machine	: Abwood (surface grinding)
Material	: En31
Wheel	: CBN
Wheel diameter	: 200 mm. max
Wheelspeed	: 46 m/s
Workspeed	: 0.1 m/s
Workpiece shape	: vee form
Coolant	: dry

Model data :

$R_r = 10$ $r_o = 15\ \mu m$

$\kappa_g = 260$ W/mK $e_{ch} = 6$ J/mm^3

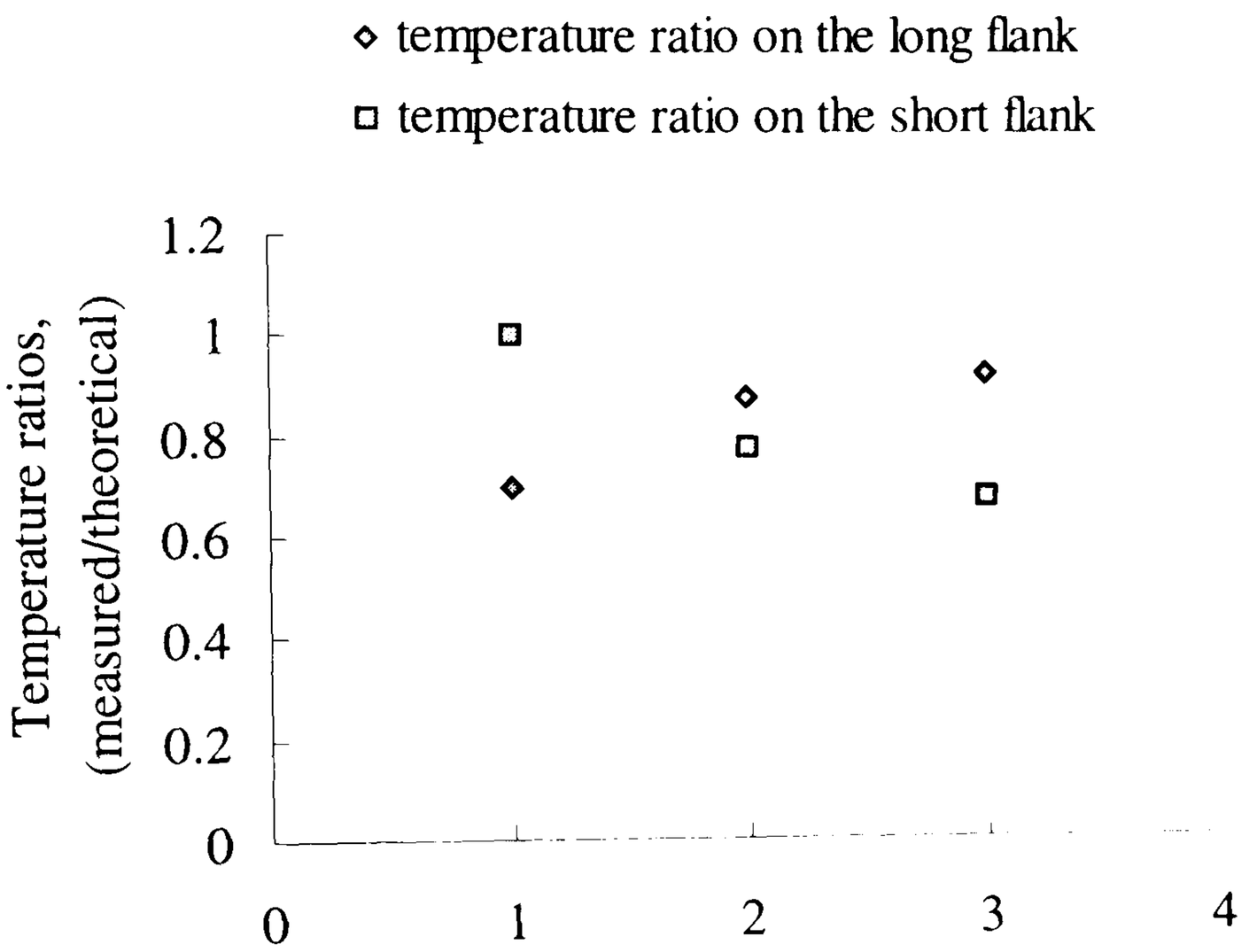

Figure 7.77 Ratios of measured and predicted temperature on the long and short flanks of the vee form with a roughness factor Rr =10 for the CBN grinding wheel

Experimental data:

Machine	: Abwood (surface grinding)
Material	: En31
Wheel	: CBN
Wheel diameter	: 200 mm, max
Wheelspeed	: 46 m/s
Workspeed	: 0.1 m/s
Workpiece shape	: vee form
Coolant	: dry

Model data :

$R_r = 10$ $r_o = 15\ \mu m$

$\kappa_g = 260$ W/mK $e_{ch} = 6$ J/mm^3

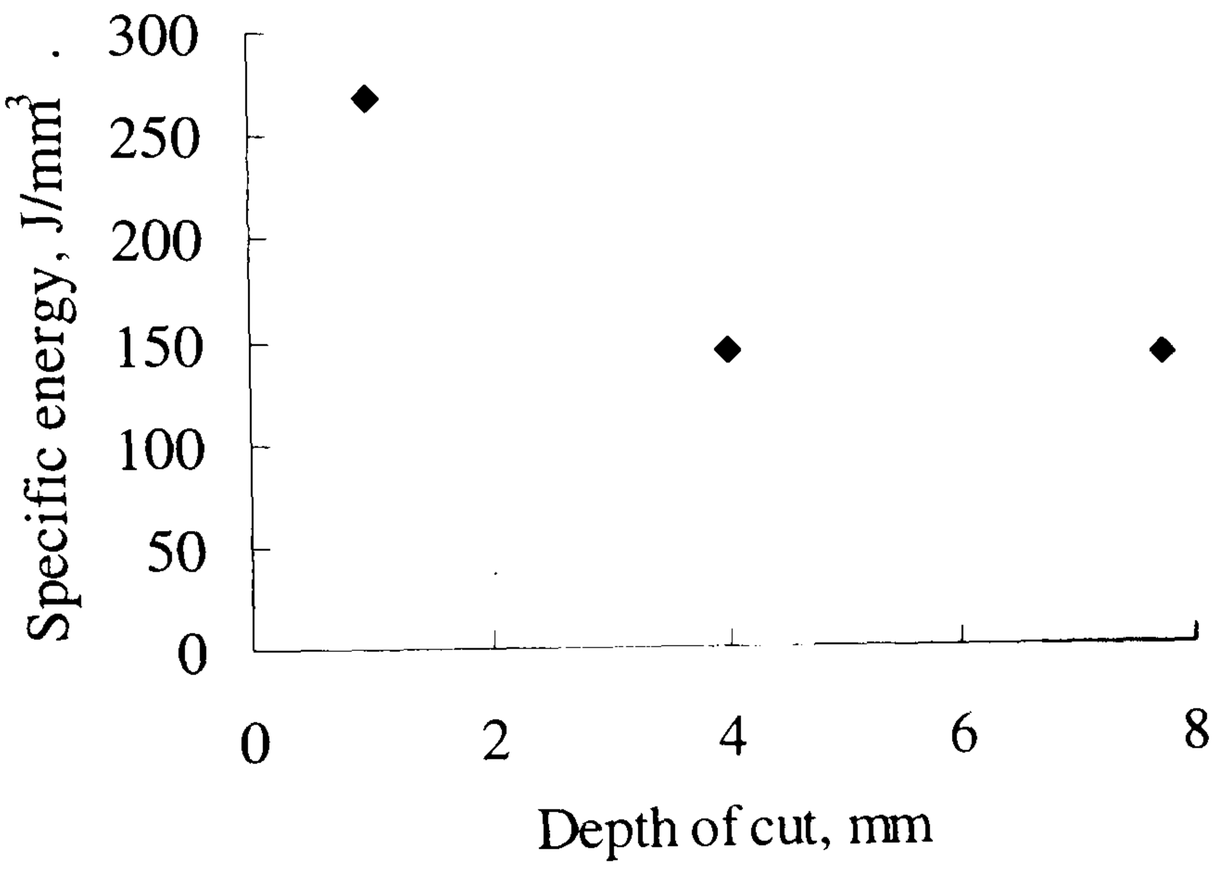

Figure 7.78 Specific energy against depth of cut for the vee form with the CBN grinding wheel at a workspeed of $v_w = 0.1$m/s

Experimental data:

Machine	: Abwood (surface grinding)
Material	: En31
Wheel	: CBN
Wheel diameter	: 200 mm. max.
Wheelspeed	: 46 m/s
Workspeed	: 0.1 m/s
Workpiece shape	: vee form
Coolant	: dry

Model data :

$R_r = 10$ $r_o = 15\ \mu m$

$\kappa_g = 260$ W/mK $e_{ch} = 6$ J/mm^3

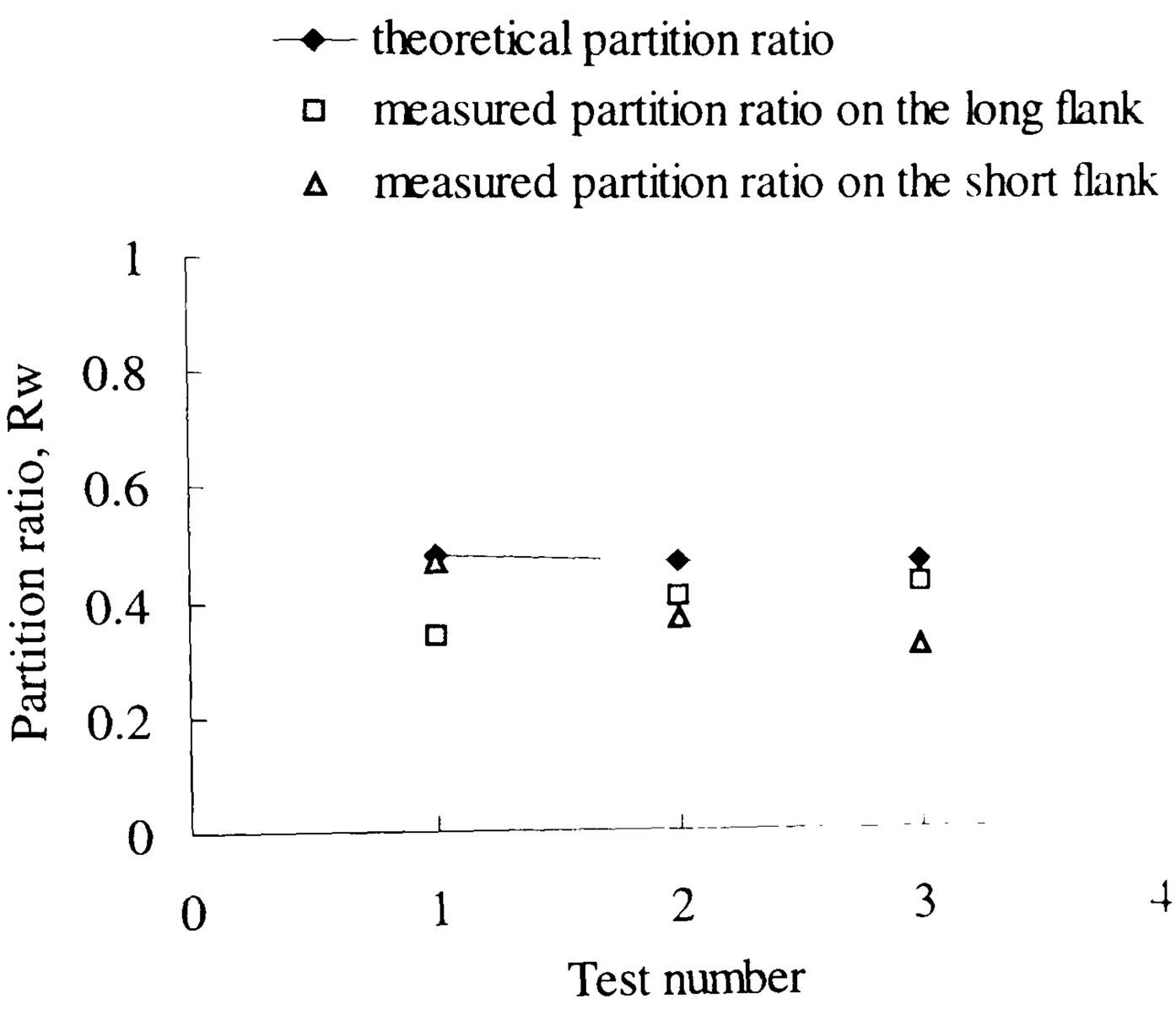

Figure 7.79 Measured and predicted partition ratios for dry vee form grinding with the CBN grinding wheel, at a workspeed of $v_w = 0.1$m/s

Experimental data:

Machine	: Abwood (surface grinding)
Material	: En31
Wheel	: 77A601H8VLNAA and CBN
Wheel diameter	: 200 mm. max
Wheelspeed	: 46 m/s
Workspeed	: 0.1 m/s
Workpiece shape	: vee form
Coolant	: dry

Model data :

$R_r = 10$ $r_o = 15\ \mu m$

κ_g =260 W/mK(CBN wheel) $e_{ch} = 6\ J/mm^3$

κ_g = 45 W/mK(alumina wheel)

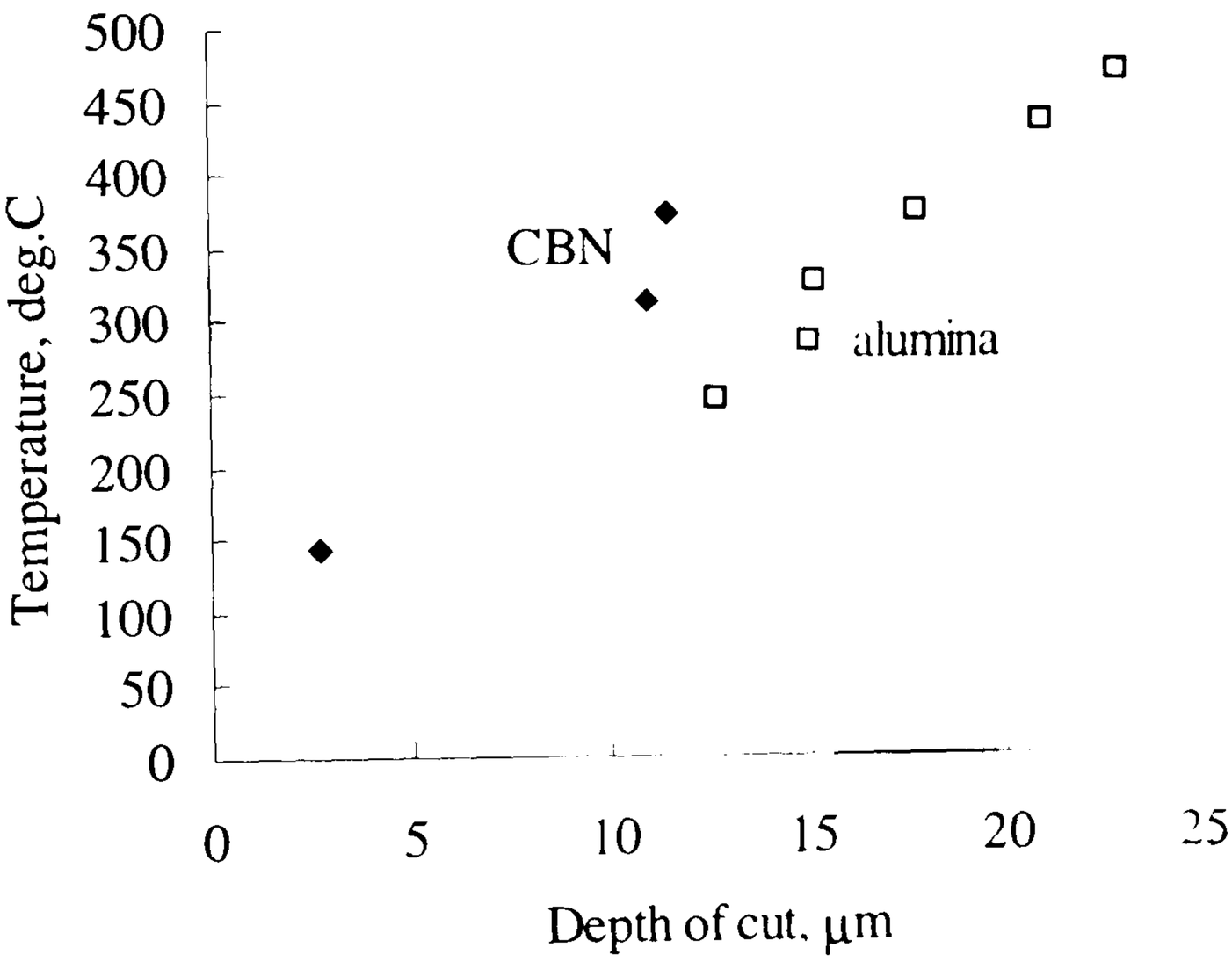

Figure 7.80 Measured temperatures against depth of cut for the CBN and alumina grinding wheel at the long flank of the vee form at a workspeed of v_w=0.1m/s

Experimental data:

Machine	: Abwood (surface grinding)
Material	: En31
Wheel	: 77A601H8VLNAA and CBN
Wheel diameter	: 200 mm. max
Wheelspeed	: 46 m/s
Workspeed	: 0.1 m/s
Workpiece shape	: vee form
Coolant	: dry

Model data :

$R_r = 10$ $r_o = 15\ \mu m$

κ_g =260 W/mK (CBN wheel) $e_{ch} = 6\ J/mm^3$

κ_g = 45 W/mK (alumina wheel)

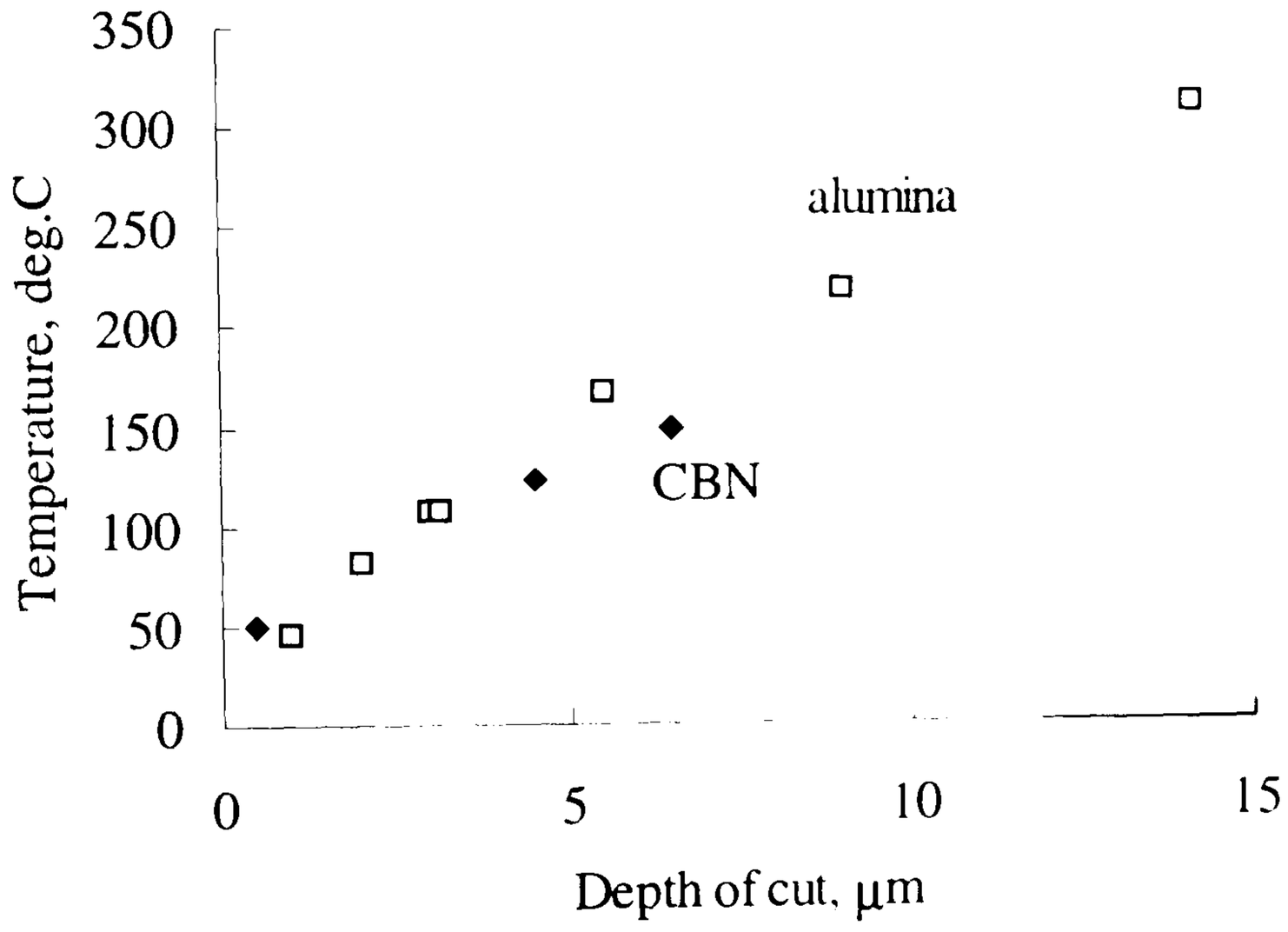

Figure 7.81 Measured temperatures against depth of cut for the CBN and alumina grinding wheels at the short flank of the vee form at a workpeed of $v_w = 0.1 m/s$

Experimental data:

Machine	: Abwood (surface grinding)
Material	: En31
Wheel	: CBN and alumina
Wheel diameter	: 200 mm, max
Wheelspeed	: 46 m/s
Workspeed	: 0.1 m/s
Workpiece shape	: vee form
Coolant	: dry

Model data :

$R_r = 10$ $r_o = 15\ \mu m$

κ_g =260 W/mK (CBN wheel) $e_{ch} = 6\ J/mm^3$

κ_g = 45 W/mK (alumina wheel)

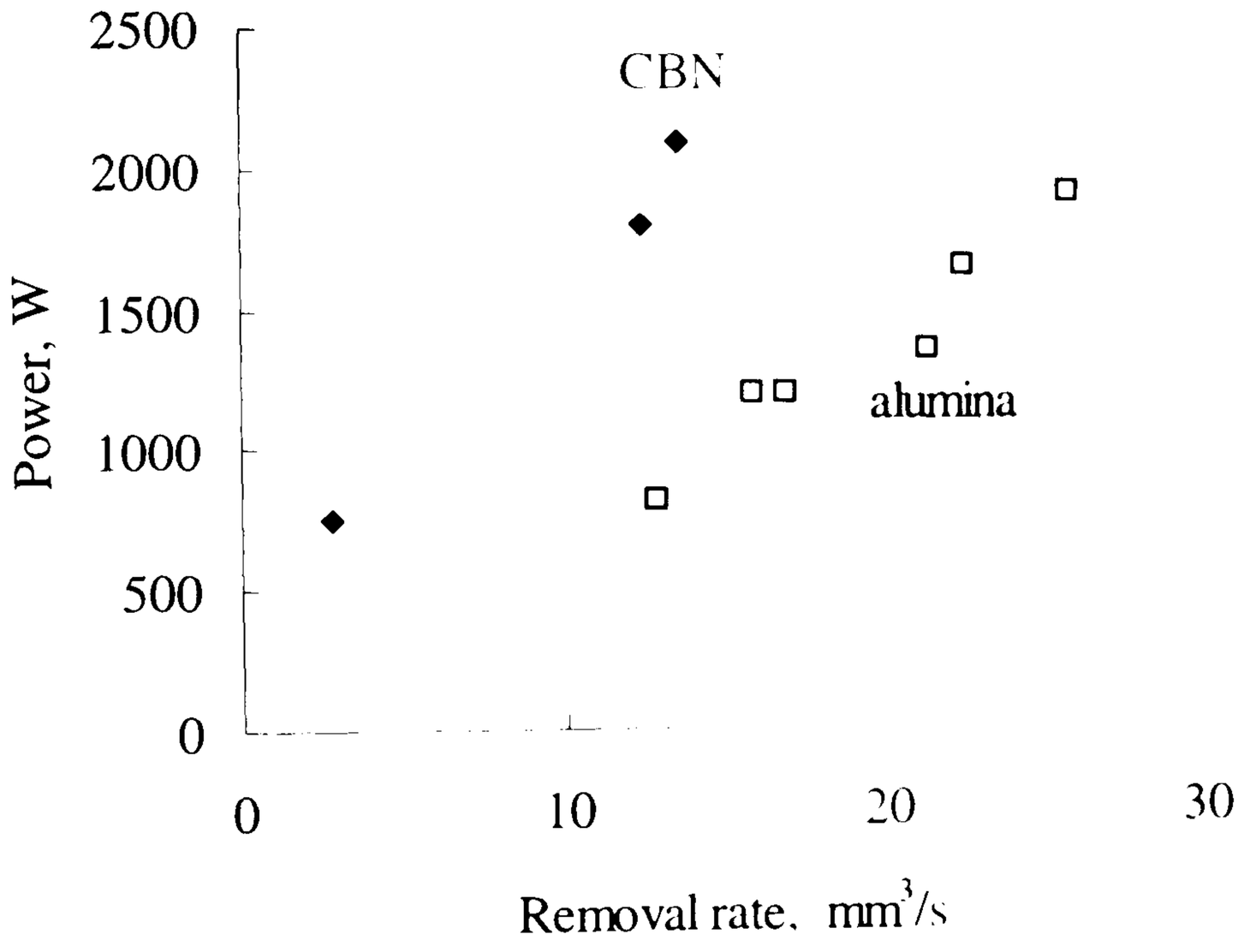

Figure 7.82 Grinding power against removal rate for the CBN and alumina grinding wheel in dry vee form grinding at a workspeed of $v_w = 0.1$m/s

Experimental data:

Machine	: Abwood (surface grinding)
Material	: En31
Wheel	: CBN and alumina
Wheel diameter	: 200 mm. max
Wheelspeed	: 46 m/s
Workspeed	: 0.1 m/s
Workpiece shape	: vee form
Coolant	: dry

Model data :

$R_r = 10$ $r_o = 15\ \mu m$

$\kappa_g = 260$ W/mK(CBN wheel) $e_{ch} = 6$ J/mm^3

$\kappa_g = 45$ W/mK(alumina wheel)

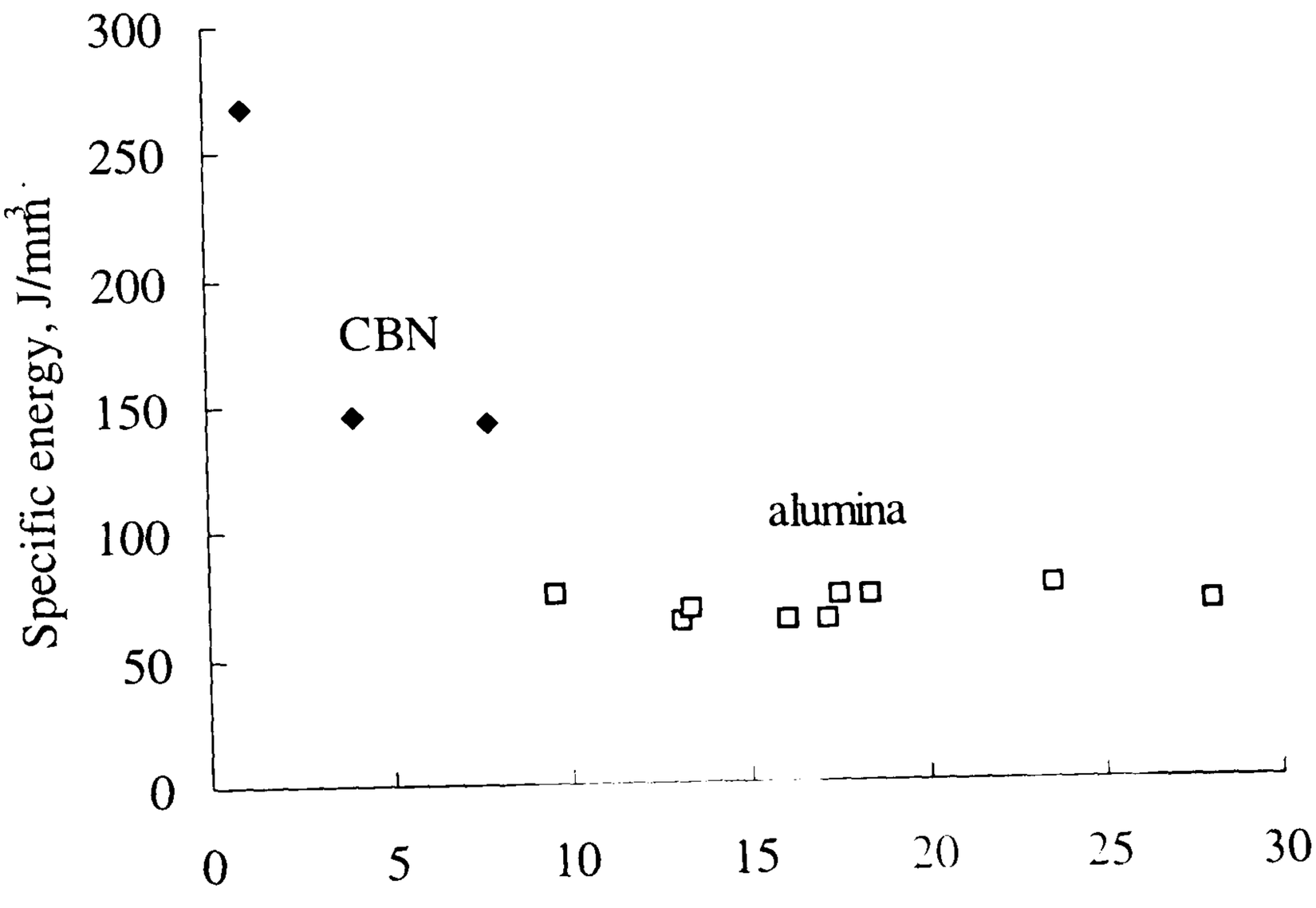

Figure 7.83 Specific energy for the CBN wheel and the alumina grinding wheel in dry vee form grinding at a workspeed of $v_w = 0.1$m/s

Experimental data:

Machine	: Abwood (surface grinding)
Material	: En31
Wheel	: CBN and alumina
Wheel diameter	: 200 mm. max
Wheelspeed	: 46 m/s
Workspeed	: 0.1 m/s
Workpiece shape	: vee form
Coolant	: dry

Model data :

$R_r = 10$ $r_o = 15\ \mu m$

$\kappa_g = 260$ W/mK(CBN wheel) $e_{ch} = 6$ J/mm^3

$\kappa_g = 45$ W/mK(alumina wheel)

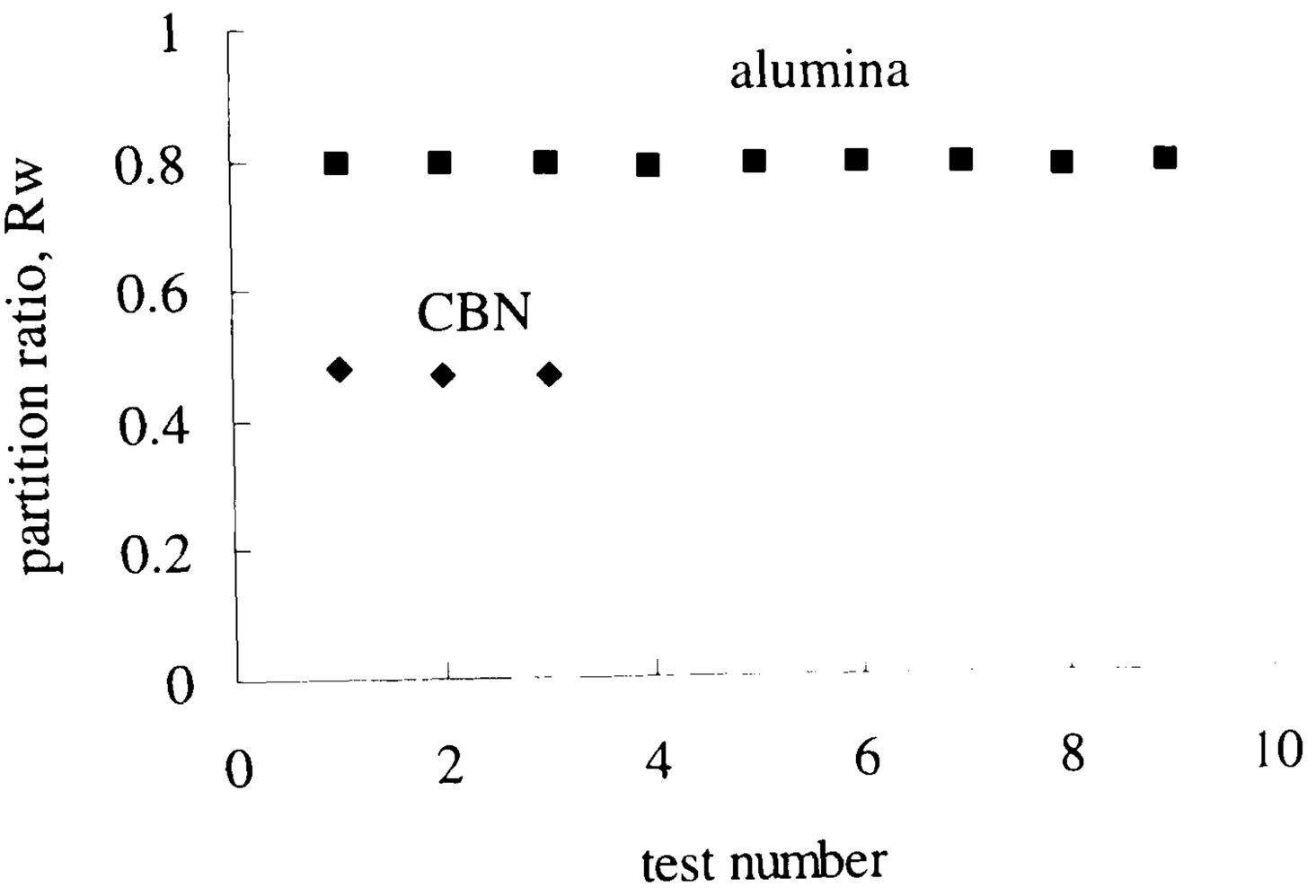

Figure 7.84 A comparison of the partition ratio prediction between the alumina wheel and the CBN wheel

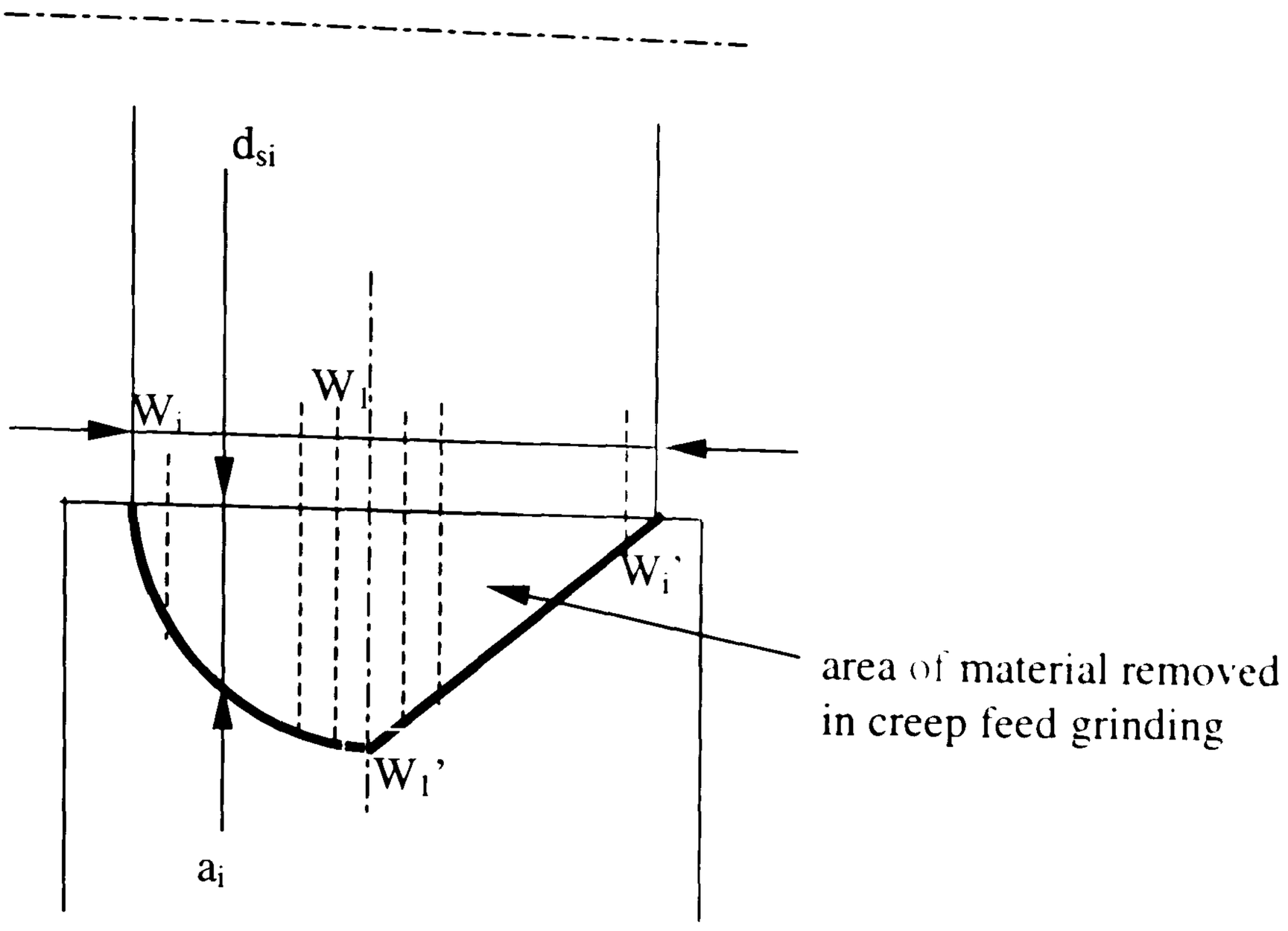

Figure 8.1 The grinding zone divided into strips

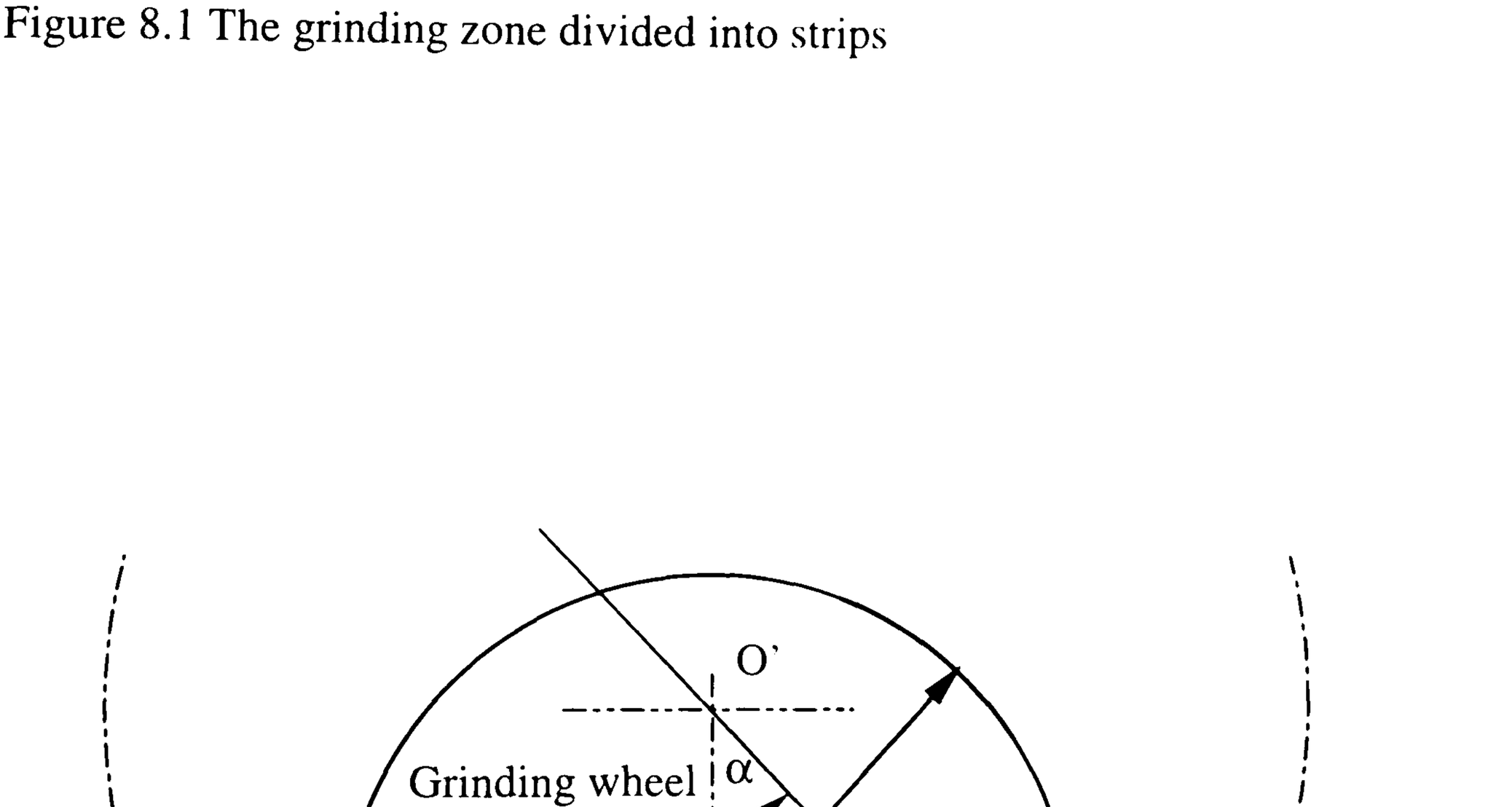

Figure 8.2. The distance z between the contact surface and the finish surface

Grinding data:

wheel type,	: alumina
workpiece material,	: En31
workspeed,	: 0.01 m/s
wheel diameter,	: 200 mm
wheel speed,	: 45 m/s
grinding width,	: 10 mm
grain thermal conductivity,	: 35 W/mK
grain radius,	: 15 μm
specific grinding energy	: 20 J/mm^3
energy to chips,	: 6 J/mm^3
heat transfer coefficient,	: 10000 W/m^{2}K

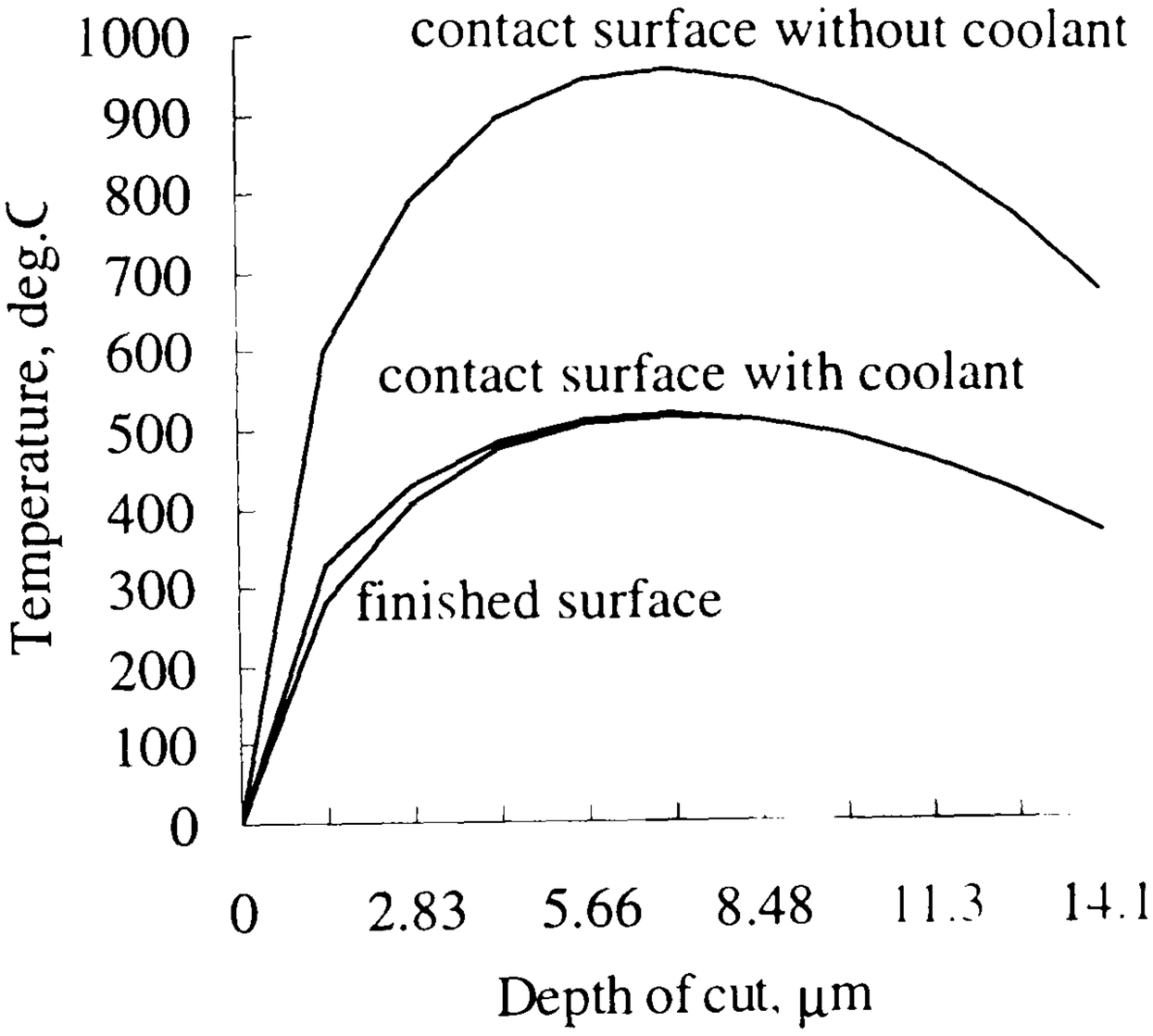

Figure 8.3 Temperature profiles across the grinding contact length with and without coolant and the finished surface for plane surface creep feed grinding.

Grinding data:

wheel type,	: alumina
workpiece material,	: En31
depth of cut,	: 1 mm
workspeed,	: 0.01 m/s
wheel diameter,	: 200 mm
wheel speed,	: 45 m/s
grinding width,	: 10 mm
grain thermal conductivity,	: 35 W/mK
grain radius,	: 15 μm
specific grinding energy	: 20 J/mm^3
energy to chips,	: 6 J/mm^3
heat transfer coefficient,	: 10000 W/m^{2}K

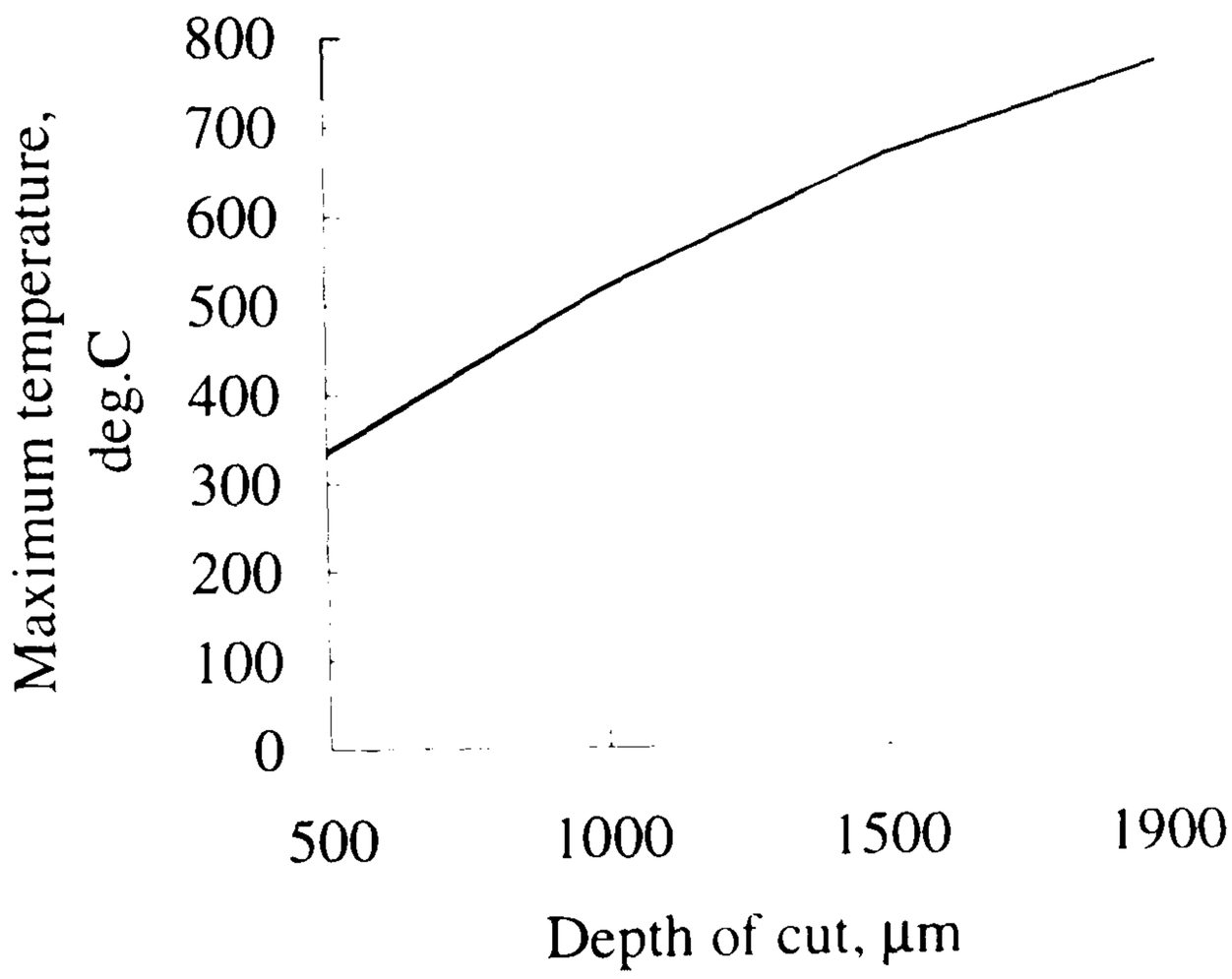

Figure 8.4 The predicted temperature varying with depth of cut

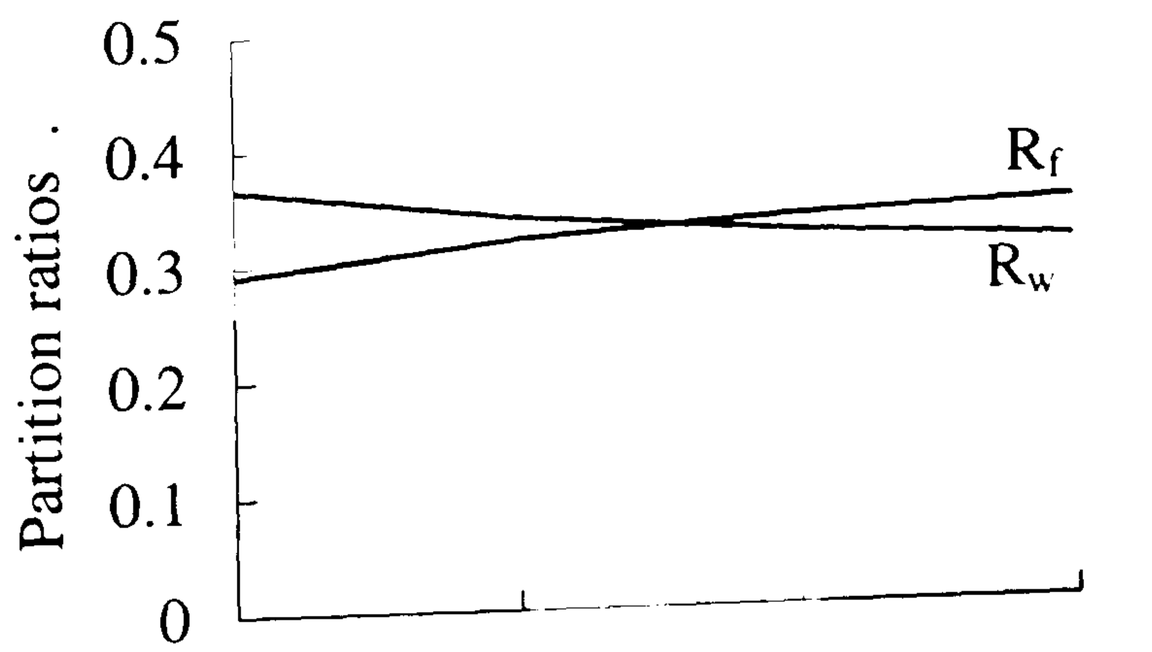

Figure 8.5 The partition ratios with varying depth of cut

Model parameter:

En31

$\kappa\rho c = 1.39\ W^2s/m^4K^2$

$\kappa_{ge} = 35\ W/mK$

$e_{ch} = 5.79E+09\ J/m^3$

$r_o = 15\ \mu m$

$R_r = 10$

$\theta^* = 350$ deg.

$v_s = 40$ m/s

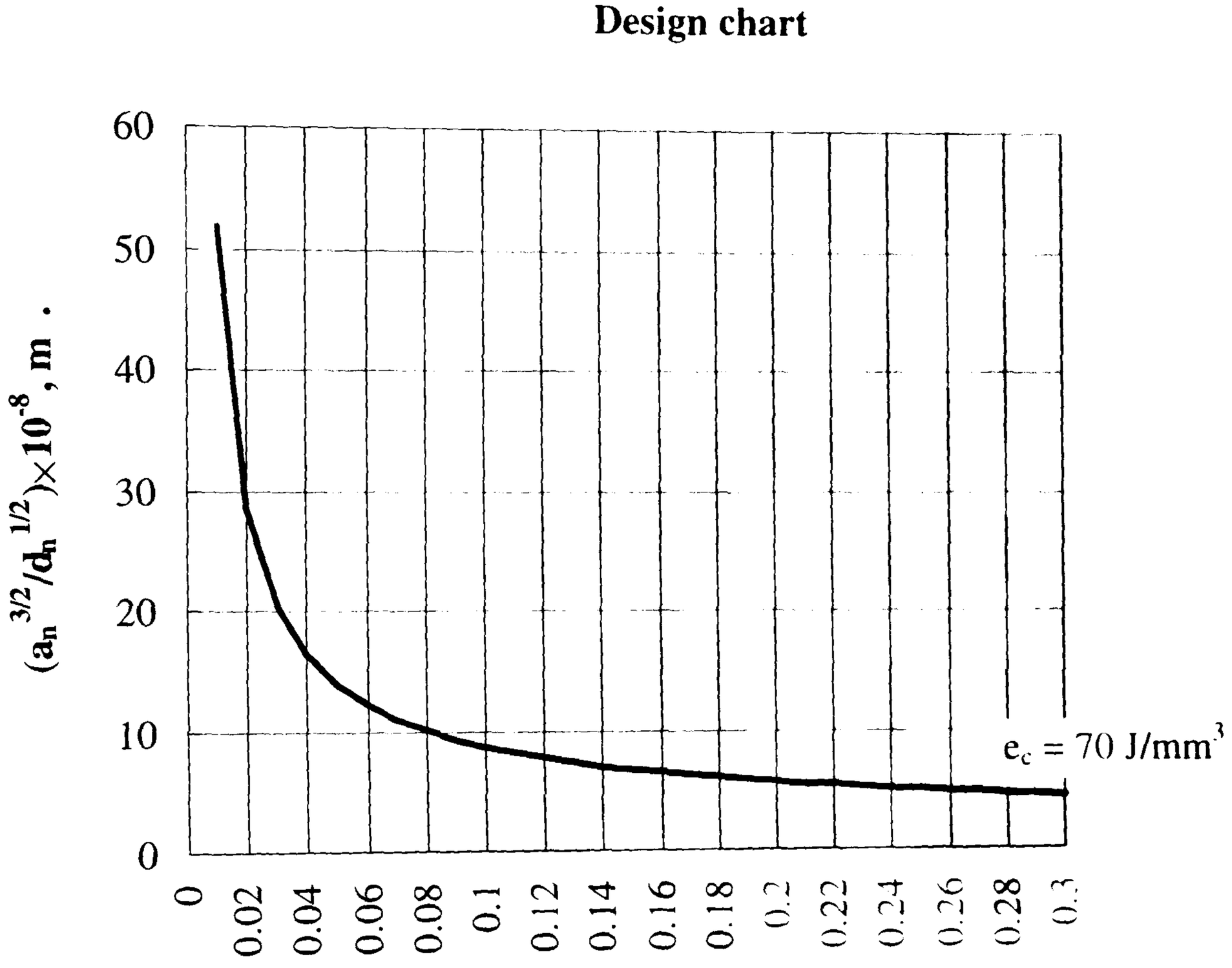

Figure 9.1 Design chart for workpiece material En31 in specific energy e_c = 70 J/mm^2

Machining data:

wheel type		: alumina (77A60IH8VLNAA)
wheel speed,	v_s	: 40 m/s
wheel diameter,	d_s	: 200 mm
grain thermal conductivity,	κ_{ge}	: 35 W/mK
grain radius,	r_o	: 15 μm
roughness ratio,	R_r	: 10 (dry grinding)
energy to chips,	e_{ch}	: 6 J/mm^3
force ratio,	μ	: 0.4

Maximum temperature-380 deg. based on (HV) - $(HV)_g \leq 5$

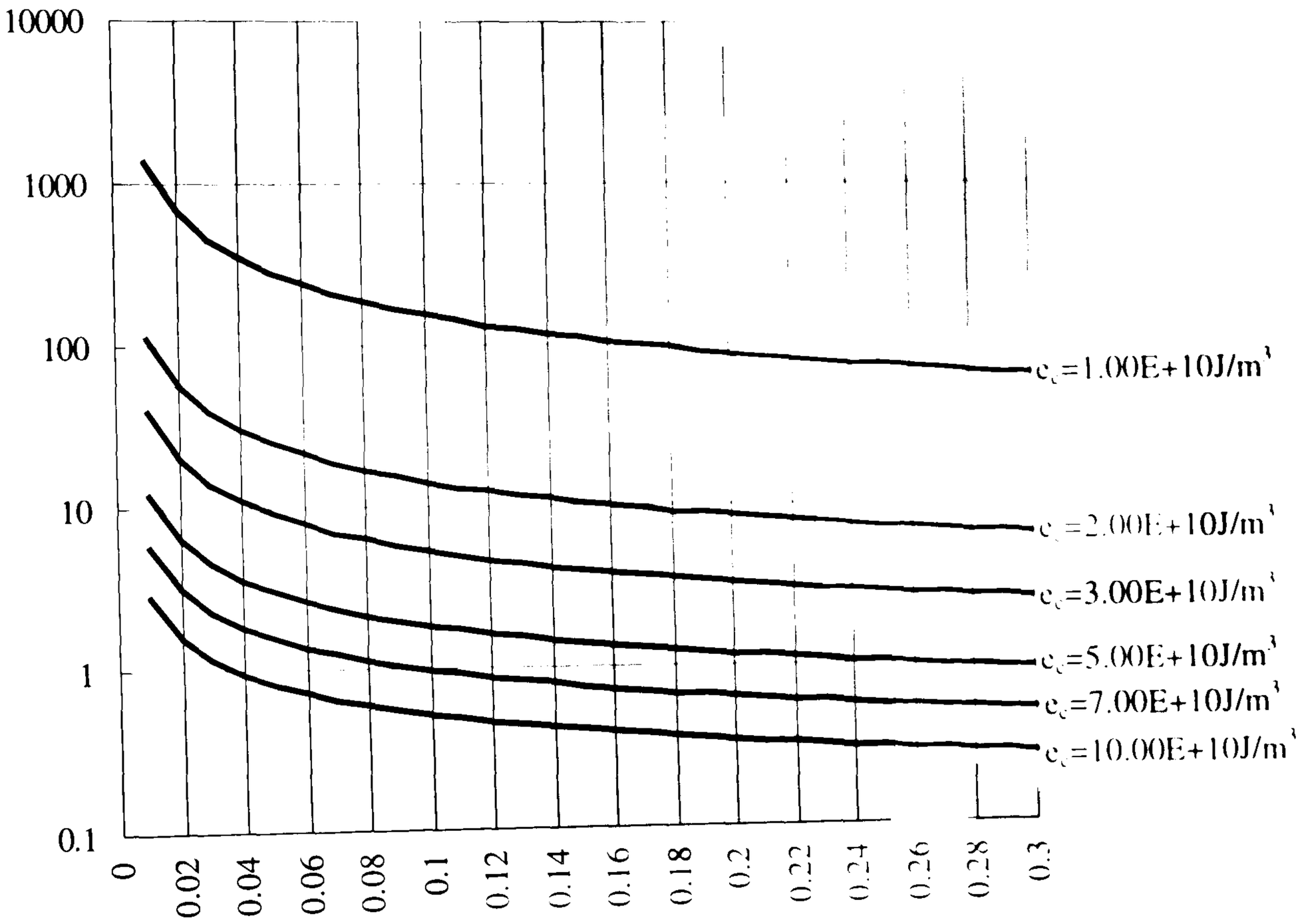

Figure 9.2 Design chart for En31 to avoid more than 5% softening

Machining data:

wheel type		: alumina (77A601H8VLNAA)
wheel speed,	v_s	: 40 m/s
wheel diameter,	d_s	: 200 mm
grain thermal conductivity,	κ_{ge}	: 35 W/mK
grain radius,	r_o	: 15μm
roughness ratio,	R_r	: 10(dry grinding)
energy to chips,	e_{ch}	: 6 J/mm^3
force ratio,	μ	: 0.4

Maximum temperature-438 deg. based on zero residual stress.

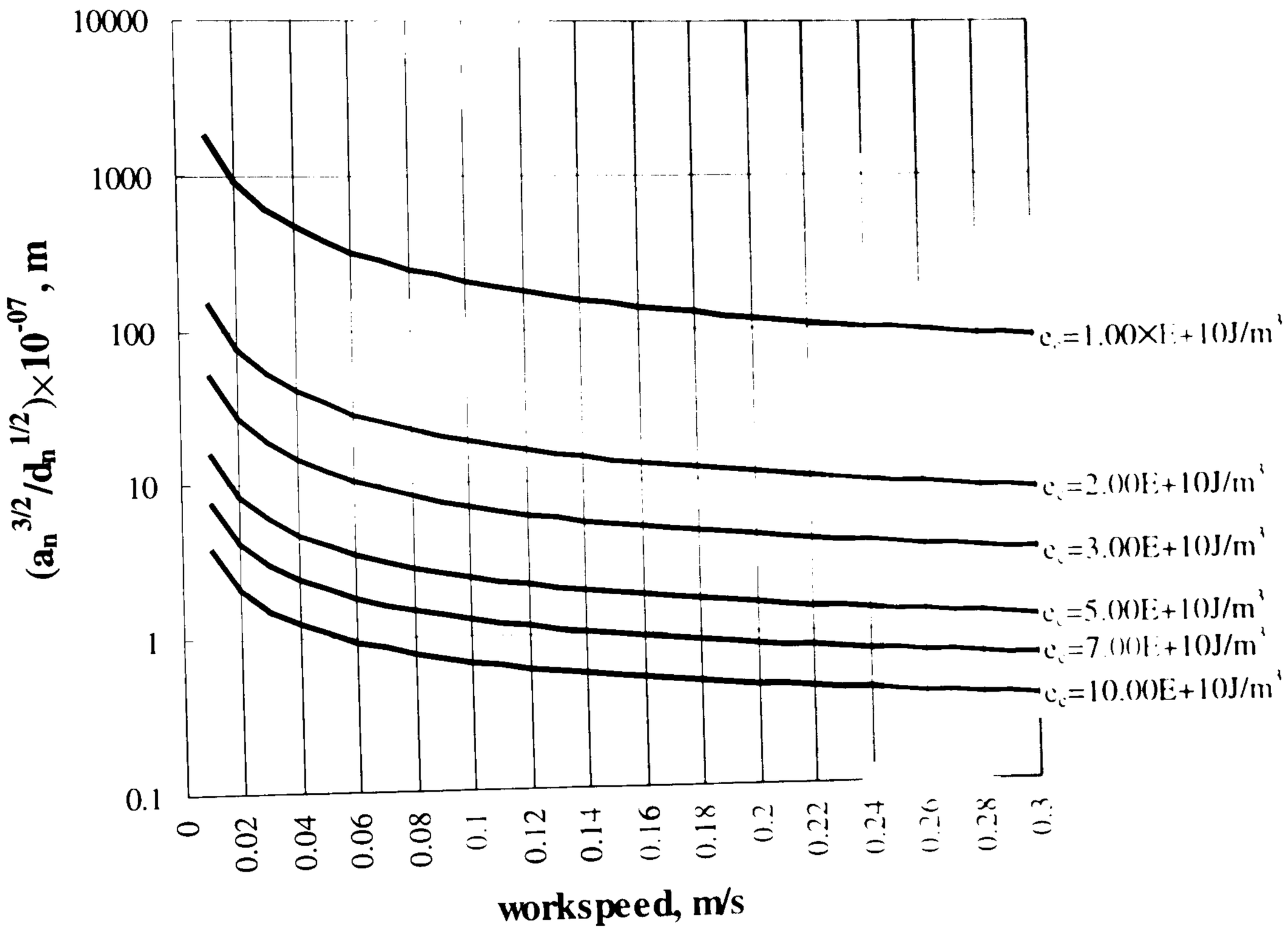

Figure 9.3 Design chart for En31 to avoid tensile residual stresses

Machining data:

wheel type		: alumina (77A601H8VLNAA)
wheel speed,	v_s	: 40 m/s
wheel diameter,	d_s	: 200 mm
grain thermal conductivity,	k_{ge}	: 35 W/mK
grain radius,	r_o	: 15μm
roughness ratio,	R_r	: 10(dry grinding)
energy to chips,	e_{ch}	: 6 J/mm^3
force ratio,	μ	: 0.4

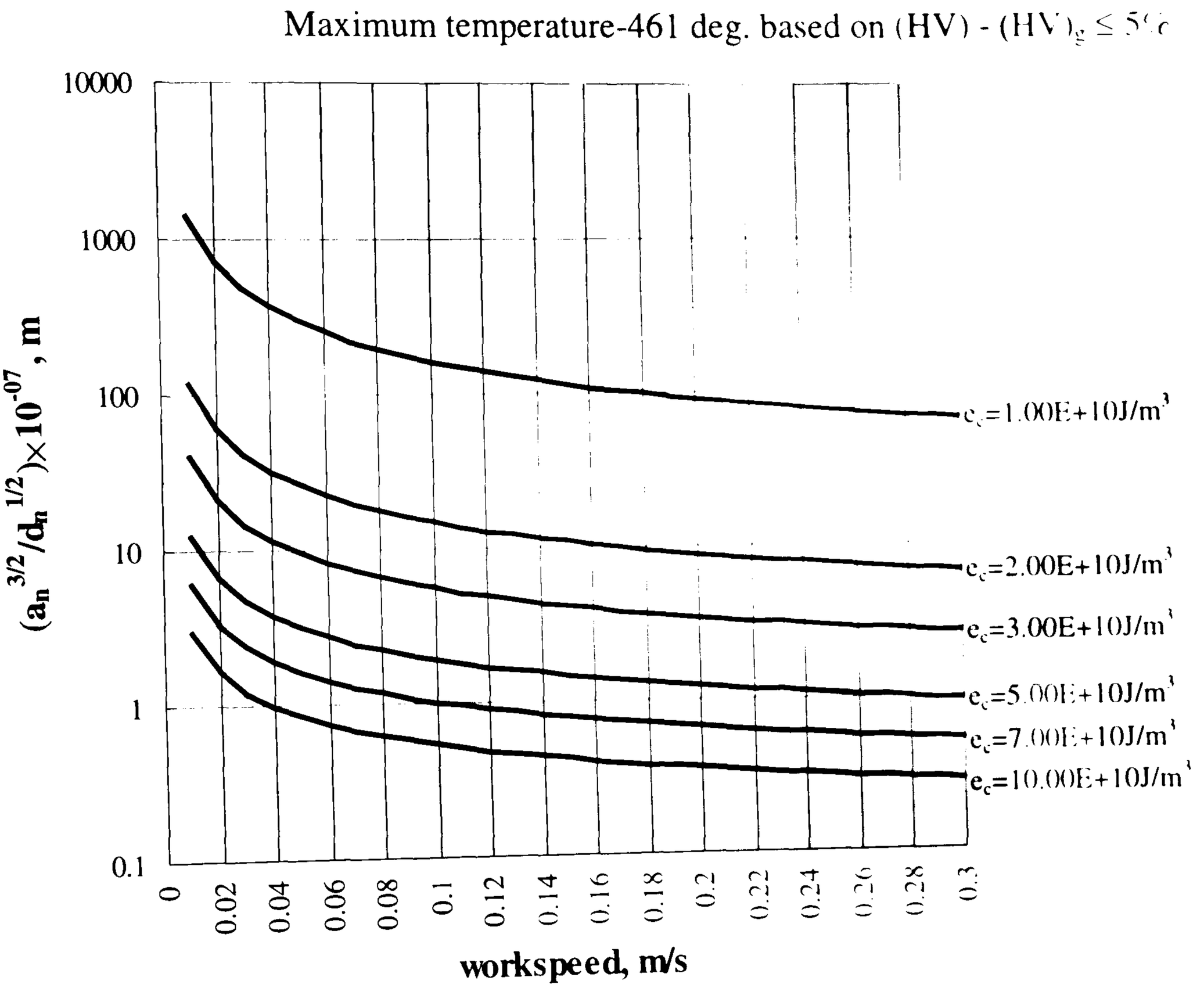

Figure 9.4 Design chart for M2 to avoid more than 5% softening

Machining data:

wheel type		: alumina (77A601H8VLNAA)
wheel speed,	v_s	: 40 m/s
wheel diameter,	d_s	: 200 mm
grain thermal conductivity,	k_{ge}	: 35 W/mK
grain radius,	r_o	: 15μm
roughness ratio,	R_r	: 10(dry grinding)
energy to chips,	e_{ch}	: 6 J/mm^3
force ratio,	μ	: 0.4

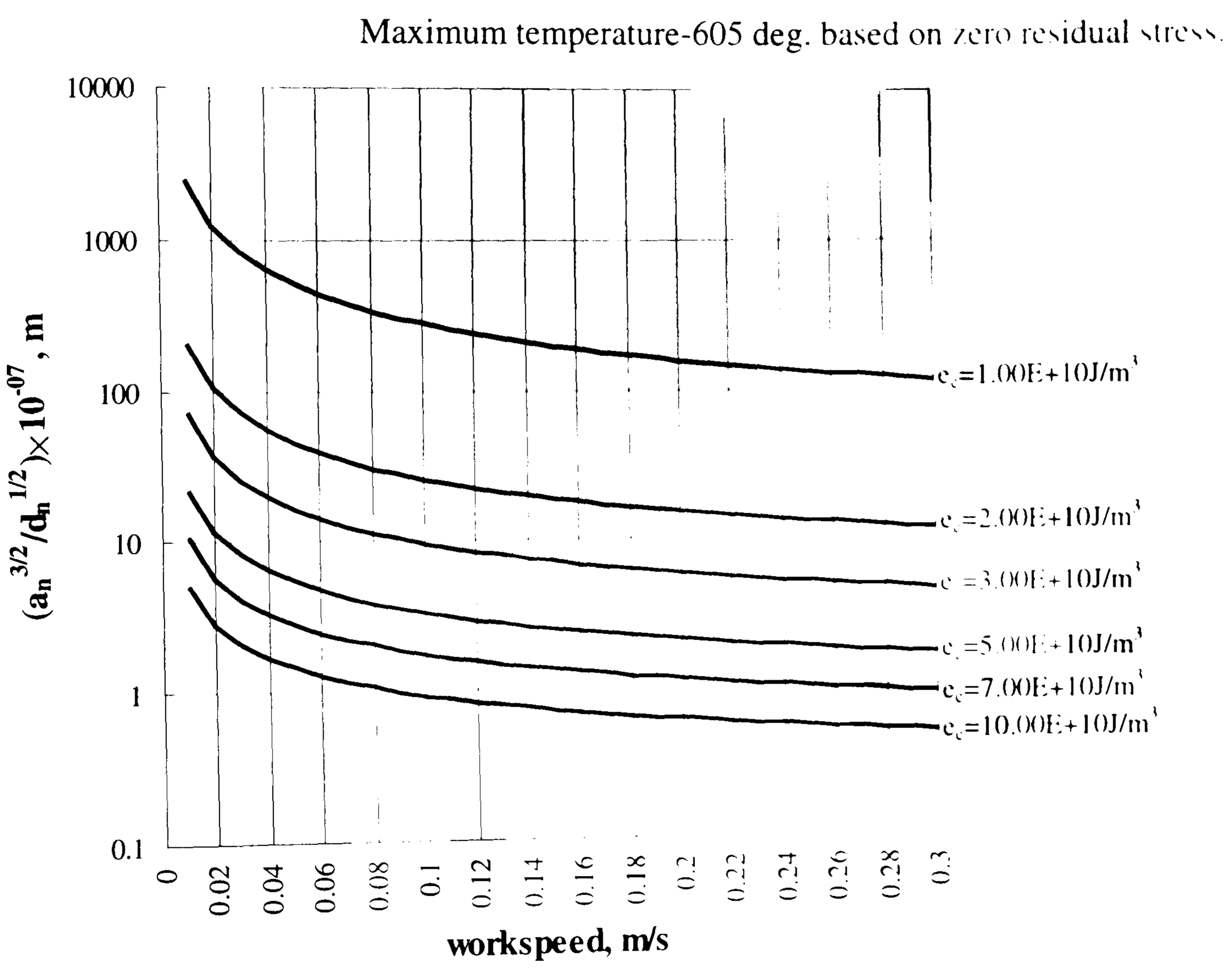

Figure 9.5 Design chart for M2 to avoid tensile residual stresses

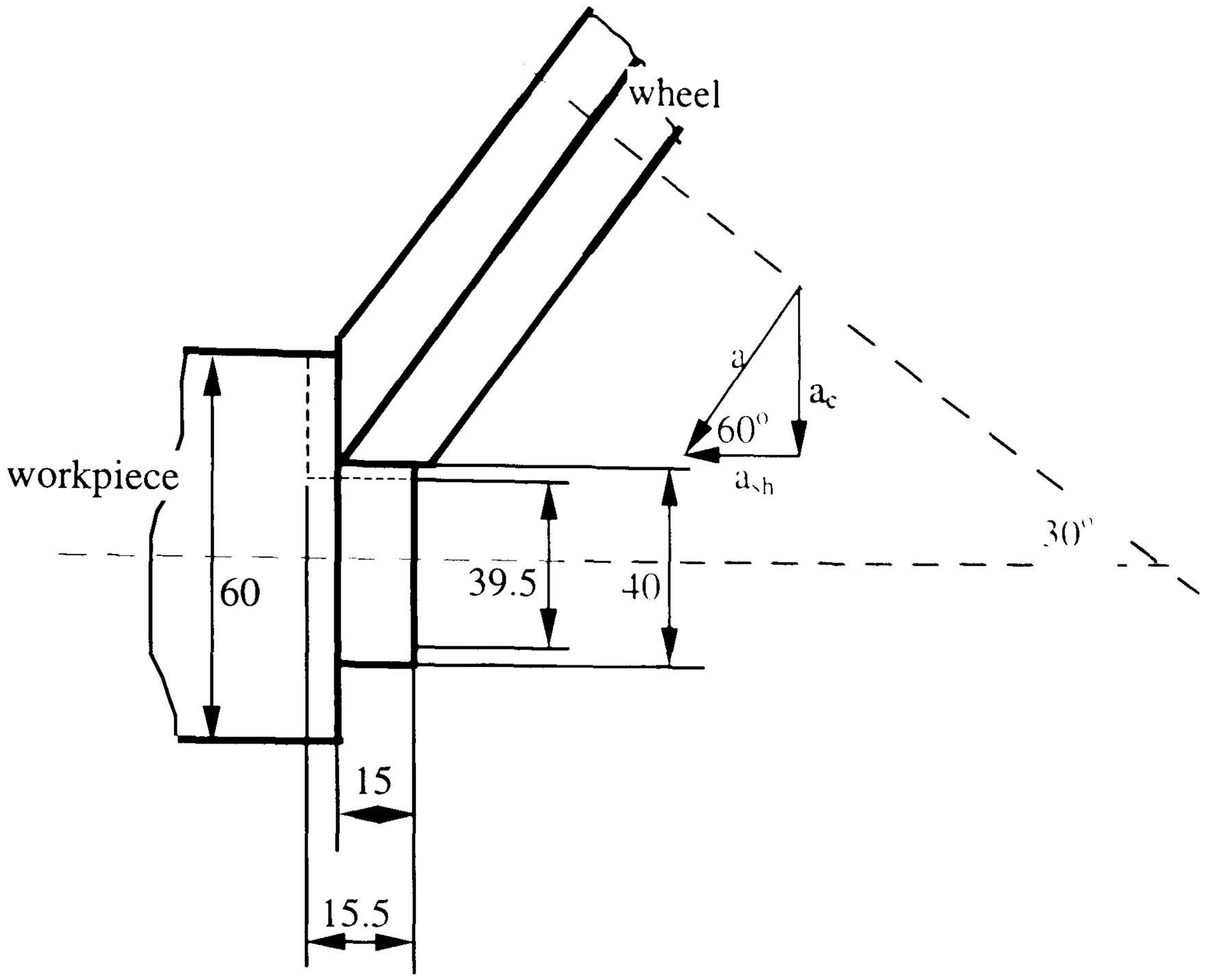

Figure 9.6 The workpiece using angle approach grinding